A Search for the Neutrinoless Double Electron Capture of ^{36}Ar and a Measurement of the Specific Activity of ^{39}Ar in Atmospheric Argon with the DEAP-3600 Detector

by

Matthew G. Dunford

A Dissertation submitted to
the Faculty of Graduate and Postdoctoral Affairs
in partial fulfilment of
the requirements for the degree of
Doctor of Philosophy

Ottawa-Carleton Institute for
Physics

Department of Physics
Carleton University
Ottawa, Ontario, Canada
July 12, 2018

Abstract

The DEAP-3600 Dark Matter detector, located 2 km underground at SNOLAB, uses up to 3600 kg of natural atmospheric argon as its detection medium. The isotopes ^{36}Ar and ^{39}Ar are present in small quantities in argon found in the atmosphere, and so are present within DEAP-3600. These isotopes can be examined in data collected for a Dark Matter search.

^{36}Ar could undergo an exotic decay process called neutrinoless double electron capture. This decay violates lepton number conservation and its observation would provide a clear indication of physics beyond the Standard Model of Particle Physics. Three modes of this decay with different final states could be detected with DEAP-3600 if they occur. A search for this decay was performed on an isotopic exposure of 6.67 kg·years with the DEAP-3600 detector. A fit to this data has yielded lower limits on the half-life of ^{36}Ar of $T_{1/2} > 4.8 \times 10^{20}$ years.

^{39}Ar is a beta-emitting isotope and is a major background for DEAP-3600 and other argon-based dark matter experiments. A measurement of the specific activity of ^{39}Ar in natural atmospheric argon has been performed on a total argon mass exposure of 2200 kg·years taken over a period of 12 months; 185 individual measurements were made. The specific activity is determined to be $(0.953 \pm 0.028)\mathrm{Bq\cdot kg^{-1}_{^{atm}Ar}}$, corresponding to a concentration of $(7.6 \pm 0.2)\mathrm{x}10^{-16}$ $\mathrm{g_{^{39}Ar}/g_{^{atm}Ar}}$.

Acknowledgments

I would first like to thank Dr. Kevin Graham and Dr. Björn Lehnert for their guidance and support over the time that I have been a part of the DEAP collaboration, and must again thank Kevin for all of the time I have spent at Carleton. I feel I have grown as a physicist, and while this is surely the point of completing a PhD, I didn't know beforehand where this journey would take me or how it would shape me; thank you both for laying down the path.

Next I would like to thank my fellow DEAP collaborators at Carleton who have helped make my time here enjoyable and who have been always been generous with their time to discuss analysis work with me (and, let's face it, lots of *non*-analysis talk and laughs over beer). Thank you Dr. Mark Boulay, Dr. Marcin Kuźniak, Dr. Rob Stainforth, Dr. Shawn Westerdale, Dr. Chris Ouellet, Andrew "Llamathrust" Erlandson, Carl Rethmeier, Ashley Kemp, Jesse Lock, Gurpreet Kaur, and Shivam Garg. Additionally, I would like to thank the DEAP collaboration collectively for being a great group of people to work alongside, if from afar.

Finally, I would like to thank Josh for putting up with me over the past few months as I wrote this thesis. Let's go for a walk now.

Table of Contents

List of Tables

List of Figures

Nomenclature

This thesis contains numerous acronyms and initialisms used within the fields of high energy physics and low background physics, as well as the components used to construct a detector such as DEAP-3600 and so a table of common abbreviations is included.

Abbreviation	Expansion
AV	Acrylic Vessel
BAT	Bayesian Analysis Toolkit
CMB	Cosmic Microwave Background
DAQ	Data Acquisition system
DEAP	Dark Matter Experiment with Argon Pulse-shape Discrimination
EC	Electron Capture
ECEC	Double Electron Capture
ERB	Electronic Recoil Band
GAr	Gaseous Argon
LAr	Liquid Argon
NRB	Nuclear Recoil Band
PMT	Photomultiplier Tube
PSD	Pulse-shape Discrimination
RAT	Reactor Analysis Tool
ROI	Region Of Interest
SM	Standard Model (of particle physics)
TPB	Tetraphenyl Butadiene
VUV	Vacuum Ultraviolet
WIMP	Weakly Interacting Massive Particle(s)

Table 0.1: Abbreviations used in this thesis.

Chapter 1

Introduction

The last one hundred years have been witness to remarkable discoveries and advancements in the field of Particle Physics. Foremost among the achievements of those ten decades has been the development of the Standard Model of Particle Physics; this model describes the electromagnetic, weak nuclear, and strong nuclear interactions of the elementary particles with great precision.

Despite these advancements there are major questions that the model has been unable to address. By observation the universe contains significantly more mass than is indicated by examining the luminous matter. This unknown material has been given the somewhat unimaginative name of *dark matter* to represent the fact that it does not interact with light, and also perhaps that we know very little about it. The "normal" matter that we are all familiar with - that is, protons, electrons, neutrons, et cetera - makes up less than 5% of the mass of the universe. In nature there are 4 known fundamental forces: gravity, electromagnetic, weak nuclear, and strong nuclear. The observations which tell us that dark matter exists also provide us a few clues about its nature. The first thing that we know is that dark matter interacts gravitationally with normal matter, and thus has mass. However, because the gravitational force is so much weaker than the other forces it can only be used to observe extremely large masses of dark matter; gravitational observation of individual particles is not possible. The next thing that we know about dark matter is that it does not interact electromagnetically, and so no observations can be performed through this force. It also does not interact via the strong force, and so again no observations are possible through this force. All that remains are interactions via the weak force; is it not clear either way whether dark matter interacts via this force but the potential exists; interactions such as the elastic scattering of a dark matter particle with an atomic nucleus are the basis of many dark matter experiments.

The DEAP-3600 experiment was constructed to search for dark matter. The experiment is located 2 km underground at the SNOLAB research facility located in Vale's Creighton mine near Sudbury, Ontario. The experiment uses a large target of more than 3 tonnes of liquid argon (LAr) and can observe the signals generated by weak-mediated scattering between dark matter particles and argon nuclei.

1.1 Outline

The main focus of the work in this thesis is a measurement of the specific activity of ^{39}Ar in atmospheric argon and a search for the radiative neutrinoless double electron capture (abbreviated 0νECEC) of ^{36}Ar. ^{39}Ar is an isotope that exists in atmospheric argon and a quantity on the order of nanograms is present within DEAP-3600. This isotope is radioactive and despite contributing to the total mass at the 10^{-13}% level it is the largest individual background, greater by several orders of magnitude than all other backgrounds combined. For DEAP-3600, as well as other current and future argon-based low background/rare event searches, understanding this isotope is vital. ^{36}Ar is an isotope which can decay via a rare process called double electron capture in which two orbital electrons are captured within the nucleus, converting two protons to neutrons and emitting two neutrinos. This rare decay can potentially proceed via an even rarer mode in which no neutrinos are emitted; this is 0νECEC. Observation of this decay would indicate physics unknown within the framework of the standard model and could provide further insight into the neutrino.

To provide the motivation for building DEAP, Chapter 2 will provide some of the evidence for the existence of dark matter. A discussion of the ^{39}Ar beta decay and its importance will be presented. Chapter 2 will also describe the process of 0νECEC, and the implications of physics "Beyond the Standard Model". Chapter 3 will describe the DEAP detector and its operation. This will include descriptions of the detector itself, the materials from which is it constructed and their properties, a description of the data acquisition system, and a description of the physics governing the generation of signals. Chapter 4 will describe the data set, along with the various parameters used in characterizing signals. This will include the analysis performed to understand how these parameters behave for ^{39}Ar and ^{36}Ar events and the cuts to select the events of interest. In Chapter 5 the results of the physics analyses for ^{39}Ar and ^{36}Ar will be presented. Finally, Chapter 6 will list the conclusions drawn from these analyses and discuss future prospects.

1.2 Terminology

This thesis contains several terms that are commonly and often broadly used in the field of particle physics. In this thesis these terms will be used in a precise context. To provide a clear definition of these terms as they are used in this thesis they are defined as below. Figure 1.1 shows a sample spectrum from data to provide a visual representation of several of these terms.

- A ***waveform*** is digital information from either a physics event, injected charge, or electronic background noise. It is produced by digitizing the charge collected by a PMT as a function of time to produce a histogram in 4 ns time bins over a trigger window of 16 μs.

- An ***event*** is an occurrence in the detector that causes the data acquisition system to trigger.
- A ***subevent*** is one of two or more events which occur by coincidence in the same trigger window.
- The ***runtime*** is the total time between the first and last events in a run; it does not account for time during which the data acquisition system was busy, known as ***dead time***.
- The ***livetime*** is the runtime that has been adjusted for detector dead time.
- A ***run*** is taken during the continuous operation of the data acquisition system. Runs are broken up into ***sub-runs*** of approximately 5 minutes to keep data files at a manageable size.
- ***Specific Activity*** refers to the activity of a radionuclide per unit mass of its corresponding element. This term can also refer to the activity of a radionuclide per unit mass of that particular isotope, though in such an instance it will be clearly stated.

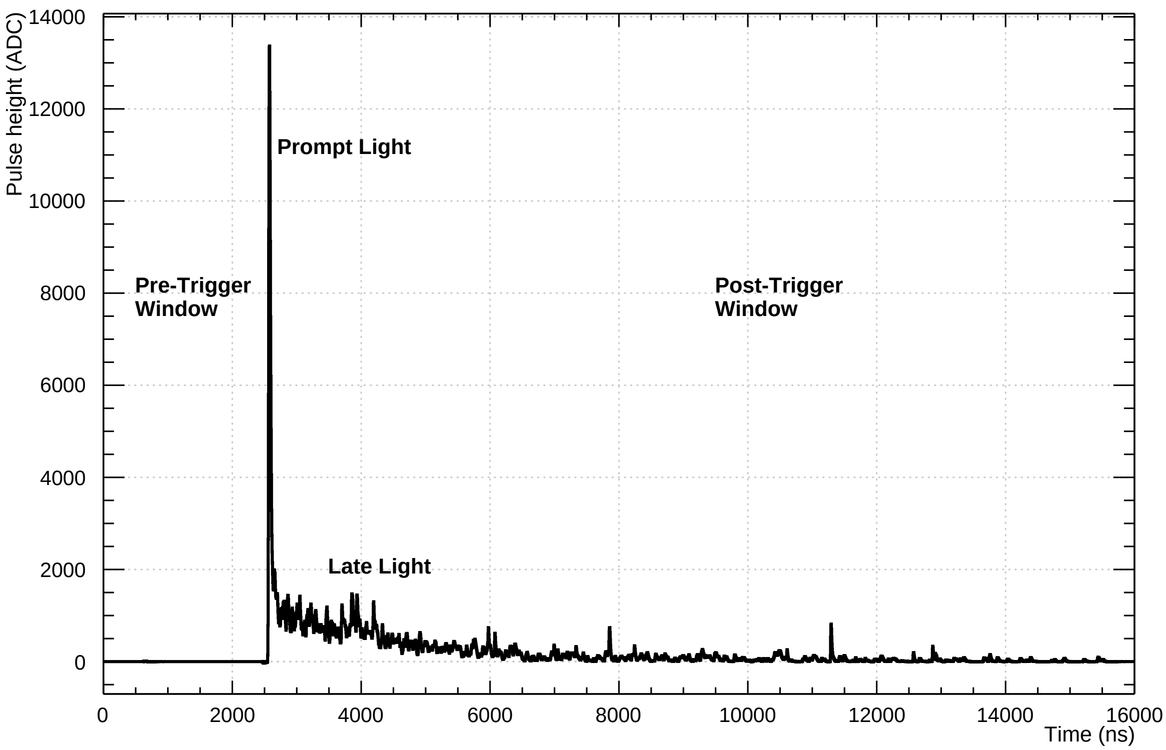

Figure 1.1: Example of an event in data, showing . This event passed the selection criteria for ^{39}Ar events.

1.3 Author's Contribution

For the ^{39}Ar analysis I developed the criteria to select ^{39}Ar decays. This included determining their individual efficiencies. The efficiencies for event selection cuts were determined through an analysis of Monte Carlo (MC) data that I generated; this MC was created with an existing Geant4 framework used by DEAP-3600. I performed all of the fits to data to extract the ^{39}Ar energy spectrum, as well as those fits used to measure systematic uncertainties from the fits. I performed the final calculations of the specific activity and its uncertainty, including a calculation of the liquid argon mass.

For the ^{36}Ar analysis I ran the MC study of three potential 0νECEC decay modes to determine a region of interest for a counting experiment; I performed the counting experiment on data that was energy-corrected by Björn Lehnert using peaks from external gamma sources. I performed fits to the ^{39}Ar spectrum from trigger board data to combine in the energy calibration with the gamma peaks. I produced toy MC spectra to test the fit's ability to find a signal.

In addition to these physics analyses I was active in monitoring the detector during the first fill with liquid argon. I have also taken regular 24 hour long data collection shifts during which I was responsible for monitoring the state of the data acquisition system, taking any special runs that have been requested, and fixing the system if any problems arose.

Chapter 2

Theory and the Physics of Signal Generation

Several experiments - including DEAP-3600 - have been built in recent years to search for dark matter. To explain the motivation for building DEAP-3600, the evidence for dark matter and a potential dark matter candidate will be briefly discussed. A description of the physics behind the generation of signals in the DEAP-3600 detector is provided along with descriptions of the physics of the two processes that are the main subject of this thesis. These processes are the beta decay of ^{39}Ar and the neutrinoless double electron capture of ^{36}Ar.

The period from the early 20th century up to present day was one which saw significant advances in the field of particle physics. Many questions arose during this period as new information was gathered, and while many of those questions have been answered a few still remain. One of those questions, a question for which answers are still sought by experiments such as DEAP-3600, deals with the significant amount of “invisible” mass in the universe. This mass - canonically referred to as “dark matter” - comprises a considerable amount of the total energy density of the universe. Figure 2.1 provides a visual representation of the fractions that compose the total energy density of the universe.

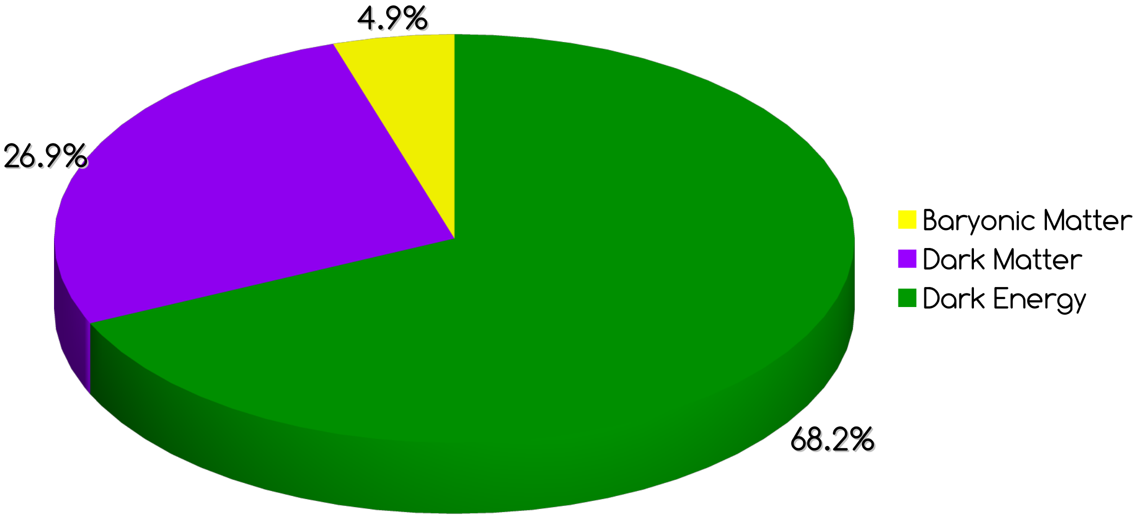

Figure 2.1: Visual representation of the total energy density composition of the universe. dark matter has been measured to be roughly 5 times more abundant than baryonic matter. This data comes from measurements of the cosmic microwave background performed by the Planck experiment [1] combined with measurements from the WMAP experiment [2]. DEAP-3600 was constructed to look for a candidate particle which could comprise some or all of the dark matter in the universe.

2.1 The Standard Model of Particle Physics

The current accepted theory which describes all known particle interactions of the electromagnetic, weak, and strong forces is called the Standard Model of Particle Physics (Standard Model, or SM). The Standard Model is, however, unable to describe several phenomena including gravity and dark matter.

Four fundamental forces of nature are known to exist; they are gravity, the electromagnetic force, the weak interaction, and the strong interaction. Gravity and the electromagnetic force are likely the two forces with which people are most familiar as we can easily observe their effects. The electromagnetic force is mediated by the photon, and though it is expected that gravity is also mediated by a particle such a particle has never been observed. The weak and strong interactions are perhaps less well known. The strong interaction is responsible for the attraction of protons and neutrons, and thus the formation of atomic nuclei. The strong interaction is only effective over very short distances (roughly the diameter of an atomic nucleus), and is mediated by gluons. The weak interaction is responsible for nuclear decays such as beta decay and is mediated by the neutral Z boson and the two charged W bosons.

All known particles are divided into two main classes, being either fermions or bosons. Fermions are particles with half-integer spins, while bosons have integer spins. Quarks and leptons, the building blocks of matter, are fermions. The particles which mediate the different fundamental forces are bosons. Hadrons are composite particles composed of quarks and exist in two classes: particles composed of three quarks are known as baryons, while particles composed of a quark-antiquark pair are known as mesons. Baryons belong to the fermion family and mesons belong to the boson family. Figure 2.2 depicts the standard model particles along with some of their properties.

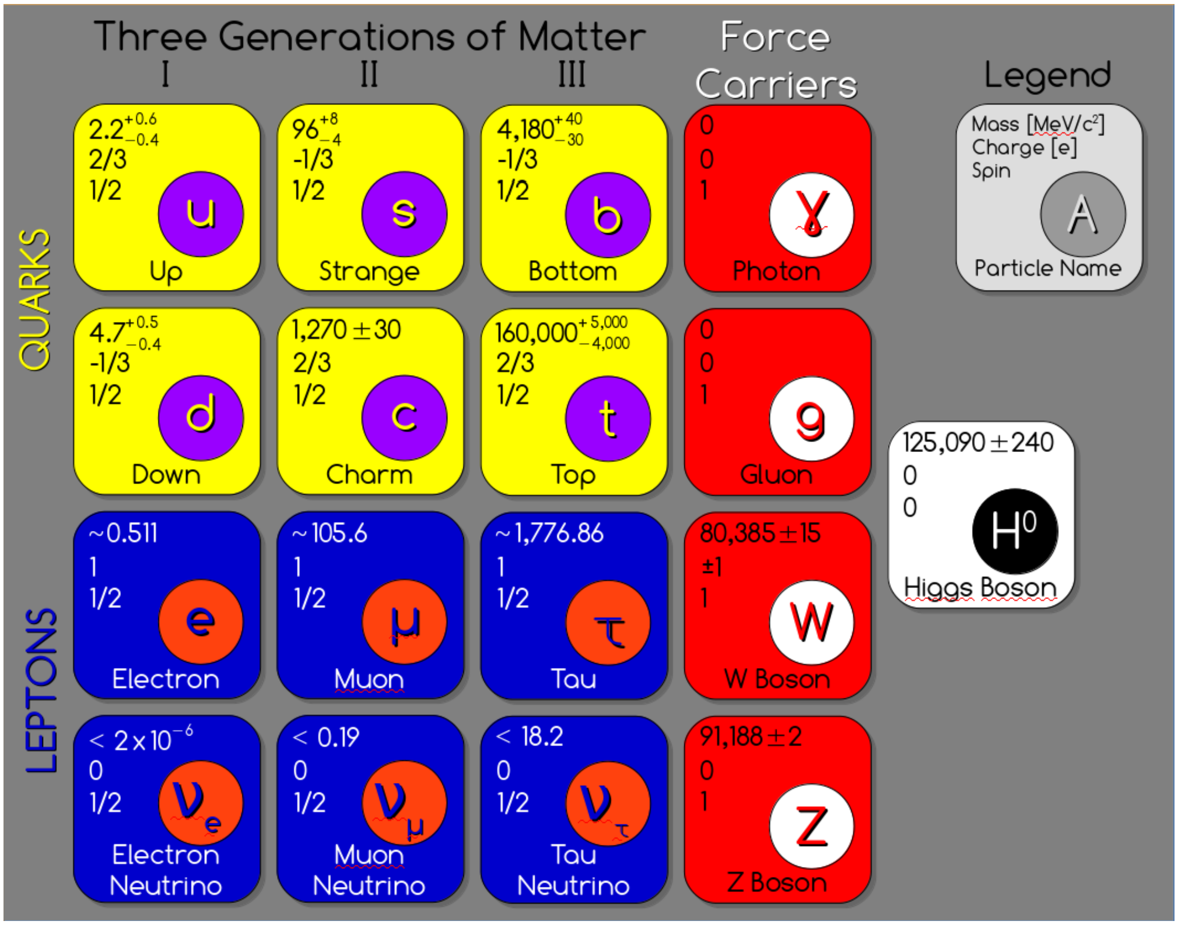

Figure 2.2: A simple depiction of the Standard Model particles. Quarks are the components of protons, neutrons, and all other baryons. Protons, neutrons, and electrons form all elemental matter. Each quark and lepton has an antiparticle partner with the same mass but opposite electric charge. The photon mediates the electromagnetic force; the gluon mediates the strong interaction; the W and Z Bosons mediate the weak interaction. The Higgs boson creates a field which gives particles their mass. Particle data is taken from the Particle Data Group [3]

In addition to other deficiencies within the Standard Model that have been mentioned, neutrinos are not completely described. A property of neutrinos that is not described is whether they have distinct antiparticles or if they are their own antiparticles. Fermions which have a distinct antiparticle include electrons and protons, and are known collectively as Dirac fermions. Another class of fermions called Majorana fermions have no distinct antiparticle and are their own antiparticle. This class of particles was theorized in 1937 by Ettore Majorana [4] but has yet to be conclusively observed. Other particles such as photons, the Z boson, and the Higgs boson are their own antiparticles, but they are not fermions.

2.2 The Evidence for Dark Matter

A large body of evidence has been gathered over the past century which conclusively shows both that dark matter exists and that there is a lot of it. Three major pieces of evidence are: observed anomalies in the rotational curves for galaxies; observations of gravitational lensing around objects far in excess than what just the visible matter could produce; observations of the structure seen in the cosmic microwave background.

Prior to the 1930s, there was a modest amount of evidence for the existence of dark matter. Previous observations and measurements had hinted at the existence of this unknown source of mass, though it wasn't until the measurements of the Coma galaxy cluster by Fritz Zwicky [5, 6] and of the rotational curves of galaxies by Vera Rubin [7–10] that the evidence became very convincing. Galactic rotational curve anomalies and gravitational lensing by dark matter will be discussed further in the following sections. The observations discussed in the following sections account for some of the evidence for dark matter, and while not intended to be a comprehensive study of the subject they will provide the motivation for constructing DEAP-3600.

2.2.1 Galactic Rotational Curve Anomalies

A galactic rotational curve describes the rotational velocities of luminous matter versus their position relative to the centre of the galaxy. The expected behaviour of this curve is increasing velocities near the dense galactic centre followed by decreasing velocities for objects further from the centre. This is the curve that one would expect if the majority of the galaxy's mass were contained in the luminous matter.

The reality is that observations of these curves do not match predictions. Stars near the edge of the galaxy have rotational velocities much greater than expected; observations have shown relatively constant velocities as a star's position increases radially outward from the centre of a galaxy, as shown in Figure 2.3. These observations indicate that the total mass of many galaxies is much greater than is indicated by the luminous matter; a very massive halo of dark matter is inferred to account from this gravity-based measurement.

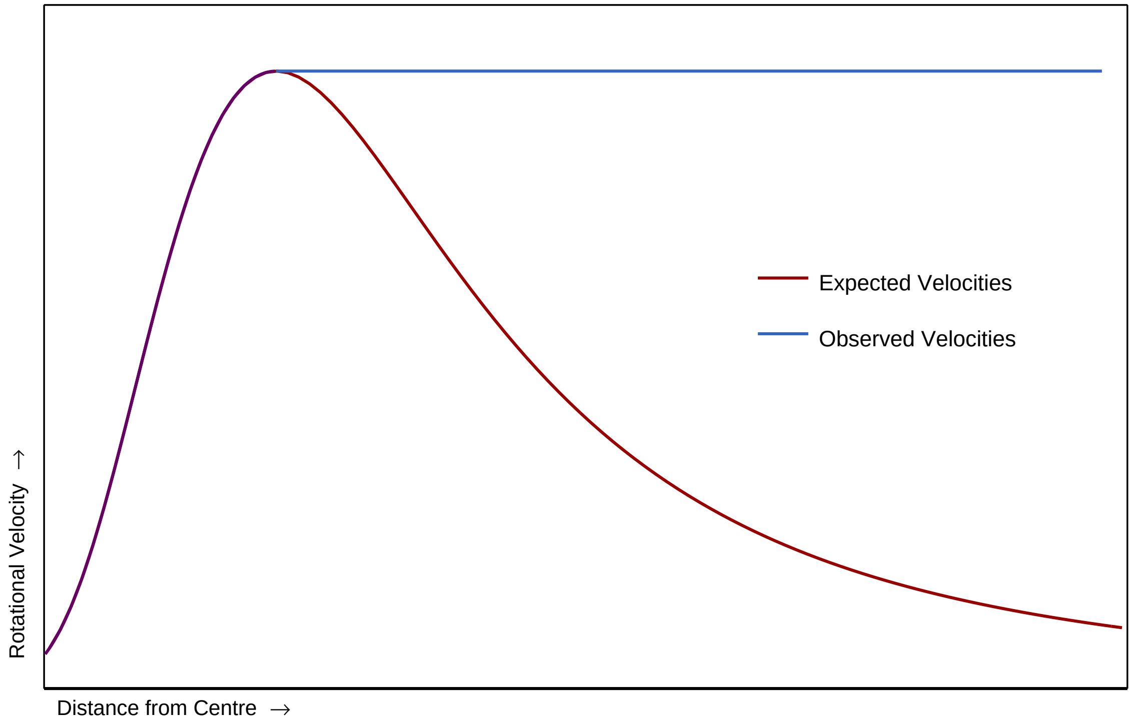

Figure 2.3: An illustration of a typical observed galactic rotational curve shown with the predicted curve. The relatively constant velocity with increasing radius is the result of an invisible halo of dark matter.

2.2.2 Gravitational Lensing by Dark Matter - The Bullet Cluster

Gravitational lensing is an effect by which electromagnetic radiation is refracted around extremely massive objects due to the warping effect of their gravity on space-time. This effect has been observed in an object known as the Bullet Cluster which consists of two colliding galactic clusters. Gravitational lensing studies of the Bullet Cluster show that there are centres of mass that do not coincide with the locations of luminous matter measured by Chandra through x-ray imaging; this observation provides significant evidence for the presence of a considerable amount of dark matter [11]. Figure 2.4 shows an image of the Bullet Cluster.

2.2.3 A Candidate for Dark Matter: Weakly Interacting Massive Particles

Weakly Interacting Massive Particles (WIMPs) are a proposed class of non-baryonic particles which have two defining characteristics: WIMPs are relatively heavy particles, with masses expected to be on the order of $\sim$100 GeV/c^2; WIMPs interact only through the force of gravity and the weak force. At the atomic scale the force of gravity is exceptionally weak and has virtually no effect on the interaction of two particles. As such, the only way to observe WIMPs directly will be through their interactions with normal matter by way of the weak force. This interaction could be the scattering between a WIMP and an atomic nucleus; the nucleus would recoil and deposit energy within the detector which could be detected as, for example, ionisation or scintillation. In DEAP-3600 the scintillation light is observed and it is this potential scattering process for which DEAP-3600 is searching. The scintillation process is described in greater detail in Section 2.5.

In liquid argon (and other noble liquids) the amount of scintillation light produced

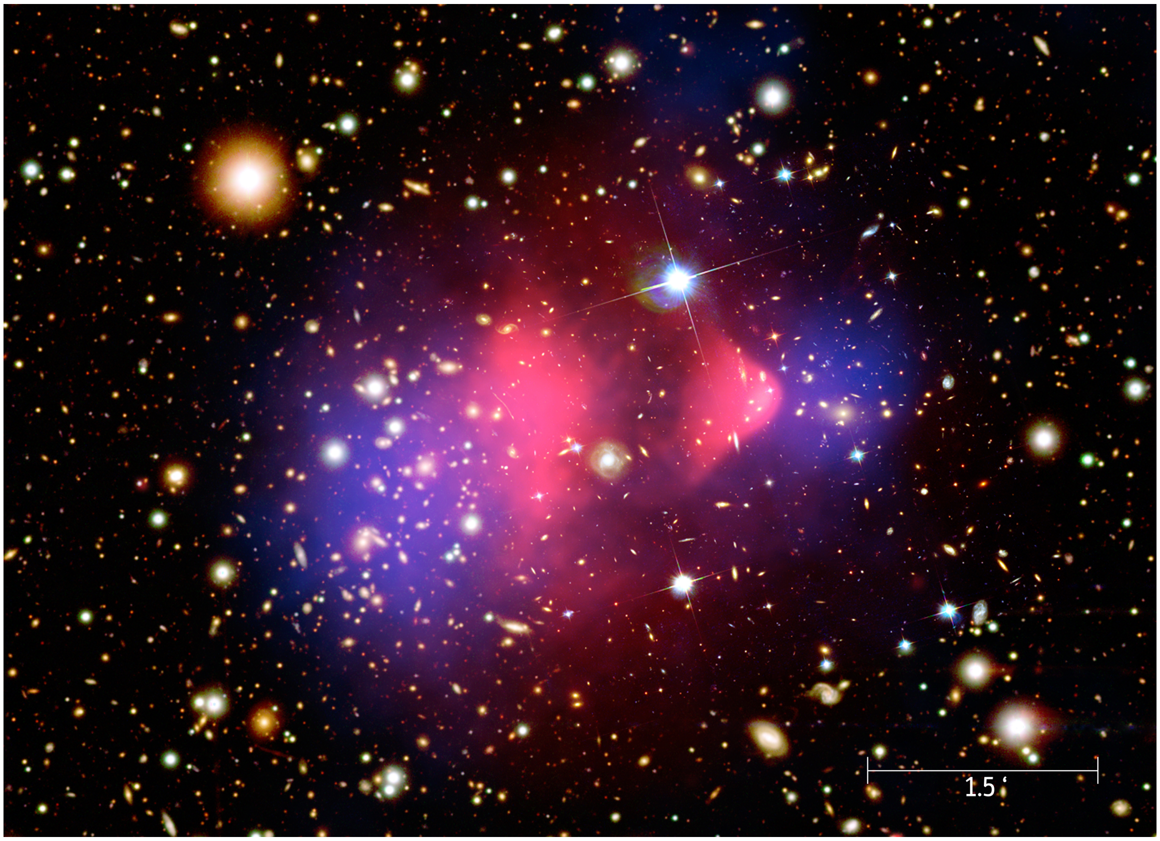

Figure 2.4: The Bullet Cluster; The visible spectrum image is overlain with an x-ray image (in pink) and with the matter distributions based on weak gravitational lensing measurements (in blue), taken with the Chandra X-ray Observatory [12]. The difference between the pink and blue regions provides a clear indication of the presence of a significant amount of non-luminous matter.

is less for a nuclear recoil than it is for an electronic recoil of the same energy. The amount of energy transferred to a nucleus during a scattering process is typically measured in keVr (keV recoil). This differs from electronic recoils which are typically measured in keVee (keV electron-equivalent); a conversion between the two energy scales is given by the following:

$$\mathrm{E}_{keVee} = \mathrm{E}_{keVr} \cdot \mathcal{L}_{eff}, \tag{2.1}$$

where $\mathcal{L}_{eff}$ is the nuclear recoil scintillation efficiency. The ratio of scintillation efficiencies between nuclear recoils and electronic recoils has been measured in liquid argon with no applied electric field, giving a value of $\mathcal{L}_{eff} = 0.25 \pm 0.01 + 0.01$(correlated) for recoils energies in the [20 - 240]keVr [13](2012) and more recently $\mathcal{L}_{eff} = 0.30 \pm 0.02$ in the [16 - 120]keVr range [14](2015). $\mathcal{L}_{eff}$ is also relatively constant within the [40 - 511]keVee range [15](preprint, 2018).

2.3 ^{39}Ar and Beta Decay

Beta decay is a type of radioactive decay in which a neutron bound in an atomic nucleus is converted to a proton, emitting an electron and an electron anti-neutrino. This process is described below:

$$^{A}_{Z}X_N \rightarrow ^{A}_{Z+1} X_{N-1} + e^- + \bar{\nu}_e. \tag{2.2}$$

The total kinetic energy of the three final state particles is the difference between the mass of the initial state and the sum of the masses in the final state; this difference is called the Q-value. This is a three-body decay and the relative angles between the momenta of the decay products can vary. This results in the final state electron emitted with a continuous spectrum of energies.

2.3.1 Beta Decay of ^{39}Ar

$^{39}_{18}\mathrm{Ar}_{21}$ is an isotope of argon with 21 neutrons. This isotope is unstable and undergoes beta decay with a half-life of (269 ± 3)years [16] to the stable isotope ^{39}K and is shown in Eq. 2.3. The Q-value for this decay is (565 ± 5) keV [17]. The mass of the daughter isotope is approximately 70,000 times greater than that of the emitted electron, and so its recoil energy is not significant. This is a unique first-forbidden decay.

$$^{39}_{18}Ar_{21} \rightarrow^{39}_{19} K_{20} + e^- + \bar{\nu}_e. \tag{2.3}$$

Figure 2.5 shows a theoretical electron energy spectrum calculated in 1969 by Behrens and Janecke [18]. This spectrum is the default spectrum used for fits to measure the ^{39}Ar specific activity. This spectrum was chosen as the default because it is implemented as the ^{39}Ar spectrum in the software with which the DEAP collaboration performs Monte Carlo simulations.

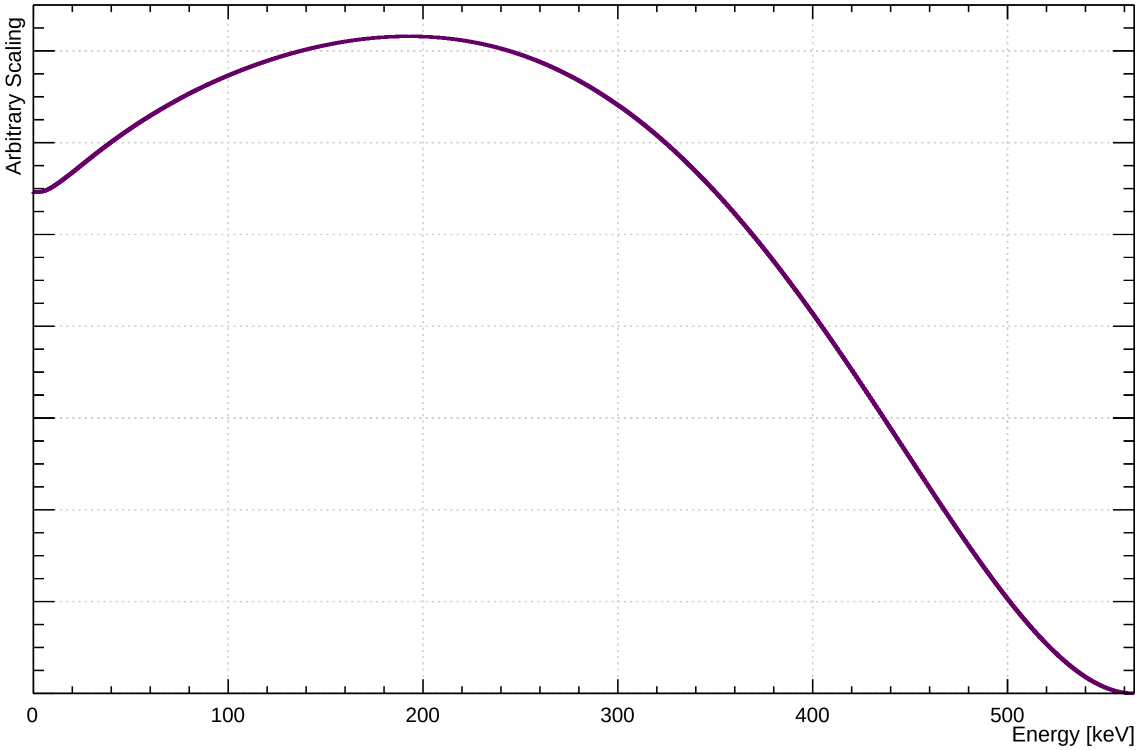

Figure 2.5: A theoretical ^{39}Ar beta decay energy spectrum calculated by Behrens and Janecke. This spectrum is used as the default model when fitting the ^{39}Ar spectrum in data.

Because there are theoretical uncertainties associated with calculating such a spectrum, a second (and more recent) spectrum is examined as a test of the theoretical model. This spectrum, from 2017, was calculated by J. Kostensalo, J. Suhonen and,

K. Zuber (KSZ) [19] using next-to-leading order weak theory and includes the microscopic quasiparticle phonon nuclear model (this model is described in [20]). This spectrum is also fit to data to estimate a systematic uncertainty associated with the theoretical model.

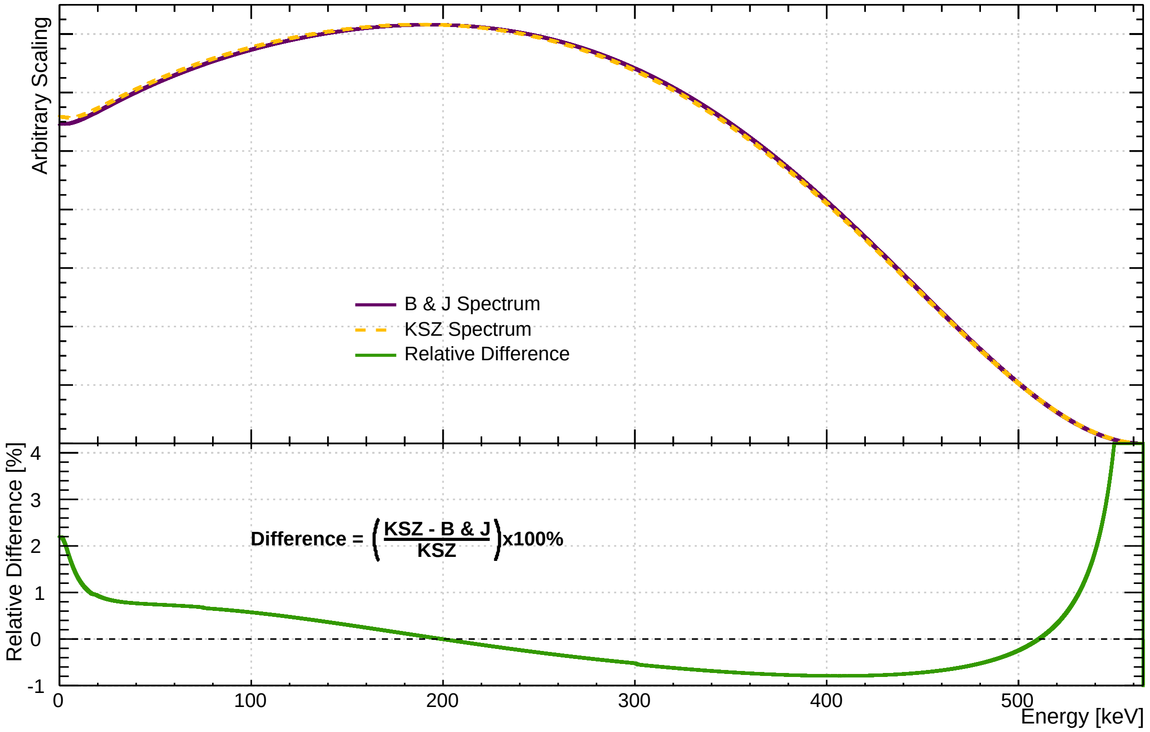

Figure 2.6: The Behrens and Janecke spectrum is compared with a spectrum calculated by Kostensalo, Suhonen, and Zuber (KSZ). The KSZ spectrum is used as a check against the Behrens and Janecke spectrum and to estimate the systematic uncertainty of the fit model.

^{39}Ar is produced in the atmosphere mainly through the interaction of a cosmic-ray induced neutron and an ^{40}Ar atom through neutron capture and subsequent neutron emission

$$ {}^{40}_{18}\mathrm{Ar}_{22} + n \rightarrow {}^{41}_{18}\mathrm{Ar}_{23} \rightarrow 2n + {}^{39}_{18}\mathrm{Ar}_{21}, \tag{2.4} $$

and to a lesser extent by neutron capture on ^{38}Ar

$$^{38}_{18}\mathrm{Ar}_{20} + n \rightarrow^{39}_{18} \mathrm{Ar}_{21} + \gamma. \tag{2.5}$$

The production of and decay of ^{39}Ar in the atmosphere are in a steady state, and so the concentration of ^{39}Ar/$^{\mathrm{atm}}$Ar is constant. This isotope is, unfortunately, both short lived enough so as to produce a strong signal and long lived enough that one cannot simply wait for it to decay away. A measurement of the specific activity of ^{39}Ar in natural atmospheric argon is also a measurement of the concentration and is one of the main goals of this work. An existing measurement of the concentration and specific activity of ^{39}Ar was published in 2007 by the WARP collaboration. For these values they measured (8.0 ± 0.6)x10^{-16} g(^{39}Ar)/g($^{\mathrm{nat}}$Ar) and (1.01 ± 0.10) Bq/$\mathrm{kg}_{^{\mathrm{atm}}\mathrm{Ar}}$, respectively [21]. A more recent measurement (2017, in arXiv pre-print) by the ArDM collaboration gives a specific activity of (0.95 ± 0.05)Bq/$\mathrm{kg}_{^{\mathrm{atm}}\mathrm{Ar}}$ [22].

2.4 Double Electron Capture, Double Beta Decay, and ^{36}Ar

Electron capture is a type of radioactive decay that occurs when a proton bound in an atomic nucleus captures an orbital electron, converting into the slightly heavier neutron and releasing an electron neutrino:

$$p + e \rightarrow n + \nu_e \tag{2.6}$$

Analogous with the decay process of electron capture (beta decay) is the exotic decay process of double electron capture (double beta decay), which essentially involves two simultaneous decays of the “single” version. Atoms for which the ground state Z - 1 (Z + 1) daughter exists at a higher energy level than the parent may have the

Z - 2 (Z + 2) daughter which exist at a lower energy level than the parent. Since radioactive decays from relative states of low energy to high energy are not favoured in nature, electron capture (beta decay) in these atoms does not occur (or is highly suppressed). Conversely, since radioactive decay occurs from relative states of high energy to low energy, double electron capture can occur in these atoms. This process is shown below:

$$2p + 2e \rightarrow 2n + 2\nu_e. \tag{2.7}$$

Consider that leptons have a property called "lepton number" where normal leptonic matter is assigned a value of one and leptonic antimatter is assigned a value of negative one; non-leptonic matter is given no lepton number (or given the value zero). In the above equation, the initial state has a total lepton number of two and the final state has a value of two; this gives the process an overall lepton number of 2 on both sides of the equation. When the lepton number is unchanged in a decay it is known as lepton number conservation. The Standard Model only includes processes for which lepton number is conserved. In the realm of physics beyond the Standard Model this conservation may be violated. A process which violates lepton number conservation is neutrinoless double electron capture (neutrinoless double beta decay):

$$2p + 2e \rightarrow 2n. \tag{2.8}$$

In this decay the initial state has a lepton number of two but the final state has a lepton number of zero, demonstrating lepton number violation. This process could occur if the neutrino is its own antiparticle. Particles of this class - Majorana fermions - are not predicted in the Standard Model, and observation of this process would provide an indication that neutrinos are Majorana fermions. A Feynman diagram of the process is shown in Figure 2.7. The "excess energy" released may be released as either an internal conversion electron, a photon, a pair of photons, or an electron-positron pair [23]. In the case of ^{36}Ar there is not enough energy to create an electron-positron pair, but the other three modes are possible.

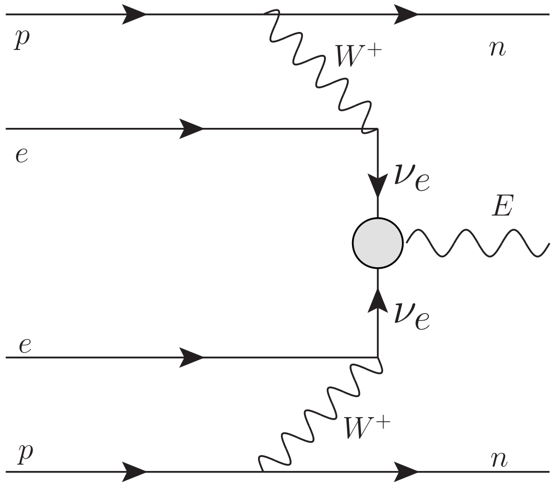

Figure 2.7: A Feynman diagram of neutrinoless double electron capture. The electrons are captured from the atom's own orbital electrons. The excess energy "E" emitted from the blob may be either an internal conversion electron, a photon, a photon pair, or an electron-positron pair.

2.5 Signal Generation in DEAP-3600

When energy is deposited in the argon, its atoms are briefly combined into excited dimer (excimer) states [24, 25]. When these states decay a photon is emitted and is eventually absorbed in a thin layer of tetraphenyl butadiene (TPB). The TPB re-emits the photon with a shifted wavelength, after which it could then be detected by one of DEAP-3600's photomultiplier tubes. This section will describe the processes of excimer creation and scintillation. TPB will be discussed further in Section 3.2.3.

Excimer States and Scintillation in Argon

Excimers are generated through either excitation of the argon atoms (Eq. 2.9) or by their ionization (Eq. 2.10), and then subsequent bonding to a neutral argon atom.

$$Ar^{*} + Ar \rightarrow Ar_2^{*} \rightarrow 2Ar + \gamma, \tag{2.9}$$

$$\begin{aligned} Ar^{+} + Ar &\rightarrow Ar_2^{+} \\ Ar_2^{+} + e^{-} &\rightarrow Ar_2^{*} \rightarrow 2Ar + \gamma, \end{aligned} \tag{2.10}$$

where the '*' denotes an excited atom or molecule and the '$^{+}$' denotes an ionized atom or molecule. Each of the above processes results in the emission of a vacuum ultra-violet (VUV) photon; this is the process of scintillation. Scintillation light from argon is emitted with a spectrum which has a peak wavelength of 126.8 nm for liquid argon at a temperature of 85 K [26]. The scintillation produces both singlet and triplet excimer states which have very different lifetimes; the singlet and triplet lifetimes have been measured to be τ_s <6.2 ns and $\tau_t = (1300 \pm 60)$ns, respectively [26]. These values are comparable to an earlier measurement which found $\tau_s = (7.0 \pm 1.0)$ns and $\tau_t = (1600 \pm 100)$ns [27].

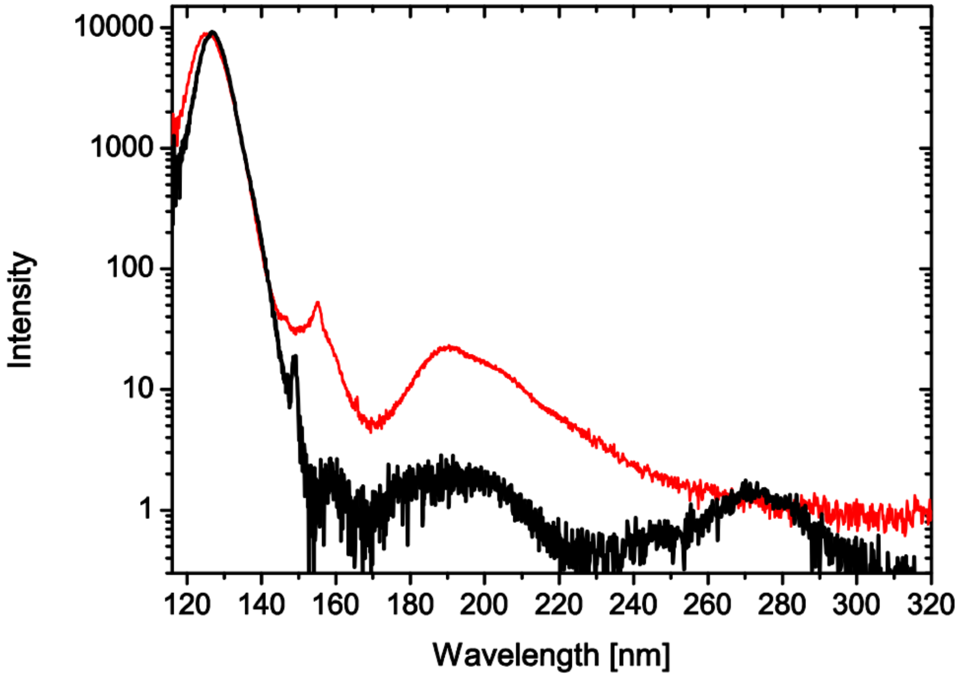

Figure 2.8: A measurement of the scintillation spectrum from GAr at 295 K (red line) and from LAr at 85 K (black line). The narrow peak in the LAr spectrum at 149.1 nm is attributed to a xenon impurity in the argon. Figure produced by Heindl et. al. in ref. [26].

Pulse-Shape Discrimination

The technique known as pulse-shape discrimination (PSD) is used by many experiments to differentiate nuclear recoils from electronic recoils [28]. The technique arises from the fact that the singlet and triplet excimer states produced in LAr have very different lifetimes, and the fact that the ratios of the excimers produced depends on the rate of energy loss of ionizing particles (dE/dx). Nuclear recoils produce a greater ratio of singlet to triplet states than electronic recoils produce; the fraction of the total light that is the early part of a waveform (prompt light) can indicate the type of recoil. If this fraction of light is plotted versus the energy of an event, one will see two distinct bands of events: a band from nuclear recoil events, the nuclear recoil band (NR band) with the fraction of prompt light around 0.7; a band from the electronic recoil events, the electronic recoil band (ER band) with the fraction of prompt light around 0.3. Figure 2.9 compares the waveforms of an electronic recoil band event with a nuclear recoil band event.

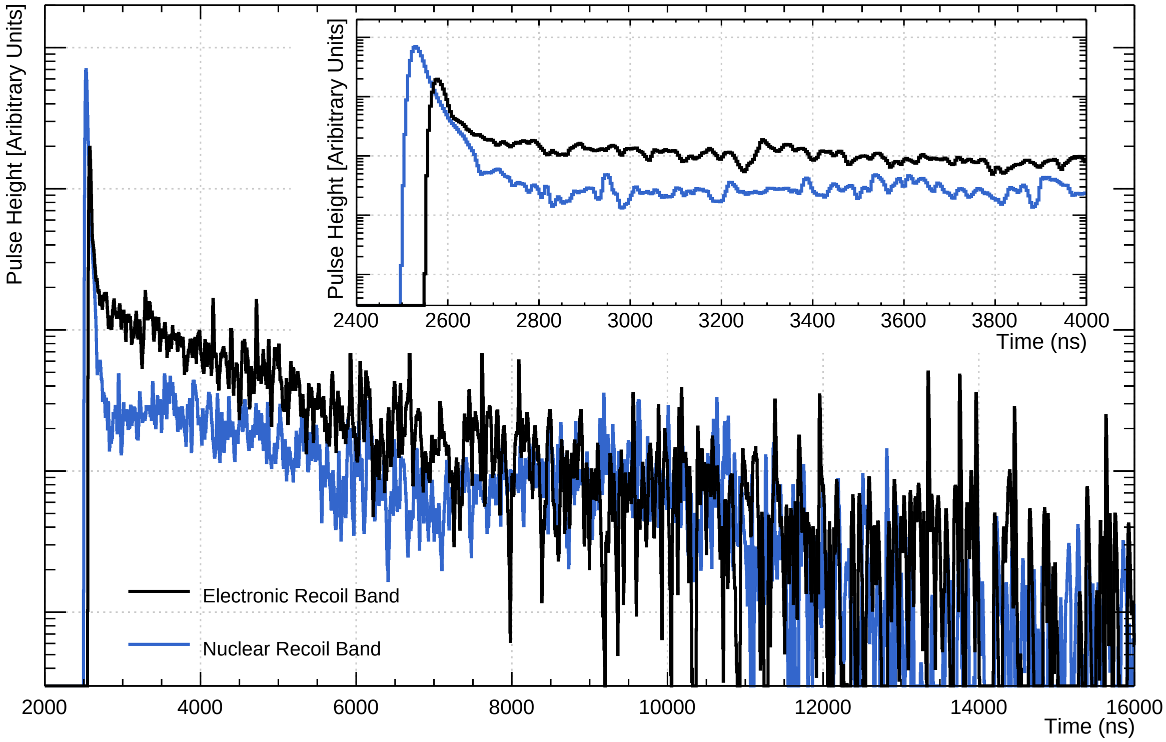

Figure 2.9: A waveform from the electronic recoil band (black) is shown with a waveform from the nuclear recoil band (blue). Each waveform has been normalized to unit area so their shapes can be compared. The nuclear recoil band waveform has significantly more of its total measured charge in the first few hundred nanoseconds compared to the electronic recoil band event. The inset shows a zoom of the early portion of the waveforms to better compare the prompt shape difference. This difference allows for pulse-shape discrimination to differentiate nuclear recoils from electronic recoils.

Chapter 3

The DEAP Experiment

The DEAP experiment began with a 7 kg liquid argon (LAr) detector known as DEAP-1. DEAP-1 was a proof-of-concept detector to show the power of pulse-shape discrimination (see Section 2.5) in separating nuclear recoils from electronic recoils - essentially separating gamma/beta background events from signal events [29, 30]. DEAP-1 has completed its main operating period and its larger sibling DEAP-3600 is currently installed at the SNOLAB research laboratory. The DEAP-3600 experiment uses a much larger target mass of LAr than DEAP-1 though it operates under the same principle of pulse-shape discrimination. This chapter will describe the DEAP-3600 detector, along with a brief description of the underground research facility which hosts DEAP-3600.

The SNOLAB Underground Research Laboratory

Experiments searching for dark matter and other rare processes such as neutrinoless double electron capture require an environment in which the background radiation is as low as possible; to this end, the backgrounds in the lab in which the experiment is proposed to reside must be understood. The DEAP-3600 experiment resides in a class 2000 cleanroom laboratory called SNOLAB. The “class 2000” classification means there is a maximum allowable concentration of 2000 airborne particles larger than

0.5 μm per cubic foot of air. SNOLAB is located on the 6800 level of the Creighton mine (that is, 6800 feet - 2072 m - below the surface) near Sudbury, Ontario. The 2 km overburden of rock corresponds to a shielding capacity of 6010 metres water equivalent (mwe) against cosmic rays, making very sensitive ultra-low background experiments a possibility. This rock shielding results in a reduction of the cosmic ray muon flux to a measured value of (0.286 ± 0.008) m^{-2}/day [31]. Both gamma and neutron backgrounds are present within SNOLAB from sources such as radon gas and the rock within which the lab is constructed. The measured gamma ray flux from the rock is given below in Table 3.1. The measured thermal neutron flux from the surrounding rock is (4145 ± 155) neutrons/m^2/day [32], and the flux of fast neutrons is estimated to be 4000 neutrons/m^2/day [32]; these neutrons are a background to the WIMP search for which DEAP-3600 was constructed. The concentration of radon gas in the SNOLAB air has been measured to be (123 ± 13)Bq/m^3 [32]; this is a combined measurement for ^{220}Rn and ^{222}Rn.

Energy [MeV]	Flux [γ/m^2/day]
4.5-5	510 ± 220
5-7	360 ± 220
> 7	180 ± 90
> 8	< 20

Table 3.1: The measured flux for various energies for gammas emitted from the rock which surrounds SNOLAB [33].

SNOLAB began as the host to the Sudbury Neutrino Observatory (SNO) [34–39], the results for which a Nobel Prize was jointly awarded in 2015 [40]. Since SNO completed its operation in the early 2000s, the underground lab has expanded greatly to a total cleanroom area of 5000 m^2 and has hosted - and continues to host - many physics experiments. A map of the SNOLAB facility is shown in Figure 3.1.

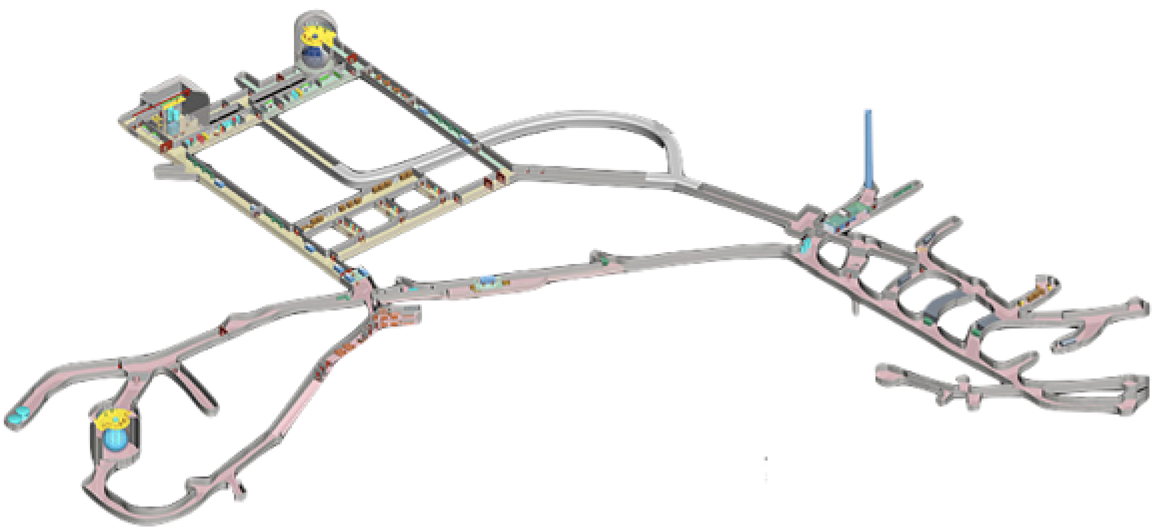

Figure 3.1: A map of SNOLAB hallways and large experimental areas. The revitalized SNO+ experiment is in the lower left. Two larger rooms in the top left, one square and one rounded, are the Cube Hall and Cryopit, respectively. DEAP-3600 resides in the Cube Hall.

Specifically, DEAP-3600 resides in the Cube Hall. The Cube Hall is approximately 18 m by 15 m, and is 20 m from floor to ceiling. The floor of the Hall is 15 m below the main level of SNOLAB, connected by a stairwell to the entrance drift. Part-way up the stairwell a mezzanine known as the deck sits at the top of DEAP-3600. The deck is where much of the experiment's process systems and data acquisition hardware are located.

3.1 The DEAP-3600 Detector: An Overview

The heart of the DEAP detector is a hollow acrylic sphere (known as the acrylic vessel, or AV) which contains liquid argon (LAr); the AV has an inner radius 846.5 mm (at LAr temperature) and a wall thickness of 50 mm. The inner surface of the AV is coated with a wavelength-shifting material which shifts the vacuum ultra-violet (VUV) light produced through interactions in the argon into the visible portion of the electromagnetic spectrum. At 255 locations around the AV are 508 mm long cylindrical acrylic light guides; attached to the end of each of these light guides is a 202 mm diameter photomultiplier tube (PMT; see Section 3.3 for more information), which are sensitive to single photons. The PMTs used are Hamamatsu model R5912-HQE which have a quantum efficiency of approximately 23% at a wavelength of 400 nm [41]. This setup is housed inside a stainless steel shell which holds dry nitrogen gas. The steel shell sits within a cylindrical tank of water with a diameter of 7.8 m; the water tank acts both as shielding from external radiation sources and as part of a veto system to tag muons passing through the detector and surrounding components. A schematic of the detector is shown in Figure 3.2. Photos taken at various stages of the construction of DEAP-3600 are shown in Figure 3.3. A complete description of the design and construction of DEAP-3600 can be found in reference [42].

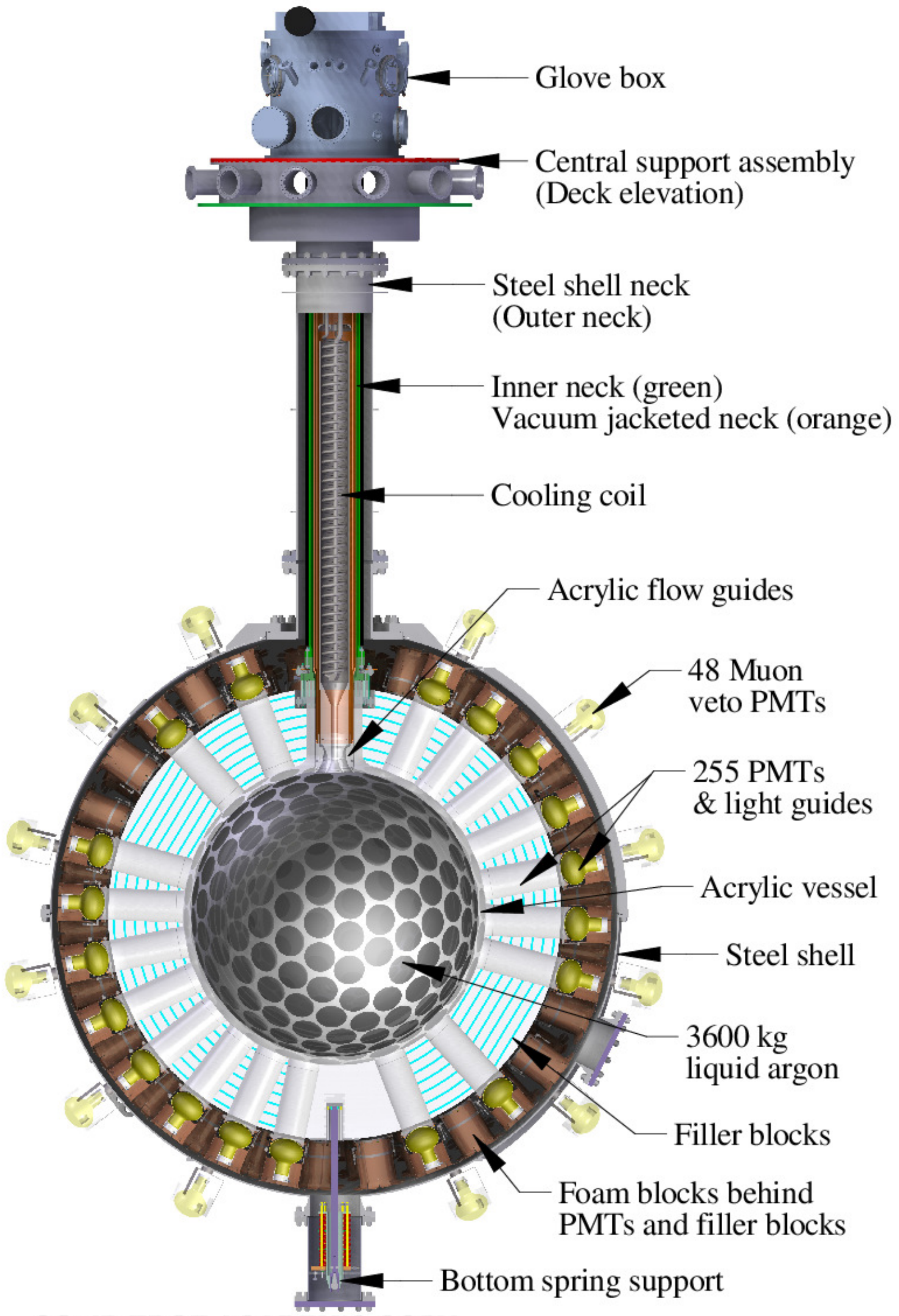

Figure 3.2: A schematic showing the components of the DEAP-3600 detector.

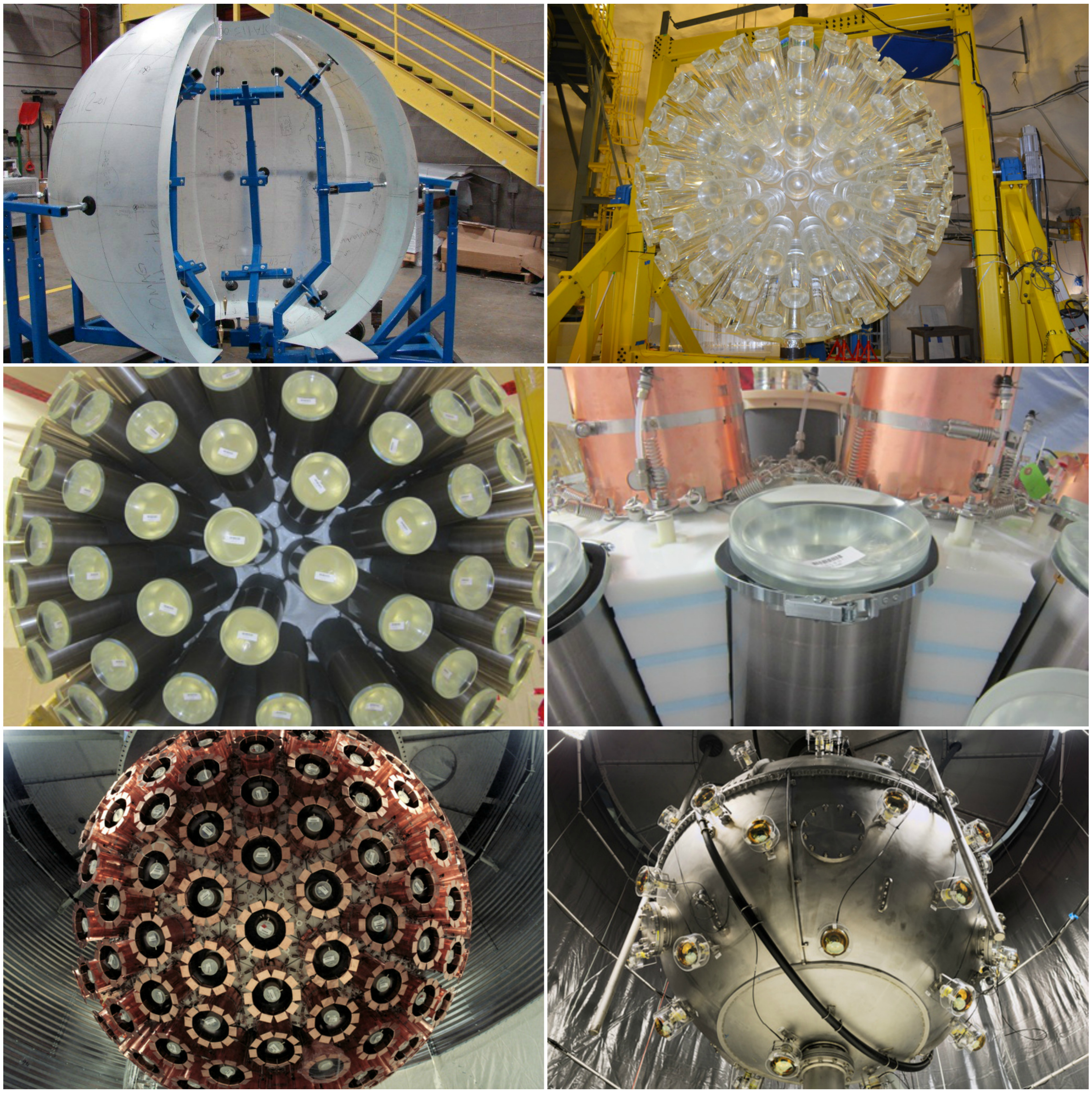

Figure 3.3: A collage of DEAP-3600 construction photos. Top left: Assembly of the acrylic vessel. Top right: All light guides bonded to the acrylic vessel. Middle left: The reflector applied the light guides. Middle right: Installation of the PMTs, PMT shielding, and filler blocks. Bottom Left: Installation of the detector in the water tank. Bottom right: The steel shell which encases the acrylic vessel; the muon veto PMTs facing into the water tank are visible.

3.2 Materials in the DEAP-3600 Detector and Their Properties

Many different materials are present in the DEAP-3600 detector. It is paramount in the design of a detector such as DEAP-3600 that the materials selected for construction are extremely radiopure. Some materials, such as the acrylic sphere and the stainless steel shell, are integral to the structural stability and/or optical requirements of the experiment even though they may introduce some radioactive backgrounds. Other materials integral to the operation of the detector, such as the liquid argon target and PMT glass, also introduce radioactive backgrounds. This section will provide descriptions of the key components and materials of DEAP-3600 and discuss their inherent radioactivity.

3.2.1 Poly(methyl methacrylate)

Poly(methyl methacrylate), perhaps better known as acrylic (or PMMA), is used for the vessel of the DEAP-3600 detector. Acrylic was chosen as the vessel and light guide material because of its optical properties; with a long attenuation length on the order of 1 m or greater [43], it can be approximately 90% transparent to the light emitted by the wavelength shifter [44] (Section 3.2.3) with some light lost due to reflection at the surfaces. In addition to its optical properties, acrylic is a structurally strong material and can be produced with high radiopurity [45, 46].

3.2.2 Argon

The noble element argon (atomic number 18) is currently present in both liquid and gas states in the DEAP-3600 detector. The abundances of various isotopes are given in Table 3.2. Natural argon (not depleted or enriched in any way) extracted from

Earth's atmosphere is used as the target medium in DEAP-3600.

Isotope	Relative Abundance [%]	Half-life	Decay Mode
^{36}Ar	0.334	Unknown†	ECEC
^{37}Ar	0	35.04 d	EC
^{38}Ar	0.063	Stable	N/A
^{39}Ar	trace	269 y	β^-
^{40}Ar	99.60	Stable	N/A
^{41}Ar	0	109.6 m	β^-
^{42}Ar	trace	32.9 y	β^-
^{43}Ar	0	5.37 m	β^-
^{44}Ar	0	11.37 m	β^-

Table 3.2: The relative abundances, half-lives, and decay modes of argon isotopes found in atmospheric argon [47]. Only stable isotopes and those isotopes with half-lives greater than one minute are listed. EC denotes electron capture, ECEC denotes double electron capture, and β^- denotes beta decay.
†Could undergo double electron capture, but the half-life has not been measured.

In addition to being a potentially good scattering target for WIMPs, argon is a favourable choice of target medium for several reasons. As the third most abundant element in the atmostphere at a concentration of 0.94% [48] argon is readily available and relatively cheap compared to other noble gases like xenon; it is easily purified to remove non-argon contaminants, radioactive or otherwise. A significant difference in the scintillation timing between electronic recoils and nuclear recoils is measured for argon which allows for signial discrimination (see Section 2.5).

Age of the Argon

Knowing the age of the argon in DEAP-3600 is important for the specific activity analysis; specifically, the time since the argon was extracted from the atmosphere and stored on or below the Earth's surface is important. After this time the rate of production of cosmogenically activated ^{39}Ar is halted, or is at least significantly reduced, and the ^{39}Ar would no longer be in equilibrium. The time since atmospheric extraction will be referred to as its age. Direct comparisons of measurements of the ^{39}Ar concentration from different argon-based experiments must consider the argon's age to be precise. With a half-life of 269 years, argon removed from the atmosphere 15 years prior would have a reduction in its ^{39}Ar content of: 1 - $2^{-15/269}$ = 3.8%; this change is greater than the uncertainty on the specific activity measurement presented in this thesis.

The filling of DEAP-3600 took place over the months of September and October, 2016; the supplier extracted argon and then it was shipped out and arrived at SNOLAB within 1 week; the argon was held in a storage container on the surface at SNOLAB for a maximum of 6 months; the argon was added to the AV within roughly 1 week after its arrival underground at SNOLAB. This makes the argon approximately 0.5 years old at the time that filling was complete and data collection had started.

An approximate reduction in the specific activity of ^{39}Ar would be: 1 - $2^{-0.5/269}$ = 0.13%. This reduction is minor and is an order of magnitude less than the uncertainty on the measurement; no corrections are made to the specific activity measurement related to age of the argon.

3.2.3 Tetraphenyl Butadiene

The VUV light produced by the scintillation of argon is not suitable for detection because many materials - including acrylic - absorb it. Furthermore, the PMTs are not sensitive to VUV light. There are however some materials which will absorb and re-emit VUV at a shifted wavelength. 1,1,4,4-tetraphenyl-1,3-butadiene ($C_{28}H_{22}$), or TPB, is an organic wavelength shifter which coats the inside surface of the acrylic shell and is used to shift the 128 nm VUV photons from the argon scintillation into the optical region. The fluorescence spectrum of TPB is shown in Figure 3.4. The peak of the spectrum is around 420 nm; the acrylic vessel and light guides are transparent to this re-emitted light. The conversion efficiency of TPB relating the number of re-emitted photons to the number of incident photons is 1.2% at an incident wavelength of 128 nm [49].

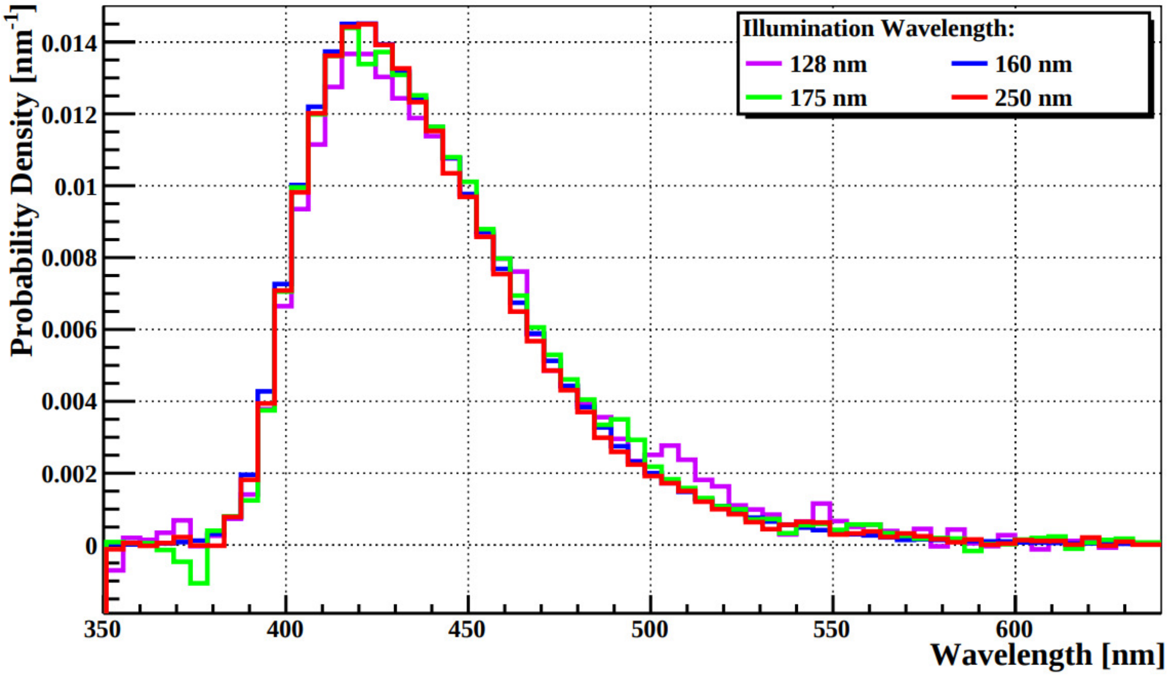

Figure 3.4: The fluorescence spectrum of TPB measured by V.M. Gehman et. al [49] for several absorbed wavelengths. Each spectrum is normalised to unit area. The spectra are peaked around 420 nm. Figure created by Gehman et al.

Application and Thickness of the TPB Coating

Before the TPB layer could be applied the inner surface of the AV needed to be cleaned of any contaminants - particularly radioactive isotopes - that may have been absorbed or adsorbed up to this stage. A custom robot known as the Resurfacer was built for this task; the Resurfacer sanded and cleared 500 μm of acrylic from the inner surface [50]. Once the resurfacing was completed, the TPB layer was deposited by vacuum evaporation. An estimated TPB thickness of $(3.00 \pm 0.02)\mu$m was achieved [51]. The efficiency for the conversion from VUV to optical wavelengths is not depenedent on the thickness of the TPB for coatings in this range [52]; the TPB response is thus expected to be uniform over the inner AV surface.

3.3 Photomultiplier Tubes

Photomultiplier tubes (PMTs) are very sensitive light detectors capable of detecting a single photon. When a photon strikes the light-sensitive end of a PMT known as the photocathode, it may liberate an electron (a "primary" electron) by way of the photoelectric effect. A high voltage is supplied to the PMT which is used to generate electric fields within the PMT which drift the primary electron to a metal plate known as a dynode. When the primary electron strikes the first dynode, several secondary electrons are ejected. Those electrons then drift to the second dynode, each ejecting more electrons which drift to the third dynode, and so on until all the electrons are collected on an anode plate. This process can amplify the original electron by a factor of up to 10^7, making the detection of a single photon possible. Figure 3.5 shows a schematic of a PMT.

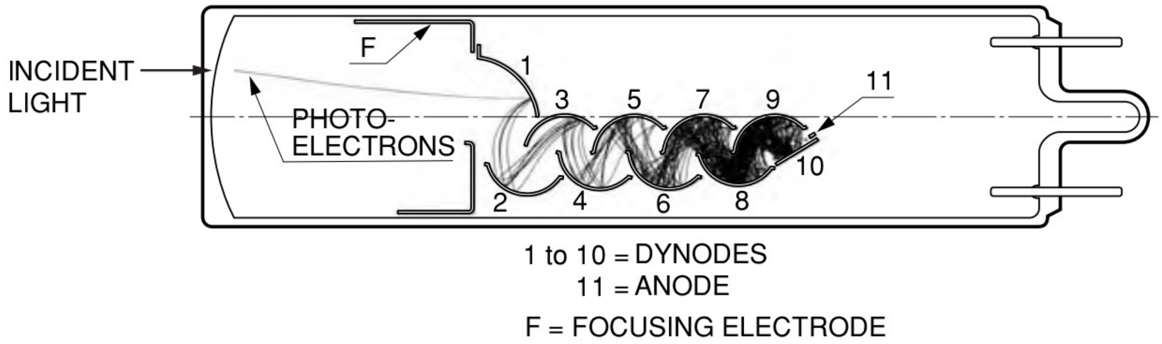

Figure 3.5: A schematic from Hamamatsu showing the multiplication process from a single electron to many electrons through the chain of dynodes [53].

Afterpulsing

Afterpulsing in PMTs is the appearance of small-amplitude pulses that occur after a signal is output. These delayed pulses can be caused by the creation of positive ions from residual gases in the PMT, drifting to the photocathode and ejecting electrons which then pass through the dynode chain. Afterpulses created in this manner can have a time delay from hundreds of nanoseconds up to several microseconds.

3.4 The DEAP-3600 Muon Veto System

The muon veto system consists of 48 PMTs (identical to those used in the original Sudbury Neutrino Observatory (SNO) [54]) which are attached to the outside surface of the steel shell, facing outward from the shell into the 7.8 m diameter water tank which encloses the DEAP-3600 detector. The PMTs can be seen in the bottom right photo in Figure 3.3. The system is used to detect incoming muons from external sources such as those produced in Earth's atmosphere that survive to the lab depth. The light-tight tank acts as a water Cherenkov detector [55]; a muon passing through the water will produce Cherenkov light [56] which can be detected by the PMTs.

A muon passing through or near the LAr volume and surrounding detector materials can produce secondary particles such as spallation neutrons; these neutrons could produce signals within the LAr volume which are indishinguishable from WIMP signals. When a muon is detected in the water tank a portion of the data (up to 5 seconds after the muon is detected) may then be removed from the data set, effectively rejecting any potential background signals that the muon might produce [57]. Tested in Monte Carlo (by other members of the DEAP collaboration), the muon veto system is expected to have a detection efficiency of greater than 96% for muons above 1 GeV [58].

3.5 The DEAP-3600 Data Acquisition System

The 255 inner PMTs and the 48 veto PMTs are connected to a robust data acquisition system (DAQ) which collects, shapes, digitizes, and stores signals from the experiment. Each PMT is connected to a signal conditioning board (SCB). The SCBs then output a signal to one of two sets of digitizers. The output from the digitizer array is read by several computers which store the data to disk. A schematic of the system is shown in Figure 3.6.

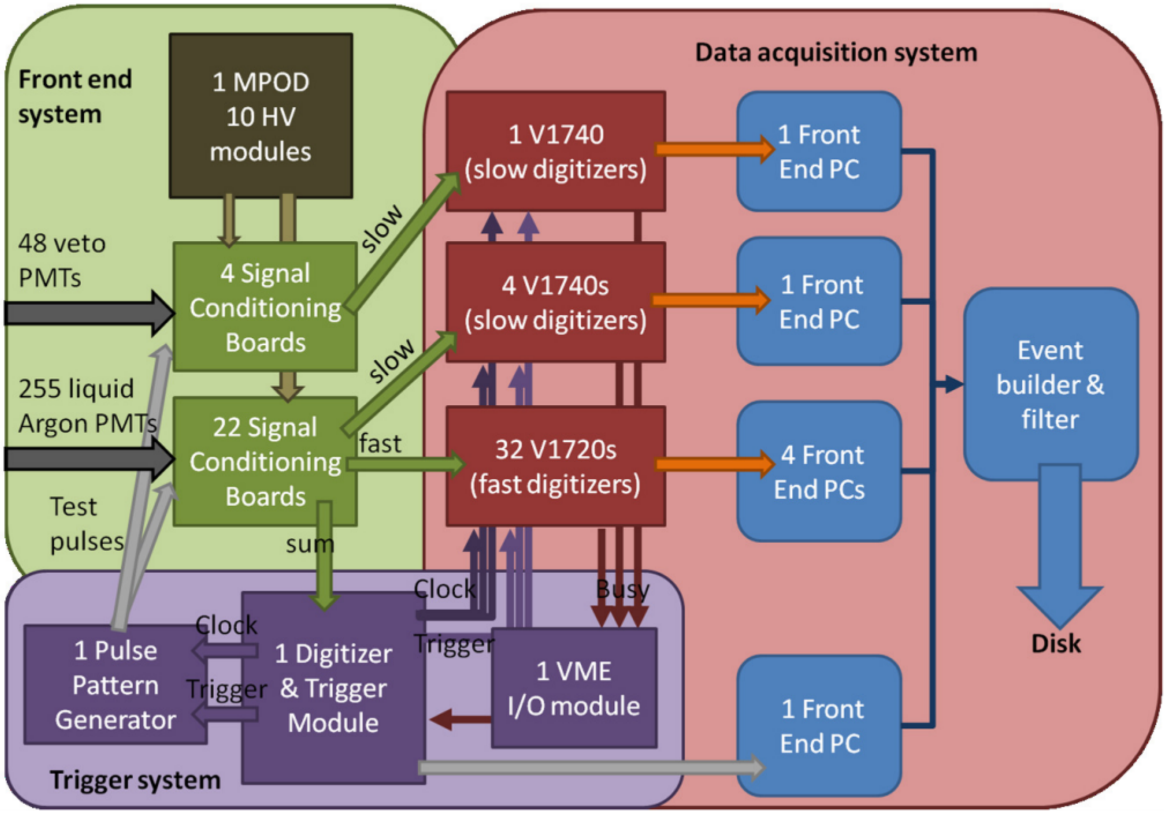

Figure 3.6: A schematic showing how the individual components of the data acquisition system are connected [59].

3.5.1 Signal Conditioning Boards

The DAQ has 26 signal conditioning boards, each with 12 channels. The SCBs are custom designed at the TRIUMF laboratory, and built at the University of Alberta.

Each PMT in DEAP-3600 is connected to its own channel, with the veto PMTs connected to 4 of the boards, and the inner PMTs connected to the remaining 22 boards. The SCBs are responsible for shaping the pulses output from the PMTs.

3.5.2 Digitizers

The DAQ includes two sets of CAEN digitizers which process the different outputs from the SCBs. The fast pulse outputs are sent to one of 32 CAEN V1720 modules (which sample the signal 250x10^6 times per second); the slow pulse outputs are sent to one of 4 CAEN V1740 modules (which sample the signal at 62.5x10^6 times per second). The digitizers convert a continuous analogue signal into a discrete digital one with time bins equal to the inverse of the sampling rate; this process is known as analogue to digital conversion (ADC).

The digital waveform output is a histogram with time bins equal to the inverse of the sampling rate. For the V1720s these time bins are $(250\text{x}10^6\ \text{s})^{-1} = 4$ ns, and for the V1740s they are $(62.5\text{x}10^6\ \text{s})^{-1} = 16$ ns. The analysis in this thesis uses the output from the V1720 digitizers; the 4 ns time bins are on the order of the lifetime of the LAr scintillation prompt component.

3.5.3 DAQ Trigger and Trigger Efficiency

The DAQ constantly monitors signals from the digitizers using two rolling windows - a narrow window and a wide window - to search for pulses. The DAQ is triggered to record a waveform in one of two ways: when instructed by an external source such as that which fires the period charge injection using a pulse pattern generator or when the integrated charge in the narrow window surpasses 1000 ADC counts. When one of these conditions is met the DAQ records a waveform; 2.5 μs before the trigger and 13.5 μs after the trigger are kept, producing a waveform of 16 μs of data. The integration windows to measure the prompt and wide charge components are 150 ns and 10 μs, respectively.

The DAQ is not always capable of detecting all signals at all energies. Specifically, lower energy events can be missed. The efficiency for the DAQ to trigger is shown in Figure 3.7. The efficiency of the trigger is 100% above a reconstructed energy of about 200 PE and above an PSD parameter value (F_{prompt}) of 0.10 [1].

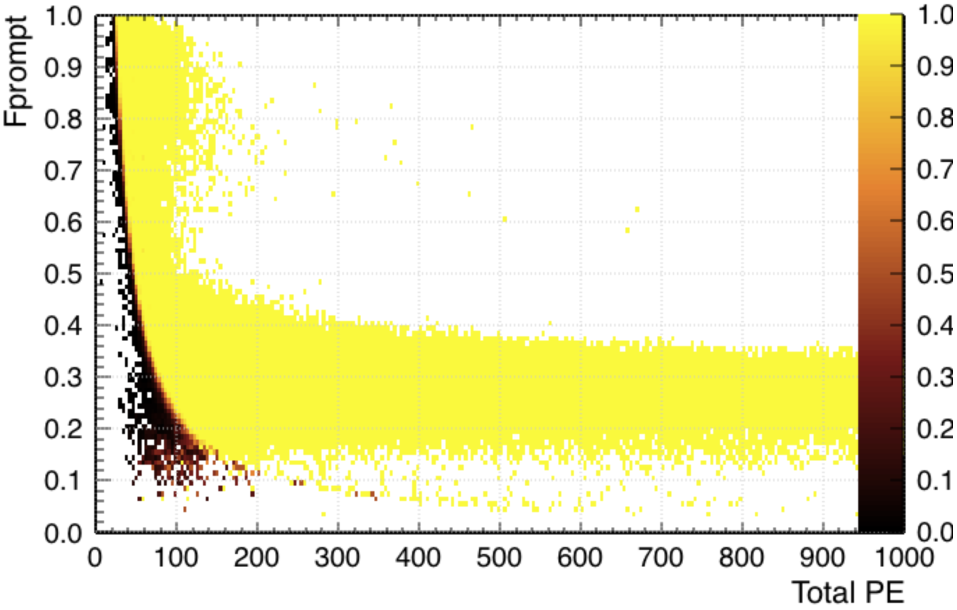

Figure 3.7: The measured trigger efficiency shown in 2D PSD space for the DEAP-3600 DAQ, where PE represents reconstructed charge of an event in photoelectrons (see Section 4.3.2) and F_{prompt} is a PSD parameter (see Section 4.3.3). The Z-axis shows the trigger efficiency. For the lowest F_{prompt} values in the electronic recoil band (around $F_{\text{prompt}} = 0.3$) the trigger efficiency is 100% above about 200 PE and above $F_{\text{prompt}} = 0.10$. This measurement was performed and this figure produced by another member of the DEAP-3600 collaboration.

^{39}Ar Region Prescaling

The rate of events in the electronic recoil band (ERB) is on the order of 3000 Hz, primarily due to the decay of ^{39}Ar. It is unnecessary to record the waveforms for each of these events and doing so would produce very large data files. To mitigate

---

[1] The parameters PE and F_{prompt} are defined in detail is Sections 4.3.2 and 4.3.3, repsectively.

the effect of the high rate only 1 out of every 100 ERB waveforms within the region dominated by ^{39}Ar beta decays and ^{39}Ar-^{39}Ar pileup are recorded; in DEAP-3600 this is known simply as prescaling. Using the charge information from the rolling windows the trigger monitors, a PSD parameter is calculated as the fraction of narrow charge (total integrated charge in the narrow window) to wide charge (total integrated charge in the wide window). Using this PSD information along with the wide charge information, the waveform is categorized into one of 5 trigger regions. A spectrum in which the different trigger regions are separated is shown in Figure 3.8; the prescaled events are those which are in Region 3. The events of interest for the analyses in this thesis are from Regions 1 and 3, and some energy calibration information comes from events in Region 5. For every event, regardless of trigger region, the narrow and wide charge information from the trigger board is stored.

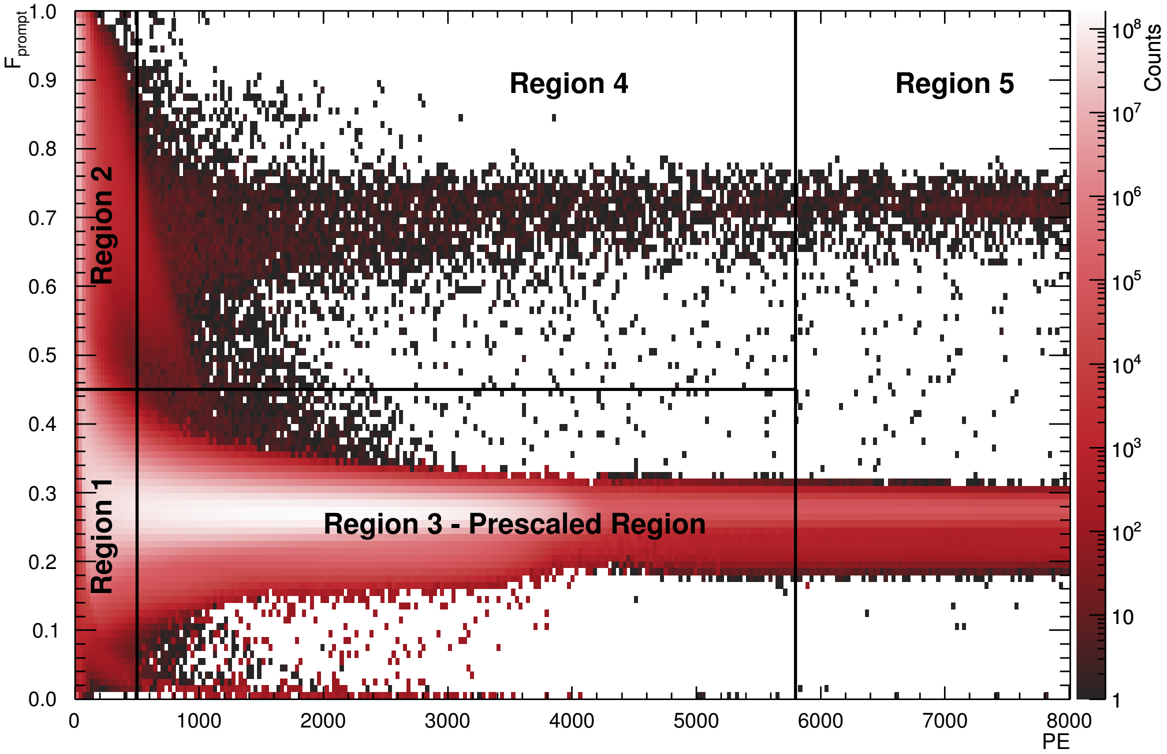

Figure 3.8: A schematic of the 5 physics trigger regions. The PE variable is a reconstructed charge estimator used in the ^{39}Ar analysis. The F_{prompt} variable is a PSD parameter calculated from reconstructed charge information (see Section 4.3.6 for details on these parameters). The boundaries shown are approximate as the actual determination is made at the trigger board level using trigger board energy information.

3.6 Electronic Recoil Backgrounds in DEAP-3600

While the DEAP-3600 detector is underground and therefore shielded from the majority of cosmic ray and cosmic ray-induced radiation present at the surface of the Earth, there are radioactive backgrounds which must be well understood for any physics analysis. The backgrounds described in this section are those which are of the greatest importance to the ^{39}Ar specific activity measurement and to the ^{36}Ar decay search which both take place within the electronic recoil band produced by PSD.

3.6.1 Electron Backgrounds

The main electron source in the LAr is from the beta decay of ^{39}Ar. At a rate of approximately 1 Bq/kg, there are roughly 2.6x10^8 ^{39}Ar decays each day in DEAP-3600. This dominates both the electronic recoil band rate and the overall trigger rate in DEAP-3600. For a dark matter search this decay is considered a background (though it can be significantly mitigated by the application of PSD); in this thesis it is only considered a background to the ^{36}Ar decay search within the electronic recoil band. Figure 3.9 shows the ranges for electrons in a range of energies for different detector materials.

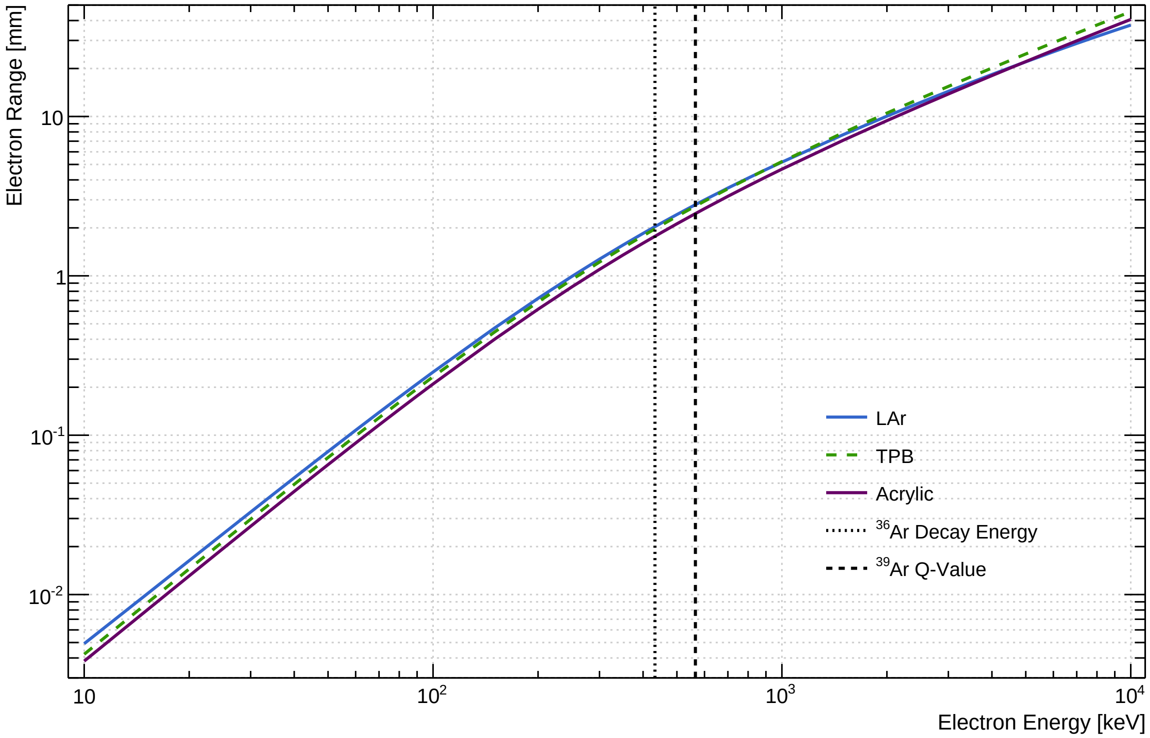

Figure 3.9: The range for an electron in LAr, TPB, and acrylic. The decay energy of ^{36}Ar and the ^{39}Ar Q-value are shown. Plots are generated using the National Institute of Standards and Technology (NIST) eStar service [60].

Energy	Range [mm]		
[keV]	LAr	TPB	Acrylic
30	0.03	0.03	0.03
100	0.25	0.23	0.21
200	0.72	0.69	0.62
300	1.27	1.22	1.10
400	1.85	1.78	1.60
500	2.42	2.36	2.12
565	2.80	2.74	2.46

Table 3.3: The range in various detector materials for an electron at different energies. 30 keV is approximately the lower bound of the fits to extract the ^{39}Ar specific activity.

Table 3.3 lists the ranges for electrons of various energies in LAr, TPB, and acrylic. Because of the range of an electron in LAr, and because the range in TPB is significantly thicker than the TPB layer, electrons produced very near the edge of the AV could deposit some of their energy in the TPB and travel into acrylic layer. These "lost edge-electrons" can deposit only a fraction of their energy in the LAr; for ^{39}Ar beta decays this will result in a small distortion to the beta energy spectrum. This effect will be discussed further in Chapter 4.

^{39}Ar

While ^{39}Ar is certainly not a background to its own specific activity measurement, it is a major background for the ^{36}Ar decay search. ^{39}Ar undergoes beta decay to the stable isotope ^{39}K with a half-life of 269 years and a Q-value of 565 keV (see Section 2.3.1 for more details). ^{39}Ar is by several orders of magnitude the dominant source of physics triggers in DEAP-3600.

^{42}Ar & ^{42}K

The rare isotope ^{42}Ar undergoes beta decay with a Q-value of 599 keV with a half-life of 32.9 years. The daughter produced in this decay is the isotope ^{42}K which also undergoes beta decay to the stable isotope of ^{42}Ca; the Q-value for this decay is 3525 keV and the half-life is 12.36 hours.

Several measurements of the abundance of ^{42}Ar in natural atmospheric argon exist, though there is disagreement between some measurements and the true concentration is yet to be determined. While the exact concentration is unknown, it is expected to be very small - much smaller than many other ERB backgrounds - and thus will have very little effect on both the ^{39}Ar and ^{36}Ar measurements described in this thesis. This decay chain is, however, of importance to dark matter searches with argon as all backgrounds must be well understood if a dark matter signal is to be confirmed.

^{85}Kr

^{85}Kr is another beta emitting isotope that could be present within the LAr volume; it has a half-life of 10.8 years [16] and a Q-value of 687 keV, and decays to the stable isotope ^{85}Rb. An existing measurement of the concentration of this isotope in atmospheric argon of (0.16 ± 0.13)Bq/L [21] would indicate that an activity of around (380 ± 310)Bq could be present in DEAP-3600. While a measurement of this activity has yet to be performed in DEAP-3600, initial observations of the data indicate that the activity may be even less than the lower 1σ bound of the given measurement.

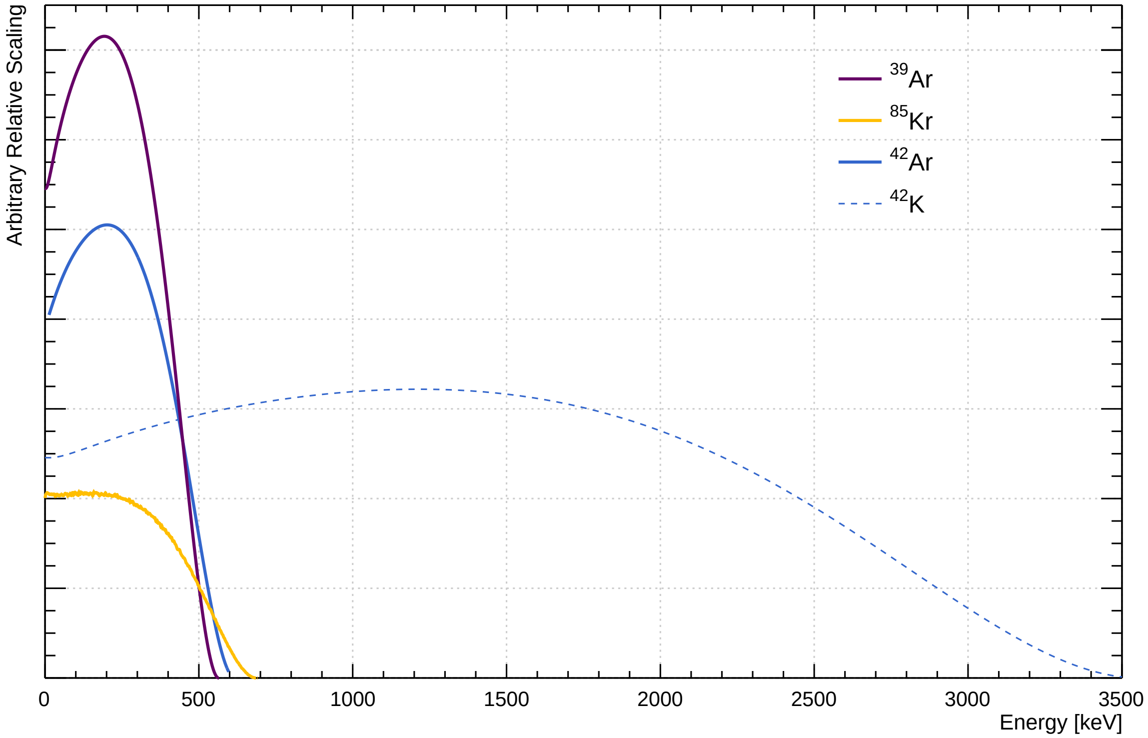

Figure 3.10: An overlay of the spectra of the various beta emitters in DEAP-3600. Scaling between spectra is arbitrary and does not indicate relative activities.

3.6.2 Gamma Backgrounds

There are several sources of gamma radiation in DEAP-3600 which are external to the LAr. The gammas from those sources have the potential to reach the LAr and deposit energy, producing a signal that is essentially indistinguishable from, for example, an ^{39}Ar beta decay. These gammas are present in the electron recoil band and represent a background to both beta decay of ^{39}Ar and the 0νECEC of ^{36}Ar.

^{60}Co

The radioisotope ^{60}Co can be found in steel, having been unintentionally implanted during the manufacturing process [61, 62]. This isotope undergoes beta decay to an excited state of ^{60}Ni, which relaxes by emitting a gamma. A simplified decay scheme is shown in Figure 3.11. ^{60}Co is present in the stainless steel shell which surrounds the acrylic vessel. A material assay of the steel shell measured the specific activity of this isotope of (15.5 ± 1.7)mBq/kg, resulting in an estimated activity of (77.7 ± 8.3)Bq from the shell.

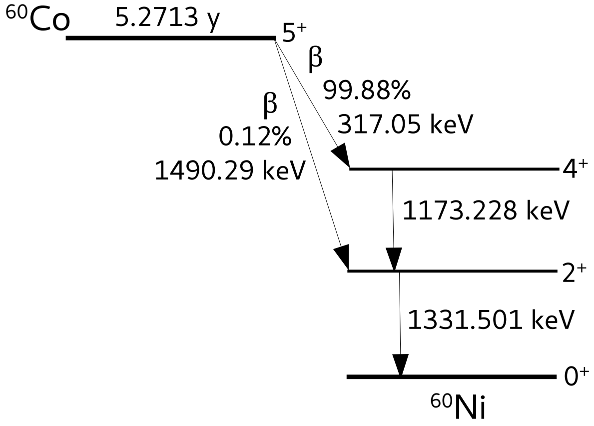

Figure 3.11: A simplified ^{60}Co decay scheme. The ^{60}Ni daughter is stable. Decay to the first excited state of ^{60}Ni is possible, but occurs is fewer than 1% of ^{60}Co decays.

^{40}K

^{40}K is one of several long-lived radionuclides that have been present in the Earth's crust since its formation, a member of the so-called primordial nuclides. ^{40}K has a half-life of 1.248x10^9 years [47] and decays by either electron capture or beta decay. A schematic of the decay is shown in Figure 3.12. An assay of the AV acrylic in DEAP-3600 resulted in a specific activity of (2.1 ± 1.8)mBq/kg corresponding to an estimated activity of (2.0 ± 1.7)Bq. Similarly, an assay of the lightguide acrylic measured an upper limit on the specific activity of 1.01 mBq/kg, which corresponds to an estimated activity of $<$ 3.87 Bq. Interestingly, the electron capture decay of ^{40}K is the primary source of ^{40}Ar on Earth.

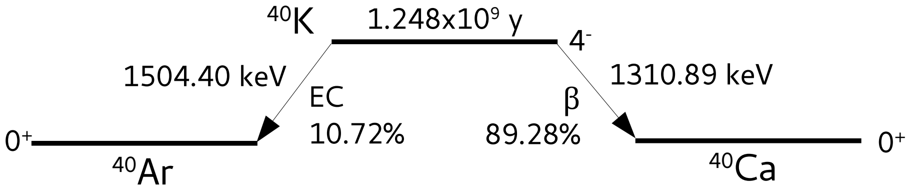

Figure 3.12: A simplified ^{40}K decay scheme. Both daughters are stable. The decay to ^{40}Ar is the largest contribution to argon reserves on Earth.

Natural Decay Chains

The natural decay chains are those which begin with one of the long-lived primordial nuclides. 3 of these nuclides are present in small quantities in either or both of the PMT glass and the AV acrylic; their decay chains and associated are described in the following pages. Schematics of the chains are shown in Figures 3.13, 3.14, and 3.15. Tables of the most prominent gammas, as well as gammas which could be backgrounds to ^{36}Ar 0νECEC decay, are presented in Appendix A. All data for the decay chains has been compiled from the National Nuclear Data Centre chart of nuclies [47].

^{232}Th

Naturally occurring thorium is almost entirely composed of ^{232}Th. This nuclide is present in both the PMT glass and in the AV acrylic.

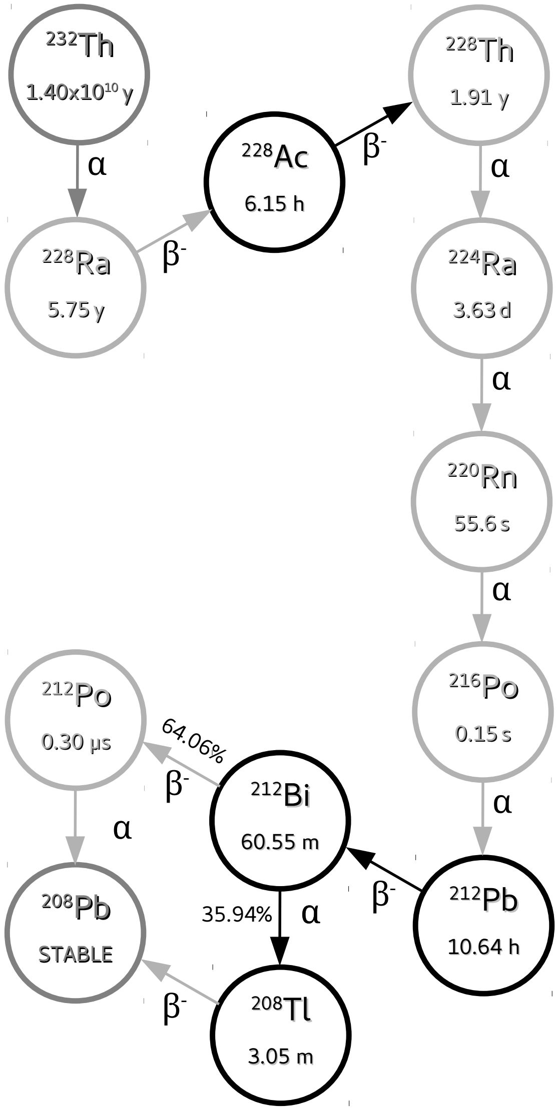

Figure 3.13: A schematic of the ^{232}Th decay chain, with each nuclide's half-life shown. For those nuclides which could undergo either an alpha and a beta decay the branching ratios are shown as a percentage of the total decays. The nuclides circled in black are those which have gammas that could be backgrounds to a ^{36}Ar 0νECEC signal.

^{238}**U**

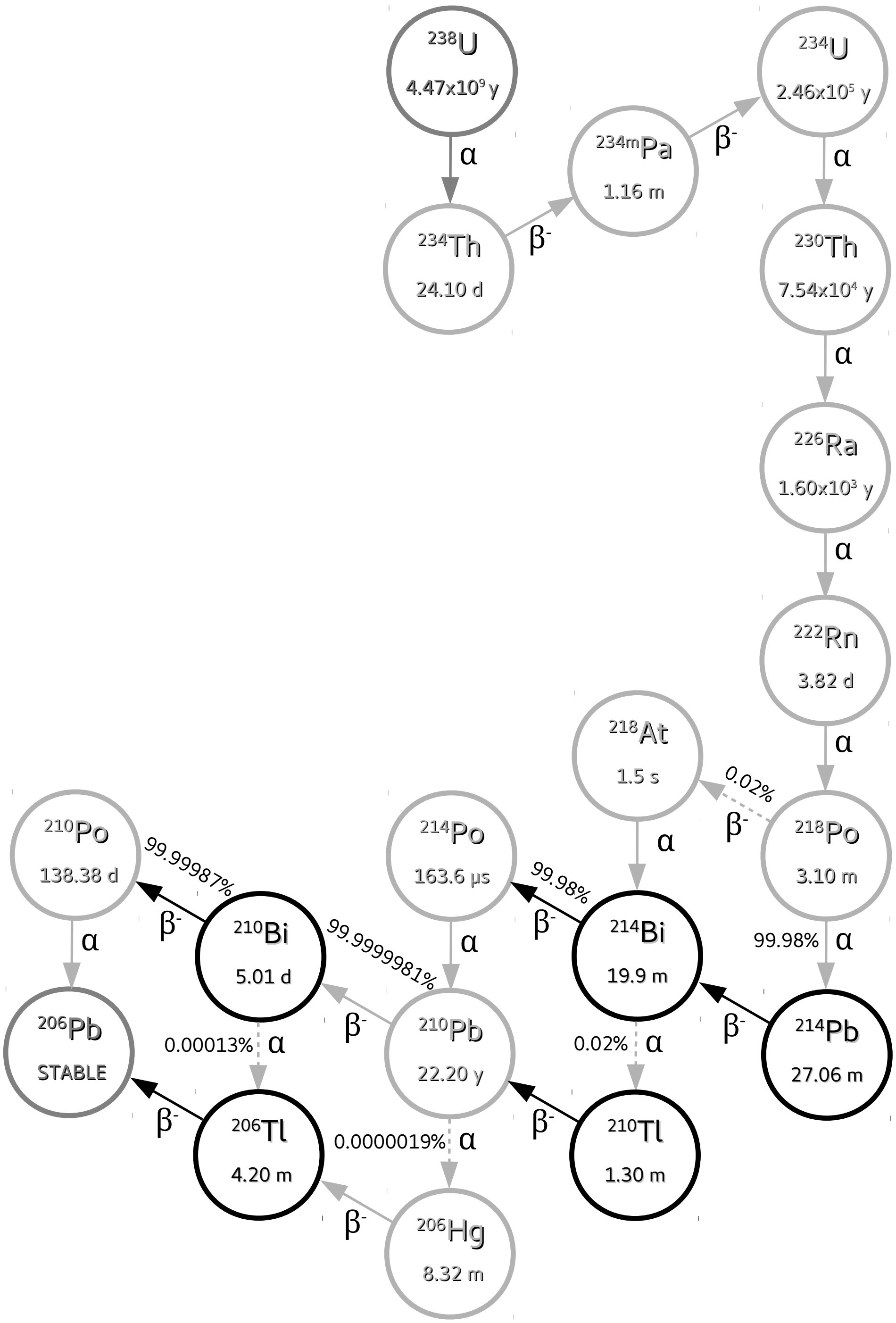

Figure 3.14: A schematic of the ^{238}U decay chain, with each nuclide's half-life shown. For those nuclides which could undergo either an alpha and a beta decay the branching ratios are shown as a percentage of the total decays. The nuclides circled in black are those which have gammas that could be backgrounds to a ^{36}Ar 0νECEC signal.

^{235}**U**

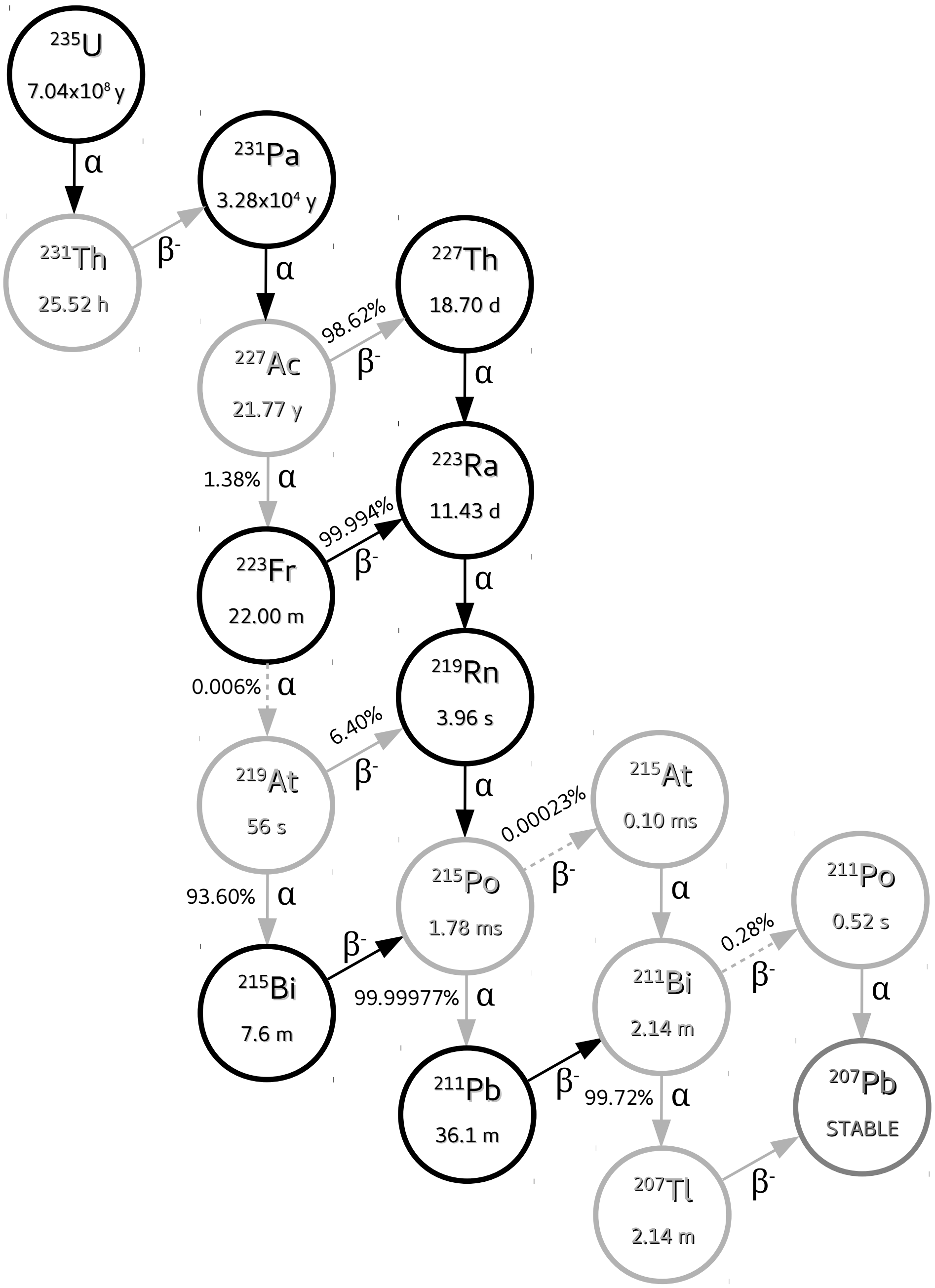

Figure 3.15: A schematic of the ^{235}U decay chain, with each nuclide's half-life shown. For those nuclides which could undergo either an alpha and a beta decay the branching ratios are shown as a percentage of the total decays. The nuclides circled in black are those which have gammas that could be backgrounds to a ^{36}Ar 0νECEC signal.

3.7 Current Status of the Experiment and Data Collection

The AV was filled for the first time throughout June and July of 2016. During the final stage of filling the contraction of a cryogenic seal at the neck/AV boundary allowed the higher pressure nitrogen from within the steel shell to penetrate the AV which effectively poisoned the argon [63–65]. The argon was vented by allowing it to slowly boil away and the AV was evacuated to a nitrogen-free state. To prevent further complications with the neck/AV seal it was decided that for the second fill the AV would be only partially filled; the AV was filled to a liquid argon mass of (3279 ± 96)kg, with the fill completed at the beginning of November, 2016. To date, the experiment has been running stably and collecting data, and the AV has remained hermetically sealed. DEAP-3600 has submitted for publication its first physics result and finding no candidate WIMP signal events [66](2017), establishing the leading WIMP-nucleon cross-section limit in argon of $< 1.2\text{x}10^{-44}\text{cm}^2$ for a 100 GeV/c^2 WIMP.

Chapter 4

Physics Data Set and Analysis

In this chapter I will discuss the data that has been analysed in this thesis. This will include a calculation of the LAr mass, a breakdown of the total LAr exposure, a description of the physics parameters used in main analyses of this thesis, and an analysis of the efficiency of cuts made on these parameters to select ^{39}Ar events and events in the ^{36}Ar peak region.

4.1 Calculating the Mass of Liquid Argon

The mass of LAr in DEAP-3600 can be calculated by finding its volume and its density. Using the cold AV radius (845.6 ± 1.9)mm and fill level - measured as its height above the centre of the AV - (551 ± 50)mm [66] the volume of liquid argon can be calculated. The volume of LAr (V_{LAr}) is a sphere with its cap removed:

$$V_{LAr} = \frac{4}{3}\pi R^3 - \frac{\pi h^2}{3}(3R - h), \tag{4.1}$$

where R is the AV radius and h is the height of the cap:

$$h = R - z = 845.6\text{ mm} - 551.0\text{ mm} = 294.6\text{ mm} \tag{4.2}$$

with uncertainty h is equal to (265 ± 50)mm. The volume is then (2.329 ± 0.067)m^3. For the volume calculation the radius and fill level uncertainties are added in quadrature.

The density of liquid argon as a function of its pressure is shown in Figure 4.1. The temperature range for LAr at 13.79 psia is 83.85 K to 86.7 K. At the lower temperature bound the density is 1417 kg/m^3; at the upper bound the density is 1399 kg/m^3. The uncertainty on the central value is taken as the difference between the central value and the upper and lower bounds as this value is larger than either the uncertainty based on the pressure variation or NIST's stated uncertainty of 0.02% of the central value. At an average LAr pressure in the AV of (13.79 ± 0.11)psia and a temperature in the middle of the liquid range (82.255 K) the density is interpolated to be (1408 ± 9)kg/m^3. Using this along with the measured LAr volume, the mass of liquid argon is measured to be (3279 ± 96)kg, where the density and volume uncertainties are added in quadrature. The quantities used in these calculations are summarized in Table 4.1

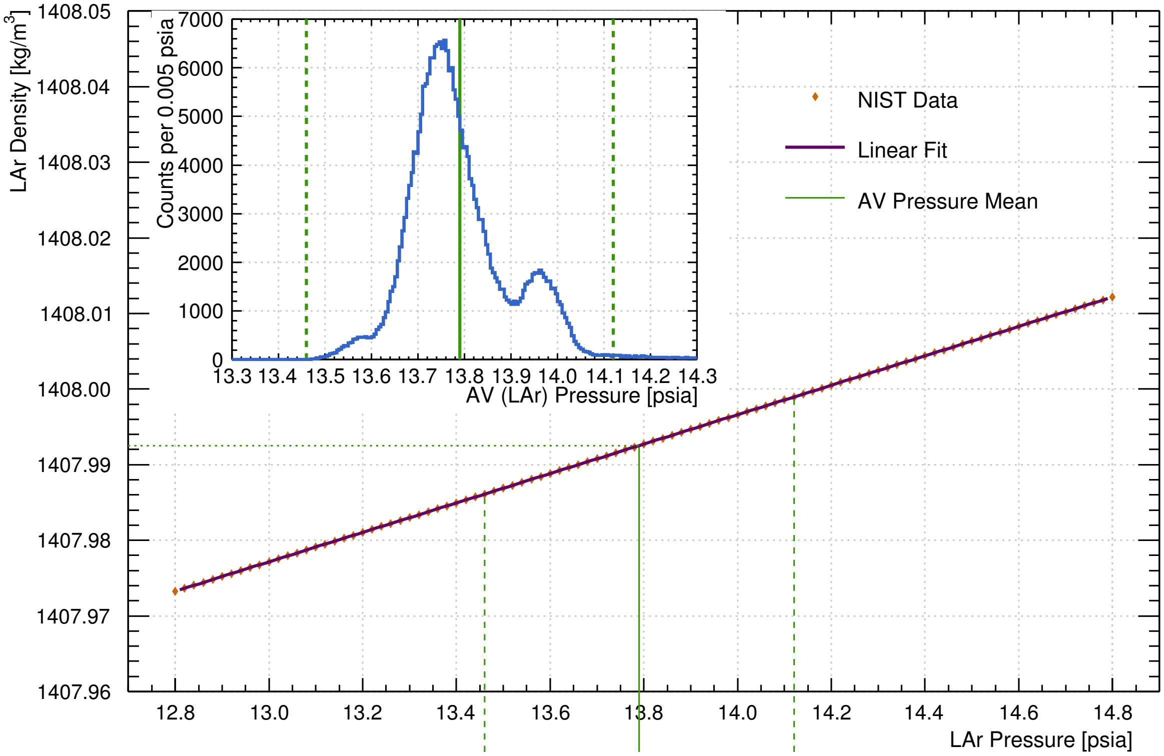

Figure 4.1: Density of 85.255 K liquid argon as a function of pressure with data from the NIST Chemistry WebBook [67]. The value of 82.255 K is in the middle of the liquid temperature range for a pressure of 13.79 psia. A first-order polynomial is fit to the NIST data to interpolate the density at the mean LAr pressure (solid line). The inset shows the LAr pressure for the data set with a mean of (13.79 ± 0.11)psia; the solid and dashed lines show the mean and a 3σ band.

Quantity	Value
AV Radius	(845.6 ± 1.9)mm
LAr Level	(551 ± 50)mm
LAr Density	$(1408 \pm 9)\mathrm{kg{\cdot}m^{-3}}$

Table 4.1: Summary of quantities used to calculate the LAr mass in DEAP-3600.

4.2 The Data Set

The data analysed in this thesis was collected from the beginning of November 2016 to the end of October 2017. A high level run selection to determine which runs are suitable for a dark matter search has been performed by DEAP-3600's data quality group, and represents a total LAr exposure of 2203 kg·years (805x10^3 kg·days) before applying corrections. The selection criteria includes runs for which all PMTs were operating with stable voltages and for which the LAr fill level measurements remained stable. A breakdown of the total runtime and LAr exposure by month is presented in Table 4.2. The cumulative LAr exposure is shown over the 1 year data collection period in Figure 4.2.

Month	Total runtime [days]	Exposure x10^4 [kg·days]
November 2016	18.17	5.917
December 2016	21.38	6.963
January 2017	20.46	6.663
February 2017	19.62	6.389
March 2017	17.20	5.601
April 2017	15.89	5.175
May 2017	17.95	5.846
June 2017	26.53	8.640
July 2017	27.64	9.001
August 2017	22.93	7.467
September 2017	20.37	6.634
October 2017	19.31	6.288
Total	**247.45**	**80.584**

Table 4.2: Breakdown of the runtime and LAr exposure by month. The runtime is the sum of the time from the first trigger to the last for each run; no corrections have been applied to the runtime at this stage. The exposure is calculated using a total measured LAr mass of (3279 ± 96)kg.

^{39}Ar Run Selection

A subset of this data is used to measure the ^{39}Ar specific activity on a run-by-run basis. From the list of runs which have passed data quality checks, only runs with a runtime of greater than 18 hours are selected. The lower limit of 18 hours is somewhat arbitrary, though is chosen such that the region beyond the ^{39}Ar energy spectrum endpoint - dominated by external gammas - has an approximate minimum of 10 events per bin when 30 PE wide bins are used. This criteria results in the selection of 185 runs which vary in runtime up to about 40 hours.

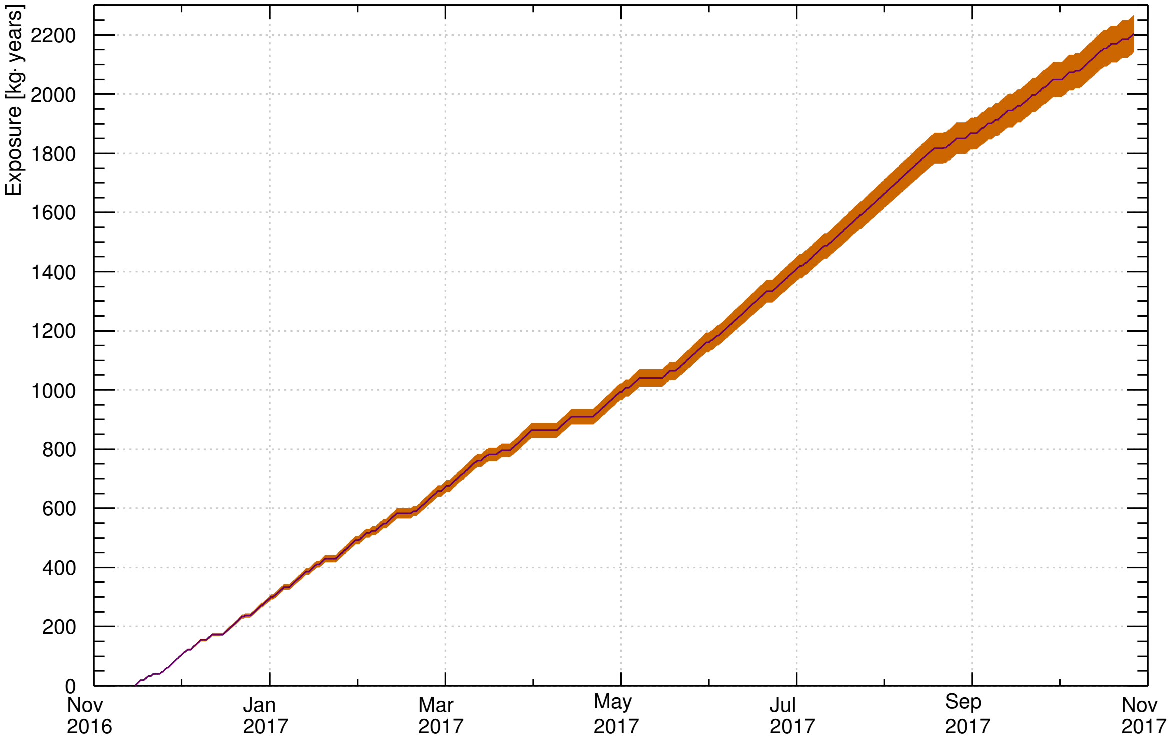

Figure 4.2: The cumulative LAr exposure for this data set. The shaded band shows the 1σ uncertainty derived from the LAr mass uncertainty.

Trigger Rate in DEAP-3600

The overall trigger rate in DEAP-3600 is dominated by ^{39}Ar beta decays, but also has contributions from gamma and alpha backgrounds. Figure 4.3 shows the event rate measured for each run in the ^{39}Ar data set.

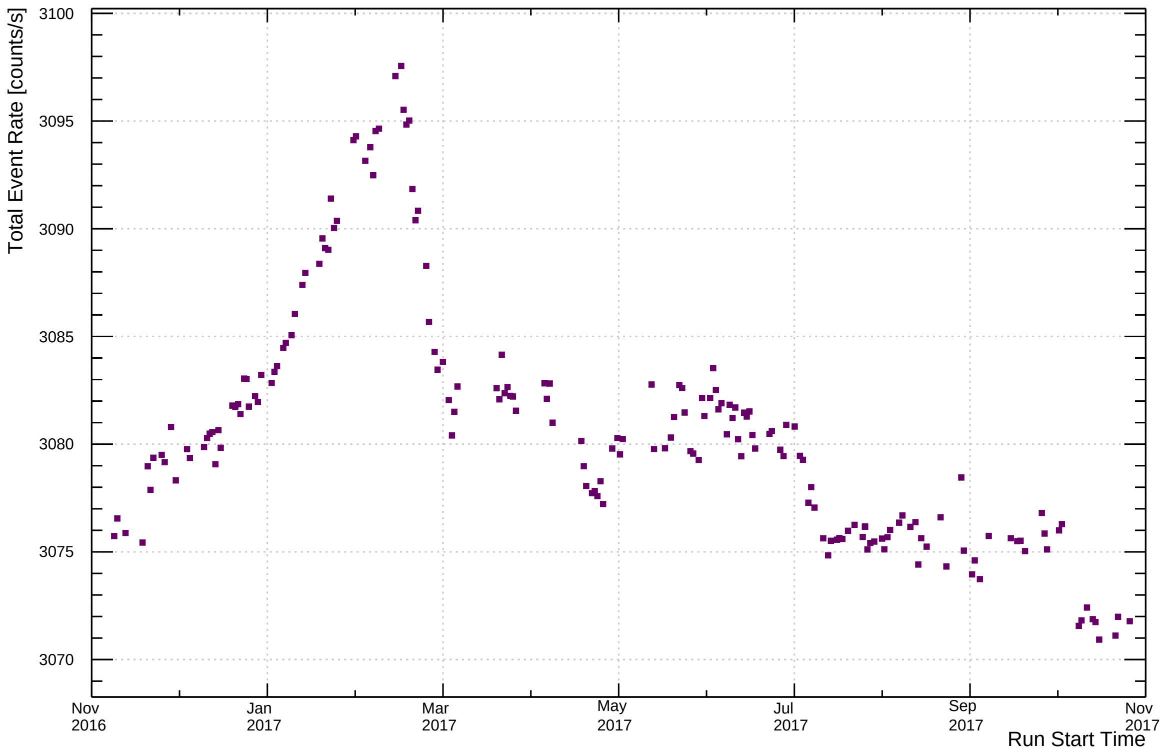

Figure 4.3: The event rate in DEAP-3600 on a run-by-run basis for each run in the ^{39}Ar data set before cuts are applied. The event rate is measured by dividing the total event count by the runtime for each run.

4.3 Description of the Parameters in Data - ^{39}Ar Analysis

Making sense of the data from an experiment such as DEAP-3600 can be complicated, as a significant amount of information is contained within the pulses output by the PMTs. Through the analysis of each waveform this information can be distilled down into parameters which describe the characteristics of an event. This section will describe these parameters. In this section the term “event” is used to broadly describe anything that triggers the DAQ, whether it is a physics process (such as a ^{39}Ar beta decay or a WIMP interaction) or something else (such as an internal calibration trigger). For a complete list of the terminology used see Section 1.2.

The following parameters listed are those used to select events for the measurement of the specific activity of ^{39}Ar in DEAP-3600's argon target, and by extension in atmospheric argon. When an event is selected, its reconstructed energy is added to a histogram to build an energy spectrum. This spectrum is intended to be an unbiased spectrum of the beta decay of ^{39}Ar though the detector response has an effect on the spectrum, particularly at low energies where the trigger efficiency is not 100%. The events in the spectrum are then counted by fitting a theoretical beta spectrum (Section 2.3.1). The event rate can be determined from the event count, and using the LAr mass the specific activity can be determined.

The cuts are designed to reduce the background as much as possible while maintaining the ^{39}Ar selection efficiency at as high a level as possible. The first two parameters listed, dtmTrigSrc and calcut, are used to remove non-physics events and result in a correction to runtime. The rest of the parameters listed are used to remove non-^{39}Ar events and result in an efficiency correction for selecting ^{39}Ar decays.

4.3.1 Non-Physics Event Removal

The following two cuts are used to remove non-physics events from the data. For each event removed in this way a reduction in the runtime is made - essentially introducing an analysis dead time - of 16 μs per event.

dtmTrigSrc

The dtmTrigSrc parameter specifies the source of the event trigger; it is simply a flag added to the data for each event when the event is written to disk. This may be from a calibration trigger from an external source or the internal pulse generator[1], or

---

[1] The internal pulse generator is part of a periodic trigger which fires at a rate of 40 Hz. It forces the DAQ to trigger and record a pulse; it also injects a test pulse once per second.

it may be from a physics trigger in one of the five energy & F_{prompt} regions; these 5 regions are shown schematically in Figure 3.8. A cut on this parameter allows one to remove non-physics events from their analysis, and results in a correction to the runtime for a run. The relevant trigger types are shown in Table 4.3.

Bit	Value [hex]	Trigger Source
2	0x2	Internal periodic trigger (PPG event)
8	0x80	External calibration trigger
11	0x400	Low energy, low F_{prompt}
12	0x800	Low energy, high F_{prompt}
13	0x1000	Medium energy, low F_{prompt}
14	0x2000	Medium energy, high F_{prompt}
15	0x4000	High energy, any F_{prompt}

Table 4.3: The relevant trigger types in DEAP-3600.

The internal periodic trigger is provided by a pulse generator and fires at a rate of 40 Hz; it injects test pulses at a rate of 1 Hz, with the other 39 samples per second used to monitor the PMTs. The external calibration trigger may come from one of the radioactive calibration sources, such as the AmBe source or the ^{22}Na source. The events matching bit 13 are mainly comprised of ^{39}Ar beta decays; in an effort to accommodate the high rate and prevent unnecessarily large data files only 1 in 100 of these events has its waveform stored. The current cut value removes instances of bits 2 and 8. As this parameter describes the different kinds of physics triggers, it can be used to separate events that are prescaled from those that are not. In this analysis, the physics triggers that are not prescaled (matching bits 11, 12, 14, and 15) are rejected such that only 1 out of every 100 of those events is kept; this rejection is done so that the event statistics are consistent across all physics triggers.

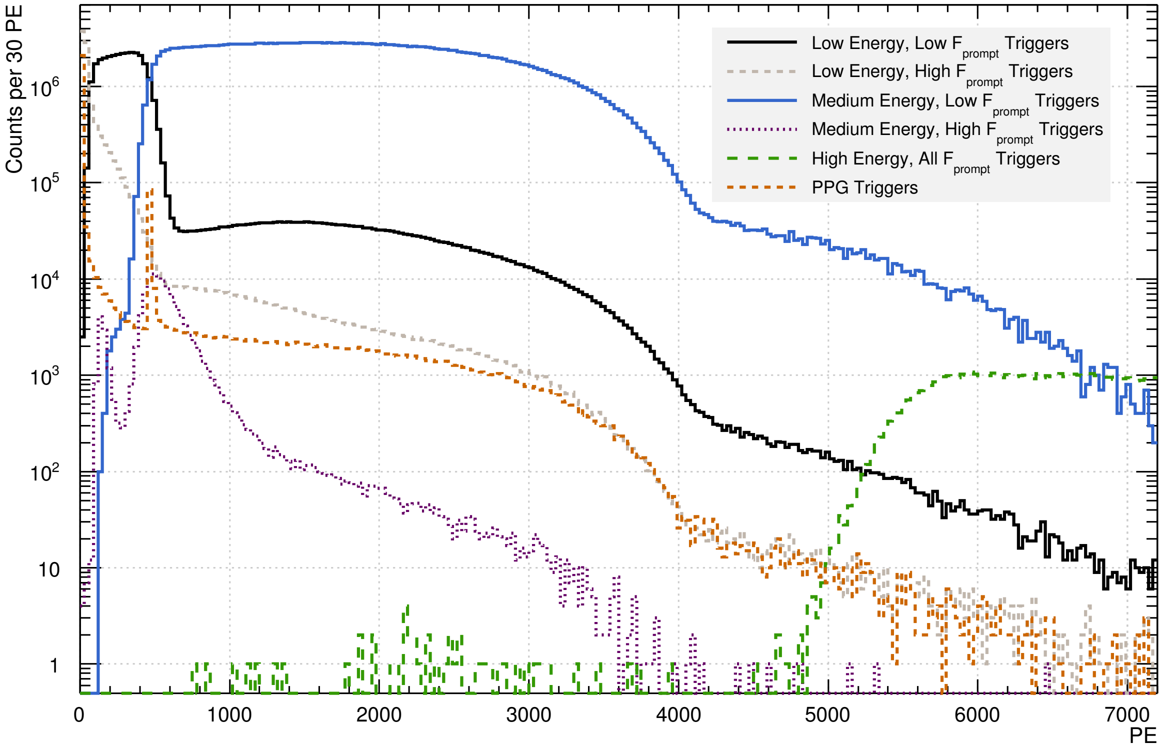

Figure 4.4: The different trigger types that comprise the ^{39}Ar spectrum are shown with no cuts applied. The "Medium Energy, Low F_{prompt} Triggers" are those triggers which are prescaled in data (see Section 3.5.3 for more details on prescaling). The triggers which are not prescaled have been cut such that 1 out of every 100 is kept so that the statistics match that of the prescaled triggers.

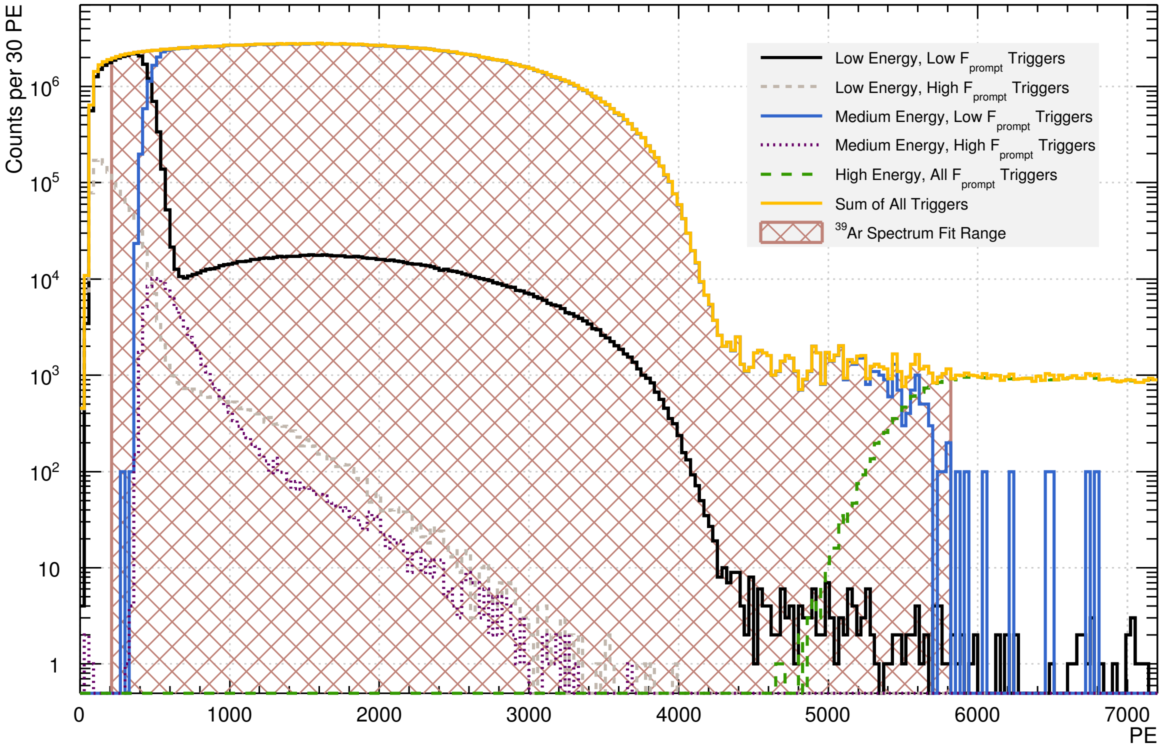

Figure 4.5: The different trigger types that comprise the ^{39}Ar spectrum are shown with all cuts applied, including that which removes the PPG and external triggers. The region over which the ^{39}Ar spectrum is fit is highlighted. The triggers which are not prescaled have been cut such that 1 out of every 100 is kept so that the statistics match that of the prescaled triggers.

calcut

The calcut parameter is a flag that is used to remove “bad” events (that is, events that would not be suitable for physics analysis). There are a number of reasons for which an event may be flagged as not suitable for analysis; these reasons, along with the value of the flag, are listed in Table 4.4. This cut generally comprises fewer than 0.01% of the total events in a run. The cut value used for data processing (bitwise, in hex) is 0x31f8 and removes any events matching bits 3, 4, 5, 6, 7, 8, 12, or 13.

Bit	Value [hex]	Reason for this Flag
0	0x1	A V1720 pulse had a bad baseline
1	0x2	A V1720 pulse reached 0 ADC (saturation)
2	0x4	Failed to find a “good” calibrated trigger time
3	0x8	A PPG event†
4	0x10	Event is soon after a PPG event†
5	0x20	A spare V1720 channel has a pulse†
6	0x40	DAQ was running busy and suppressing readout of digitizers
7	0x80	Trigger/digitizers are out of sync‡
8	0x100	Event timestamps are appearing out-of-order‡
9	0x200	There are no digitizers in the event (generally due to pre-scaling)
10	0x400	Event came from a non-physics trigger source
11	0x800	SQT info used for a non-SPE-like pulse
12	0x1000	SQT info used for a pulse where the charge integral was truncated
13	0x2000	SQT info used for a pulse > 1000 pC

Table 4.4: All calcut flags. SQT is Smart QT, an algorithm implemented in the V1720 digitizers' front end program to encode the waveforms.
†Not suitable for physics analyses.
‡The DAQ will stop or crash soon after this occurs.

4.3.2 PE

The PE parameter is the value of the total reconstructed charge of an event and is a measurement of the number of photoelectrons (hence PE) in a pulse. This energy estimator parameter does not correct for effects such as PMT afterpulsing which can add erroneous charge to a pulse. The parameter is regularly calibrated for each PMT using a system of acrylic fibres into which 435 nm light pulses are injected; the fibres are wrapped around the light guides of 20 PMTs spread across the AV. Two daily data runs of about 10 minutes in length are taken to monitor the PMTs using one of the fibres for each run. From each run a plot like that in Figure 4.6 is produced to measure the average charge output by the PMT due to a single photo electron (SPE).

Using the calibration the PE value for each pulse is measured. Figure 4.7 shows a PE spectrum in data.

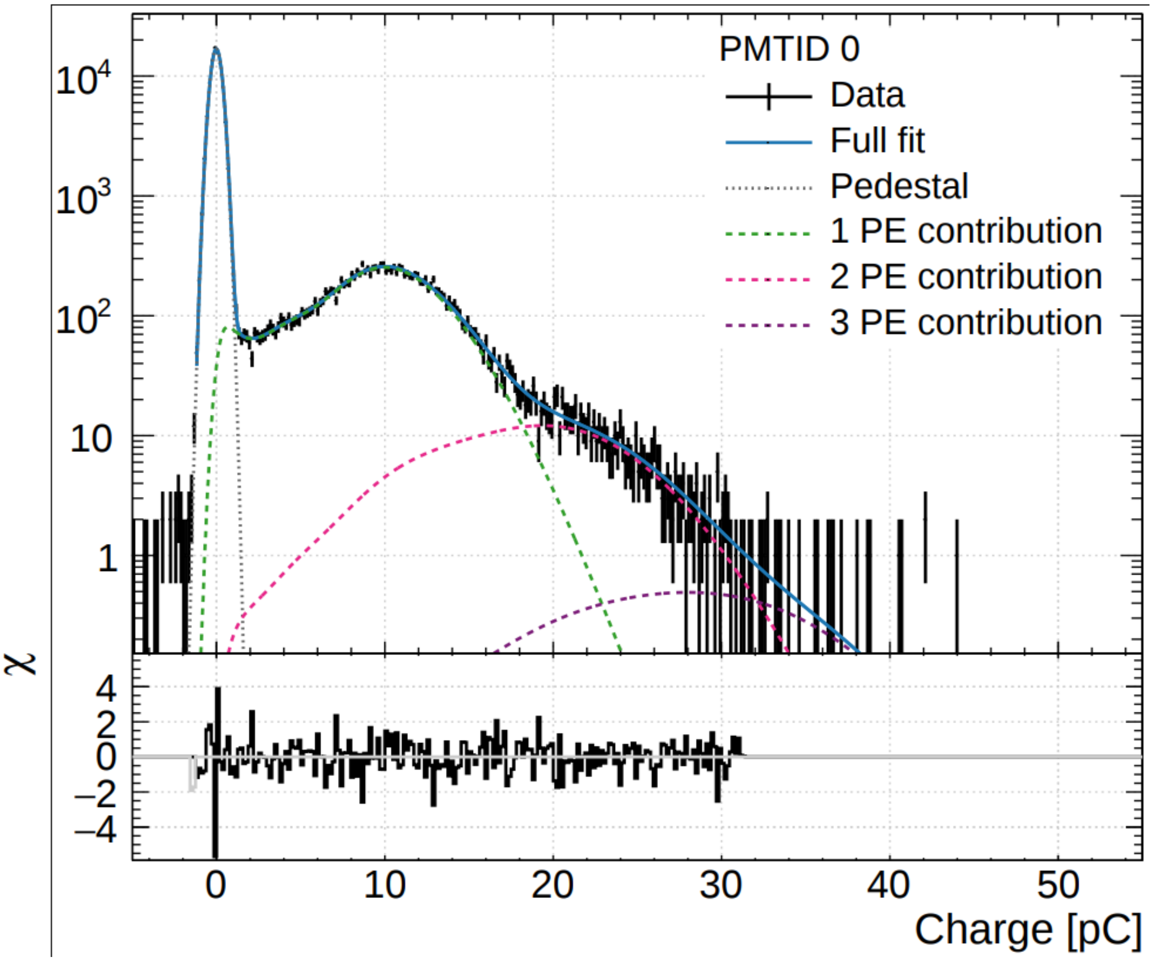

Figure 4.6: A measured SPE curve from one of the DEAP-3600 PMTs. The single photoelecton portion of the curve is highlighted in the top histogram. The lower panel shows the fit residuals between the data and the model sum of the 1, 2, and 3 photoelectron contributions. Figure is taken from a DEAP-3600 paper which has been recently submitted for publication [68] and was created by other members of the DEAP collaboration.

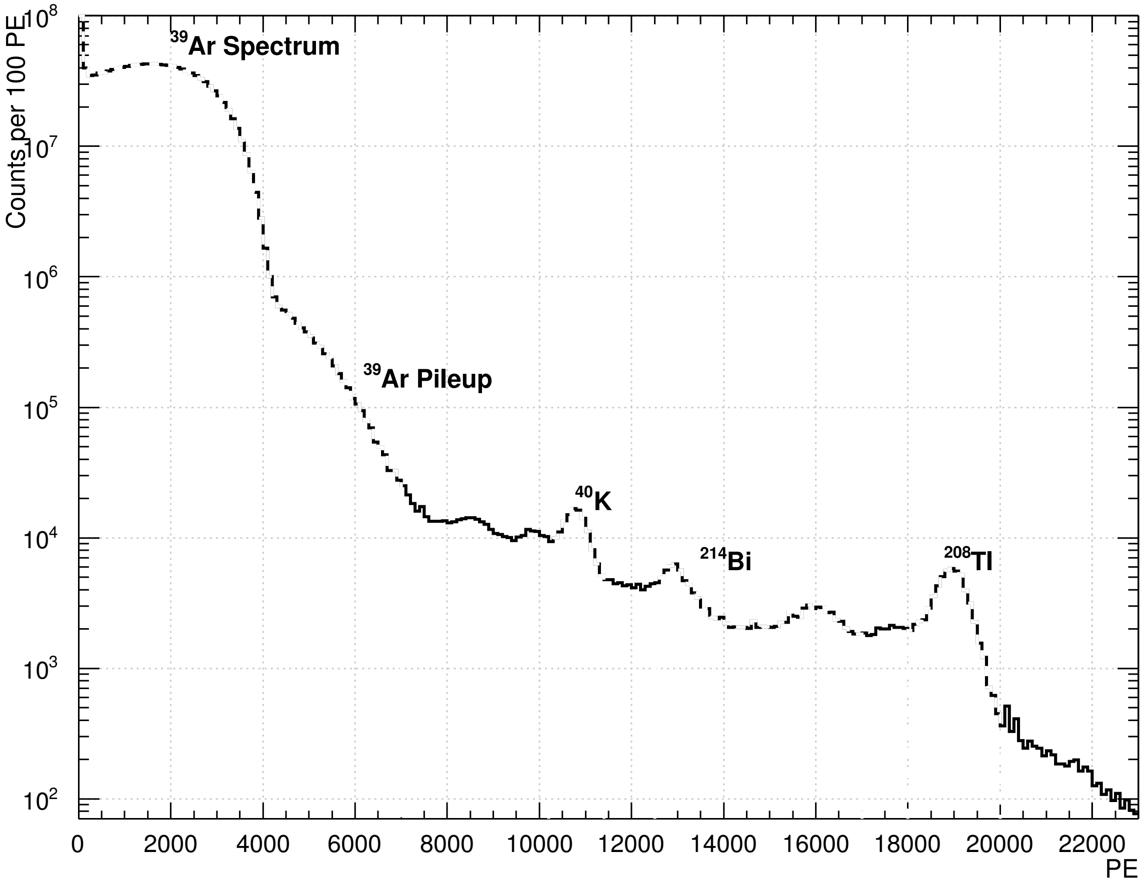

Figure 4.7: A PE spectrum in data. No PSD cut is made; the majority of events in DEAP-3600 are in the low F_{prompt} region known as the electron recoil band. The dashed portions of the histogram and the accompanying labels represent the dominant contributions to the spectrum at those energies. This spectrum represents approximately 6 days of data.

4.3.3 F_{prompt}

F_{prompt} is the PSD parameter used in DEAP-3600; it is the parameter through which DEAP-3600 produces its remarkable discrimination power between electronic recoil events and nuclear recoil events in argon. F_{prompt} is the fraction of charge from all of the inner PMTs in the first 150 ns (the prompt light window) with the total charge in 10 μs; this is shown in Eq. 4.3.

$$\mathrm{F}_{\mathrm{prompt}} = \frac{\sum_{i=1}^{255} Q_{i,\mathrm{prompt}}}{\sum_{i=1}^{255} Q_{i,\mathrm{full}}}, \tag{4.3}$$

where the charge, Q, is in PE for a given PMT and i are the PMT IDs. Figure 4.8 shows a waveform with the integration windows indicated.

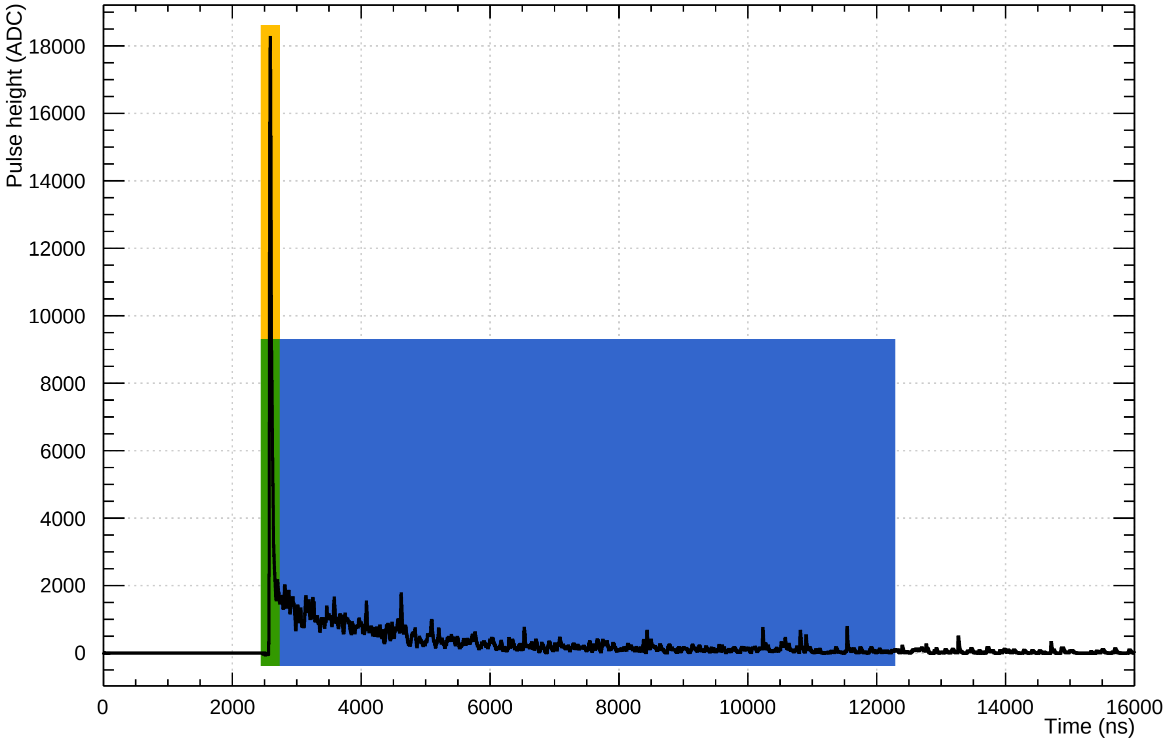

Figure 4.8: An example of a single pulse to show the integration windows with which $\mathrm{F}_{\mathrm{prompt}}$ is calculated. Highlighted are the prompt (yellow) and wide (blue) integration windows, with the overlap shown in green. This is an event that would be selected as part of the ^{39}Ar specific activity analysis, with a reconstructed charge of 3504 PE and an $\mathrm{F}_{\mathrm{prompt}}$ value of 0.259.

$\mathrm{F}_{\mathrm{prompt}}$ together with the PE energy estimator can be used to build a 2D parameter space in which the nuclear recoil and electronic recoils bands can clearly be identified. Figure 4.9 shows a 2D plot of PE vs $\mathrm{F}_{\mathrm{prompt}}$.

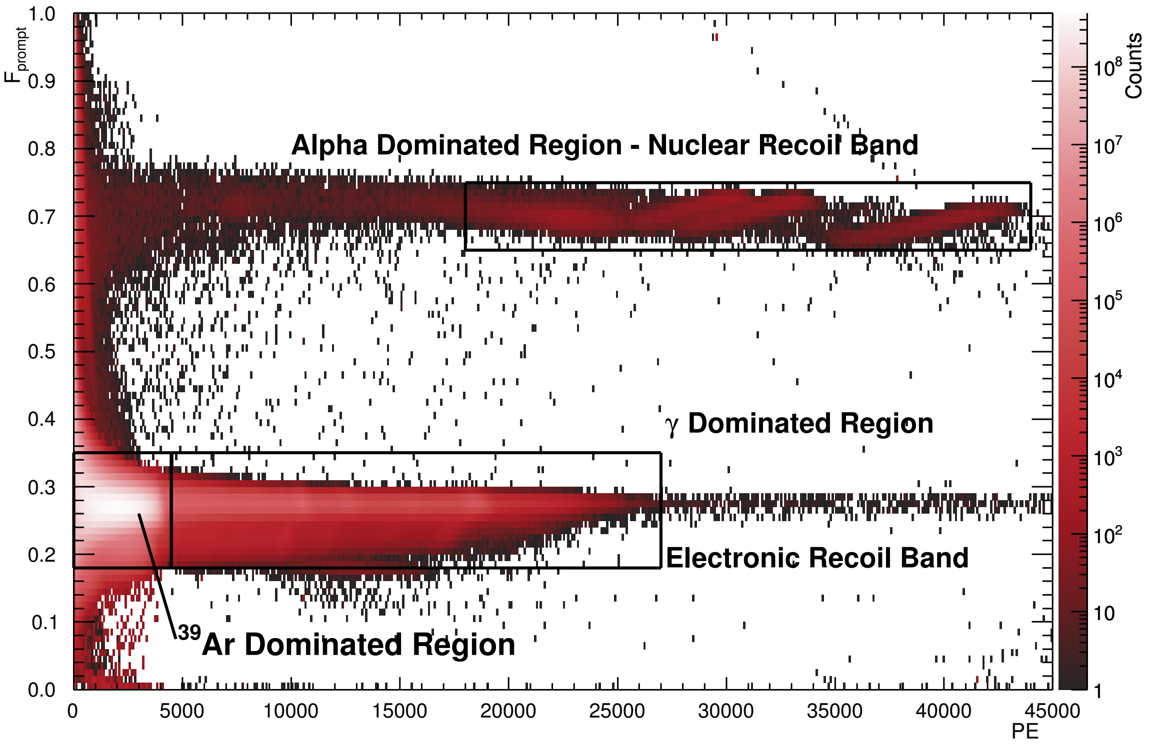

Figure 4.9: Pulse-shape discrimination in DEAP-3600. Livetime and pileup cuts have been applied. The nuclear recoil band (at $F_{\mathrm{prompt}} \approx 0.70$) and the electronic recoil band (at $F_{\mathrm{prompt}} \approx 0.30$) are clearly seen.

4.3.4 Pileup Removal

A pileup event is one in which two or more separate events occur, by chance, within the same trigger window. With such a high event rate in DEAP-3600 this is a common occurrence, happening more than 100 times per second. There are several different classes of pileup events, and two parameters are used to remove these events.

subeventN

The subeventN parameter measures the number of subevents in a given 16 μs window, and is used to separate single recoil events from subevents which have occurred in the same event window and returns an integer value. Events in data are only included if subeventN is exactly 1, meaning the processor identified a single event in the trigger window. This parameter is able to identify when the second subevent occurs after the initial event which triggered the detector. An example of a waveform with two distinct subevents is shown in Figure 4.10

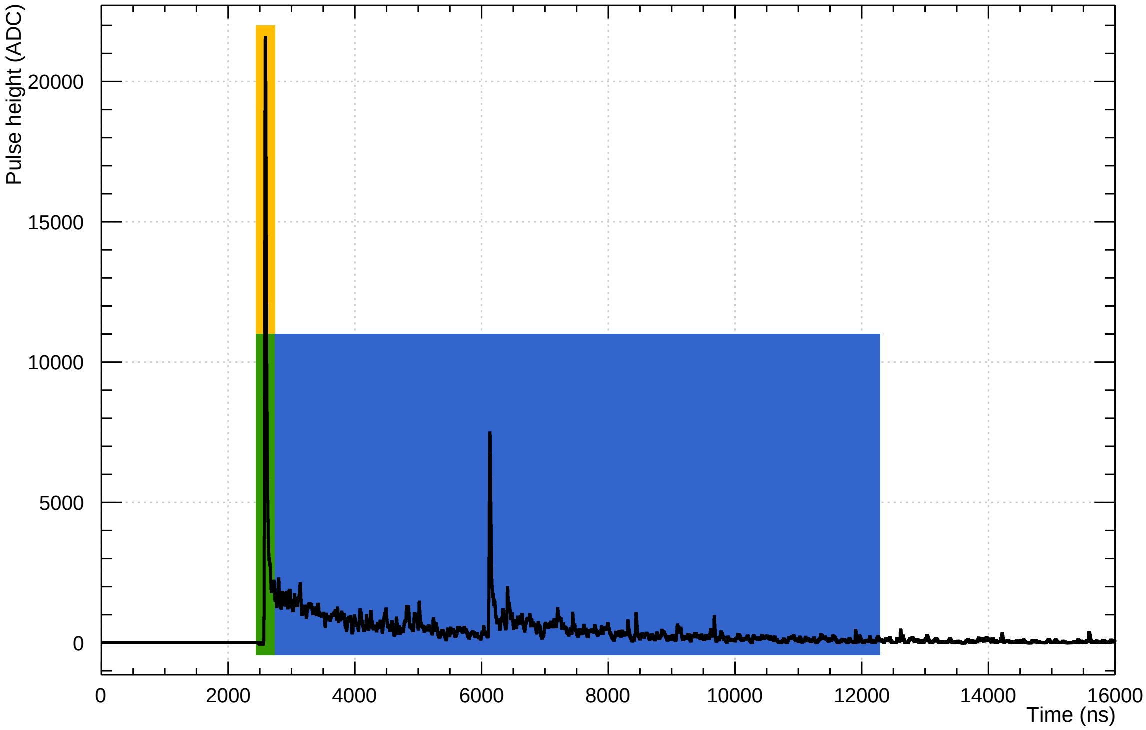

Figure 4.10: An example of a pileup event identified as having subeventN = 2. The smaller pulse occurs within the integration window of the initial trigger, adding to the total energy of the event and altering the PSD parameter. Highlighted are the prompt (yellow) and wide (blue) integration windows, with the overlap shown in green.

numEarlyPulses

The numEarlyPulses parameter is a measurement of how many peaks/sub-peaks are present in the pre-trigger portion of the trigger window. Events are removed from data if there are more than 3 sub-peaks in the pre-trigger window. This parameter is used to determine when the tail of a previous event leaks into the current trigger window. There may not always be additional pulses within the trigger window so some of these events are not technically pileup; however these events would represent a distortion to any observed energy spectrum as only a portion of the total charge of the event is measured. Figure 4.11 shows an example of such a waveform.

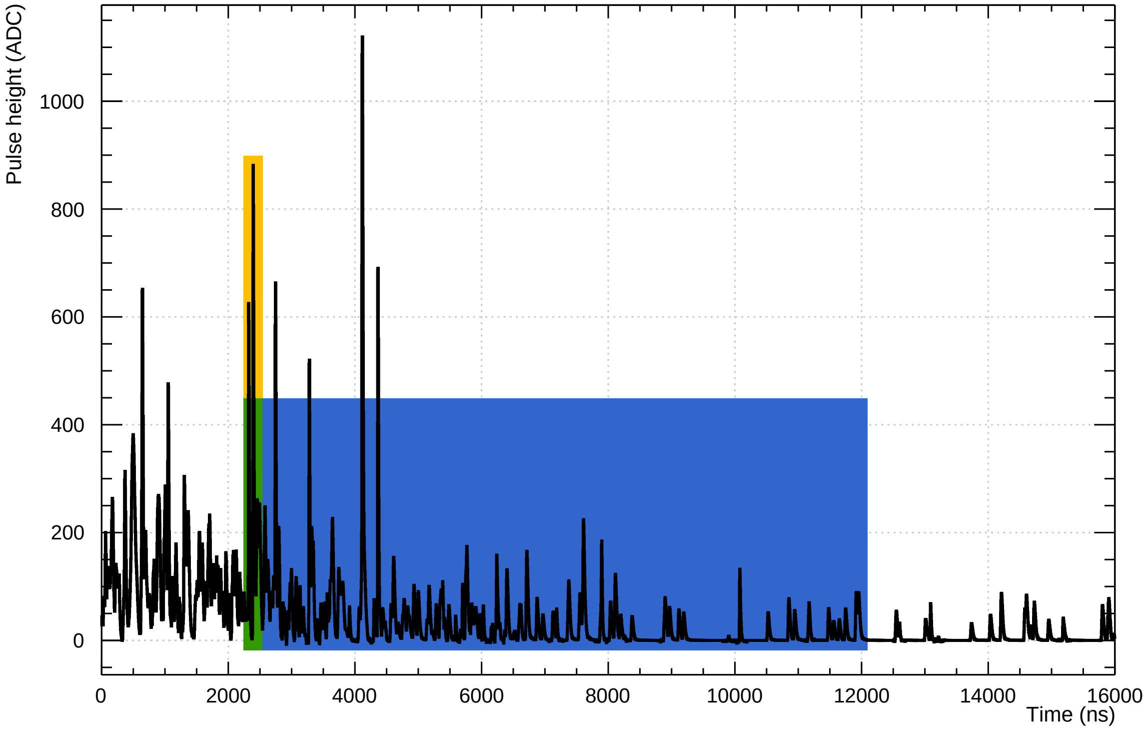

Figure 4.11: An example of an event flagged as having numEarlyPulses greater than 3. This event reconstructed with an energy of 257 PE and an F_{prompt} of 0.12 which would place it within the cut boundaries of ^{39}Ar event selection. Highlighted are the prompt (yellow) and wide (blue) integration windows, with the overlap shown in green.

This parameter also determines when a small amount of light from a previous event has leaked into a triggered event. Figure 4.12 shows an example of such a waveform; in this waveform a pulse has trigged the DAQ but some charge is present before the trigger occurs; this could be charge from a previous event leaking in which would cause a slight distortion to the total charge measured.

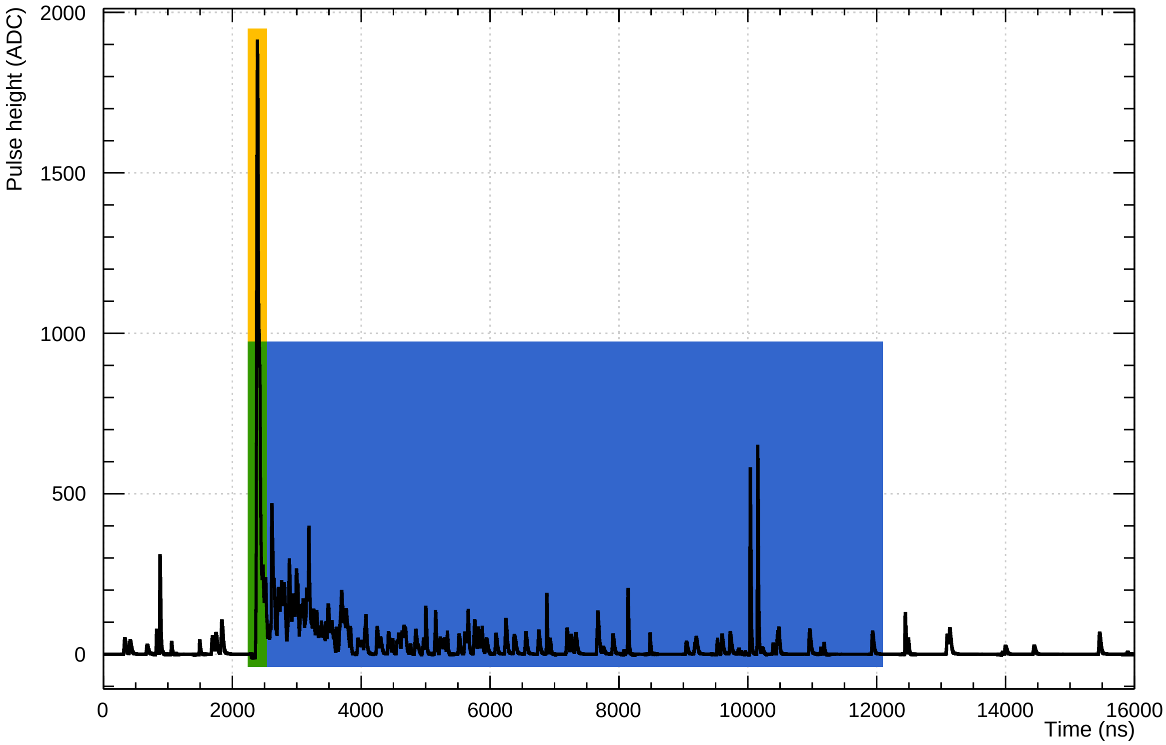

Figure 4.12: Another example of an event flagged as having numEarlyPulses greater than 3. Highlighted are the prompt (yellow) and wide (blue) integration windows, with the overlap shown in green.

4.3.5 Effect of All Cuts Combined

The cut-flow for processing data, designed to select ^{39}Ar events, is given by the following with events are removed from data if:

- dtmTrigSrc & 0x82
- calcut & 0x31f8
- subeventN > 1
- numEarlyPulses > 3
- $\mathrm{F_{prompt}} < 0.10$ or $\mathrm{F_{prompt}} > 0.50$

The progressive effect of the cuts to produce a ^{39}Ar-dominated PE spectrum is shown in Figure 4.13. Figure 4.14 show the rate of events in the ERB that pass these selection cuts.

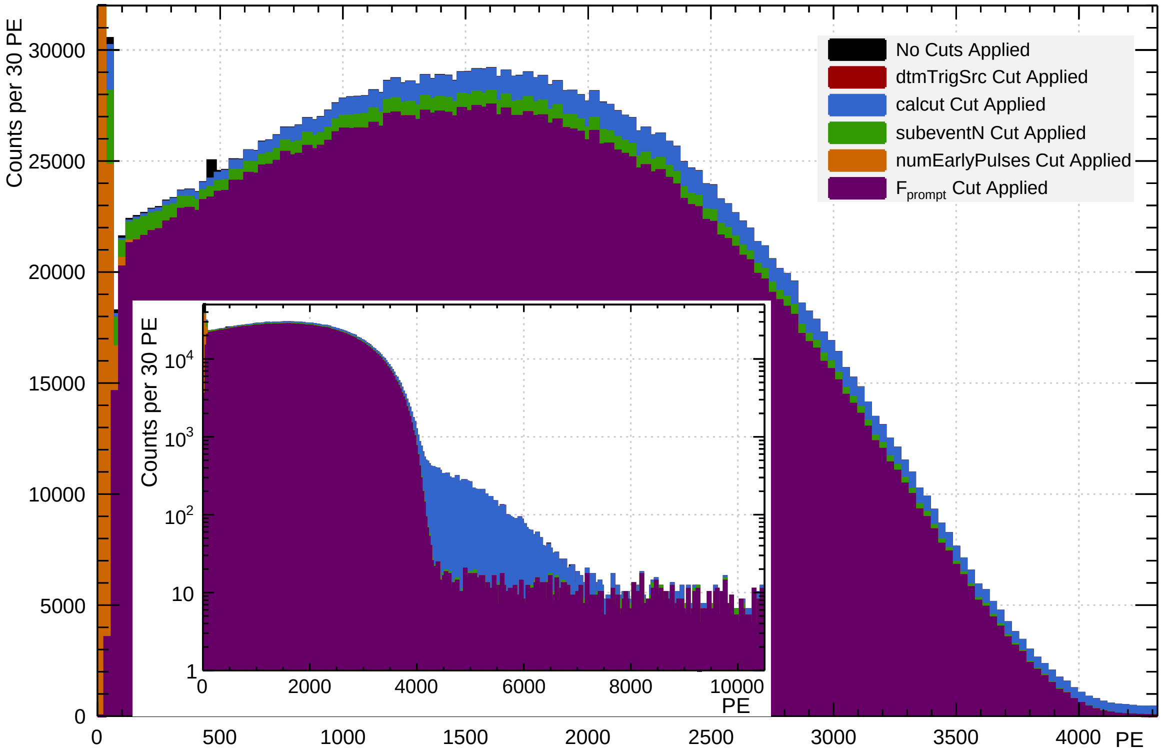

Figure 4.13: Progressive effect of the cut sequence in data. Cuts are applied in the order shown in the legend. This data is from a single run with a runtime of 26 hours. The effect of some of the cuts is not visible at this scale. The inset shows the same cuts in log scale so that the effect of the pileup cuts can be seen in the region beyond the ^{39}Ar spectrum endpoint where pileup dominates the ERB.

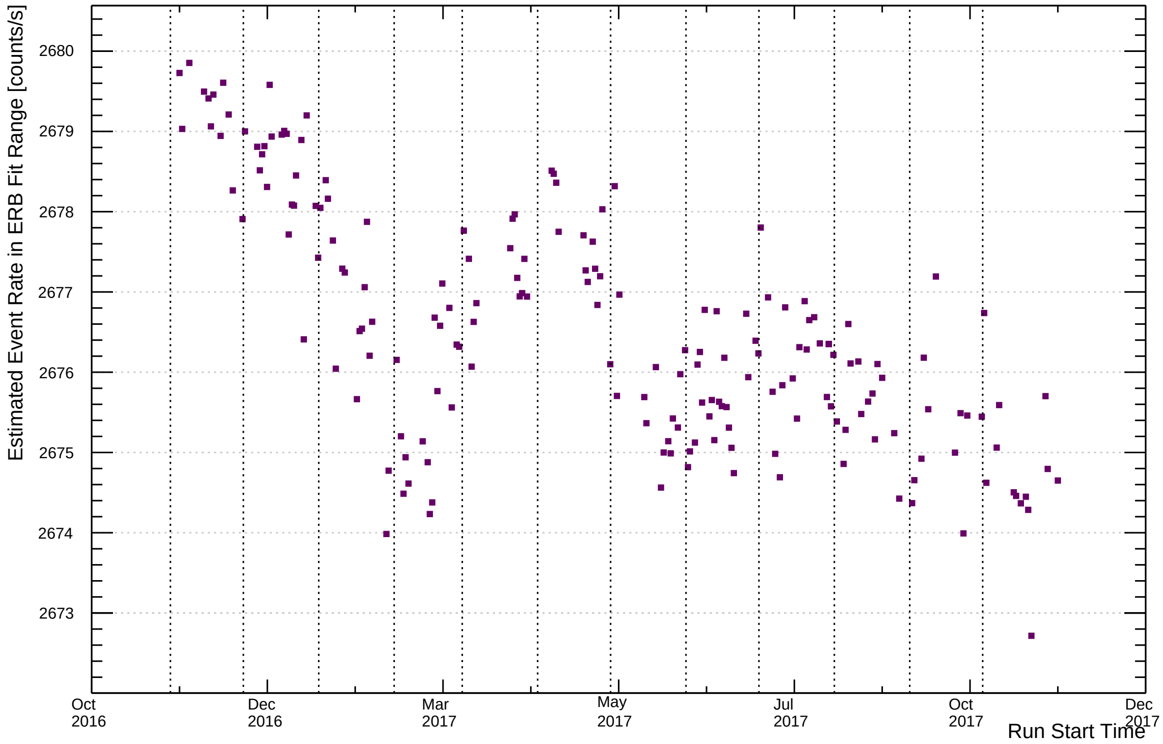

Figure 4.14: The event rate on a run-by-run basis for each run in the ERB that pass all of the ^{39}Ar selection cuts. The event rate is measured by dividing the event count in the fit range by the runtime for each run.

4.3.6 Other Variables and Cuts Examined

There are two additional parameters that were examined to determine how effectively they could be used to select ^{39}Ar events. Through the following analyses it was determined that these parameters/cuts do not improve the selection of ^{39}Ar events, and so they are not included in the cut-flow.

$\mathbf{F_{maxPE}}$

The F_{maxPE} parameter is the fraction of the total charge that is measured by the PMT with the greatest charge in an event. This parameter is used to separate events like electron recoils which produce light isotropically from within the LAr volume (low

F_{maxPE}) from events such as Cherenkov light produced in the PMT light guides (high F_{maxPE}); F_{maxPE} spectra from data and MC are shown in Figure 4.15.

This parameter is one of a standard set of cuts for a dark matter search, which takes place in a different region of the F_{maxPE}:PE spectrum. Through an analysis of this parameter in the electron recoil band, it has been determined that an F_{maxPE} cut is not necessary; after a cut on F_{prompt}, the high F_{maxPE} events are removed. The spectra of events in data, along with ^{39}Ar and several backgrounds from MC are shown in Figure 4.16. No clear difference exists between ^{39}Ar recoils and, for example, gamma recoils, so a cut on this parameter cannot be used to separate ^{39}Ar from backgrounds and thus no cut is made.

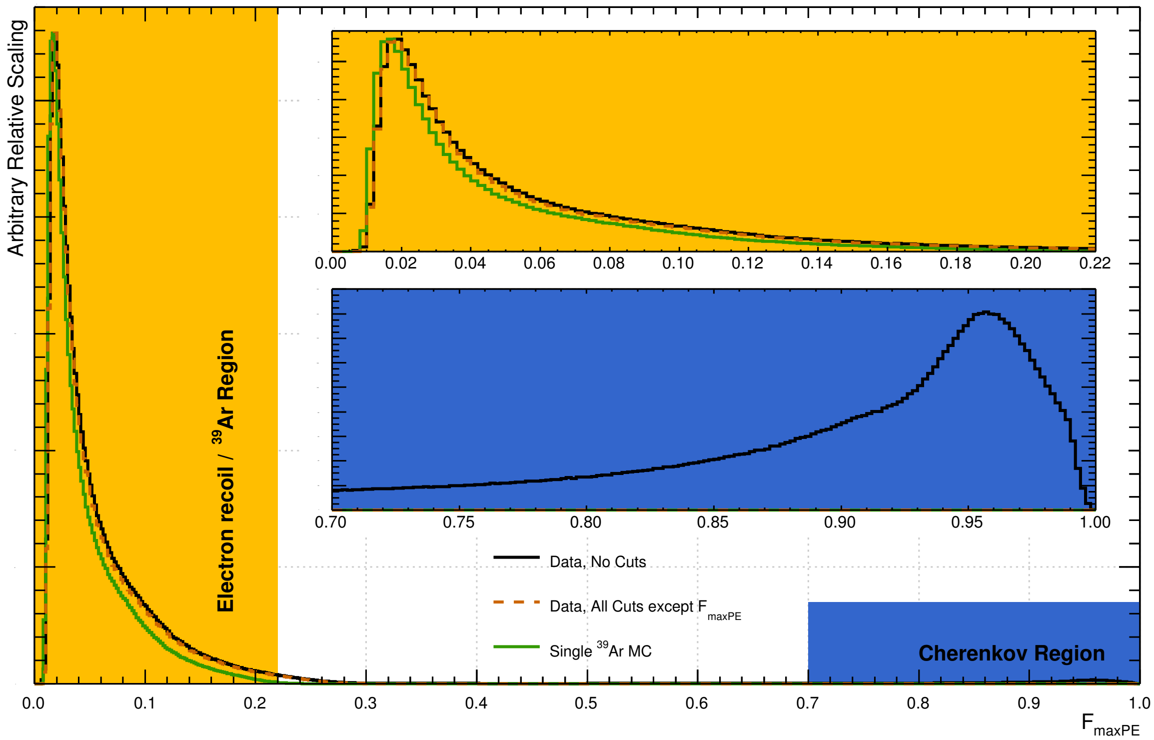

Figure 4.15: F_{maxPE} spectra from data and from ^{39}Ar MC are shown. The histogram from MC is scaled to match the maximum bin of the data histogram so that the shapes can more easily be compared. The two regions dominated by either electron recoil events or Cherenkov events are highlighted. The inset focuses on the low F_{maxPE} region so the spectra from ^{39}Ar MC and selected ^{39}Ar candidate events in data may be compared.

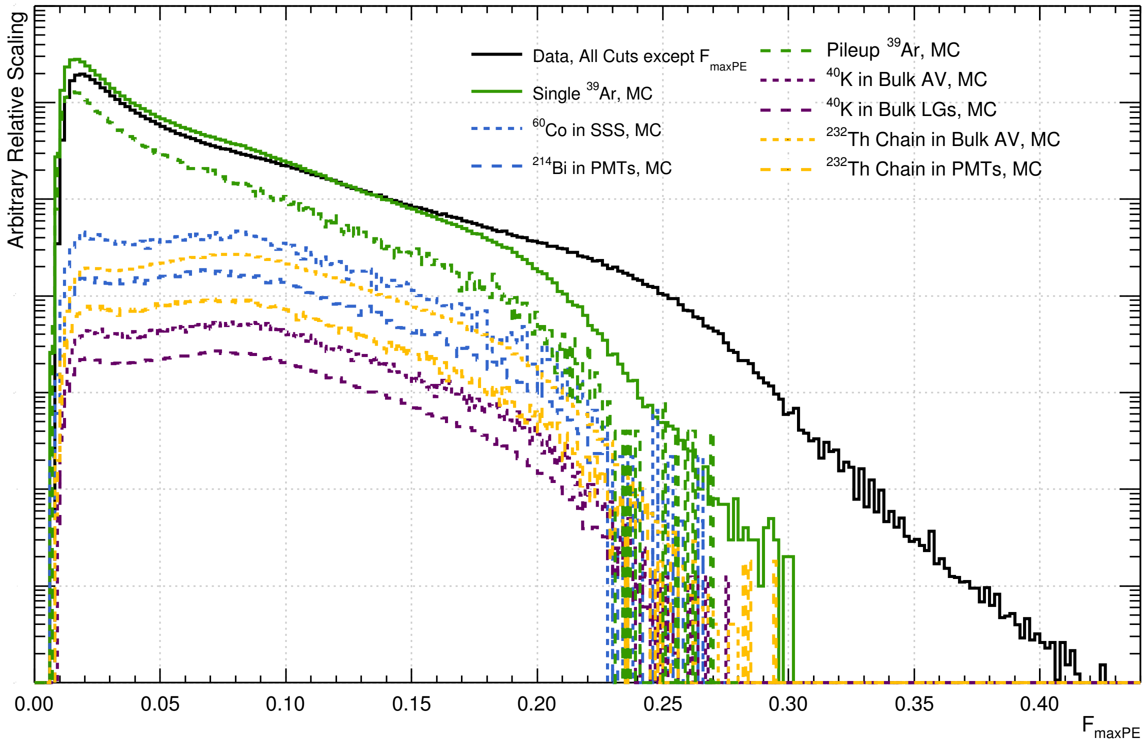

Figure 4.16: F_{maxPE} spectra from data, ^{39}Ar MC, and several dominant background MC are shown. The difference seen in the endpoints of the spectra in data and ^{39}Ar MC is not explained by examining the spectra from background sources.

deltaT

The deltaT parameter is a measure of the time between subsequent triggers and can be used to removed events which occur very close together in time. A pair of events close in time is potentially one for which late light from the first event leaks into the following event, contributing to the pileup spectrum. Figure 4.17 shows the effect of this cut in data when it is applied after all other cuts. In the 26 hour long run shown in the figure the cut removes 3 counts within the ^{39}Ar fit range; this is roughly 0.0001% of the total events in the spectrum fit range and so is negligible.

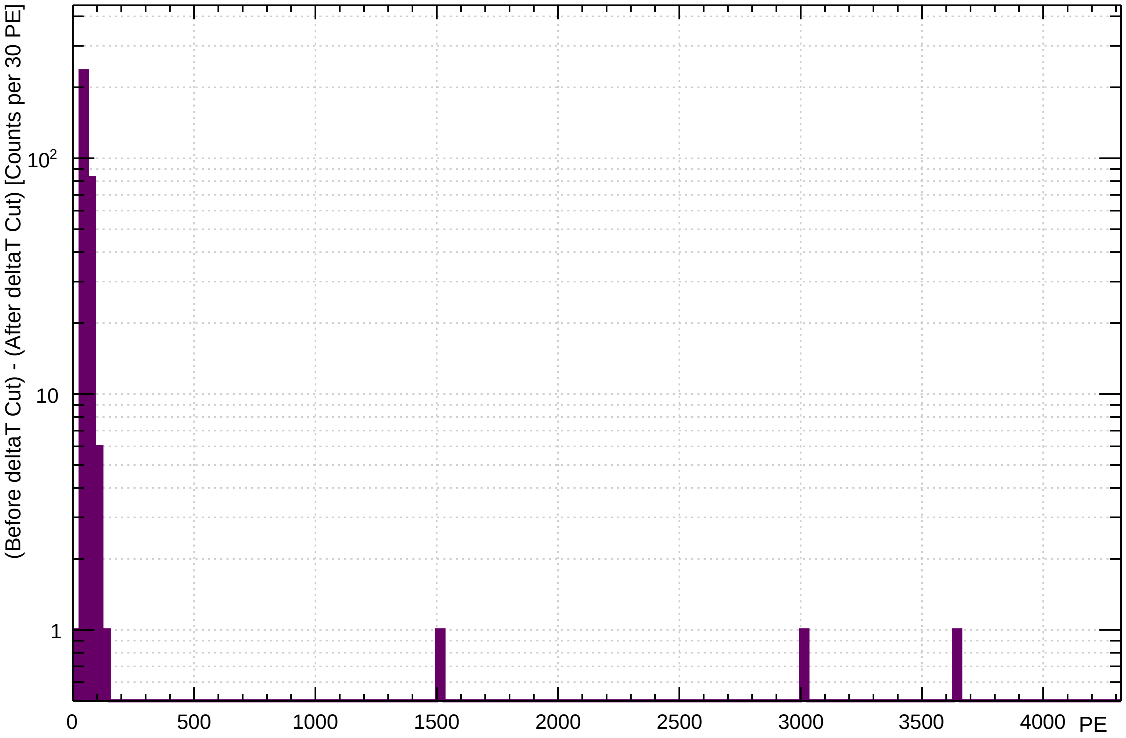

Figure 4.17: The effect of the deltaT cut in data from a 25 hour run; the spectrum from after the deltaT cut is subtracted from the spectrum before the cut.

4.4 Efficiency of ^{39}Ar Event Selection Cuts

The cuts described in the previous section are designed to select single ^{39}Ar events and reject other types of events. Even so, gamma events are effectively indistinguishable from single beta events. Furthermore the cuts can occasionally remove single ^{39}Ar events. A series of MC simulations have been performed to understand how well the cuts perform at selecting single ^{39}Ar events. This section will describe those simulations along with the cut efficiencies associated with selecting ^{39}Ar events.

4.4.1 Monte Carlo Simulations of Signal and Backgrounds

Several Monte Carlo (MC) simulations were generated for this analysis to determine the effects of various cuts. Simulations are generated through the framework of the Reactor Analysis Tool (RAT), a custom tool which combines Geant4 with ROOT. RAT allows for the analysis of both data and MC in a modular way such that different event processors can be turn on or off. The full DEAP-3600 detector geometry is implemented in RAT so that physics processes can be accurately simulated. This section will briefly describe each simulation and the reasons for which each was performed. For each simulation a LAr fill level of 551 mm above the centre of the AV was used; this corresponds to the current measured fill level in DEAP-3600. The simulated daq trigger was set to 451, a value which establishes the trigger with the same settings as for the collected data though with no prescaling factor. A full spectrum of the background listed in this section is shown in Figure 4.18.

Single ^{39}Ar

This simulation was generated to study the expected behaviour of ^{39}Ar decays in DEAP-3600 and to study their distribution in different parameter spaces. For the simulation, electrons are randomly and uniformly generated within the LAr volume. The electron's initial momentum is randomly generated using an energy which is sampled from a theoretical spectrum for ^{39}Ar beta decay calculated by Behrens and Janecke (shown in Figure 2.5).

Pileup ^{39}Ar

Pileup MC was generated to study the effect and the efficiency of the subeventN and numEarlyPulses cuts on pileup events, and to study the distribution of this type of event in different parameter spaces. Similar to the single ^{39}Ar simulation, initial subevents are isotropically generated within the LAr volume with an energy sampled from the theoretical beta spectrum. A second subevent is generated at a random time within the 13.5 μs window following the first event; with enough statistics this covers all possible scenarios of a second subevent within the same 16 μs window as the subevent which caused the trigger at 2.5 μs.

^{60}Co in the Stainless Steel Shell

The decay of ^{60}Co is described in Section 3.6.2. The gammas produced in the decay of this isotope have a chance to reach the LAr and produce a signal that is effectively indistinguishable from an ^{39}Ar decay.

^{214}Bi in PMT Glass

The decay of ^{214}Bi is described in Section 3.6.2. As with ^{60}Co, the gammas produced in this decay may reach the LAr and produce a signal.

^{40}K in Light Guide and AV Acrylic

The decay of ^{40}K is described in Section 3.6.2. This isotopes exists in the acrylic in DEAP-3600, and two separate simulations are performed for ^{40}K in the acrylic that comprises the vessel wall and in the acrylic of the light guides which couple the PMTs to the vessel.

^{232}Th in PMT Glass and AV Acrylic

The decay of this isotope is actually a chain of decays and is described in Section 3.6.2. Several of the daughter isotopes decay and generate gammas which can interact and produce a signal in the LAr.

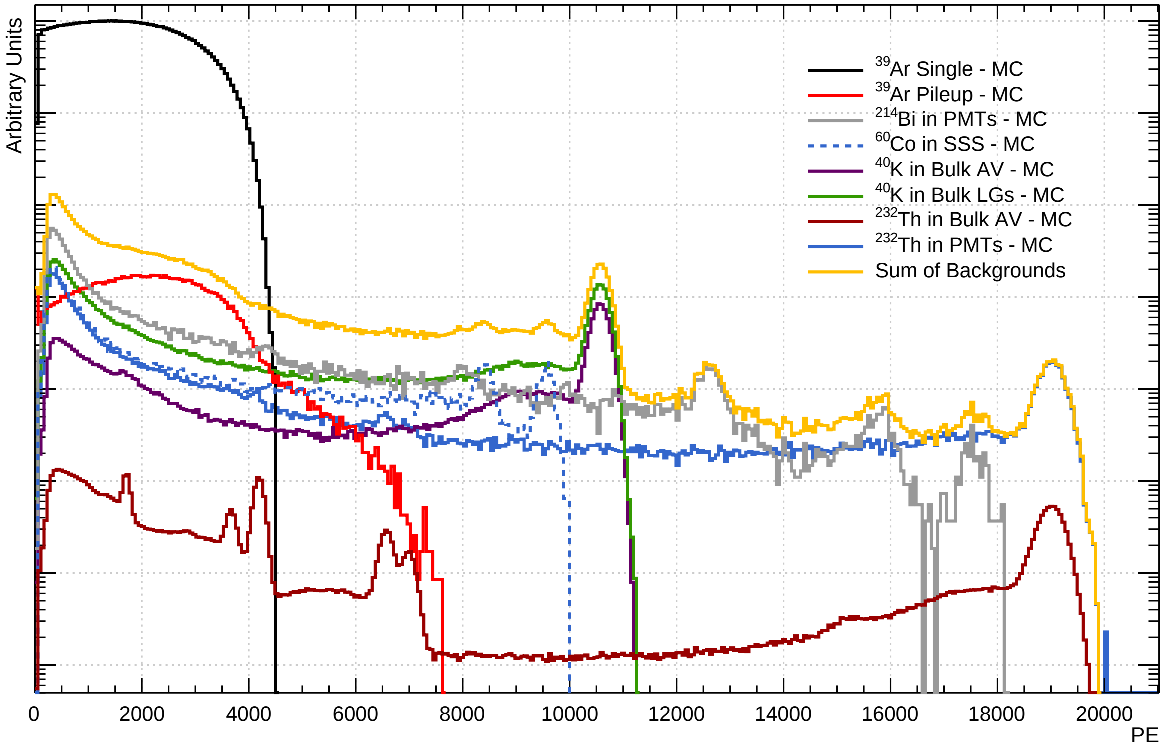

Figure 4.18: Background spectra from MC are compared with single-recoil ^{39}Ar. Each spectrum is shown after pileup and PSD cuts have been applied. The spectra are scaled relative to each other based on initial estimates of the activities from a manual fit to data in the ER band [69].

4.4.2 SubeventN and numEarlyPulses

The phenomenon of pileup in data can be difficult to deal with because there are many different contributions. The main contribution is ^{39}Ar with ^{39}Ar, and contributions from an ^{39}Ar event with a gamma background event or three ^{39}Ar events in the same time window are both present. There are four different scenarios which are to be considered; the different scenarios are as follows:

(i) Pileup events that are correctly identified by subeventN as a pileup event

(ii) Pileup events that are incorrectly identified by subeventN as a single event

(iii) Single events that are correctly identified by subeventN as a single event

(iv) Single events that are incorrectly identified by subeventN as a pileup event

Scenarios (i) and (ii) will be dealt with separately, and scenarios (iii) and (iv) will be dealt with together.

Scenario (i)

This scenario deals with pileup events that are correctly identified as a pileup event. The main classes of pileup events are: two coincident ^{39}Ar decays, three coincident ^{39}Ar decays, and ^{39}Ar coincident with a ERB or NRB background. To get an idea of what the rates of different types of pileup events might be, an estimated activity of the ^{39}Ar is used. The rate of background events in the ERB is approximately 12.2 Hz, and the rate of events in the NRB is approximately 25 Hz. With a measured LAr mass of 3279 kg and an assumed specific activity of 1.0 Bq·kg^{-1}, the estimated activity of ^{39}Ar in DEAP-3600 is 3279 Bq; 100% detection efficiency for all events is assumed and for simplicity the trigger rate is taken as 3334 Hz (the sum of the three main contributions). For every pileup event the first event triggers the detector and fixes the time window; any other event that occurs within the next 13.5 μs, which is the length of the post-trigger window, should be counted as pileup. Assuming 100% detection efficiency of ^{39}Ar events, the expected rates for different types of pileup events are shown in Table 4.5. The pileup rate is calculated as follows:

$$R_p = (R_1 \cdot t)R_2, \tag{4.4}$$

where R_1 is the rate of the first event, t is the time window, their product is the average number of events in the time window, and R_2 is the rate of the second event.

Source	Estimated Rate [Hz]	Fraction of Event Rate [%]
Double ^{39}Ar	145.15	4.35
Triple ^{39}Ar	6.42	0.19
^{39}Ar + NRB background	1.11	0.03
^{39}Ar + ERB background	0.54	0.02

Table 4.5: Expected rates for different classes of pileup events in DEAP-3600

This gives a total estimated pileup rate of 153.22 Hz. With this estimate the average number of ^{39}Ar events per pileup event can be calculated:

$$N_{^{39}Ar} = \tag{4.5}$$

$$\begin{aligned}(2 \text{ events}) \times (145.15/153.22) + (3 \text{ events}) \times (6.42/153.22)\\ +(1 \text{ event}) \times (1.11/153.22) + (1 \text{ event}) \times (0.54/153.22)\\ = 2.03 \text{ events.}\end{aligned}$$

From this simple estimate one can see that to first order each pileup event consists of 2.03 ^{39}Ar events. For the ^{39}Ar rate an uncertainty of 5% on the assumed specific activity is taken and the mass uncertainty of 96 kg is also considered; the uncertainty on the assumed ^{39}Ar event rate is then 189 Hz. The uncertainty on the estimated pileup rate is then dominated by the largest pileup contributor - the double ^{39}Ar pileup - and the rate becomes (153 ± 17)Hz. This results in an estimated number of ^{39}Ar events per pileup event of (2.03 ± 0.11), equal to 5.4% uncertainty. Although the argument is somewhat circular, this fraction will be used to calculate the uncertainty on the number of pileup events added back into the event count.

Scenario (ii)

This scenario deals with pileup events which are identified as single events. These events which also pass the numEarlyPulses and F_{prompt} cuts will distort the energy spectrum of the single ^{39}Ar decays. From ^{39}Ar pileup MC 96.01% of events are correctly identified after both pileup cuts; after the F_{prompt} cut there are 96.38% of the total events remaining. Figure 4.19 shows a comparison of the spectrum of single ^{39}Ar decays with that of ^{39}Ar-^{39}Ar pileup both before and after cuts are applied.

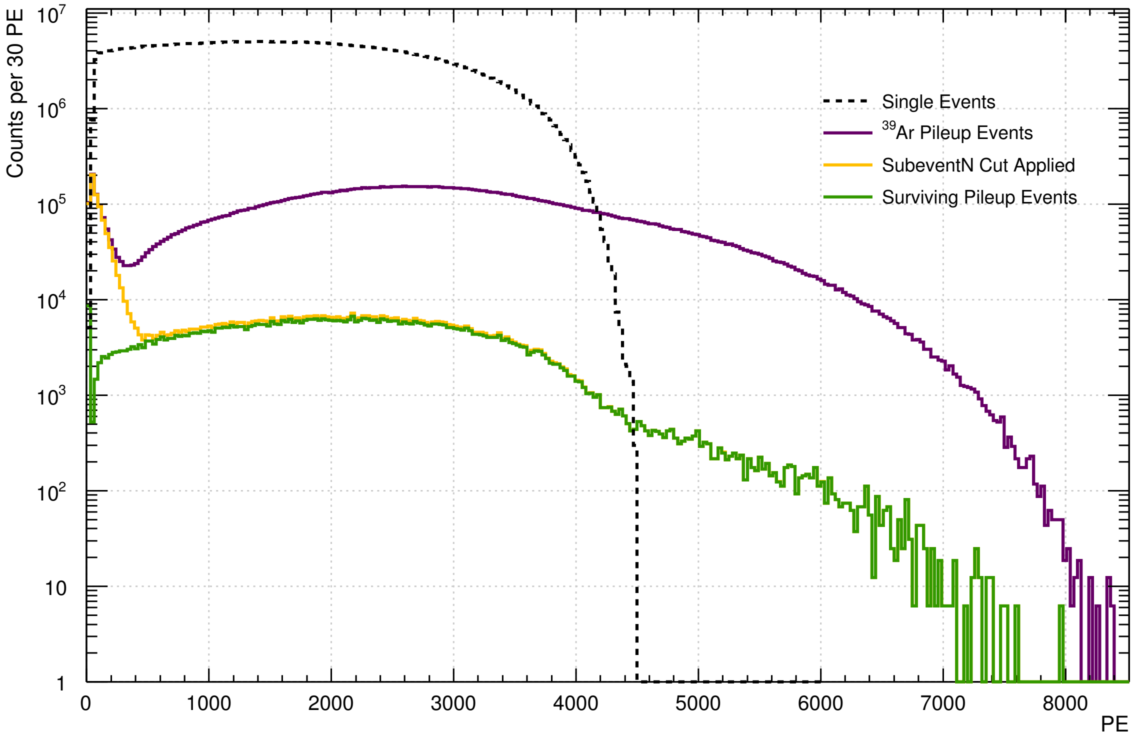

Figure 4.19: From MC, single ^{39}Ar events are compared with ^{39}Ar pileup events, and the effect of the pileup cuts is shown. The spectrum of pileup events with no cuts (purple) is shown alongside the spectrum of surviving pileup events which pass both the pileup and F_{prompt} cuts (green). Aside from at very low energy, the F_{prompt} cut removes so few events that the difference between the spectrum after the numEarlyPulses cut is nearly identical to the spectrum after the F_{prompt} cut which follows it; because of this the spectrum after numEarlyPulses cut (and before the F_{prompt}) is not shown. The pileup spectra are scaled to estimated rates relative to the single ^{39}Ar spectrum.

Scenarios (iii) and (iv)

These two scenarios deal with single ^{39}Ar events and how the pileup cuts affect them. Events that are correctly identified by subeventN are the events that we want to keep; from the single ^{39}Ar MC, 99.87% of events survive a subeventN cut. The efficiency, ϵ, is calculated as an average over bins:

$$\epsilon = \frac{\sum\limits_{i=n}^{m} \zeta_i}{\sum\limits_{i=n}^{m} \eta_i}, \tag{4.6}$$

where ζ_i are the bin contents from the spectrum after the cut, η_i are the bin contents from the spectrum before the cut, and n and m are the starting and ending bin numbers, respectively. The spectrum of the efficiency for subeventN applied to single ^{39}Ar is shown in Figure 4.20; the average value over all bins within the spectrum fit range is 99.87%, which shows that subeventN is very good at correctly identifying single ^{39}Ar decays.

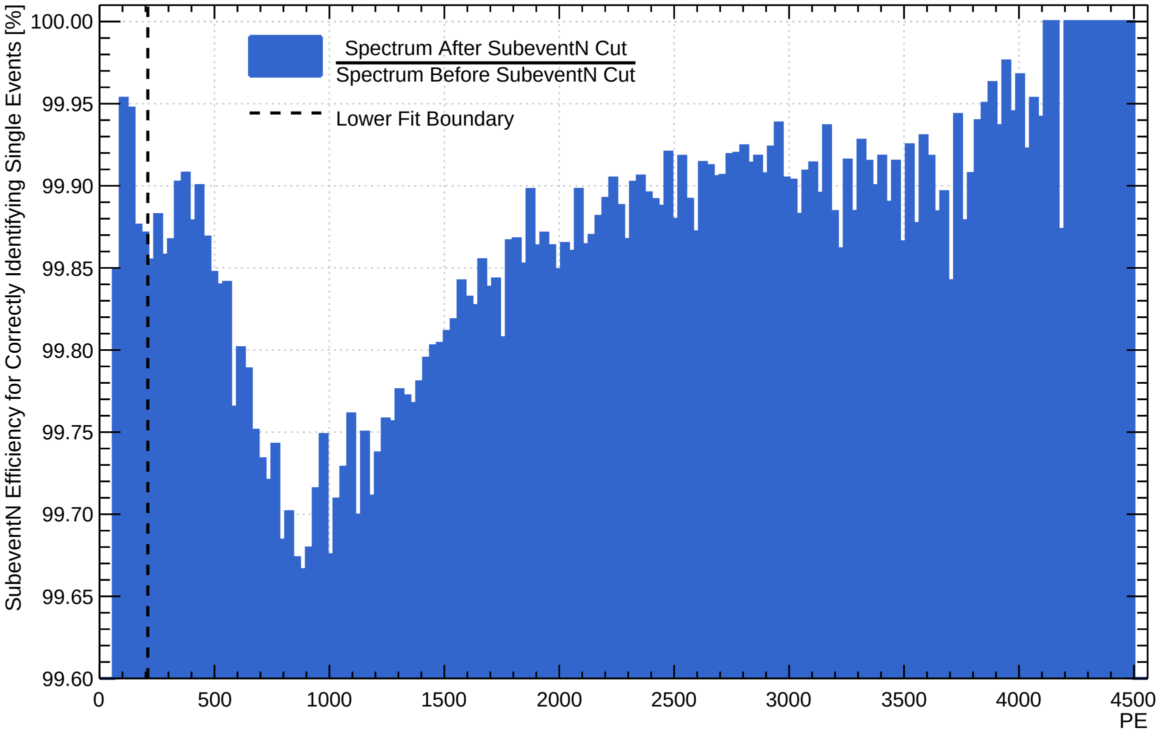

Figure 4.20: The cut efficiency for subeventN calculated bin-by-bin as per Eq. 4.6. A slight energy dependence can be seen in the efficiency spectrum, however the difference less than 0.5%.

This same procedure to determine the cut efficiency is applied for the numEarlyPulses cut. The cut efficiency is greater than 99.99% for this parameter; the spectrum of the efficiency per bin is shown in Figure 4.21.

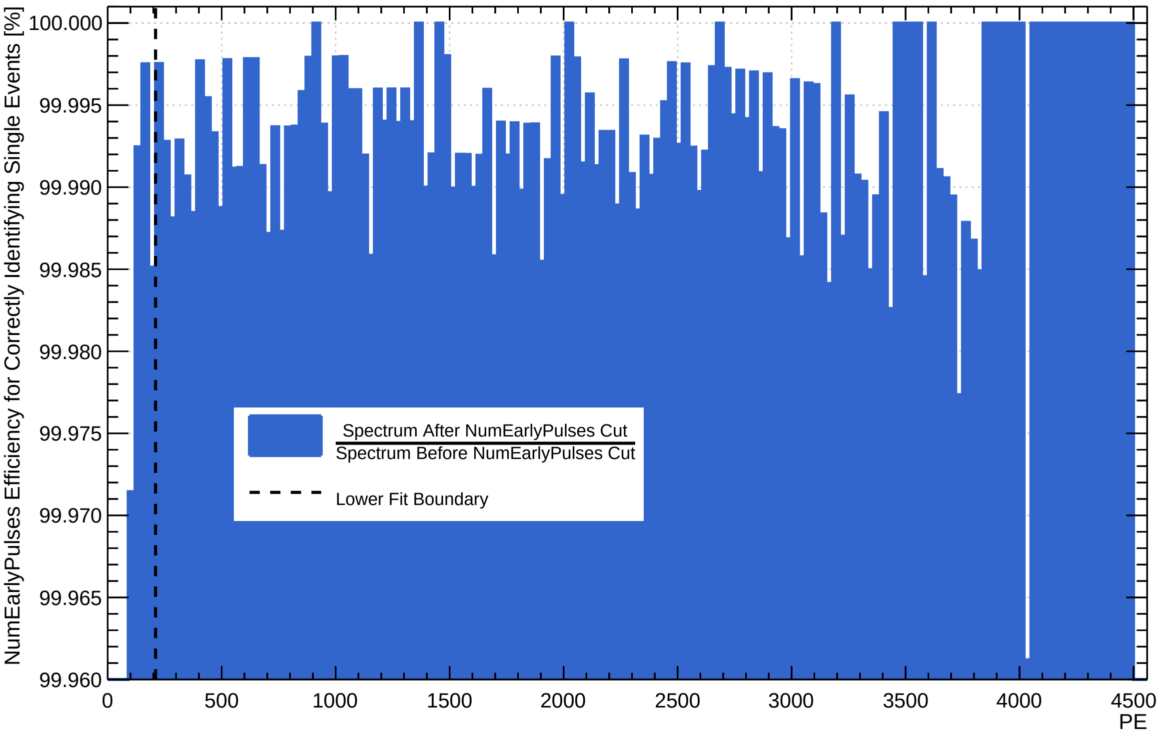

Figure 4.21: The cut efficiency for numEarlyPulses calculated bin-by-bin as per Eq. 4.6.

A pileup component that has not yet been considered is the pileup between a pulse tail that (re)triggers the detector and an ^{39}Ar event which occurs later but still within the trigger window. The rate of numEarlyPulses removal can be calculated by measuring the total number of events removed by this cut in the ERB F_{prompt} and dividing by the runtime. This rate is found to be about 60 Hz. The pileup rate between this and an ^{39}Ar event is: 60x3279x0.0000135 = 2.7 Hz. Taking this rate over one day of data the number of pileup events here is 2.3x10^{5}; using once again an assumed specific activity of 1 Bq/kg$_{\text{atmAr}}$ the number of ^{39}Ar events in the same period is 2.8x10^{8}. The pileup between a numEarlyPulses event and an ^{39}Ar event represents less than 0.1% of the total number of events; this is negligible when compared to expected dominant systematics such as the LAr mass uncertainty of about 3% and will not be used in this analysis.

4.4.3 $\mathbf{F_{prompt}}$

Between data and MC a slight difference in the location of the ERB in $\mathrm{F_{prompt}}$ is seen. To characterize the difference a fit to each spectrum has been performed to determine the location of each distribution's peak. Figure 4.22 shows the $\mathrm{F_{prompt}}$ spectra from data and MC. These spectra have been fit with the function described in Eq. 4.9; this fit function is the convolution of an asymmetric Lorentz distribution and Gaussian of mean zero, described in equations 4.7 and 4.8, respectively. There is no strong motivation for using this function, however it fits the distributions well and a complete understanding of the shape of the distribution is not required. A clear shift is seen between the distributions in data and MC; this shift is possibly due to differences in the MC optical model compared to the true optical model. This shift should be accounted for when comparing $\mathrm{F_{prompt}}$ cuts in data and MC.

$$L(x; x_0, \alpha, \beta, \gamma, \Phi) = \begin{cases} \left[\dfrac{\Phi}{1 + 4\left(\frac{x - x_0}{\gamma}\right)^2}\right]^{\alpha}, & x \leq x_0 \\ \left[\dfrac{\Phi^{\frac{\alpha}{\beta}}}{1 + 4\left(\frac{x - x_0}{\gamma}\right)^2}\right]^{\beta}, & x > x_0 \end{cases}, \tag{4.7}$$

where x denotes $\mathrm{F_{prompt}}$ values, x_0 [$\mathrm{F_{prompt}}$] is the peak of the spectrum, γ [$\mathrm{F_{prompt}}$] is the full width at half maximum of the peak, Φ [dimensionless] is a normalisation parameter, α [dimensionless] is a scaling parameter for the low $\mathrm{F_{prompt}}$ portion of the spectrum, and β [dimensionless] is a scaling parameter for the high $\mathrm{F_{prompt}}$ portion of the spectrum. The Gaussian is given by:

$$f(x; \sigma) = \frac{1}{\sqrt{2\pi}\sigma} e^{\frac{-x^2}{2\sigma^2}}, \tag{4.8}$$

where σ [$\mathrm{F_{prompt}}$] is the width of the Gaussian. Finally, the convolution of the two functions:

$$f_{F_{\mathrm{prompt}}}(x; x_0, \alpha, \beta, \gamma, \Phi, \sigma) = L(x; x_0, \alpha, \beta, \gamma, \Phi) f(x; \sigma) \tag{4.9}$$

For each fit, all variables are allowed to float. Figure 4.22 shows the $\mathrm{F_{prompt}}$ in data and MC.

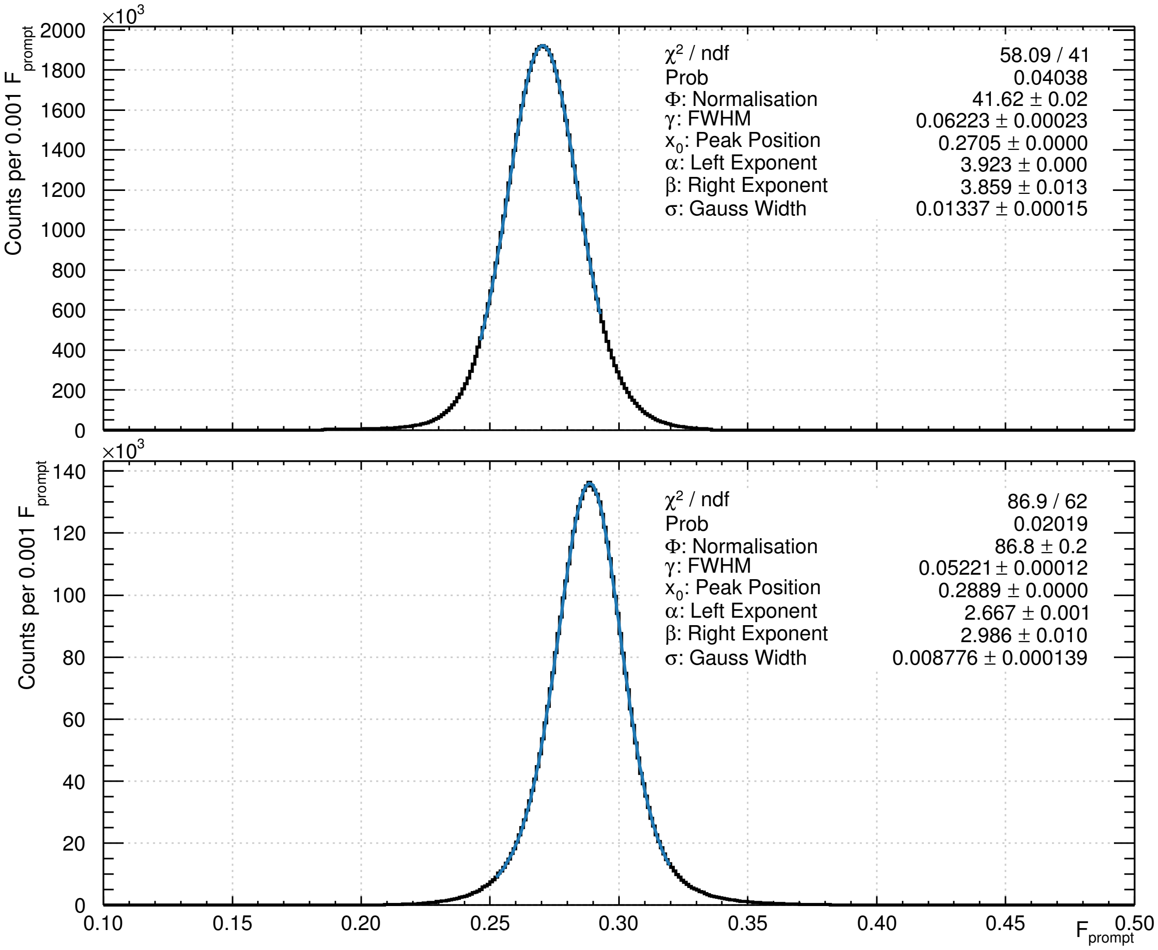

Figure 4.22: Upper panel: an $\mathrm{F_{prompt}}$ spectrum from data after all cuts have been applied. Lower panel: an $\mathrm{F_{prompt}}$ spectrum from single ^{39}Ar MC after all cuts have been applied. The fit function used is described in Eq. 4.9.

The $\mathrm{F_{prompt}}$ spectra peak in data and MC has peak positions of 0.2705 and 0.2889, respectively. This shift of (0.2889 - 0.2705) = 0.0184 must be accounted for when applying the cut in data as the cut values and cut efficiency are determined from MC.

The efficiency of the $\mathrm{F_{prompt}}$ cut for selecting ^{39}Ar decays is determined by examining the single event ^{39}Ar MC. This MC is also used determine the efficiency of the cut. After the pileup cuts have been applied a cut is made on $\mathrm{F_{prompt}}$ which keeps events in the range of 0.1184 to 0.5184; the spectrum before the $\mathrm{F_{prompt}}$ cut is compared to that from after the cut. This comparison gives a cut efficiency of 100% above 210 PE.

4.5 Fitting the ^{39}Ar Spectrum

The trigger efficiency of the data acquisition system is not 100% for all energies, and events at low energies sometimes will not trigger the system. This means that many low-energy events are not observed or recorded. To estimate how many of these events are lost, a theoretical ^{39}Ar beta spectrum is convolved with a Gaussian to approximate detector resolution effects to produce a model which is fit to data using the Bayesian Analysis Toolkit (BAT) software [70]. The BAT software is based on Bayes' Theorem [71] and uses Markov Chain MC (MCMC) to generate posterior probability distributions and estimate model parameters. Unless otherwise stated, the central values and uncertainties quoted for the fit parameters are the means and 90% quantiles measured from the marginalized distributions, respectively.

The model ^{39}Ar beta spectrum is that described in section 2.3.1 and shown in Figure 2.5. The fit is given a constant prior and returns the normalisation of the model spectrum as a parameter, k, which is the logarithm of the number of counts. The model includes three parameters to set the energy scale: a linear term which converts from deposited energy to reconstructed PE, a constant term to account for dark noise and stray light that can be detected in the PMTs, and a quadratic term. For each energy scale parameter a constant prior is used. The parameter ranges for the linear scale term, quadratic scale term, and linear resolution term are (7.3 -

7.8)PE·keV^{-1}, (-0.00015 - 0)PE·keV^{-2}, and (0 - 6), respectively. The energy scale term is shown in Eq. 4.10 and is applied to the model histogram.

$$\Omega_0 = \omega_1 + \omega_2 E + \omega_3 E^2, \tag{4.10}$$

where ω_1 is the constant energy term [PE], ω_2 is the linear energy term [PE/keV], ω_3 is the quadratic term [PE/keV^2], and E is the energy at the bin centre. The function is applied bin by bin, across all bins in each model. The constant energy term, ω_1, is not easily extracted from the ^{39}Ar spectrum and so unless otherwise stated it is fixed for all fits. The value of this parameter has previously been measured to be (1.2 ± 0.2)PE by another member of the DEAP-3600 collaboration [72]. This value was determined by the measuring rates of dark noise and stray light in the PMTs, estimating the number of dark noise/stray light single-photoelectron events in a 10 μs integration window, and summing the contribution from all 255 PMTs.

The resolution parameter is given in Eq. 4.11.

$$\sigma_0 = \sqrt{\phi E_{PE}}, \tag{4.11}$$

where ϕ is the resolution parameter, and E_{PE} is the PE value from the model at the bin centre. The resolution parameter uses a flat prior in the fit.

In addition to the ^{39}Ar model, the fit includes a model of the ERB background and a spectrum of surviving pileup events - both of which include the detector resolution effects and energy scale term - and all three spectra are fit simultaneously; the ERB background and pileup spectra use Gaussian priors each with a mean of 1 and a sigma of 0.3 for their normalisations; the parameters are allowed to float in the fits and are both constrainted in the range (0 - 3). For each of these spectra a starting normalisation is taken from an assumed rate of events and the known runtime; the normalisation parameter in the fit is the fraction of these default normalisations. For the surviving pileup spectrum a rate of 5.361 Hz is assumed and is used to set the normalisation of this spectrum; for a 24 hour runtime this corresponds to $4.63\text{x}10^5$ events. The value of 5.361 Hz was intially estimated from pileup rates and a pileup rejection efficiency estimate from Monte Carlo. For the ERB background spectrum an assumed rate of 12.2 Hz is used to set the normalisation of this spectrum; the rate is an combined initial estimate of non-^{39}Ar event rates from the ERB.

For the ^{39}Ar fits a Poisson uncertainty is used for the statistical uncertainty in the bins. A binned likelihood fit is performed which calculates the folowing function and maximizes the sum across those bins:

$$\sum_{i=1}^{n_B}\left[\mathrm{D}_i \times \ln(\mathrm{M}_i) - \left[\mathrm{D}_i \times \ln(\mathrm{D}_i) - \mathrm{D}_i + \frac{\ln(\mathrm{D}_i \times (1 + 4\mathrm{D}_i \times (1 + 2\mathrm{D}_i)))}{6} + \frac{\ln(\pi)}{2}\right]\right], \tag{4.12}$$

where n_B is the number of bins in the fit ranges, D_i are the bin contents in the data spectrum and M_i are the bin contents in the model spectrum; the model spectrum here is the sum of the ^{39}Ar model, the ERB background model, and the surviving pileup model and contains the fit parameter dependences.

A series of plots showing the prior information and the posterior distribution for each free parameter are shown in Figure 4.23 for a typical run in data. Figure 4.24 shows all of the parameter correlations for a typical run in data.

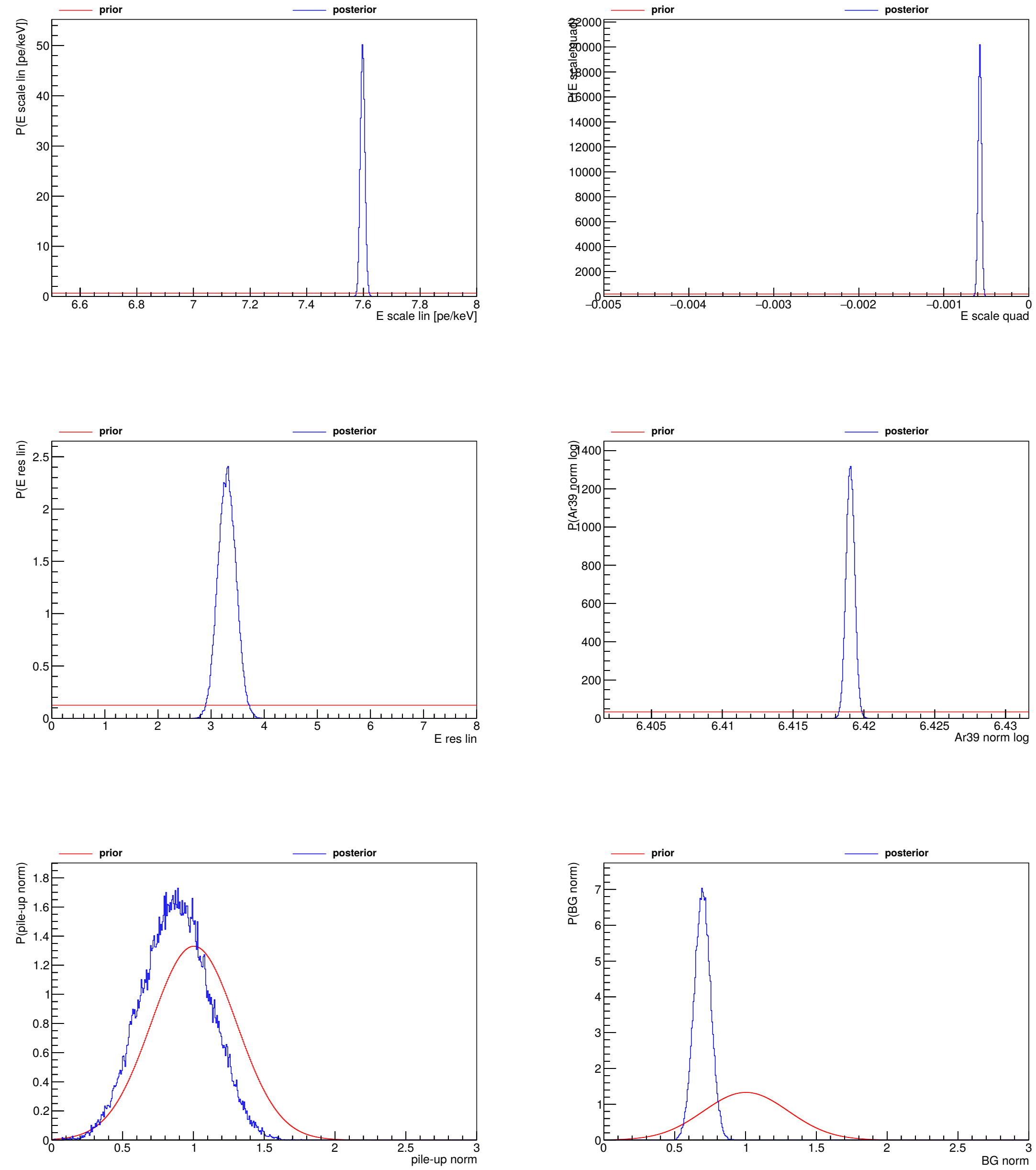

Figure 4.23: Knowledge update plots for a typical run in data; shown are the prior and posterior distributions. Top left: the linear energy scale parameter with a flat prior. Top right: the quadratic energy scale parameter with a flat prior. Middle left: the linear energy resolution parameter with a flat prior. Middle right: the ^{39}Ar normalisation parameter with a flat prior. Bottom left: the surviving pileup spectrum normalisation parameter with a Gaussian prior. Bottom right: the ERB background spectrum normalisation parameter with a Gaussian prior.

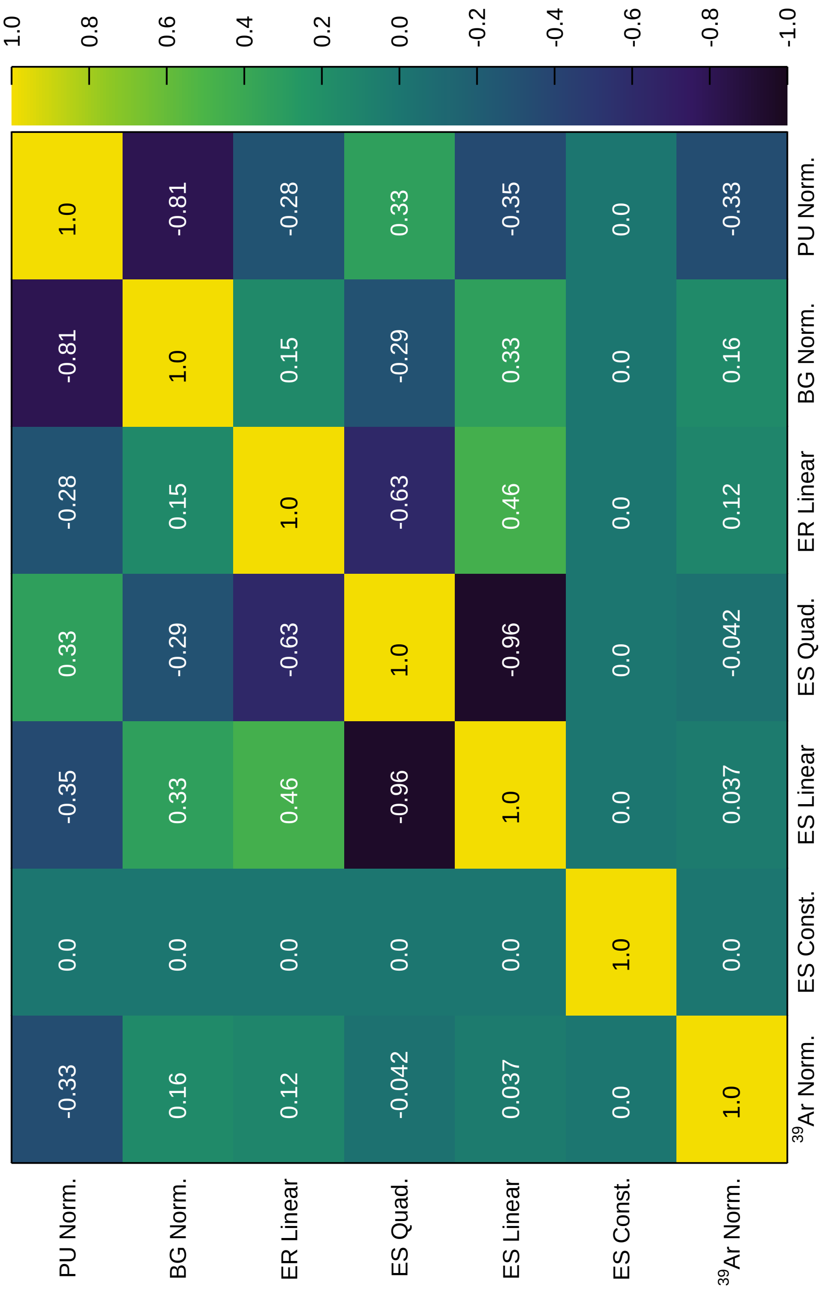

	PU Norm.	BG Norm.	ER Linear	ES Quad.	ES Linear	ES Const.	^{39}Ar Norm.
PU Norm.	1.0	-0.81	-0.28	0.33	-0.35	0.0	-0.33
BG Norm.	-0.81	1.0	0.15	-0.29	0.33	0.0	0.16
ER Linear	-0.28	0.15	1.0	-0.63	0.46	0.0	0.12
ES Quad.	0.33	-0.29	-0.63	1.0	-0.96	0.0	-0.042
ES Linear	-0.35	0.33	0.46	-0.96	1.0	0.0	0.037
ES Const.	0.0	0.0	0.0	0.0	0.0	1.0	0.0
^{39}Ar Norm.	-0.33	0.16	0.12	-0.042	0.037	0.0	1.0

Figure 4.24: Parameter correlations from the ^{39}Ar fit for a typical data run. The parameter labels are as follows: PU Norm. - pileup spectrum normalisation, BG Norm. - ERB background spectrum normalisation, ER Linear - linear energy resolution parameter, ES Quad. - quadratic energy scale parameter, ES Linear - linear energy parameter, ES Const. - constant energy paramter, ^{39}Ar Norm. - ^{39}Ar spectrum normalisation.

Figure 4.25 shows a fit to MC generated data; the fit is able to correctly extract the individual components and returns the parameters that were used to generate the sampled spectra.

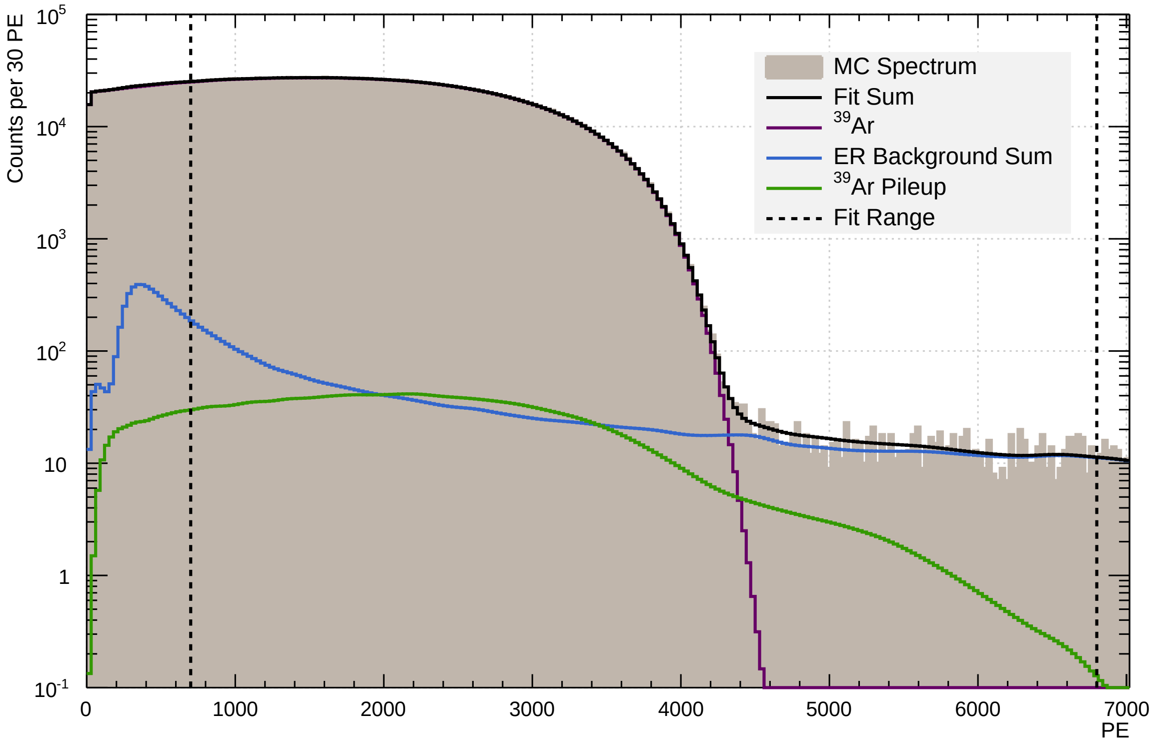

Figure 4.25: A fit to MC generated data. The spectra which make up the MC data are constructed by randomly sampling spectra output by the fitting code with all of the energy and resolution parameters fixed.

4.5.1 Choosing the Bin Width

An energy calibration was performed using the gamma peaks from ^{40}K (1461 keV) and ^{208}Tl (2615 keV) were used to determine the energy resolution in the ER band [73]. A plot of the calibration is shown in Figure 4.26. When the calibration is extrapolated down to the ^{39}Ar spectrum region the energy resolution ranges from roughly 2.5-8%. Taking a 5% resolution at 1000 PE gives a bin width of 50 PE, and taking 3% at the spectrum endpoint of 4400 PE gives a bin width of 130 PE.

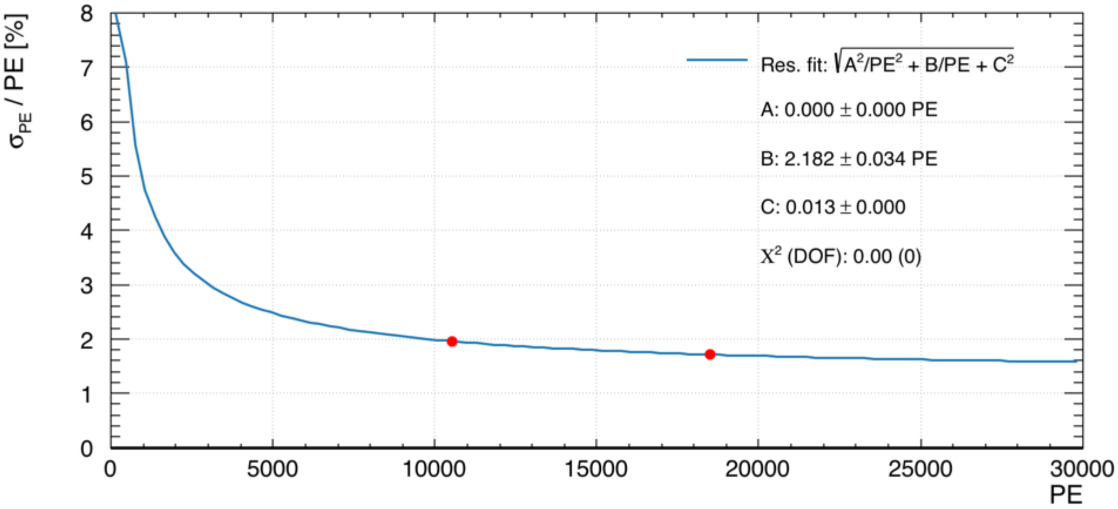

Figure 4.26: The energy resolution of the PE spectrum in the ERB as measured using two gamma peaks; ^{40}K at 1461 keV and ^{208}Tl at 2614 keV.

For the fits to measure the ^{39}Ar activity it was decided to use a bin width of 30 PE when building the energy spectra histograms; 30 PE was taken as a compromise between a having smooth spectrum and sufficient bin statistics, while staying roughly in the range of the resolution. To test how much the bin width affects the fit parameters, a series of fits were performed for each data run using bin widths which vary from 10 PE to 100 PE in 10 PE steps. The fit results for the ^{39}Ar normalisation are shown in Figure 4.27; a selection of 4 runs is presented, with the runs roughly spaced to divide the data set into quarters and representative of the entire data set. As seen in the figure, varying the bin width has an effect on the ^{39}Ar normalisation of less than 0.1% which is well within the statistical fit uncertainty. The negligible effect on the ^{39}Ar normalisation translate to a negligible effect on the specific activity measurement.

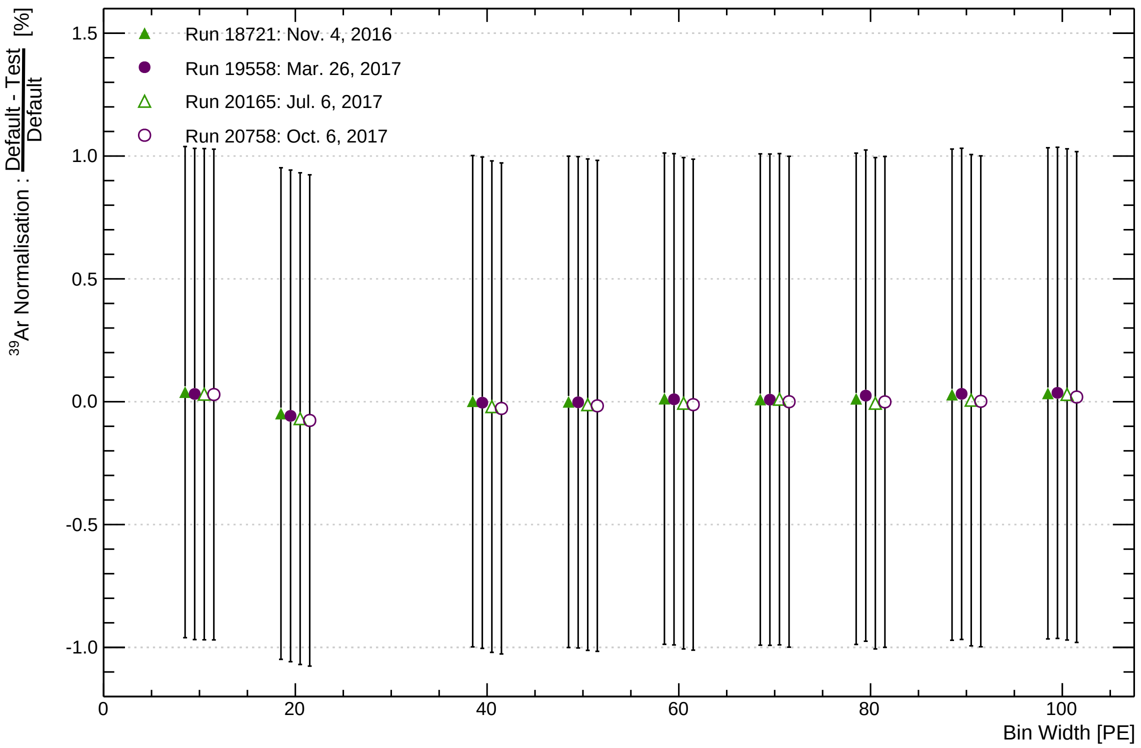

Figure 4.27: The effect of varying the bin width on the ^{39}Ar normalisation. 30 PE is the default bin width and the points are not shown. The error bars are propagated from the 90% CI statistical fit uncertainties.

Table 4.6 shows the energy scale results from each fit for a single run (18721) which is representative of the data set. The choice of bin width is seen to have a negligible effect on the fit parameters.

Bin Width	ω_2	ω_3	ϕ	χ^2/NDF
PE	PE/keV	PE/keV^2	PE$^{0.5}$	
10	7.597 ± 0.010	-5.75x10^{-4} $\pm0.25\times10^{-4}$	3.29 ±0.21	654.0/557
20	7.598 ±0.010	-5.76x10^{-4} $\pm0.25\times10^{-4}$	3.29 ±0.21	350.9/277
30†	7.597 ±0.010	-5.76x10^{-4} $^{+0.25\times10^{-4}}_{-0.26\times10^{-4}}$	3.30 ±0.22	252.2/183
40	7.598 ± 0.010	-5.77x10^{-4} $\pm0.25\times10^{-4}$	3.28 ±0.21	197.5/136
50	7.597 ± 0.010	-5.75x10^{-4} $\pm0.25\times10^{-4}$	3.28 ±0.21	171.3/108
60	7.598 ± 0.010	-5.78x10^{-4} $\pm0.25\times10^{-4}$	3.29 ±0.21	153.7/90
70	7.598 ± 0.010	-5.79x10^{-4} $\pm0.25\times10^{-4}$	3.33 $^{+0.22}_{-0.21}$	138.3/76
80	7.600 ± 0.010	-5.74x10^{-4} $^{+0.25\times10^{-4}}_{-0.24\times10^{-4}}$	3.28 ±0.21	129.8/66
90	7.598 ± 0.010	-5.78x10^{-4} $\pm0.25\times10^{-4}$	3.28 ±0.21	134.9/58
100	7.599 ± 0.010	-5.79x10^{-4} $\pm0.25\times10^{-4}$	3.30 ±0.21	110.50/52

Table 4.6: The results of fits using different bin widths on a single 26 hour data run. For each fit the constant energy scale parameter is fixed. The uncertainties shown are the 90% CI for the parameter; the uncertainties are generally slightly asymmetric, though the differences are small. Variations in the energy scale parameters are negligible. These results are representative of the data set.
† The default bin width.

4.5.2 Choosing the Fit Range

The fit range for the PE spectrum is 210 PE to 5820 PE. The lower bound was chosen such that the fit is performed in a region for which the trigger efficiency is 100%; the trigger efficiency is shown in Figure 3.7. The choice of the upper bound is not as strongly motivated, chosen such that a sufficient amount of the ERB background and surviving pileup spectra are included for the fit to extract their normalisations. To determine if these choices for the fit range has an effect of the fit results, several different fit ranges have been tested. The results of these fits where the lower bound is varied are shown in Table 4.7. The results of these fits where the upper bound is varied are shown in Table 4.8.

Varying the lower bound adds a greater or lesser portion of the ^{39}Ar data spectrum to the fit and it was unclear before the tests whether this would have a significant impact on the fit. From these tests it is seen that varying the lower bound has a negligible effect on the energy scale parameters. Varying the upper bound also has a negligible effect on the energy scale parameters, though this was to be expected as moving the upper bound simply adds more or less of the background spectra into the fit.

Test	Fit Range PE	ω_2 PE/keV	ω_3 PE/keV^2	ϕ PE$^{0.5}$	χ^2/NDF
1	120 - 5820	7.593 ± 0.010	-5.66x10^{-4} $\pm 0.24 \times 10^{-4}$	3.26 ±0.21	302.8/186
2	150 - 5820	7.595 ±0.010	-5.71x10^{-4} $\pm 0.25 \times 10^{-4}$	3.27 ±0.21	258.2/185
3	180 - 5820	7.598 ±0.010	-5.77x10^{-4} $\pm 0.25 \times 10^{-4}$	3.30 ±0.21	252.7/184
Default	210 - 5820	7.597 ±0.010	-5.76x10^{-4} $^{+0.25\times10^{-4}}_{-0.26\times10^{-4}}$	3.30 ±0.22	252.2/183
4	240 - 5820	7.597 ±0.010	-5.74x10^{-4} $\pm 0.25 \times 10^{-4}$	3.29 ±0.21	251.7/182
5	270 - 5820	7.600 ±0.011	-5.81x10^{-4} $\pm 0.25 \times 10^{-4}$	3.32 ±0.21	245.6/181
6	300 - 5820	7.599 ±0.011	-5.79x10^{-4} $\pm 0.25 \times 10^{-4}$	3.31 ±0.21	244.2/180
7	330 - 5820	7.596 ±0.011	-5.73x10^{-4} $\pm 0.26 \times 10^{-4}$	3.31 ±0.21	239.4/179
8	360 - 5820	7.597 ±0.011	-5.74x10^{-4} $\pm 0.26 \times 10^{-4}$	3.29 ±0.21	239.4/178
9	390 - 5820	7.596 ±0.011	-5.73x10^{-4} $\pm 0.26 \times 10^{-4}$	3.28 ±0.21	239.3/177

Table 4.7: The results of fits over different ranges on a single 26 hour data run; the upper bound is fixed and the lower bound is varied by 1 bin at a time. For each fit the constant energy scale parameter is fixed. The uncertainties shown are the 90% CI for the parameter; the uncertainties are in general slightly asymmetric, though the differences are small. Below 120 PE the fit is strongly influenced by the decreasing trigger efficiency and so fits in that range are possibly not representative of the data. These results are representative of the data set.

Test	Fit Range PE	ω_2 PE/keV	ω_3 PE/keV^2	ϕ PE$^{0.5}$	χ^2/NDF
1	210 - 5640	7.595 ±0.010	-5.71x10^{-4} $\pm 0.25 \times 10^{-4}$	3.28 ±0.21	243.1/177
2	210 - 5670	7.595 ±0.010	-5.71x10^{-4} $\pm 0.25 \times 10^{-4}$	3.28 ±0.21	244.0/178
3	210 - 5700	7.595 ±0.010	-5.72x10^{-4} $\pm 0.25 \times 10^{-4}$	3.28 ±0.21	244.5/179
4	210 - 5730	7.596 ±0.010	-5.73x10^{-4} $\pm 0.25 \times 10^{-4}$	3.29 ±0.21	246.0/180
5	210 - 5760	7.597 ±0.010	-5.75x10^{-4} $\pm 0.25 \times 10^{-4}$	3.29 ±0.21	248.9/181
6	210 - 5790	7.597 ±0.010	-5.76x10^{-4} $\pm 0.25 \times 10^{-4}$	3.29 ±0.21	252.2/182
Default	210 - 5820	7.597 ±0.010	-5.76x10^{-4} $^{+0.25\times10^{-4}}_{-0.26\times10^{-4}}$	3.30 ±0.22	252.2/183
7	210 - 5850	7.597 ±0.010	-5.75x10^{-4} $\pm 0.25 \times 10^{-4}$	3.29 ±0.21	251.8/184
8	210 - 5880	7.598 ±0.010	-5.77x10^{-4} $\pm 0.25 \times 10^{-4}$	3.30 ±0.21	254.4/185
9	210 - 5910	7.598 ±0.010	-5.78x10^{-4} $\pm 0.25 \times 10^{-4}$	3.30 ±0.21	256.7/186
10	210 - 5940	7.598 ±0.010	-5.78x10^{-4} $\pm 0.25 \times 10^{-4}$	3.30 ±0.21	257.8/187
11	210 - 5970	7.599 ±0.010	-5.79x10^{-4} $^{+0.25\times10^{-4}}_{-0.24\times10^{-4}}$	3.31 ±0.21	258.2/188
12	210 - 6000	7.599 ±0.010	-5.79x10^{-4} $\pm 0.25 \times 10^{-4}$	3.31 ±0.21	259.2/189

Table 4.8: The results of fits over different ranges on a single 26 hour data run; the lower bound is fixed and the upper bound is varied by 1 bin at a time. For each fit the constant energy scale parameter is fixed. The uncertainties shown are the 90% CI for the parameter; the uncertainties are in general slightly asymmetric, though the differences are small. These results are representative of the data set.

The effect on the ^{39}Ar normalisation is also examined to determine whether the fit range can have a significant effect, as a dependece on the fit range would translate into uncertainty in the measured specific activity. Figures 4.28 and 4.29 show the effect of varying the fit range; a selection of 4 runs is presented, with the runs roughly spaced to divide the data set into quarters and representative of the entire data set. The figures show that the lower fit range has a negligible effect on the normalisation, and hence would have a negligible effect on the specific activity. For the upper bound variations, the observed differences from the normalisations using the default fit range are much smaller compared to varying the lower bound, though this is expected because no portions of the ^{39}Ar spectrum are added or removed. All of these tests combined suggest that the choice of the fit range is an appropriate one.

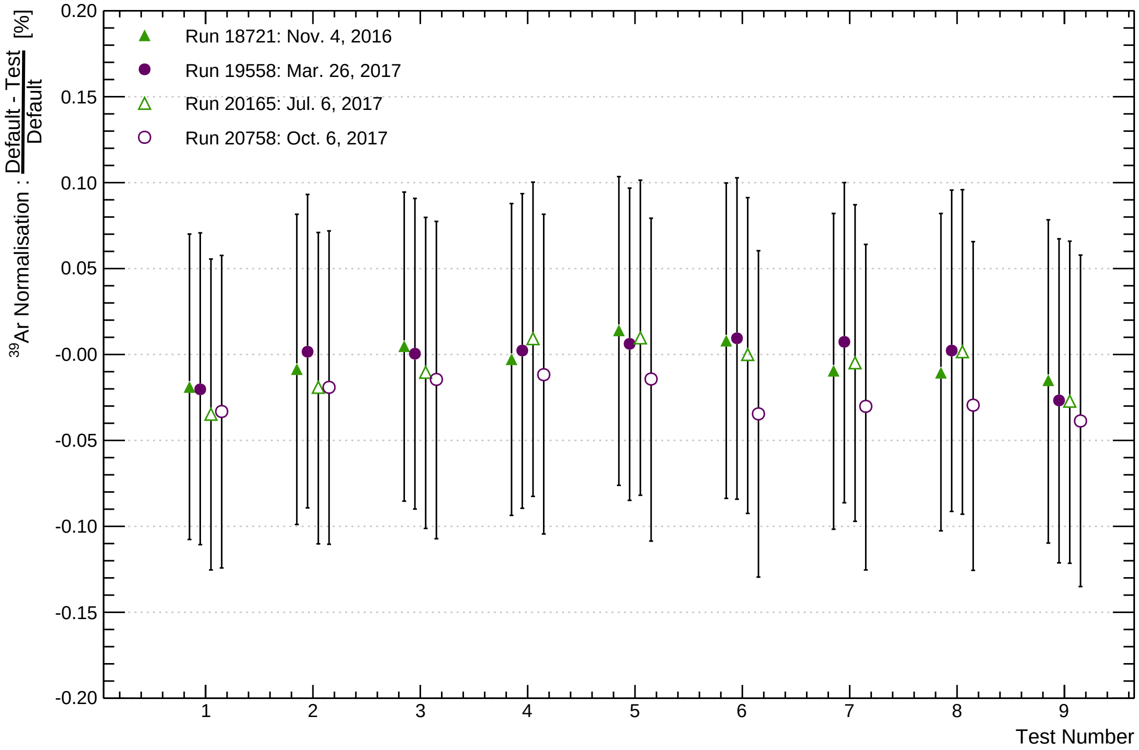

Figure 4.28: Effect of the lower fit PE range bound on the ^{39}Ar normalisation in data. Moving the lower bound of the fit has a negligible effect on the ^{39}Ar normalisation, with differences well within the fit uncertainties. The tests are numbered 1 through 9; the ranges for each test are listed in Table 4.7.

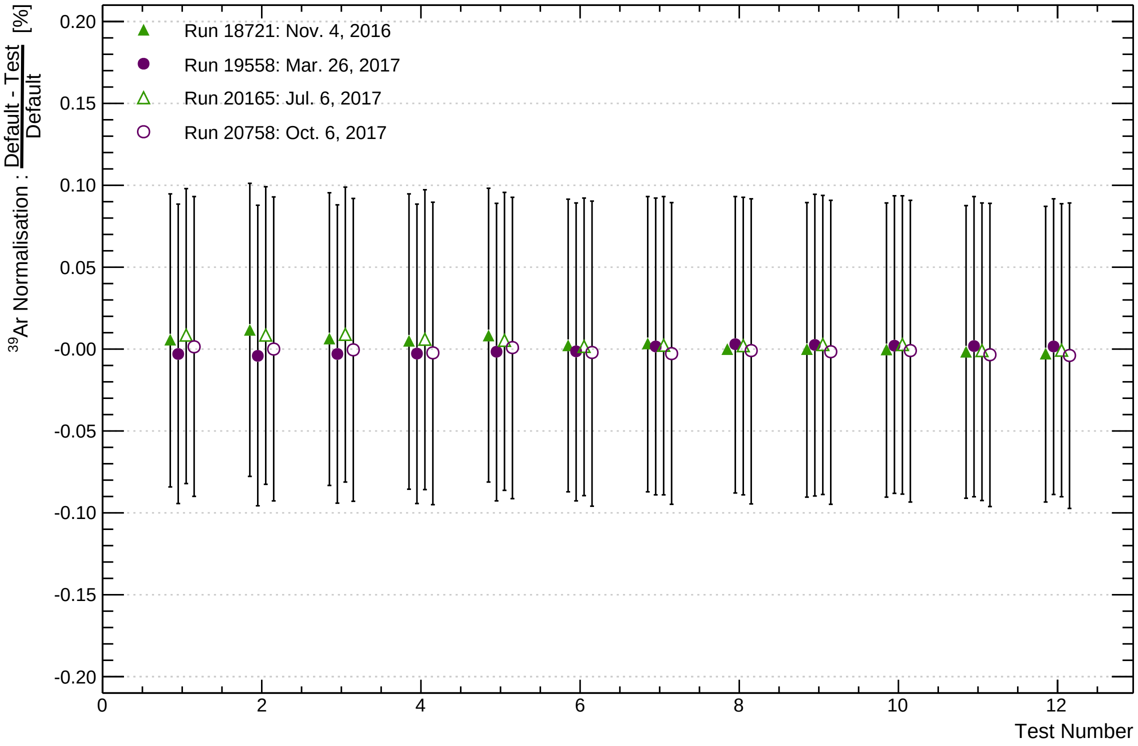

Figure 4.29: Effect of the upper fit PE range bound on the ^{39}Ar normalisation in data. Moving the upper bound of the fit has a negligible effect on the ^{39}Ar normalisation, with differences well within the fit uncertainties. The tests are numbered 1 through 12; the ranges for each test are listed in Table 4.8.

4.5.3 Varying the Detector Response Model

Several tests of the fit function have been performed. Using the default Behrens and Janecke theoretical spectrum, three additional energy scale models have been tested. These are listed in Eq. 4.13, 4.14, and 4.15. The first test is a simple model with no constant energy offset or quadratic energy term:

$$\Omega_1 = \omega_2 E. \tag{4.13}$$

The second test is with a model with no constant energy offset:

$$\Omega_2 = \omega_2 E + \omega_3 E^2. \tag{4.14}$$

The third and final test is a model with no quadratic energy term:

$$\Omega_3 = \omega_1 + \omega_2 E. \tag{4.15}$$

For each model, the parameters $\omega_{1,2,3}$ are as described in Eq. 4.10. The three additional models have been tested alongside the default model (Eq. 4.10) in data. For each model the fit is performed on each run of the ^{39}Ar data set and compared to the fits with the default model for those runs. These tests shown in Figure 4.30.

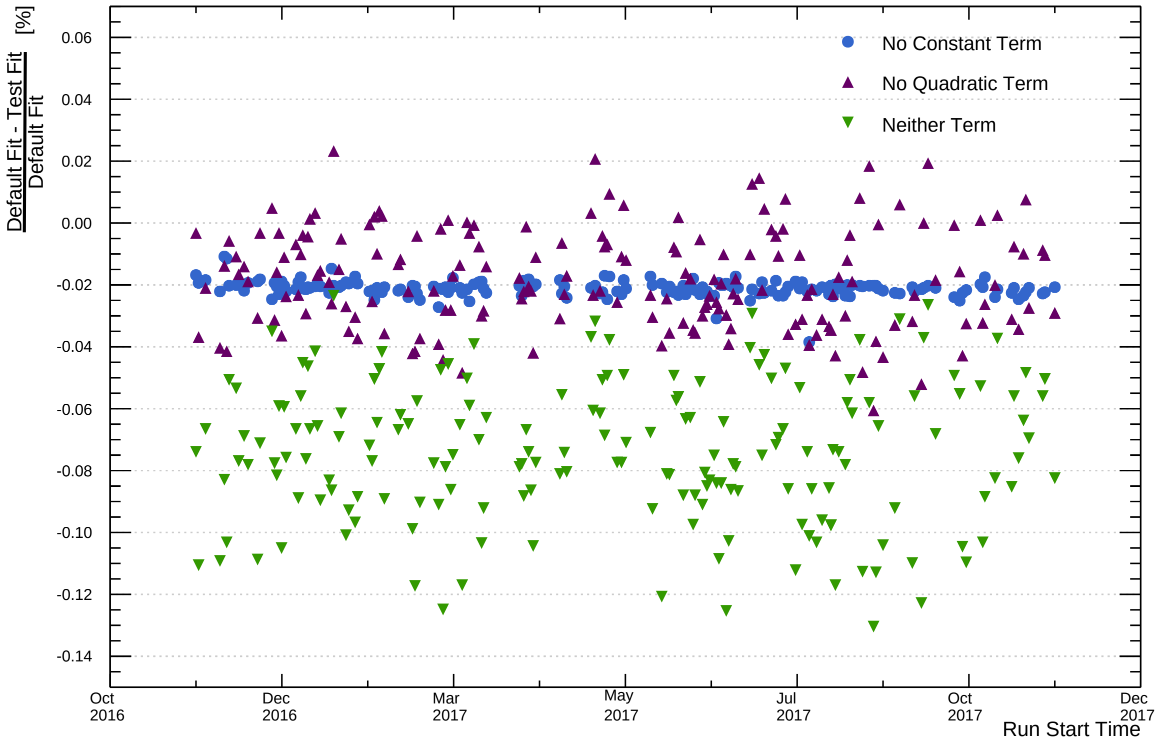

Figure 4.30: Tests of three additional detector response model functions in data. Shown is the percent difference between the test fit ^{39}Ar normalisation and the default fit ^{39}Ar normalisation. When the constant term is turned off the quadratic term is allowed to float in the fit (the default behaviour). When the quadratic term is turned off the constant term is fixed to 1.2 PE (also the default behaviour).

When either of the constant or quadratic terms are turned off the other term is able to compensate somewhat and the effect on the ^{39}Ar normalisation is minor, with a maximum variation of around 0.06%. When both terms are turned off the normalisation is increased, though with a maximum increase of about 0.13%. Since both parameters are turned on in the fits used to extract the specific activity, no systematic is assigned here.

4.5.4 Testing Position Dependence of the Fit Parameters

It is possible with such a large volume of LAr that optics may play a significant role in the behaviour of the energy scale. To test this, the detector has been divided into 5 regions of equal LAr volume (shown in Figure 4.31) and the fit performed for the spectrum from each region. To determine which region an event falls into, an event position reconstruction processor is included when the data is processed. The data used for the following fits was taken during a period in which the light yield (linear energy scale parameter ω_2) was relatively constant in November, 2016. A data set of 9.74 runtime-days is selected; when this is divided into 5 regions, each region will have statistics in the ERB background dominated portion of the spectrum comparable to roughly two days of undivided data. Figure 4.32 shows the radial distribution of events as a function of their reconstructed energy.

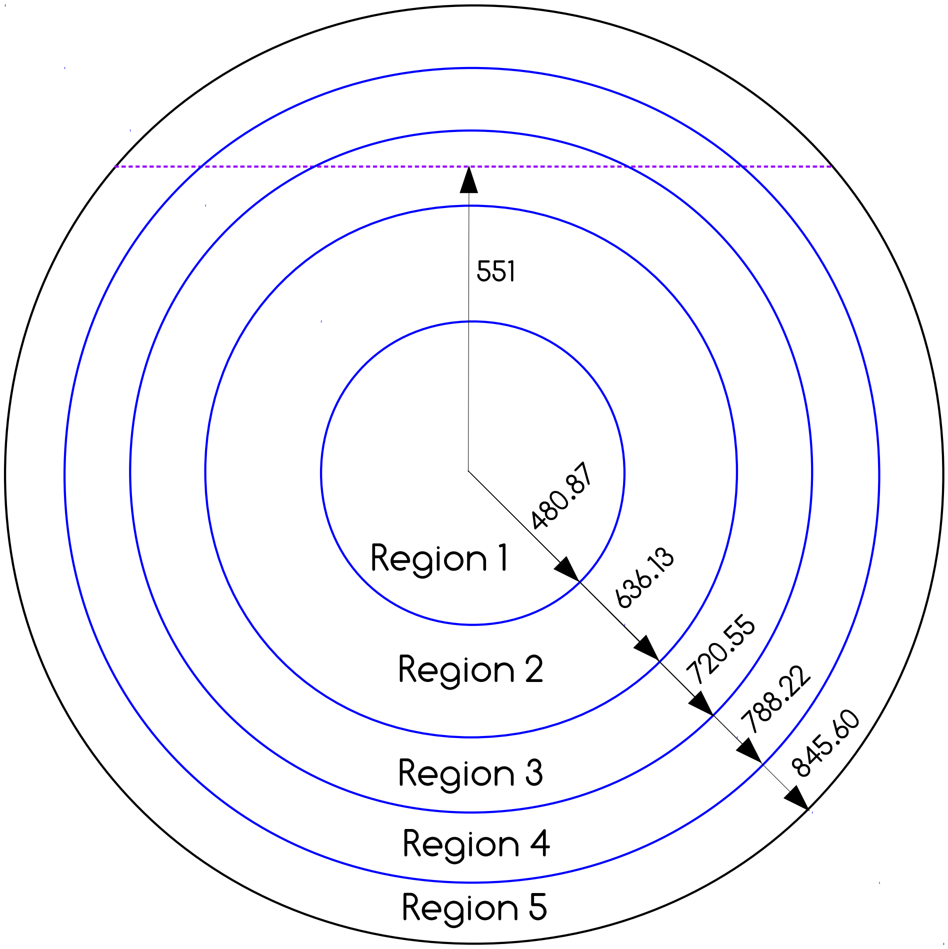

Figure 4.31: The 5 equal volumes of LAr, with the LAr fill level shown (dashed purple). All measurements are in mm.

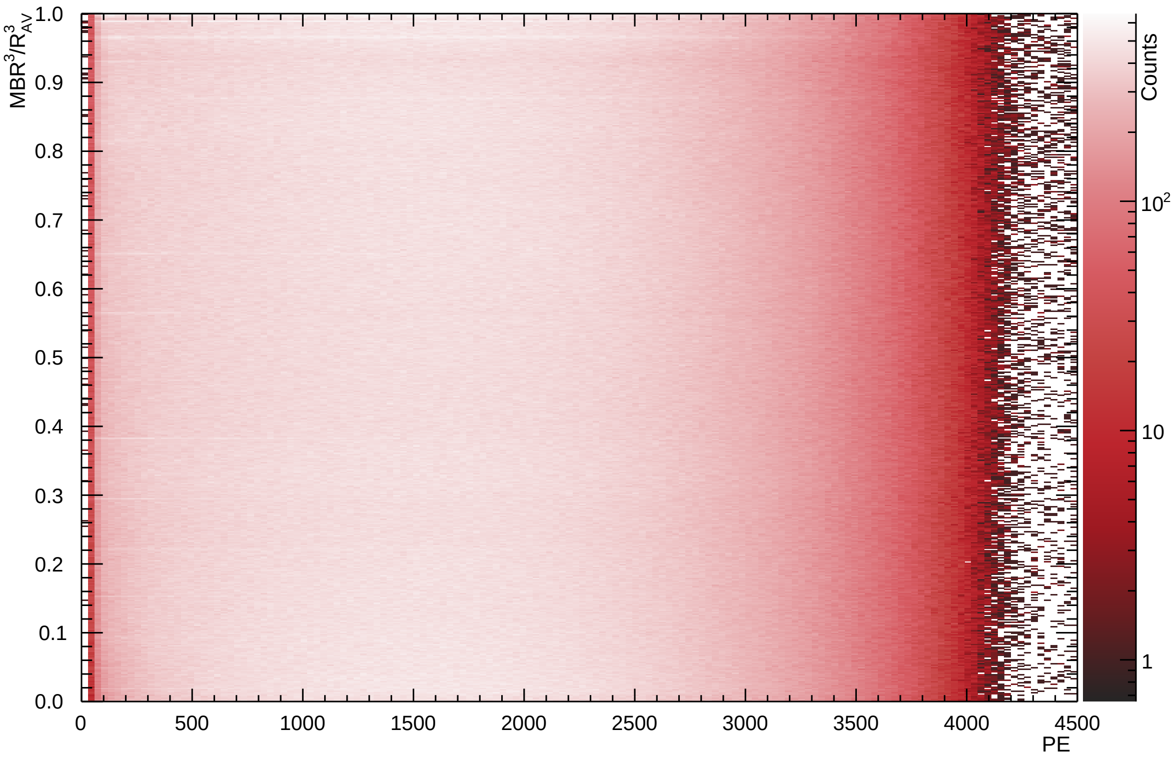

Figure 4.32: The radial distribution of events in the ER band across the AV is shown as a function of energy. The reconstructed radius term is cubed and normalized to give the fraction of the total AV volume.

Separating the AV into Radial Volumes

The next set of figures are the results from the fits to each radial region. Figure 4.33 shows the 5 fit outputs and the 5 data spectra. A difference in the spectral shapes in data can be seen at reconstructed energies below 500 PE; this difference is thought to be caused by a observed bias in the position reconstruction used to separate the events into the 5 regions.

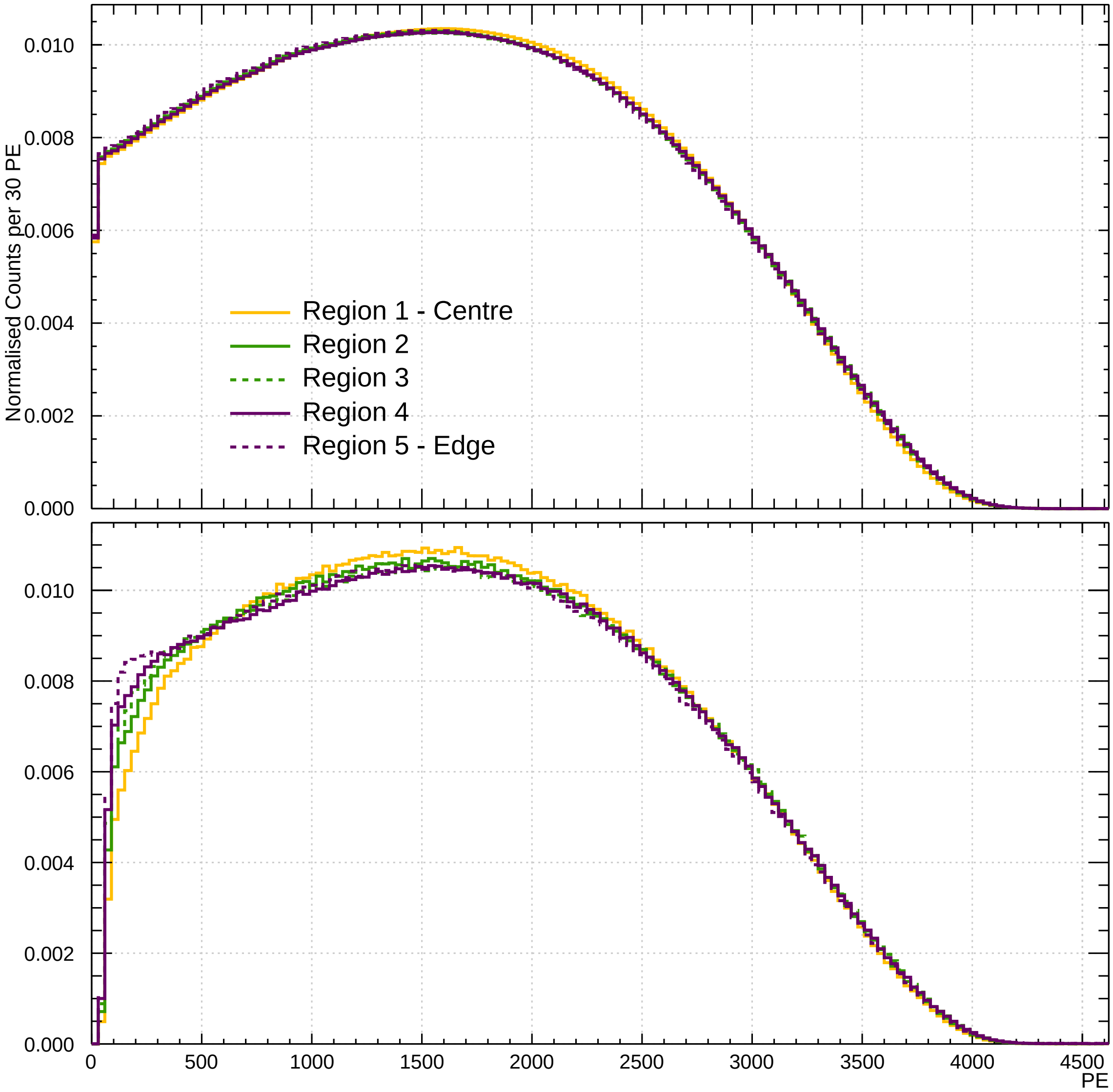

Figure 4.33: Top panel: The model spectra measured by the fits in the 5 radial regions are overlain. Each spectrum is normalised to unit area so their shapes can be compared. Bottom panel: The energy spectra in each region that are inputs for the fit. Each spectrum is normalised to unit area.

Figure 4.34 shows the result of the linear energy scale parameter from each fit, along with the result of a fit to the same data set using an unsorted spectrum. Differences from the unsorted spectra fit are seen in particular for the central and edge regions;

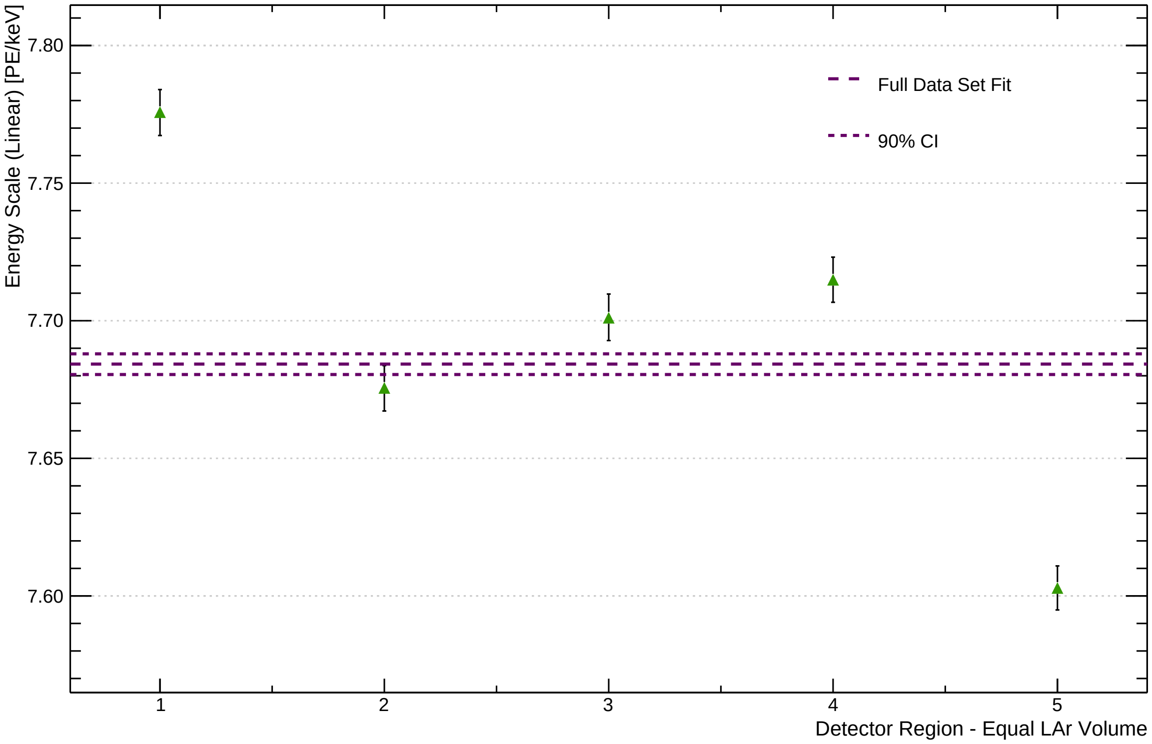

Figure 4.34: The linear energy scale term from each of the 5 radial region fits is compared with the the fit to the full detector volume. The uncertainties shown are 90% quantiles from the marginalized distributions. The regions are numbered with 1 at the centre of the AV and 5 at the edge.

Figure 4.35 shows the quadratic energy scale parameter from the fits. Once again the central and edge regions diverge from the fit to the unsorted spectrum.

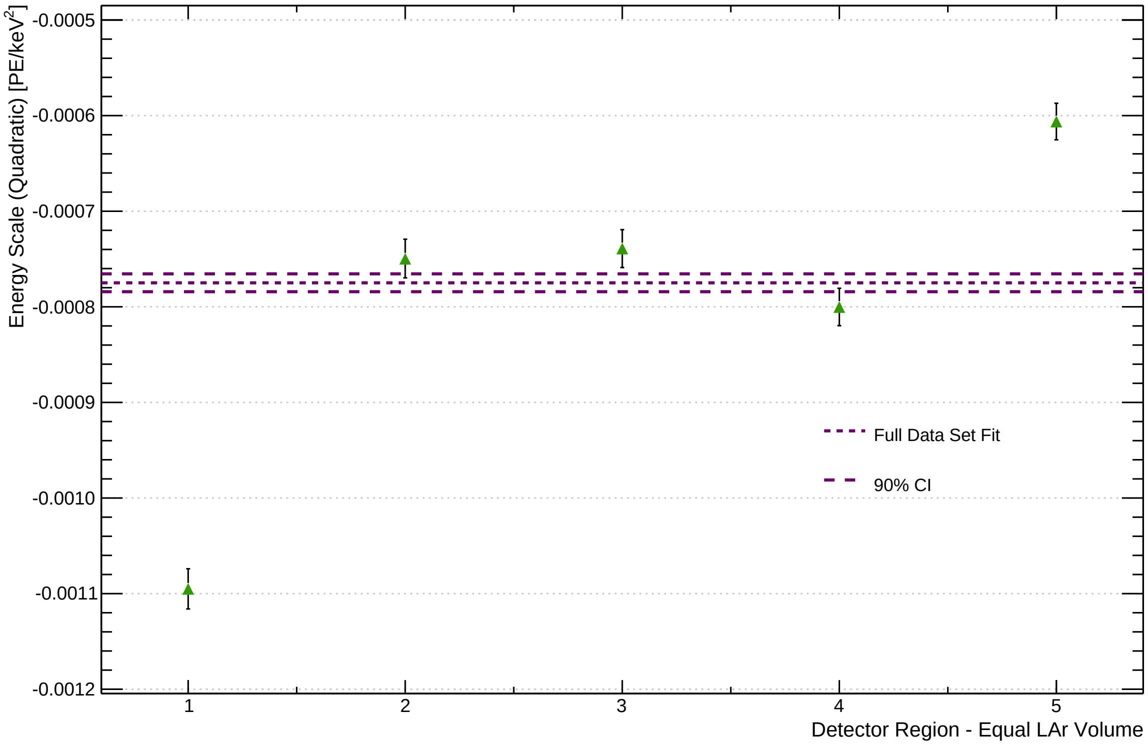

Figure 4.35: The quadratic energy scale term from each of the 5 radial region fits is compared with the the fit to the full detector volume. The uncertainties shown are 90% quantiles from the fits.

Figure 4.36 shows the linear energy resolution paramter from the fits.

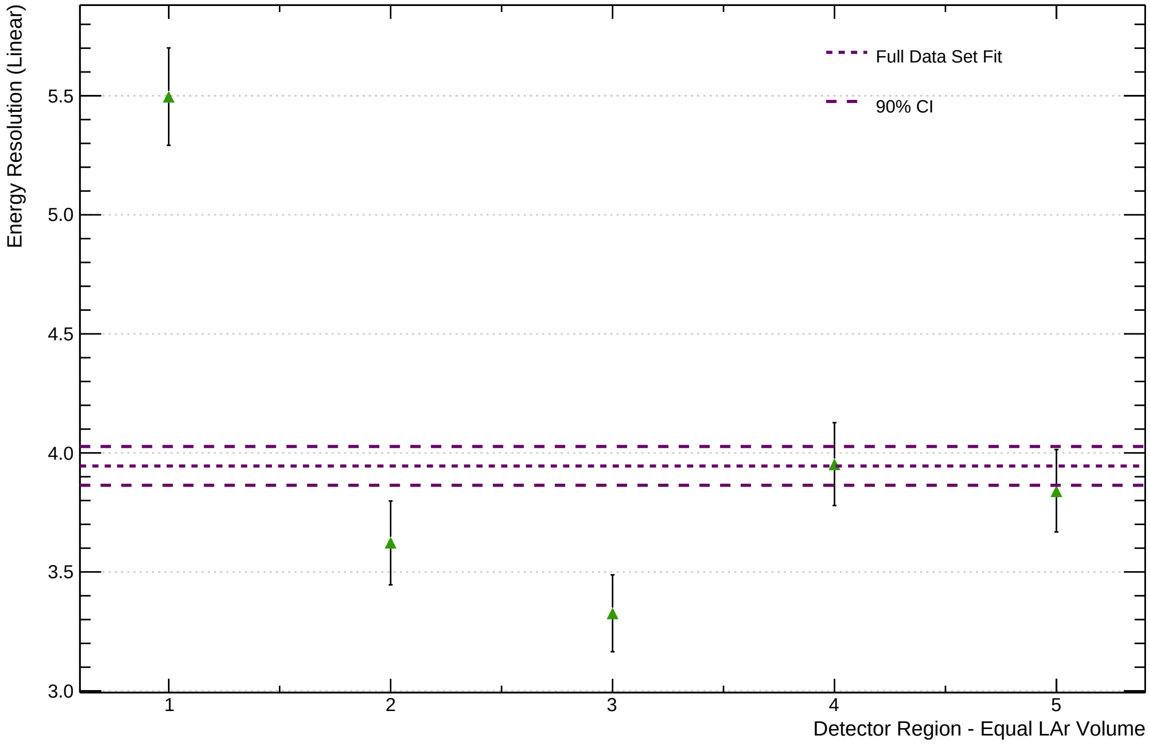

Figure 4.36: The linear energy resolution from each of the 5 radial region fits is compared with the the fit to the full detector volume. The uncertainties shown are 90% quantiles from the fits. The regions are numbered with 1 at the centre of the AV and 5 at the edge.

Figure 4.37 shows the ERB background normalisation parameter from the fits. The fits show less ERB background at the centre of the AV and more at the edge when compared to the fit to the unsorted spectrum. The ERB background spectrum is dominated by external gamma sources which would be more likely to deposit energy at the edge of the AV rather than at the centre.

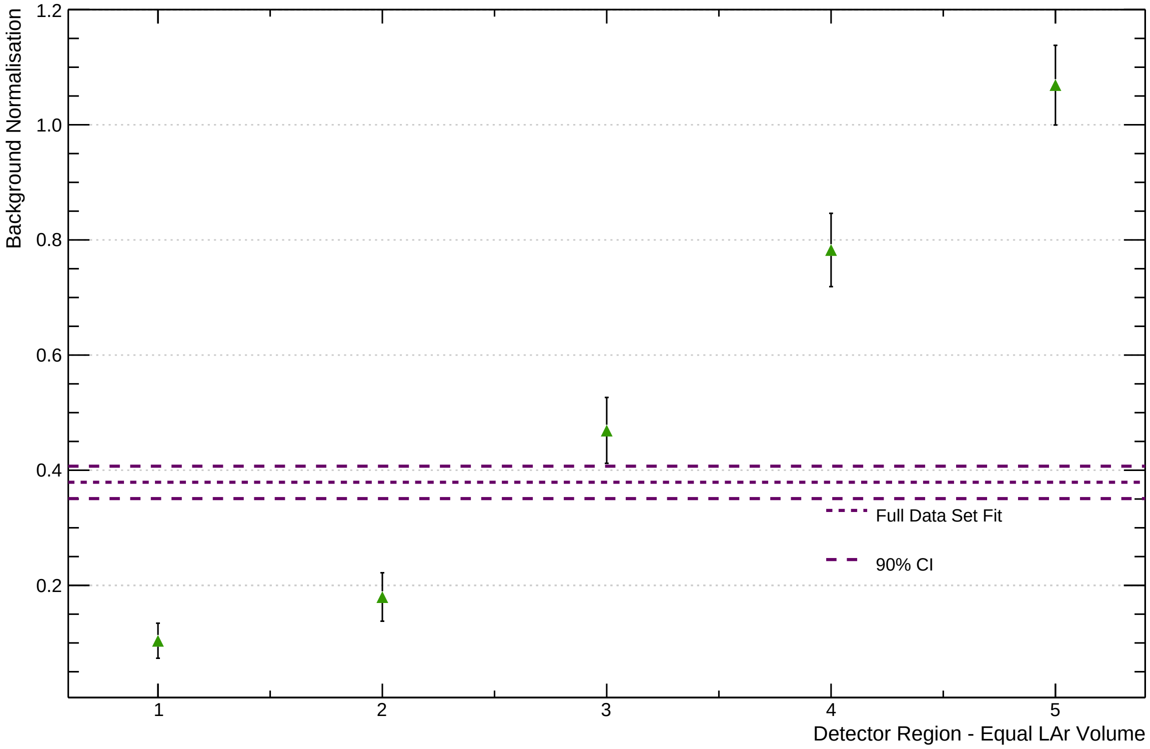

Figure 4.37: The background normalisation from each of the 5 radial region fits is compared with the the fit to the full detector volume. The uncertainties shown are 90% quantiles from the fits. The regions are numbered with 1 at the centre of the AV and 5 at the edge.

Finally, Figure 4.38 shows the surviving pileup normalisation parameter from the fits. Each result is lower than the normalisation from the unsorted spectrum. The normalisation from the unsorted spectrum is greater than values measured for shorter data sets and it is possible that there are additional systematics which are not accounted for that dominate when the statistics are very high.

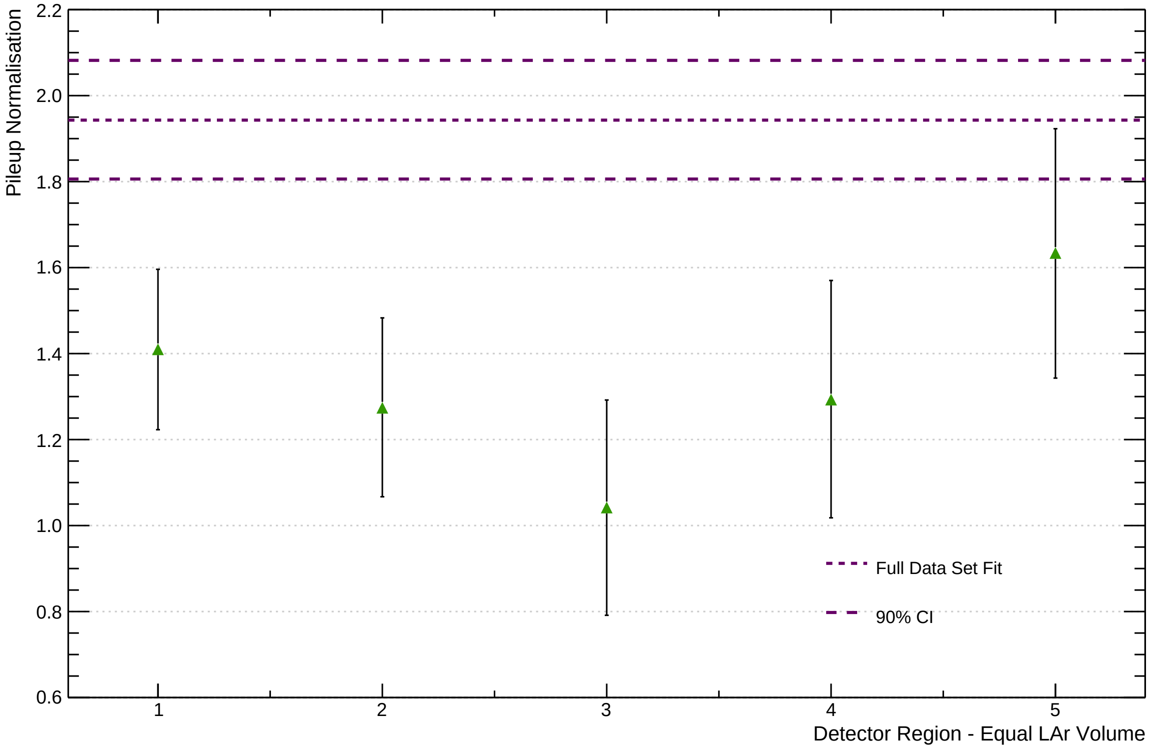

Figure 4.38: The pileup normalisation from each of the 5 radial region fits is compared with the the fit to the full detector volume. The uncertainties shown are 90% quantiles from the fits. The regions are numbered with 1 at the centre of the AV and 5 at the edge.

These fits would appear to show a variation in the detector response as a function of position in the detector. However, there is an observed bias in the position reconstruction and it is not clear how much of each discrepancy is a result of this bias. The bias can be seen in Figure 4.39; events tend to reconstruct toward the edge of the AV rather than the centre.

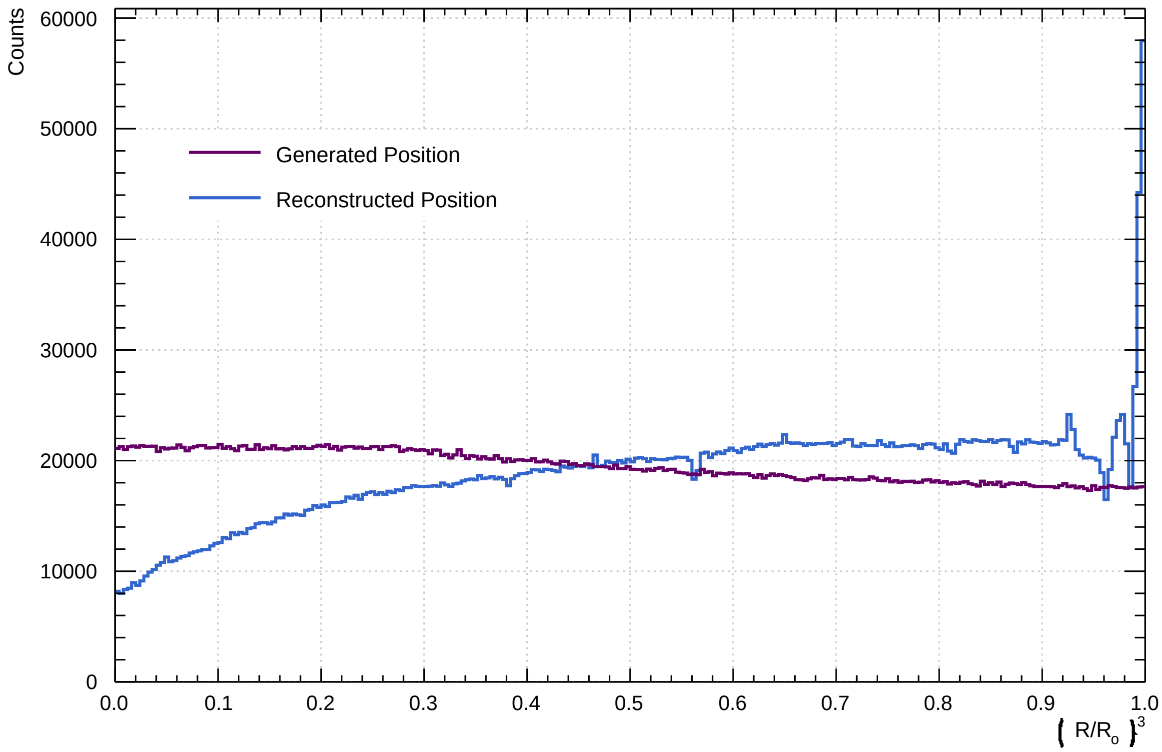

Figure 4.39: A comparison of the distribution of where in the AV events were generated with where events were reconstructed; R is the generated or reconstructed radius value, and R_0 is the inner AV radius. The events were generated uniformly within the LAr; the slight decrease in the generated positions that begins around 0.28 is due to the liquid level in the AV.

Because the effect of the reconstruction bias cannot easily be decoupled from the fits, and because the fits used to measured the specific activity use the full, unsorted spectra, no systematic uncertainty or correction is assigned due to position dependent detector response.

Separating the AV into Halves

In addition to the 5 radial regions the detector has been divided into 6 regions along the Cartesian axes (ie. (+X, -X)). The point (0, 0, 0) is located at the centre of the AV and the Z-axis is aligned with the neck of the detector. A data set of 9.74 runtime-days is selected; it is divided into pairs or triples of runs depending on the total runtime, giving 5 sets of data. This ensures there are enough events in the gamma-background & surviving pileup dominated region of the spectrum to properly extract their normalisations. The distributions of events along each axis are shown in Figures 4.40, 4.41., 4.42.

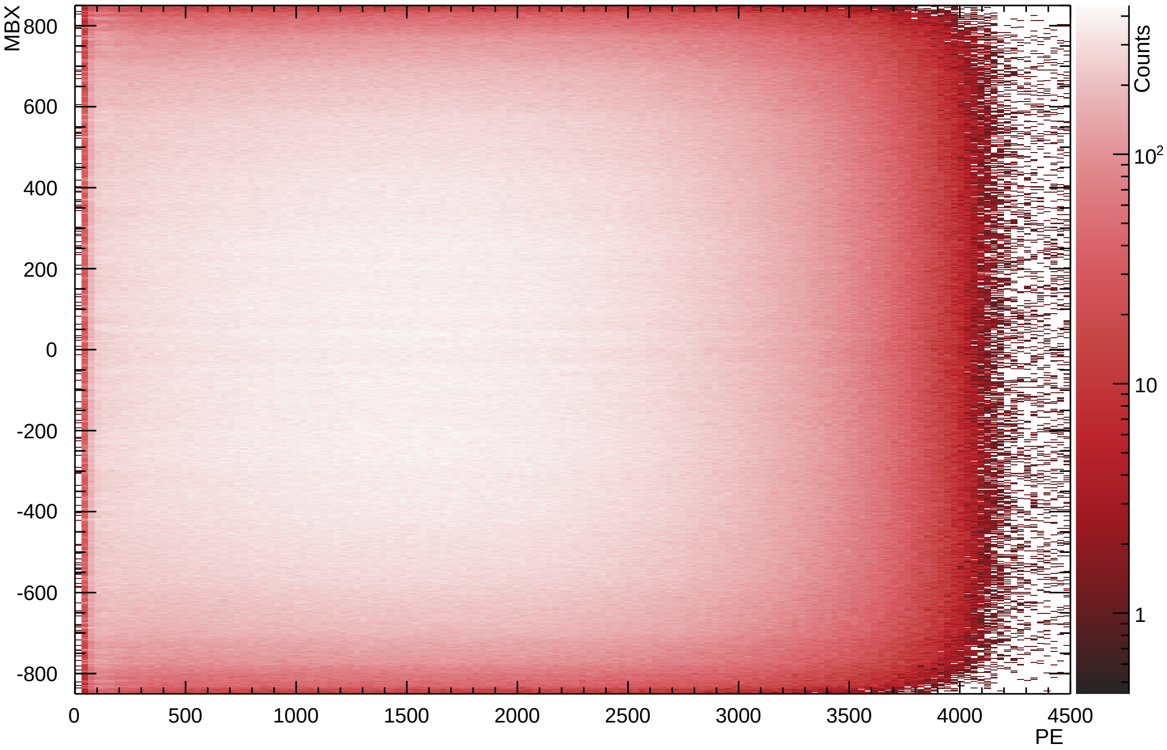

Figure 4.40: The distribution of events along the X-axis of the AV. The distribution is symmetric as expected.

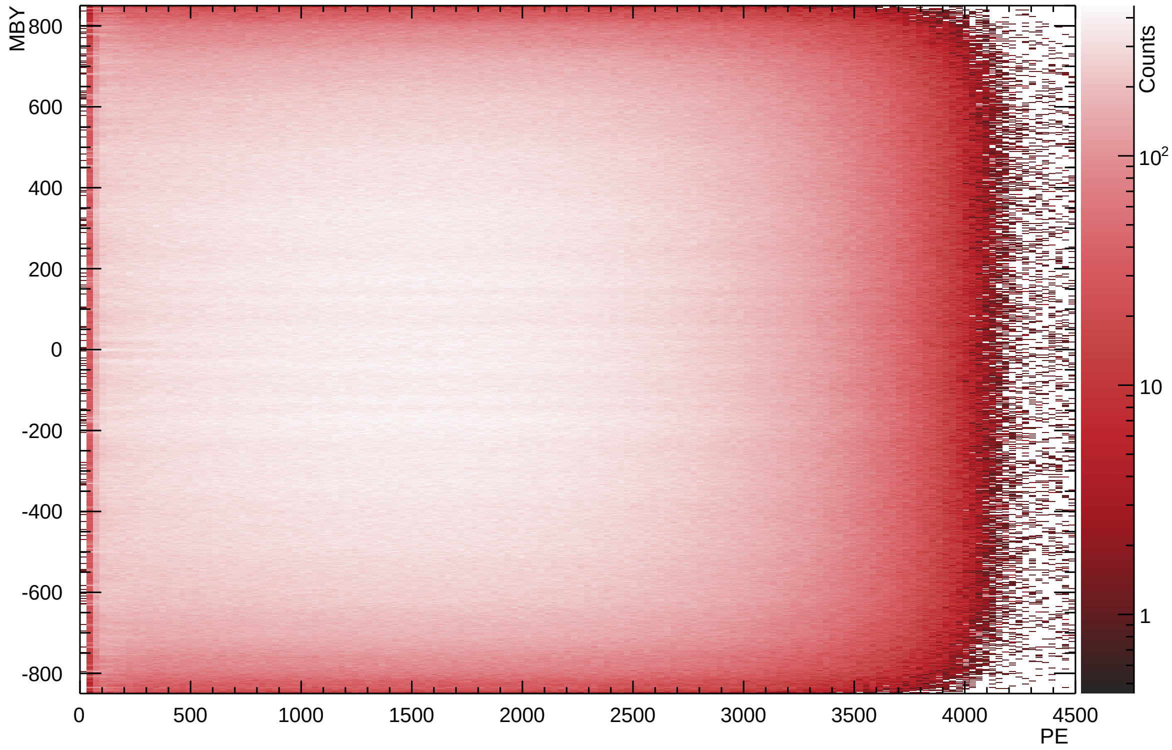

Figure 4.41: The distribution of events along the Y-axis of the AV. The distribution is symmetric as expected.

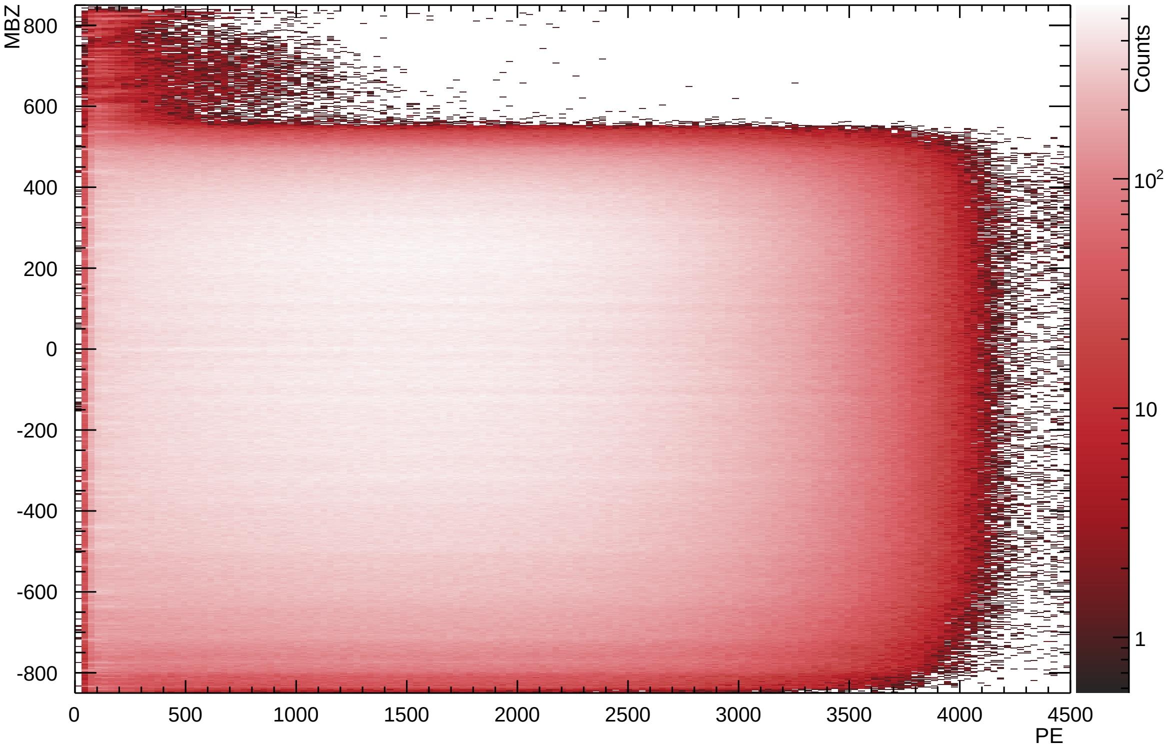

Figure 4.42: The distribution of events along the Z-axis of the AV. The distribution is asymmetric due to the LAr fill level at Z = 551 mm.

The results of the fits are shown in Figures 4.43, 4.44, 4.45, 4.46, and 4.47. These fits show much better agreement to the full, unsorted spectrum fit when compared to the fits to radially-sorted data. The largest deviation from the full spectrum fit is seen in the ERB background normalisation parameter when the detector is divided in the Z-direction. This is, however, expected because splitting the detector along this axis does not produce two equal LAr volumes due to the fill level, and so there is more LAr in which an external gamma may interact in the negative-Z region compared to the positive-Z region.

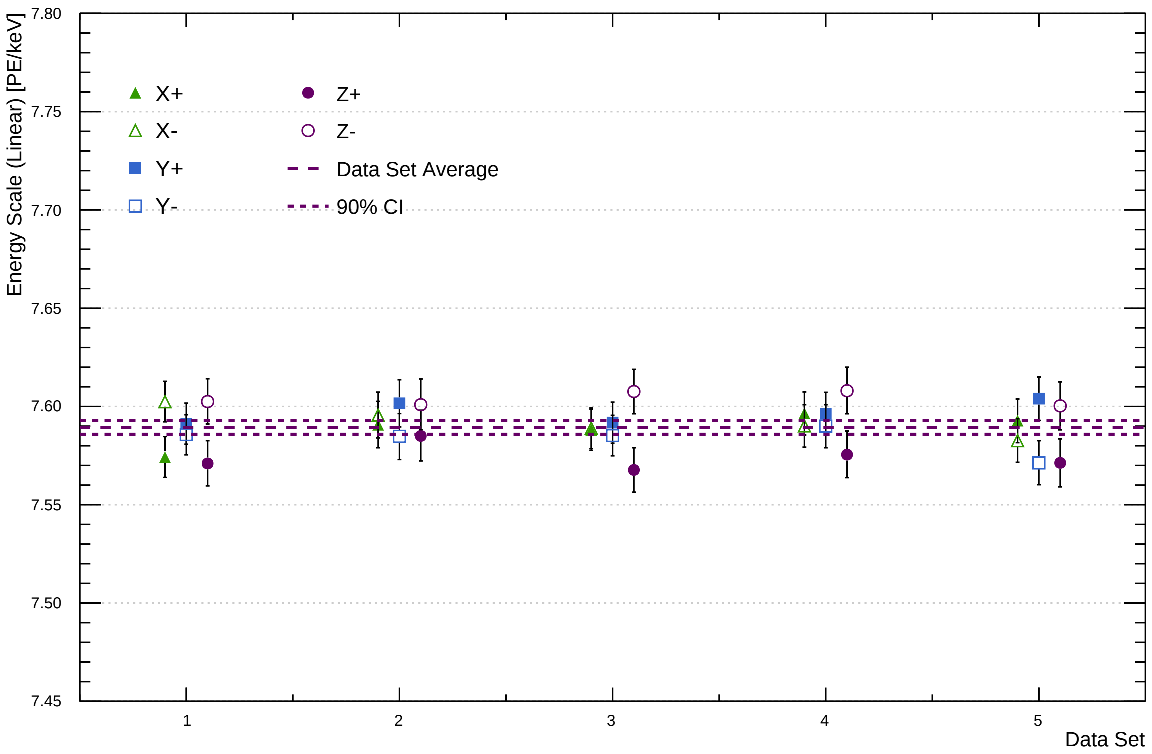

Figure 4.43: Fits along the 3 Cartesian axes divided into two regions about the origin. The uncertainties shown are the 90% CI values from the marginalized distributions.

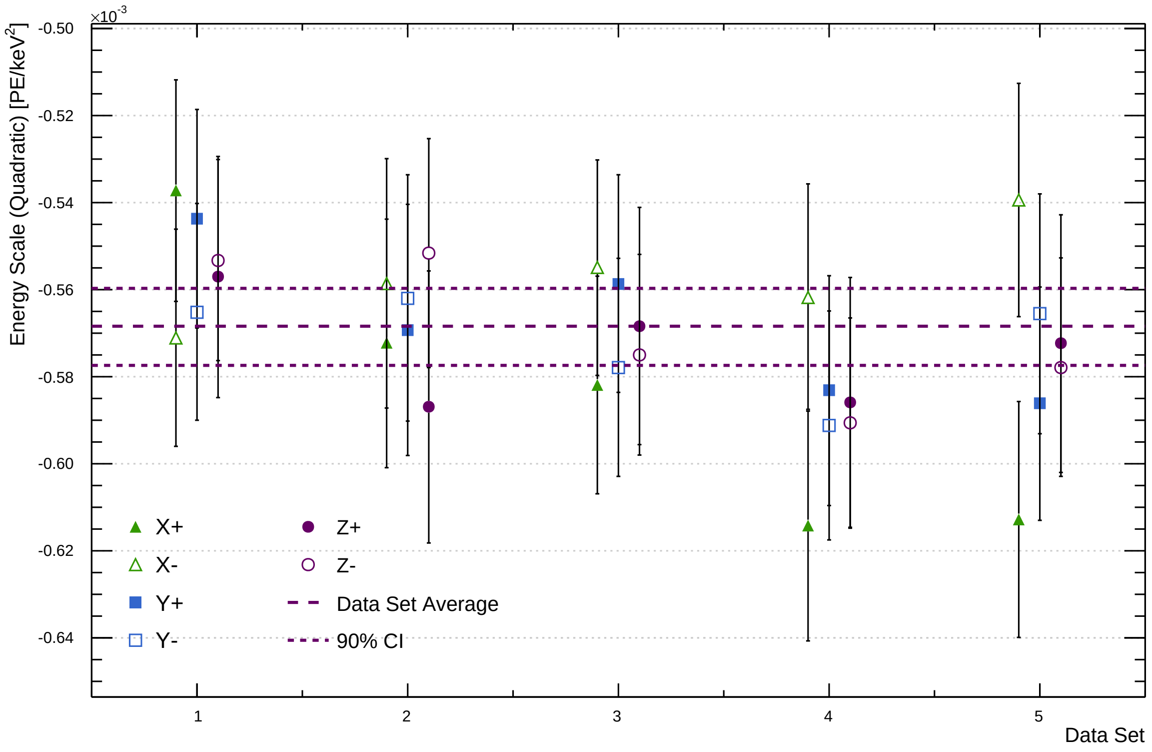

Figure 4.44: Fits along the 3 Cartesian axes divided into two regions about the origin. The uncertainties shown are the 90% CI values from the marginalized distributions.

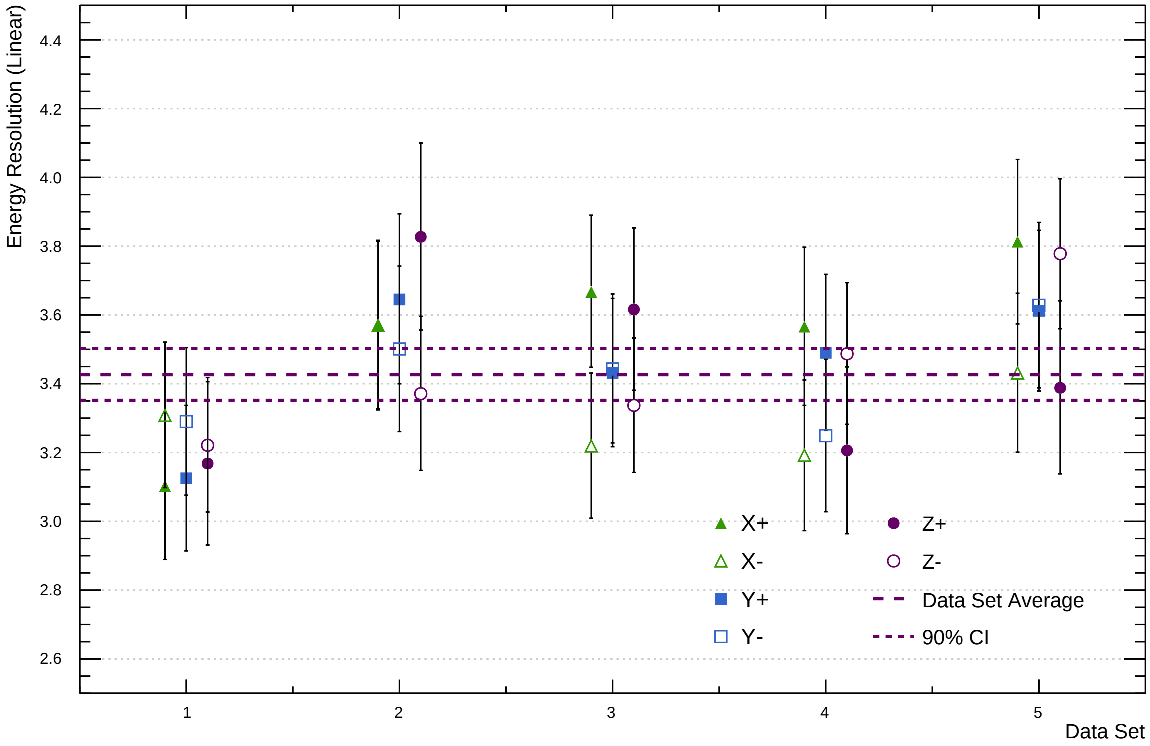

Figure 4.45: Fits along the 3 Cartesian axes divided into two regions about the origin. The uncertainties shown are the 90% CI values from the marginalized distributions.

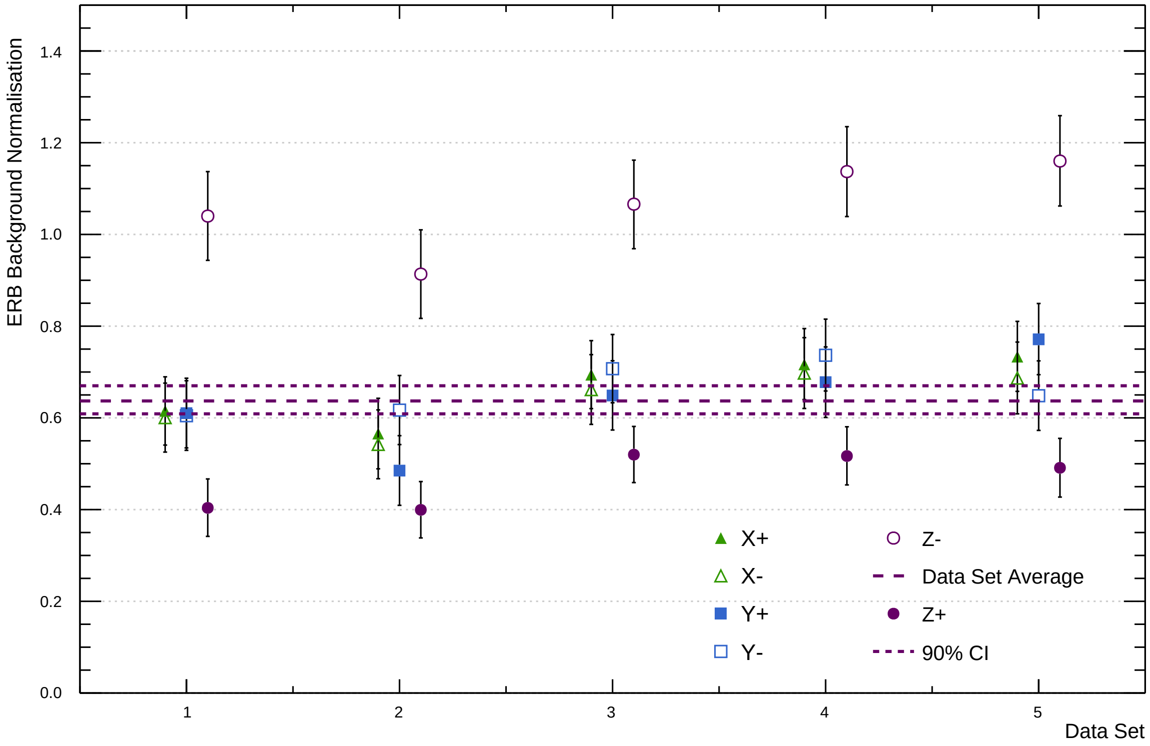

Figure 4.46: Fits along the 3 Cartesian axes divided into two regions about the origin. The uncertainties shown are the 90% CI values from the marginalized distributions.

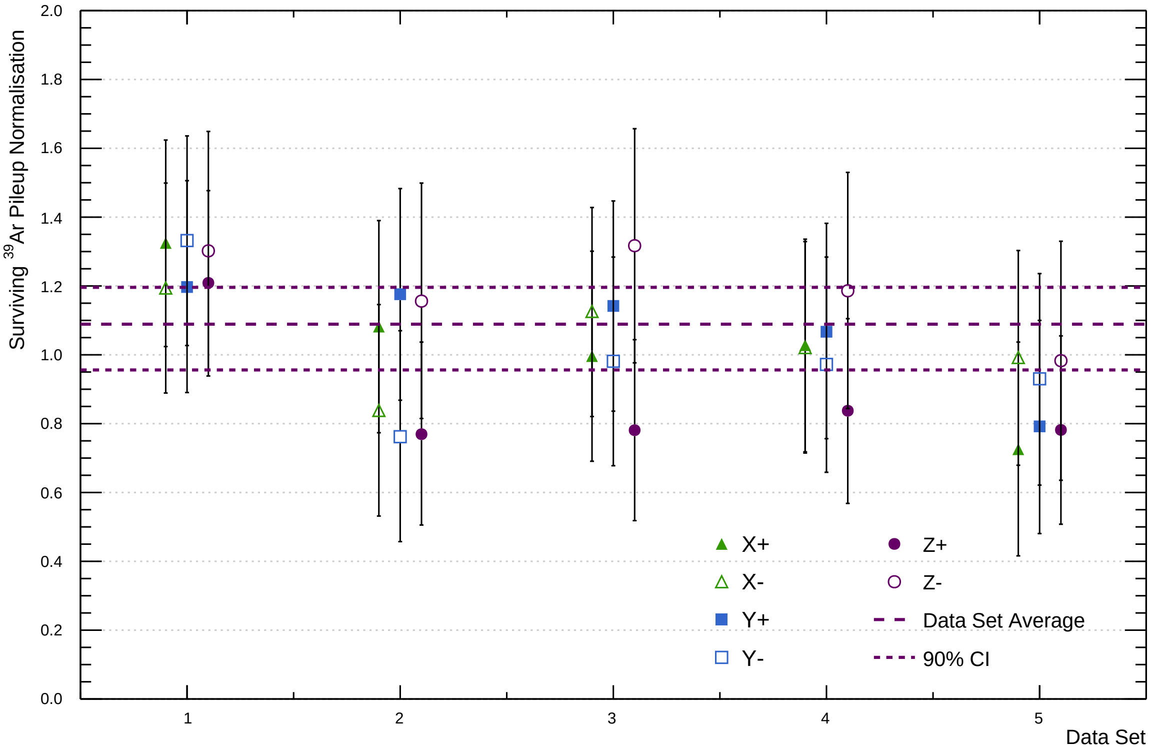

Figure 4.47: Fits along the 3 Cartesian axes divided into two regions about the origin. The uncertainties shown are the 90% CI values from the marginalized distributions.

4.6 ^{36}Ar Analysis Parameters

Not all of the parameters described in Section 4.3.6 are used in the search for the neutrinoless double electron capture of ^{36}Ar. This is because the expected location of the peak for this decay lies within the ^{39}Ar beta decay spectrum, and hence the region which is prescaled. To look at 100% of the data as opposed to merely 1%, the unprocessed information from the trigger boards is examined. Only the dtmTrigSrc parameter cut mentioned previously is used for this analysis. The rest of the ^{39}Ar analysis parameters are calculated based on reconstructed information, or measured directly from the event waveforms. Since the waveforms are not stored for prescaled events, those parameters cannot be calculated.

The charge measured by the trigger board is what is used to determine whether or not an event falls within the prescaled region (medium energy, low F_{prompt}. See Table 4.3); this information is stored for every event.

4.6.1 dtmWideQ and dtmNarrowQ

The charge information is stored in two parameters called dtmNarrowQ and dtmWideQ - shortened herein to NarrowQ and WideQ - representing the charges in the prompt window and the full window, respectively. The windows used to measure these parameters are ‘rolling’ windows which continuously integrate the summed output of the PMTs; the narrow and wide windows are 177 ns and 3100 ns, respectively. The dtmWideQ parameter is analogous to the PE parameter described in the previous section, and provides a measure of the total charge of an event. NarrowQ and WideQ are the sum of the charge collected by the trigger board in the narrow and wide integration windows, respectively. A wideQ spectrum is shown in Figure 4.48.

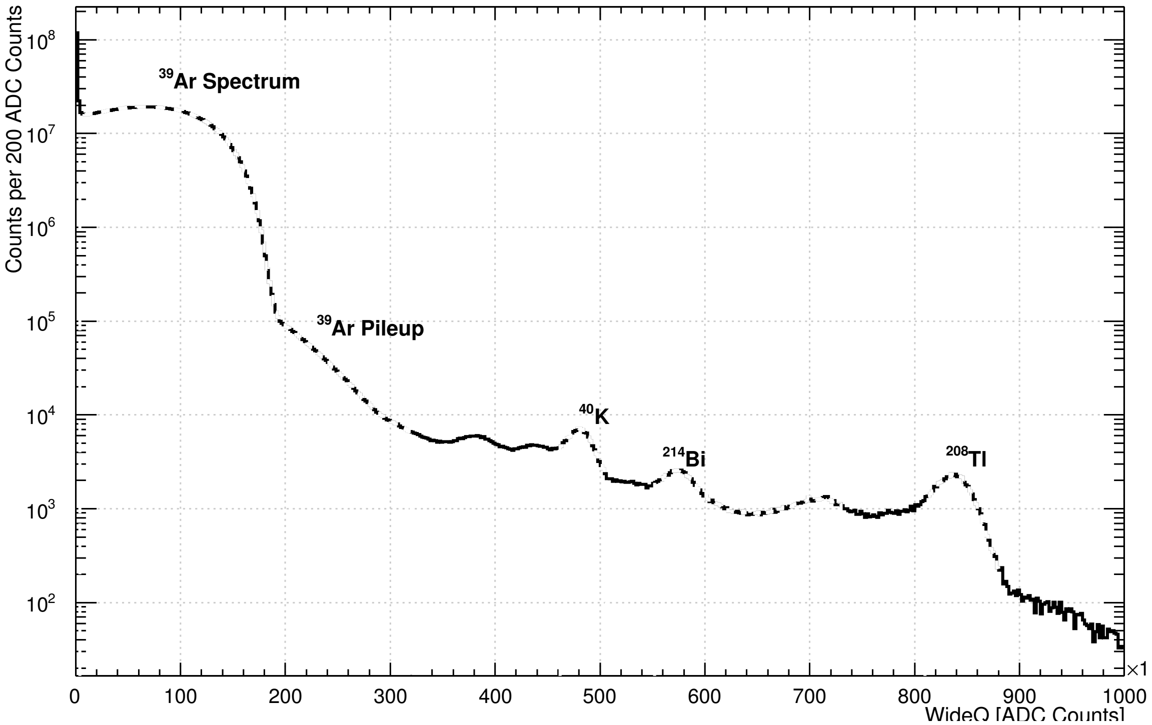

Figure 4.48: A WideQ spectrum in data. No cuts have been made. The dashed portions of the histogram and the accompanying labels represent the dominant contributions to the spectrum. This plot represents approximately 6 days of data.

4.6.2 $\mathbf{d_{prompt}}$

Analogous to $\mathrm{F_{prompt}}$, $\mathrm{d_{prompt}}$ is a PSD parameter that describes the fraction of total light in the prompt window. The calculation is shown in Eq. 4.16:

$$\mathrm{d_{prompt}} = \frac{\mathrm{narrowQ}}{\mathrm{wideQ}} \tag{4.16}$$

4.7 A Counting Experiment to Search for ^{36}Ar

A simple way to search for this decay is do a counting experiment. The counting experiment is one in which events are counted in a region of interest expected to contain the signal peak; this event count is compared to the expected number of background events which is counted from sidebands surrounding the region of interest.

4.7.1 Energy Calibration of the Trigger Board Spectrum

Since the DAQ only stores 1% of the waveforms from the region in which the ^{36}Ar peak is expected (due to prescaling, see Section 3.5.3), the trigger board information for the ^{36}Ar measurements is analysed. The trigger board information for every event is stored and examining this data maximizes the exposure. For both the counting experiment and the likelihood fit (Section 4.8.1) the 247 day data set is corrected from the trigger board energy to energy in keV using a wide spectrum energy calibration.

The energy calibration examines the ^{39}Ar spectrum and several of the higher energy gamma peaks in the trigger board ERB. The ^{39}Ar spectrum from the trigger board is fit in a range from 40x10^3 wideQ to 220x10^3 wideQ to extract the energy scale parameters. The gamma peaks are fit with a Gaussian to determine their mean wideQ energy and then compared to the known energy in keV. The calibration is shown in Figure 4.49. The energy-dependent energy resolution is also measured, and is shown in Figure 4.50.

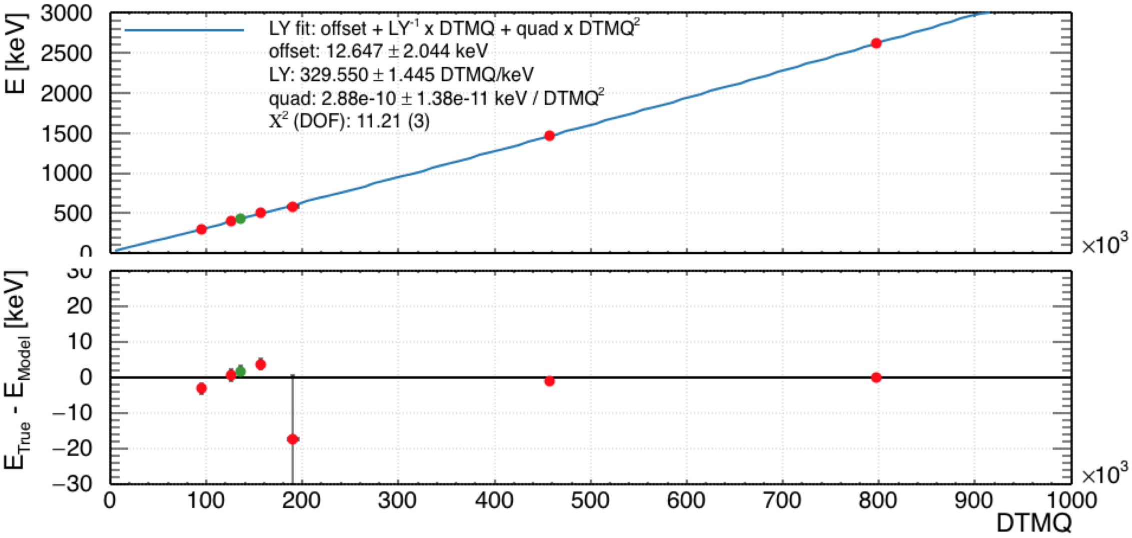

Figure 4.49: Energy calibration of the trigger board data comparing the known energy to the measured energy from the trigger board (DTMQ). At higher energies the points are from gamma peaks of ^{208}Tl at 2614 keV, ^{40}K at 1461 keV, and ^{208}Tl at 583 keV. In the ^{39}Ar spectrum range the points are at 300, 400, and 500 keV. The green point is shown at the ^{36}Ar peak energy, but is not used in the fit.

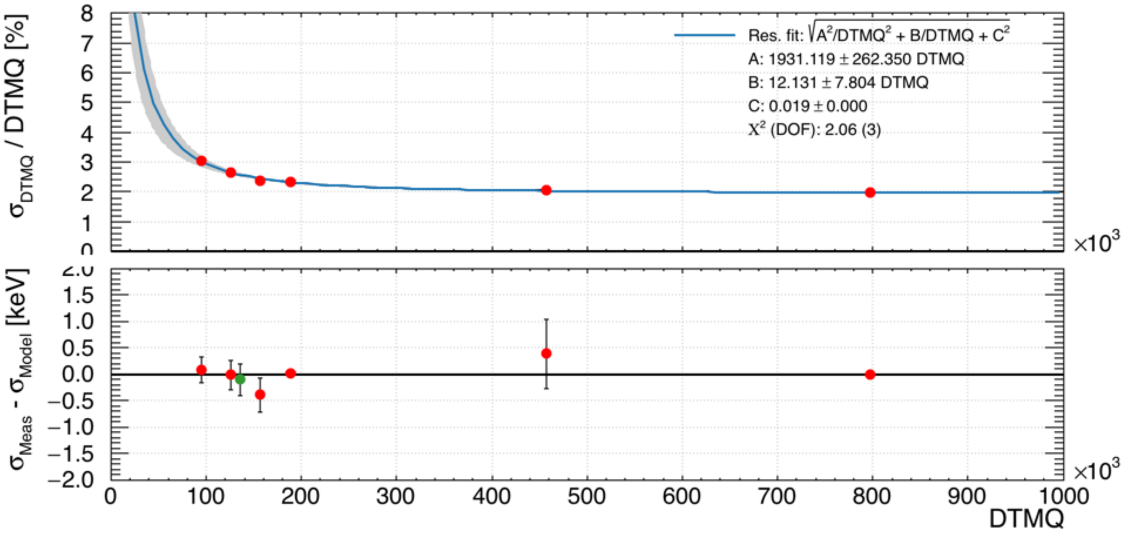

Figure 4.50: The energy resolution from the calibration. Here, DTMQ is the trigger board energy. For the gamma peaks the energy resolution is measured by fitting a Gaussian to find the peak width. For the ^{39}Ar points the resolution is calculated using the resolution parameter from the fit with the trigger board energy at each point. The green point is taken at the ^{36}Ar peak energy, but is not used in the fit.

This calibration is applied to each run of the data set; the runs are then combined into a single energy spectrum. This spectrum is shown in Figure 4.51.

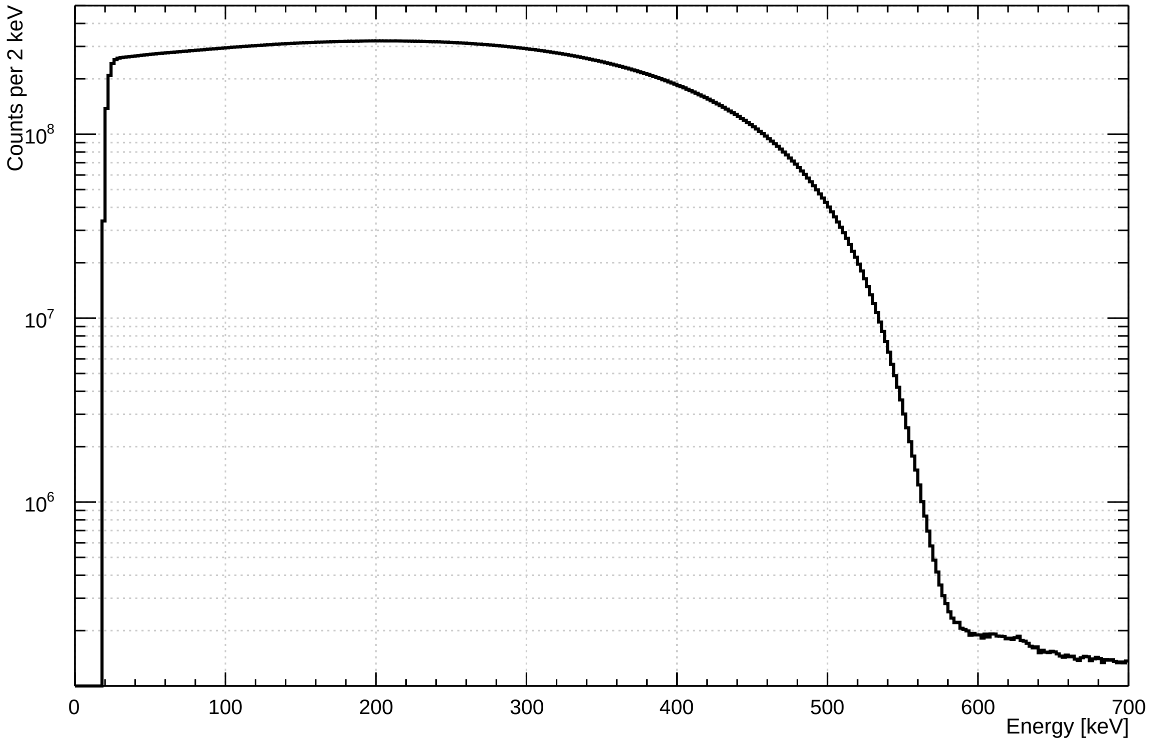

Figure 4.51: The full energy calibrated data spectrum.

4.7.2 MC Estimate of DEAP-3600's Sensitivity

For this sensitivity study, three MC simulations of a 0νECEC signal were run. Each simulation included two Auger electrons corresponding to electron capture from the K and L shells, with respective energies of 2.47 keV and 0.23 keV. For the first simulation (which is herein referred to as the 'internal conversion (IC) electron mode' simulation) the decay energy of 429.88 keV is released as an internal conversion electron. For the second simulation the decay energy is released as a single photon ('single photon mode' simulation). The third simulation mimics the previous, except 2 photons which share the decay energy are emitted ('double photon mode' simulation); their directions are randomly chosen and are not correlated. For all simulations the decay products are generated simultaneously for each event. Figures 4.52 shows the full energy peak (at a total of 432.58 keV) for each of these simulations. From the MC the number of events in the peak for each mode were measured; the values are 99.9%, 81.6%, and 78.7% for the IC electron, single photon, and double photon modes, respectively.

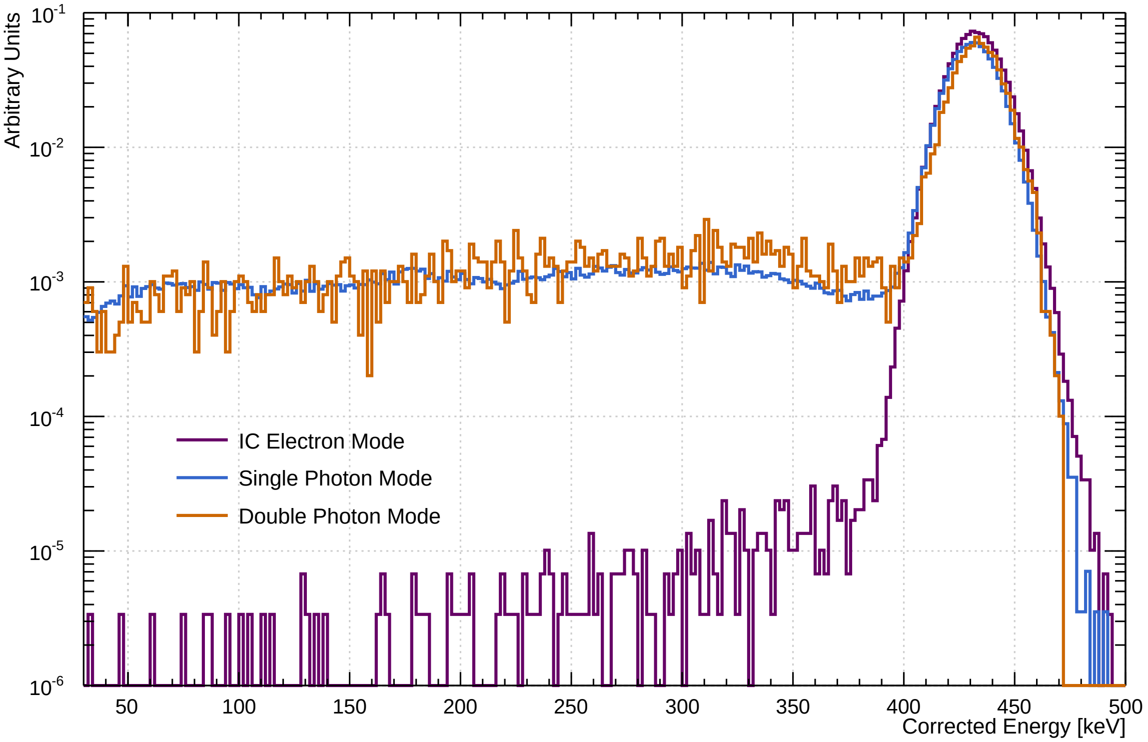

Figure 4.52: The corrected energy spectra from the 3 ^{36}Ar simulations. Each spectrum has been normalised to unit area. In the IC electron mode simulation most events are contained in the full energy peak. In the single photon mode simulation the long tail at energies lower than the peak energy is due to photons escaping the LAr having deposited only a fraction of their energy. In the double photon mode simulation, once again the tail is due to photons escaping the LAr; the coarser appearance of this spectrum compared to the other two is due to lower statistics in the MC.

4.7.3 Figure of Merit Calculations

To determine an optimal search region for a counting experiment that will search for an ^{36}Ar 0νECEC signal. This will be achieved by calculating a Figure of Merit to determine for which region of interest (ROI) width the ratio of signal detection efficiency to the expected background variations is maximized. First, the mean peak energy from each of the 3 simulations is measured by fitting a Gaussian to the peak; this will be used as the centre of the ROI. Next, an ROI window is chosen and for each simulation the number of signal events which fall in that window is calculated; this number is divided by the total number of events in the full spectrum to get the efficiency of detecting the signal in that window. The expected background in the ROI is measured from MC spectra which have been rate-scaled based on a manual fit to data. With this the expected background variation is calculated. The efficiency is then used to determine a Figure of Merit (FOM). The ROI width is then increased and this process repeated. The efficiency and FOM plots for each simulation are shown in Figures 4.53, 4.54, and 4.55.

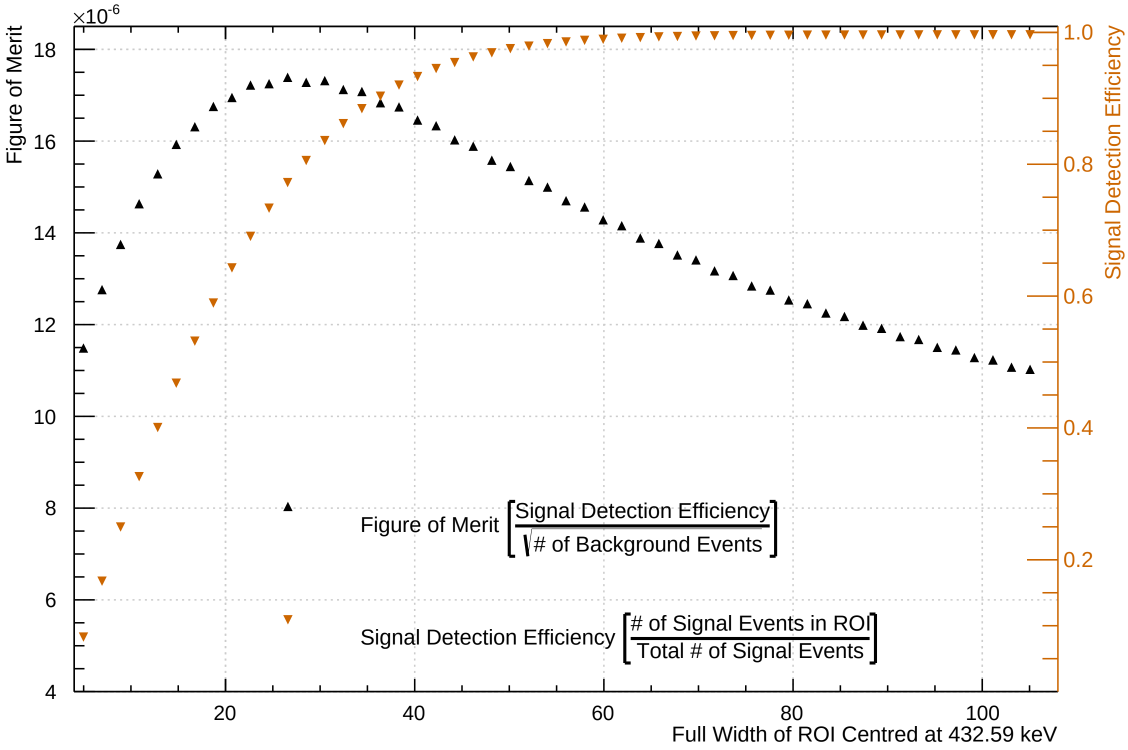

Figure 4.53: The effect of varying the ROI width on the signal detection efficiency (orange) and the ratio of efficiency to the expected background variations (black) in the same ROI (Figure of Merit) for the IC electron mode simulation. This estimate is used to determine a potential peak search region for a counting experiment.

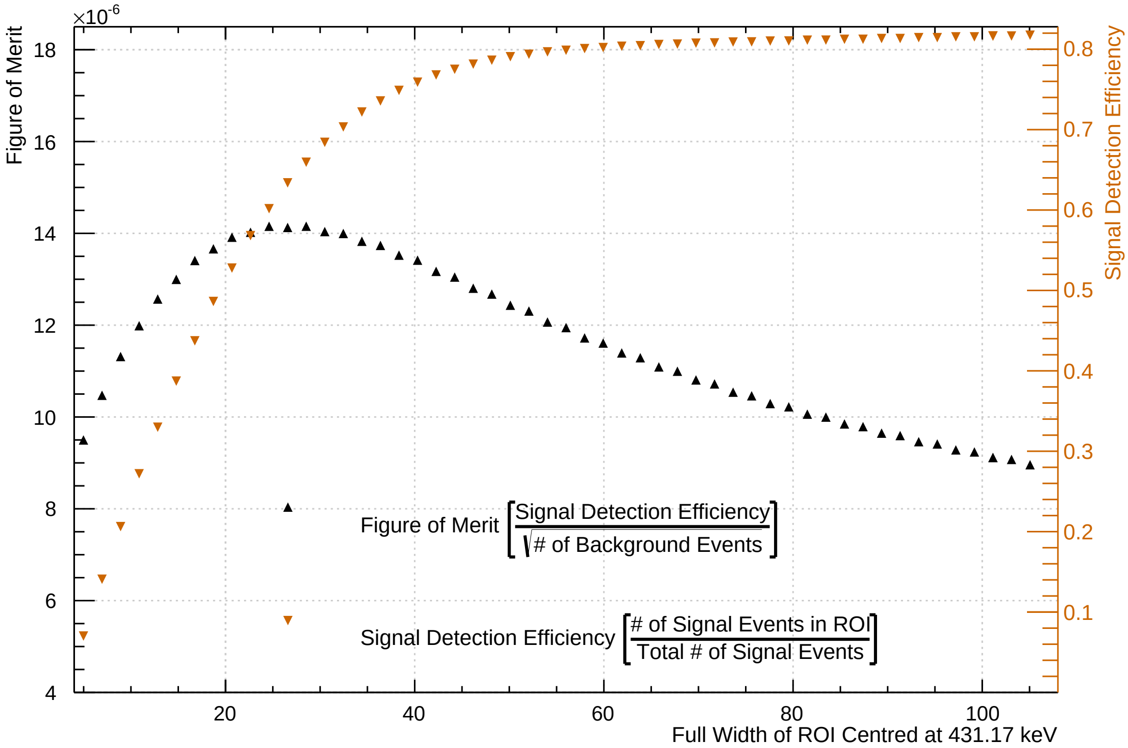

Figure 4.54: The effect of varying the ROI width on the signal detection efficiency (orange) and the ratio of efficiency to the expected background variations (black) in the same ROI (Figure of Merit) for the single mode simulation. This estimate is used to determine a potential peak search region for a counting experiment.

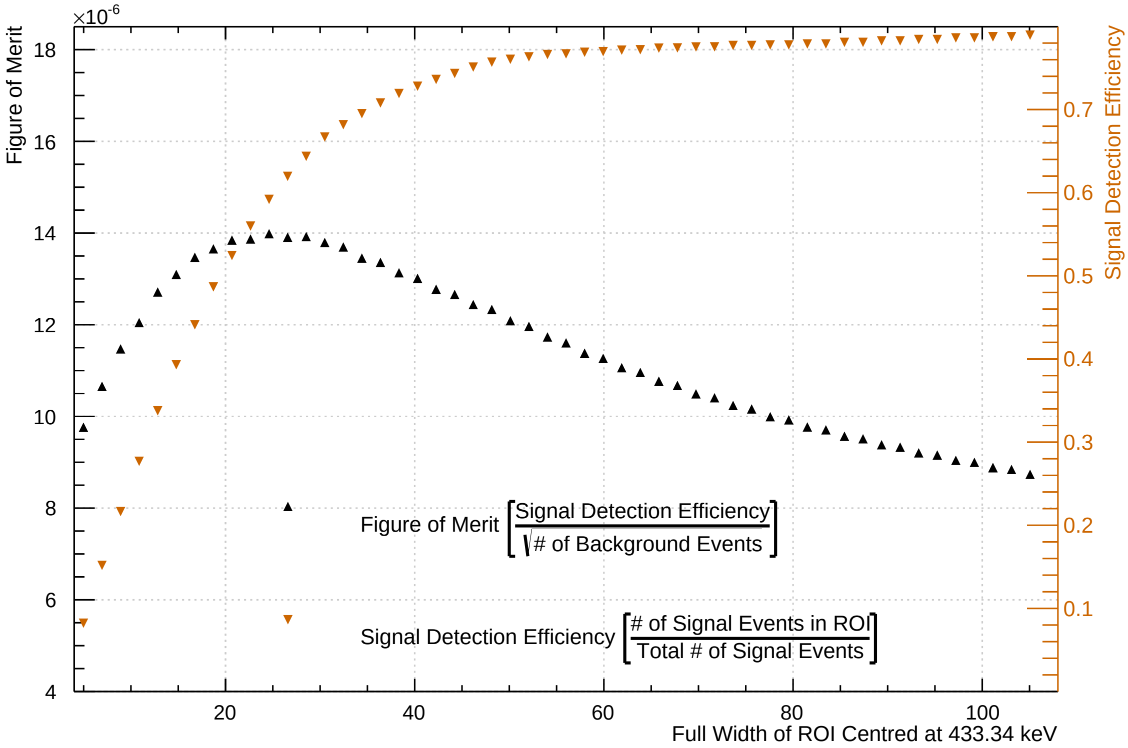

Figure 4.55: The effect of varying the ROI width on the signal detection efficiency (orange) and the ratio of efficiency to the expected background variations (black) in the same ROI (Figure of Merit) for the double photon mode simulation. This estimate is used to determine a potential peak search region for a counting experiment.

The results of the Figure of Merit calculation are presented in Table 4.9. From these calculations an ROI of (432 ± 14)keV is chosen, with a full ROI width of 28 keV being the middle of the range of optimal ROIs for the three decay modes. It should be noted that while this ROI could maximize the sensitivity to find a signal peak, any ROI can be used in the counting experiment.

MC Final State	Signal Detection Efficiency In ROI [%]	Optimal ROI Width [keV]	Figure of Merit
IC Electron	82.34	28	1.74x10^{-5}
Single Photon	69.59	30	1.42x10^{-5}
Double Photon	63.69	26	1.40x10^{-5}

Table 4.9: The values from the Figure of Merit calculations for each simulation. The 'optimal' ROI widths as determined by the FOM are shown.

4.7.4 Half-Life Sensitivity Estimate

With all of the above information an expected half-life sensitivity for 1 year of data collection has been calculated. The known mole fraction of ^{36}Ar in atmospheric argon is (0.3336 ± 0.0004)%; converting this to a mass fraction gives a value of (0.3004 ± 0.0004)% and the total mass of ^{36}Ar in DEAP-3600 is (9.9 ± 0.3)kg. The mass corresponds to (1.6 ± 0.5)x10^{26} atoms. Since the branching ratios for the different decay modes are unknown the sensitivity is calculated three times, each assuming 100% branching for that mode. The values are shown in Table 4.10.

MC Final State	Expected Background Events	90% CI Background Variation	Estimated Sensitivity [x10^{21} years]
IC Electron	2,241,652,400	78,121	1.2
Single Photon	2,416,849,904	81,116	0.98
Double Photon	2,073,773,648	75,138	0.97

Table 4.10: The sensitivity for each of the three decay modes is estimated from MC.

The estimated sensitivity of a counting experiment in DEAP-3600 is approximately 1x10^{21} years. This is comparable to the existing GERDA limit which is

$t_{\frac{1}{2}} > 3.6 \times 10^{21}$, though because GERDA's argon is external to its detectors it is only sensitive to the single photon mode.

4.8 A Fit to Data to Search for 0νECEC

A procedure to fit the data and search for the ^{36}Ar 0νECEC signal has been implemented. The fit is similar to that used in the ^{39}Ar specific activity measurement and uses the BAT software described previously. The fit model has two main components: a background spectrum consisting of the theoretical ^{39}Ar model described in previous sections, and a Gaussian which models the signal spectrum. The data spectrum on which the fit is performed is the energy-calibrated spectrum shown in Figure 4.51; the spectrum is fit in the range 380 keV to 470 keV; the results of a fit to this data are presented in Section 5.2.2.

The fit parameters include the peak mean and width for the signal of interest; these parameters are constrained by Gaussian priors. The fit also includes four energy parameters: a constant scale term, a linear scale term, and a quadratic scale term, and a linear resolution term; each of these paramters is given a flat prior. A normalisation term for the background is included and is given a flat prior. The main parameter of interest for these fits is the inverse half-life which is a component in a scaling factor for the signal model. For the ^{36}Ar fits a Gaussian uncertainty is used for the systematic uncertainty in the bins. A binned likelihood fit is performed which calculates the folowing function and maximizes the sum across all bins in the fit range:

$$\sum_{i=1}^{n_B} \left[-\frac{1}{2} \times \left(\frac{\mathrm{D}_i - \mathrm{M}_i}{\sigma_i} \right)^2 - \frac{1}{2} \ln(2\pi) - \ln(\sigma_i) \right], \tag{4.17}$$

where n_B is the number of bins in the fit range, D_i is the bin content of the data spectrum, M_i is the bin content of the signal model spectrum and contains the fit parameter dependences, and σ_i is the uncertainty in the data bin.

4.8.1 Testing the Fit

Two MC tests have been performed to test the ability of the fit to identify an ^{36}Ar peak over the considerable ^{39}Ar background. For the tests a simple toy MC was applied rather than simulating the full detector and all related physics. First, the background spectra (^{39}Ar) were produced by randomly sampling spectra with the detector energy response included; this produced a new set of spectra with the required statistics to compare with the 247 runtime-day data set.

For the ^{36}Ar signal peak a Gaussian with a mean of 430 keV and width equal to the measured energy resolution at the peak mean of 11.1 keV was produced; this Gaussian was then randomly sampled to produce a spectrum with the number of counts consistent with a half-life of 1.98x10^{18} years, assuming a detection efficiency of 100%. The fit is shown in Figure 4.56. This half-life produces a small peak though the fit can clearly identify it; the blue 'background only' model very clearly diverges from the data and the fit measures a half-life of 1.68x10^{18} years.

An second signal spectrum was produced by increasing the half-life by one order of magnitude; this fit is shown in Figure 4.57 and measures a half-life of 1.48x10^{19} years. In addition to the tests where a signal was present the background spectrum was tested on its own; this fit is shown in Figure 4.58. The background-only fit finds no signal and returns a lower limit on the half-life of ^{36}Ar ECEC of $T_{1/2} >$ 2.7x10^{20} years at 90% CI.

This MC study could be indicating that a small bias exists between the input to the toy MC and the output of the fit for spectra with signal included. The background-only fit appears to be consistent with the input.

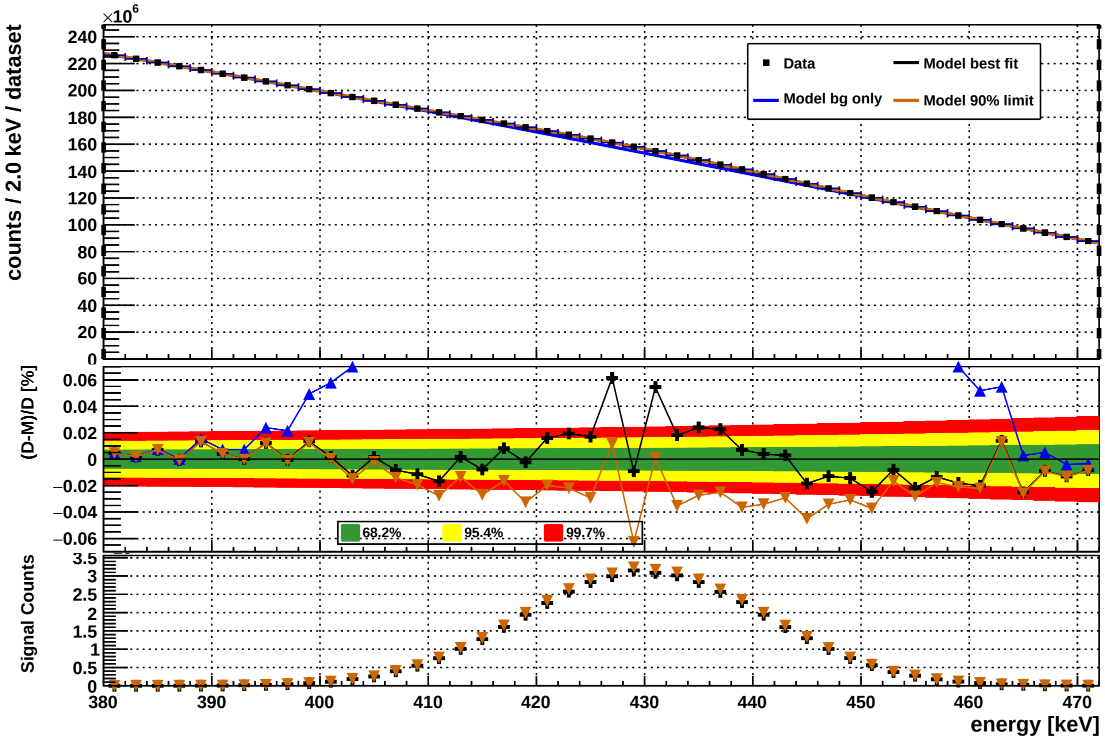

Figure 4.56: Output of the fit to toy MC. The top panel shows the portion of the data spectrum on which the fit is performed. The middle panel shows the fit residuals along with 1, 2, and 3 σ bands. The bottom panel shows the estimated number of events in the region where the model best fit differs from the background only model.

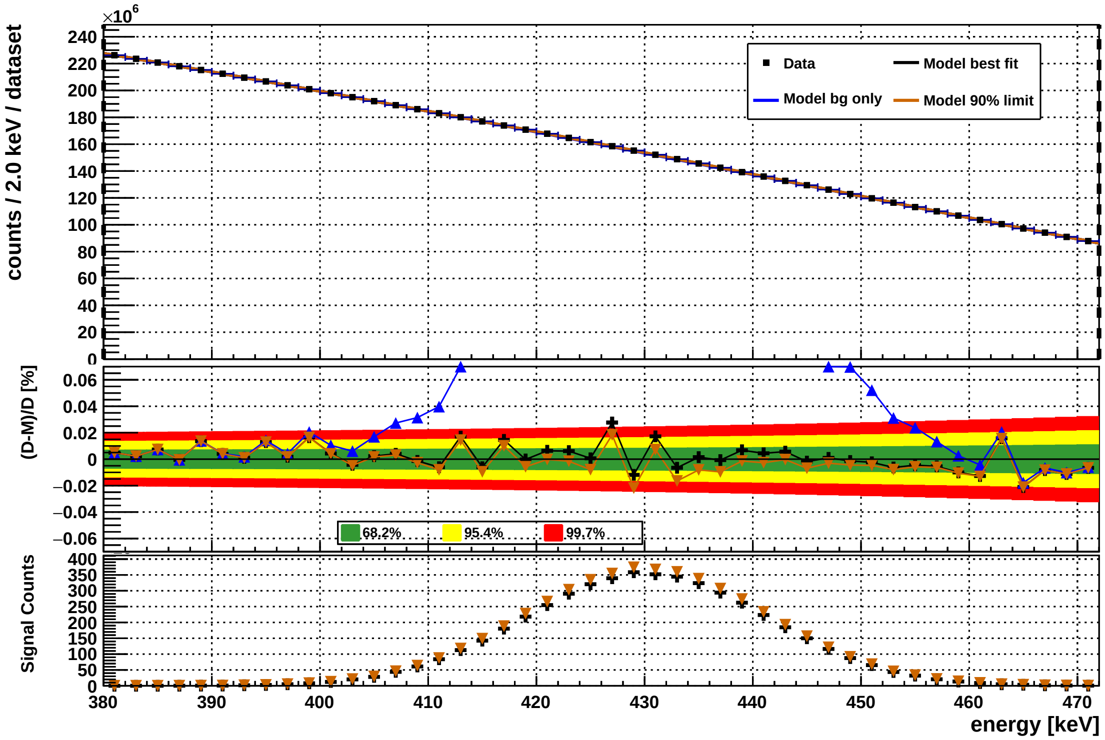

Figure 4.57: Output of the fit to toy MC. The top panel shows the portion of the data spectrum on which the fit is performed. The middle panel shows the fit residuals along with 1, 2, and 3 σ bands. The bottom panel shows the estimated number of events in the region where the model best fit differs from the background only model.

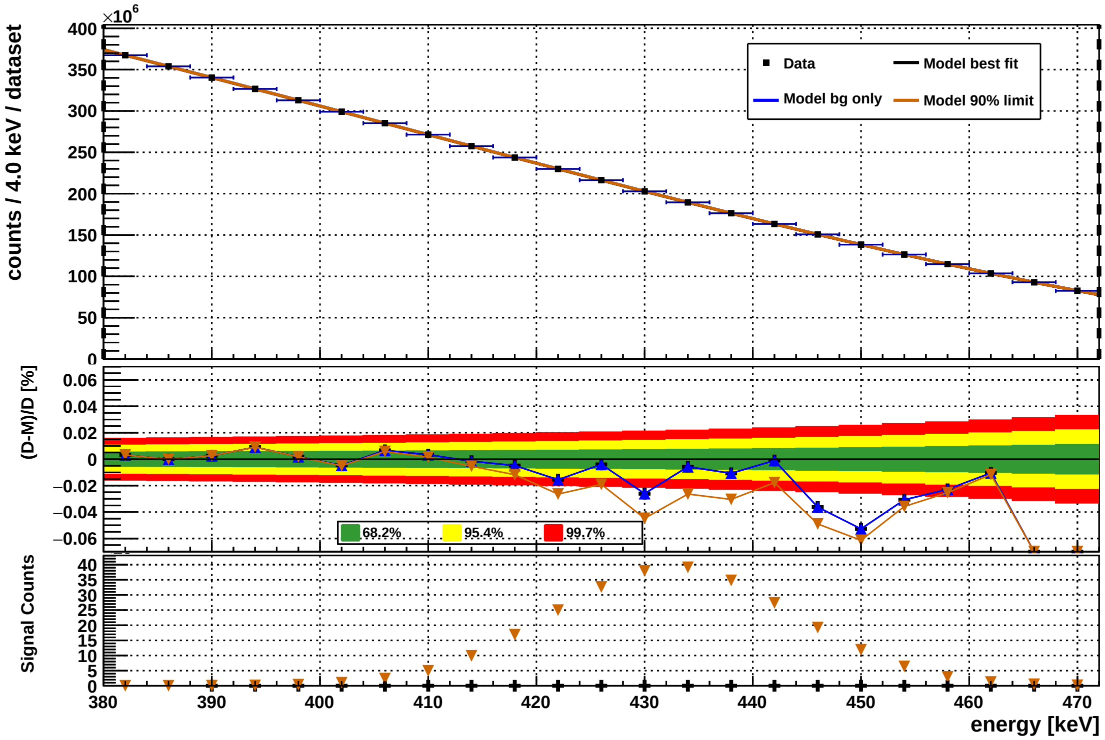

Figure 4.58: Output of the fit to toy MC. No signal spectrum is present, and the toy MC data is background only. The top panel shows the portion of the data spectrum on which the fit is performed. The middle panel shows the fit residuals along with 1, 2, and 3 σ bands. The bottom panel shows the estimated number of events in the region where the model best fit differs from the background only model.

Figure4.59 shows the knowledge update plots for the signal peak parameters in the background-only fit. Figure 4.60 shows the parameter correlations for all parameters in the fit. Table 4.11 summarizes the results of these tests.

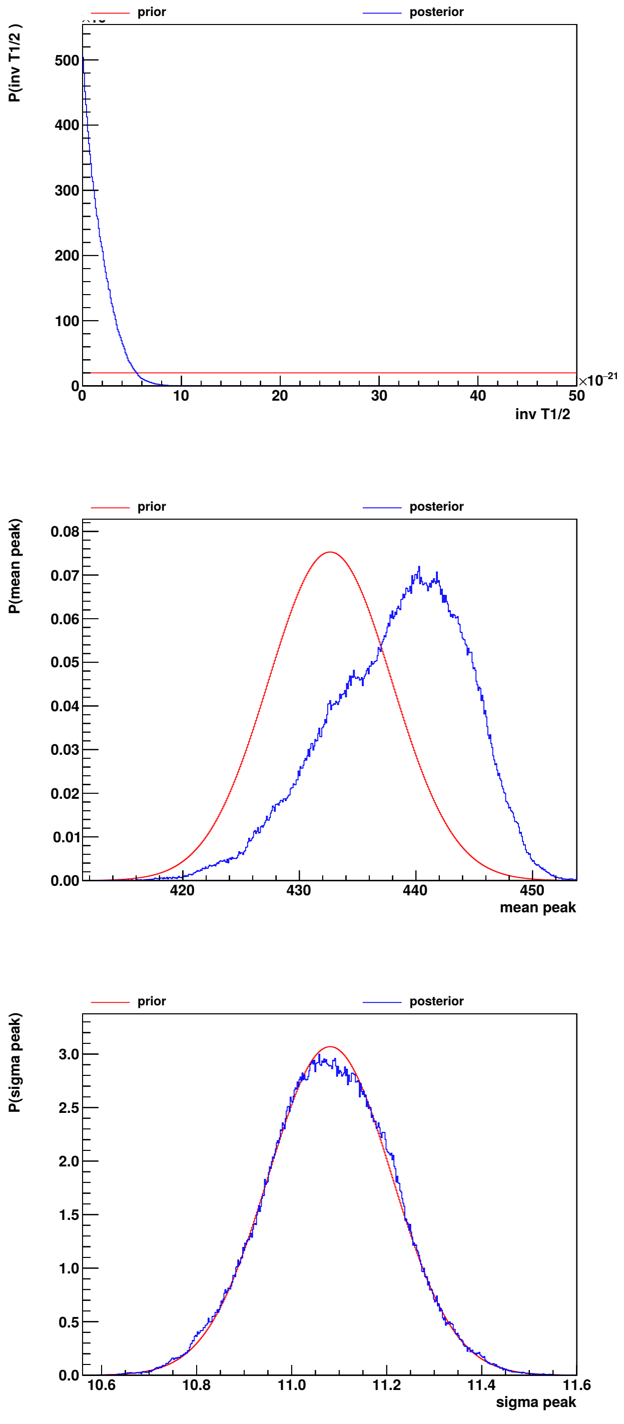

Figure 4.59: The knowledge update plots for the signal peak parameters in the ^{36}Ar background-only toy MC fit. From the top down: The inverse half-life of the signal peak with a flat prior, the peak mean with a Gaussain prior, and the peak width with a Gaussian prior.

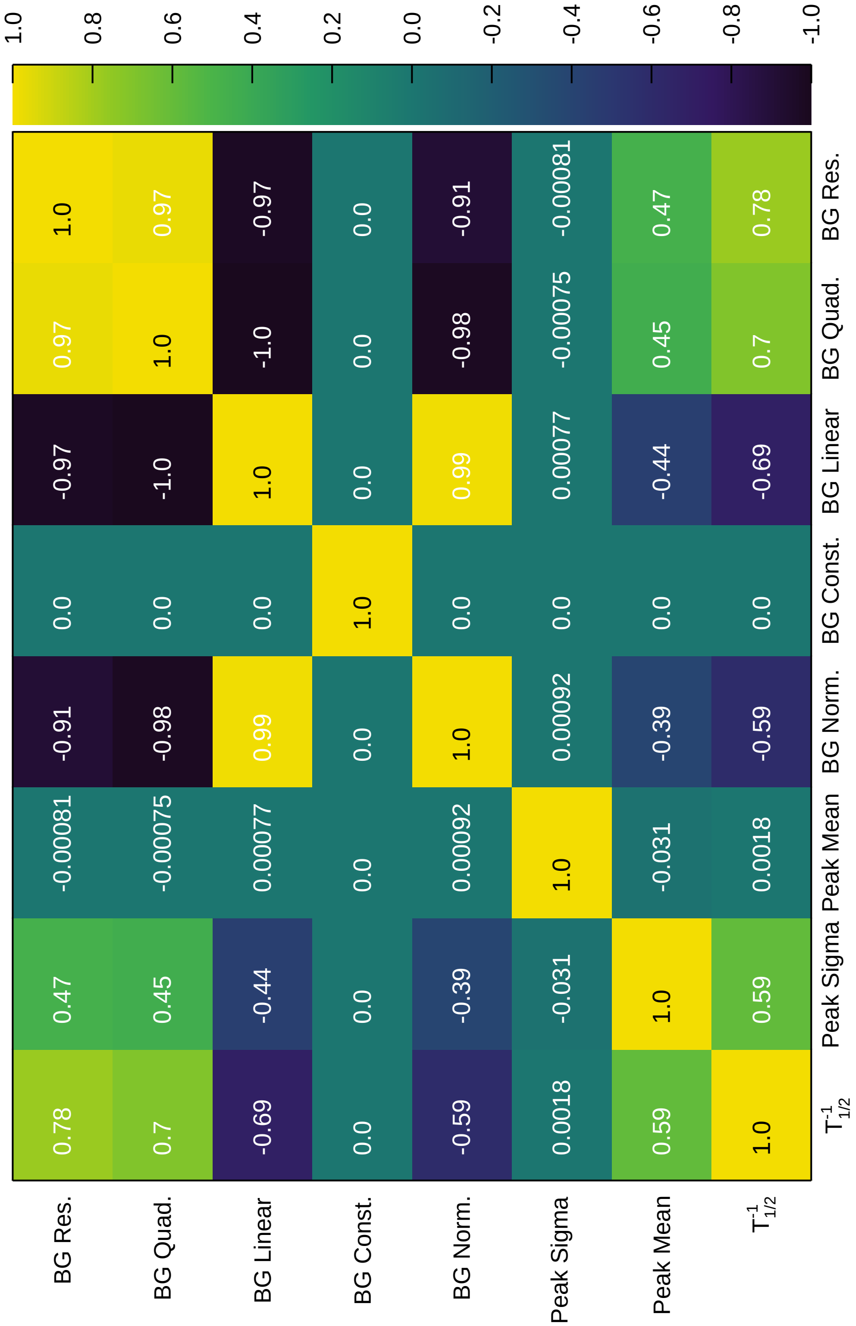

	BG Res.	BG Quad.	BG Linear	BG Const.	BG Norm.	Peak Sigma	Peak Mean	$T^{-1}_{1/2}$
BG Res.	1.0	0.97	-0.97	0.0	-0.91	-0.00081	0.47	0.78
BG Quad.	0.97	1.0	-1.0	0.0	-0.98	-0.00075	0.45	0.7
BG Linear	-0.97	-1.0	1.0	0.0	0.99	0.00077	-0.44	-0.69
BG Const.	0.0	0.0	0.0	1.0	0.0	0.0	0.0	0.0
BG Norm.	-0.91	-0.98	0.99	0.0	1.0	0.00092	-0.39	-0.59
Peak Mean	-0.00081	-0.00075	0.00077	0.0	0.00092	1.0	-0.031	0.0018
Peak Sigma	0.47	0.45	-0.44	0.0	-0.39	-0.031	1.0	0.59
$T^{-1}_{1/2}$	0.78	0.7	-0.69	0.0	-0.59	0.0018	0.59	1.0

Figure 4.60: Parameter correlations from the ^{36}Ar background-only toy MC fit. From bottom left to bottom right the parameters are: BG Res. - background model resolution parameter, BG Quad. - background model quadratic energy parameter, BG Linear - background model linear energy parameter, BG Norm. - background model normalisation parameter, Peak Sigma - width of the Gaussian signal model, Peak Mean - mean of the Gaussian signal model, $T^{-1}_{1/2}$ - inverse half-life parameter.

Test Number	Input Peak Values			Fit Results		
	Mean [keV]	Sigma [keV]	$T_{1/2}$ x10^{18} yr	Mean [keV]	Sigma [keV]	$T_{1/2}$ x10^{18} yr
1	430	11.1	1.98	430.02 ± 0.04	11.11 ± 0.05	1.68 ± 0.04
2	430	11.1	19.8	430.1 ± 0.3	11.1 ± 0.2	14.8 ± 0.6
Background Only	–	–	–	438 ± 7	11.1 ± 0.1	> 270 90% CI

Table 4.11: The input and output parameters from the ^{36}Ar toy MC fit testing. The central values quoted are the means of the marginalized distributions and the uncertainties are the 90% quantiles from these disributions.

Chapter 5

Results of Physics Analyses

5.1 Specific Activity of ^{39}Ar in Natural Atmospheric Argon

The measurement of the specific activity of ^{39}Ar has been performed on 185 individual data runs ranging from 18 hours long to 40 hours long. This section shows the results of the fits to those runs for each parameter.

5.1.1 Parameters from the Default Fits

In this section the energy scale parameters, energy resolution parameter, and the ERB background and pileup spectra normalisations from the default fits are presented. The constant energy scale parameter is not shown here as this parameter was fixed in the fits used to measure the specific activity.

The linear energy scale parameter is shown first in Figure 5.1. A general downward trend is seen in this parameter that is outside the range of the statistical fit uncertainty; the changes over time can be the result of, for example, temperature changes in and around the AV, changes in the operating temperature of the DAQ hardware, or slow contamination of the argon due to outgassing of the acrylic. This change could also be correlated with the 5 keV uncertainty in the endpoint energy. A similar change in this parameter is seen when examining the ^{40}K and ^{208}Tl gamma peak positions so this trend is not the result of changes in the ^{39}Ar but rather is related to the detector response.

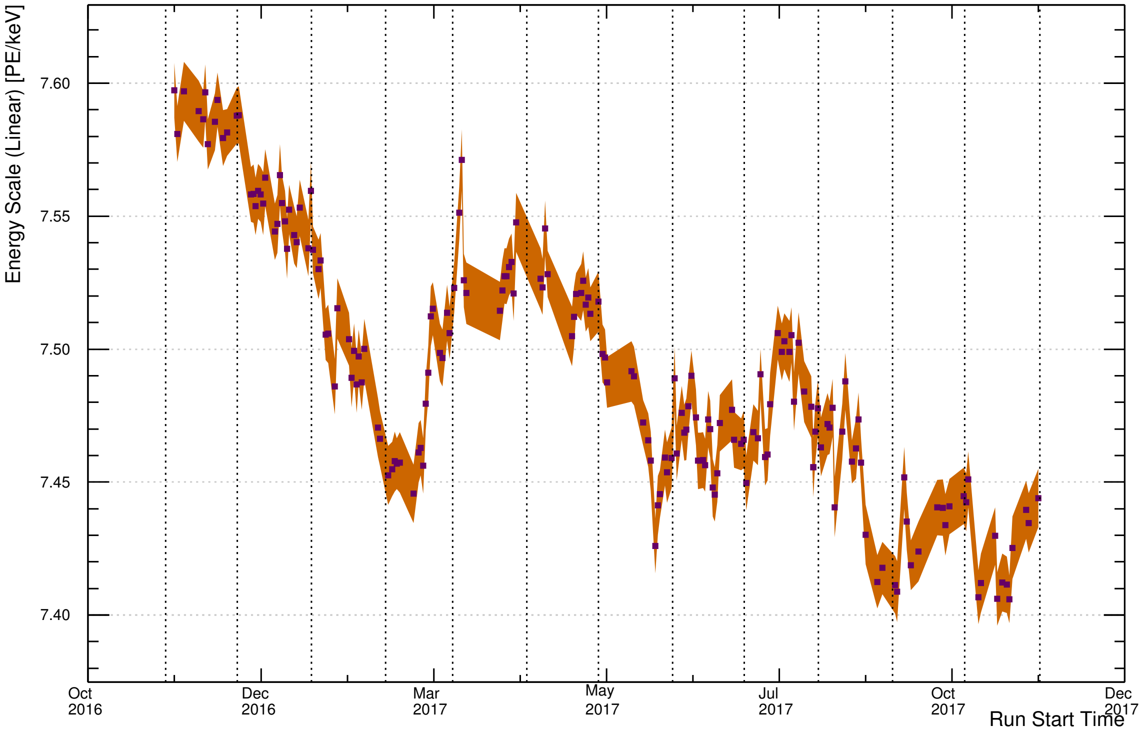

Figure 5.1: The linear energy scale term (ω_2) from each fit with a 90% CI is shown.

In Figure 5.2 the quadratic energy scale parameter is shown. This parameter is seen to be stable over the run period, with variations at the level of the 90% CI statistical fit uncertainty band.

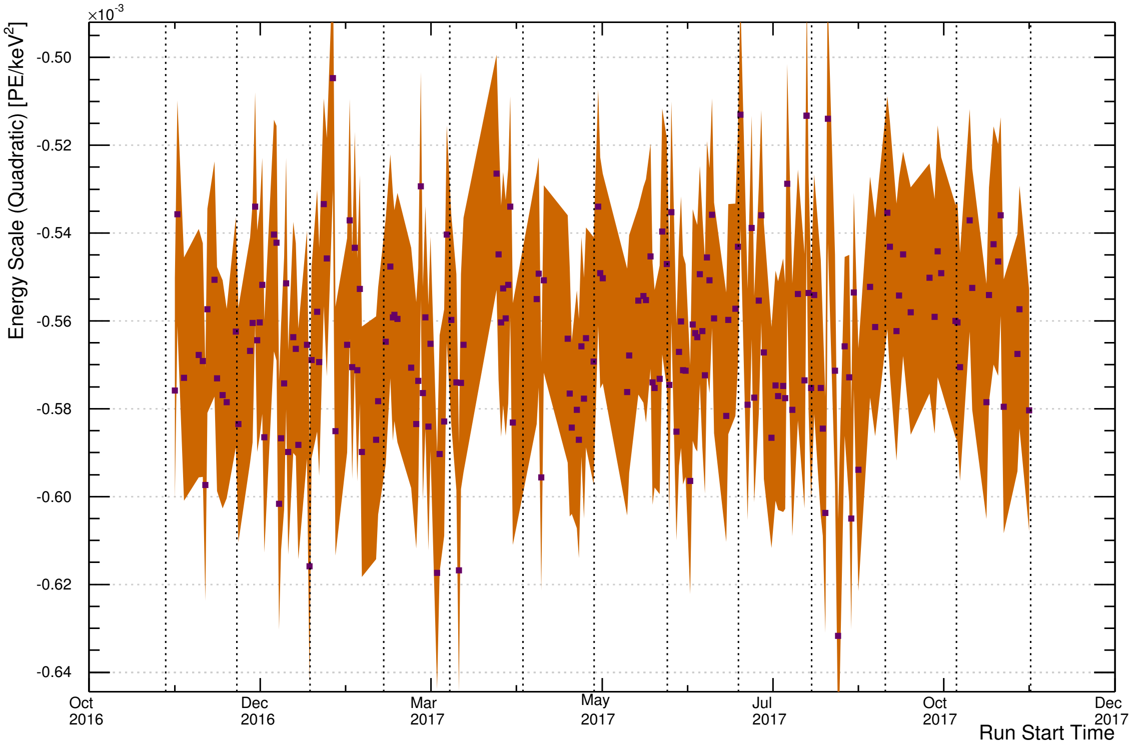

Figure 5.2: The quadratic energy scale term (ω_3) from each fit with a 90% CI is shown.

Figure 5.3 shows the linear energy resolution parameters. This parameter is also seen to be stable over the run period, having variations at the level of the 90% CI statistical fit uncertainty band. The resolution at a given PE value is, for example at 2000 PE, approximately $\sqrt{3.5 \times 2000} \approx 84$ PE, which is (84 PE)/(2000 PE) $\approx 4.2\%$.

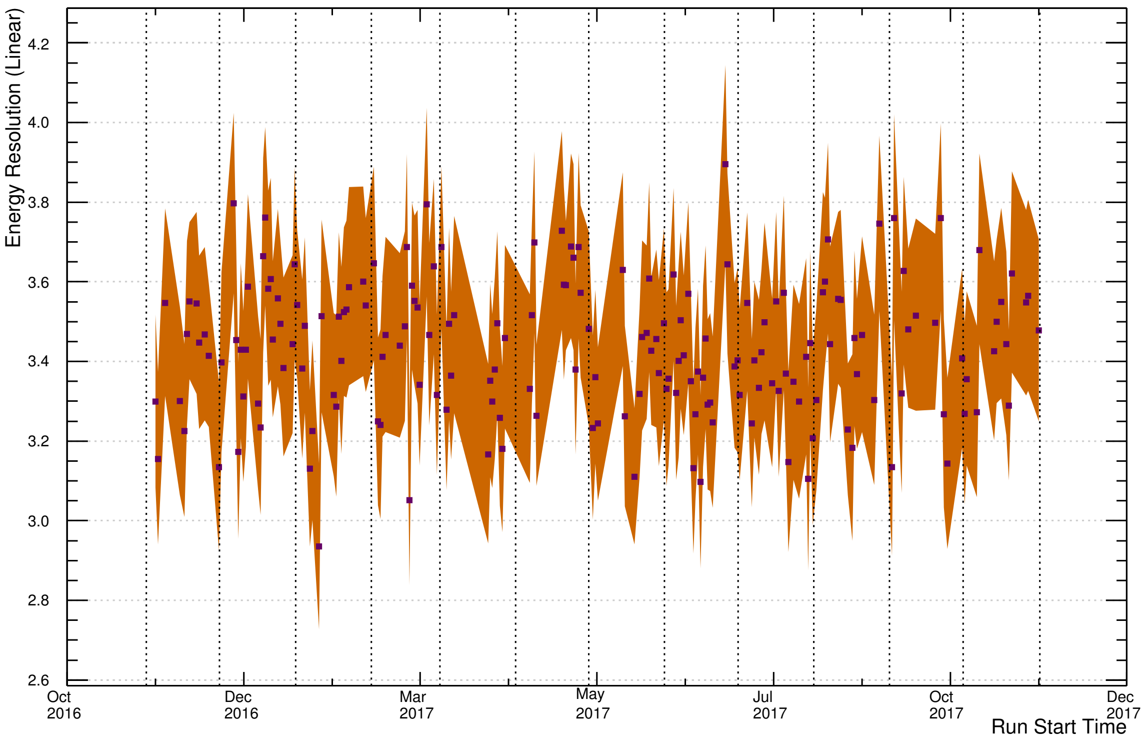

Figure 5.3: The linear energy resolution term (ϕ) from each fit with a 90% CI is shown.

Figures 5.4 and 5.5 show the ERB background and surviving pileup spectrum normalisations, respectively. The ERB background normalisation is stable over the data set; this is expected as the many of the sources of these backgrounds are external long-lived radioisotopes whose decays are expected to be essentially constant over a one year period. For the surviving ^{39}Ar pileup normalisations a minor downward trend could be present, though the trend is within the 90% CI statistical fit uncertainty band. Such a trend could be due to the decay of ^{39}Ar whose activity would decrease by about 0.25% over a period of one year.

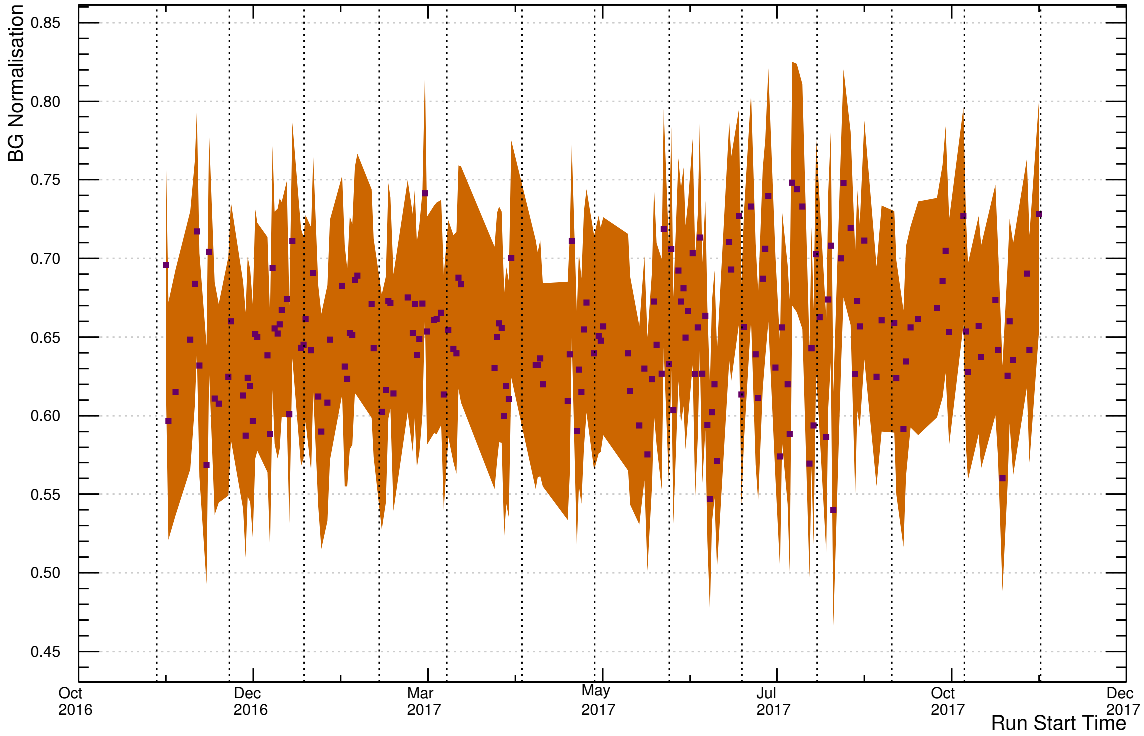

Figure 5.4: The ERB background normalization parameter from each fit with a 90% CI shown.

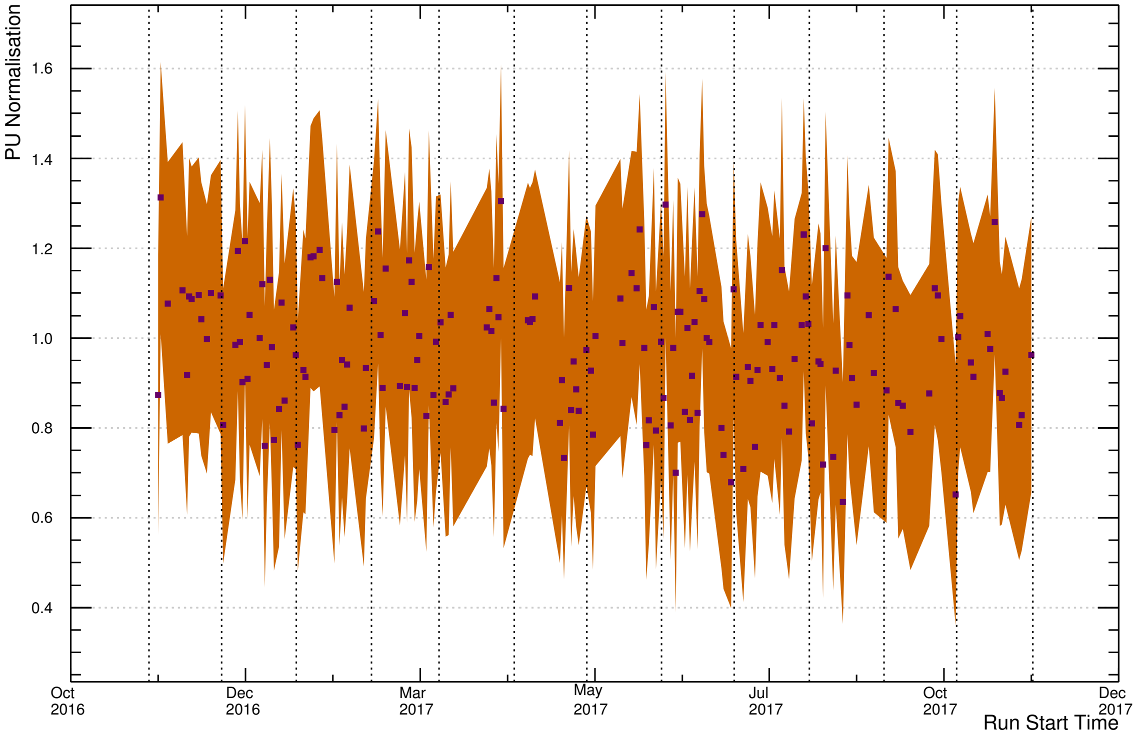

Figure 5.5: The surviving ^{39}Ar pileup background normalisation from each fit with a 90% CI shown.

5.1.2 Varying the Fit Parameters

To further understand how much the fit parameters can affect the ^{39}Ar normalisation, a series of fits in which the parameters are varied have been performed on each run in the data set. From these fits the systematic uncertainties associated with each parameter have been estimated. Three fits are performed for each of the energy scale and resolution parameters:

- Fit (1) a fit for which all parameters except the ^{39}Ar normalisation and the parameter of interest are fixed to the values from the default fit.

- Fits (2_{min}) & (2_{max}) fits for which the parameter of interest is fixed to the value from the default fit ± one half of the maximum variation across all runs in the data set and the ^{39}Ar normalisation allowed to float.

The results for the fits (1) are negligibly different than the default fits and so no points are shown in the following figures. Figure 5.6 shows the maximum and minimum variations in the ^{39}Ar normalisation due to the constant energy scale parameter. Figure 5.7 shows the maximum and minimum variations in the ^{39}Ar normalisation due to the linear energy scale parameter. Figure 5.8 shows the maximum and minimum variations in the ^{39}Ar normalisation due to the quadratic energy scale parameter. Figure 5.9 shows the maximum and minimum variations in the ^{39}Ar normalisation due to the linear energy resolution parameter.

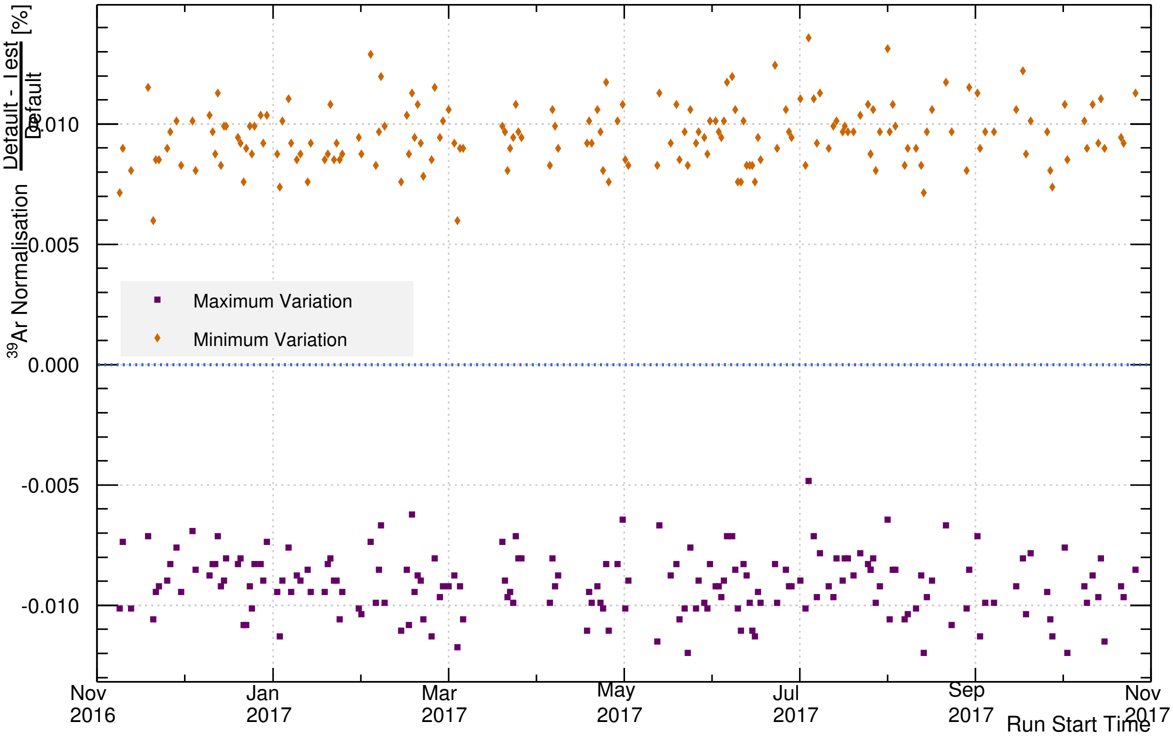

Figure 5.6: Effect on the ^{39}Ar normalisation for maximum and minimum variations of the constant energy scale parameter.

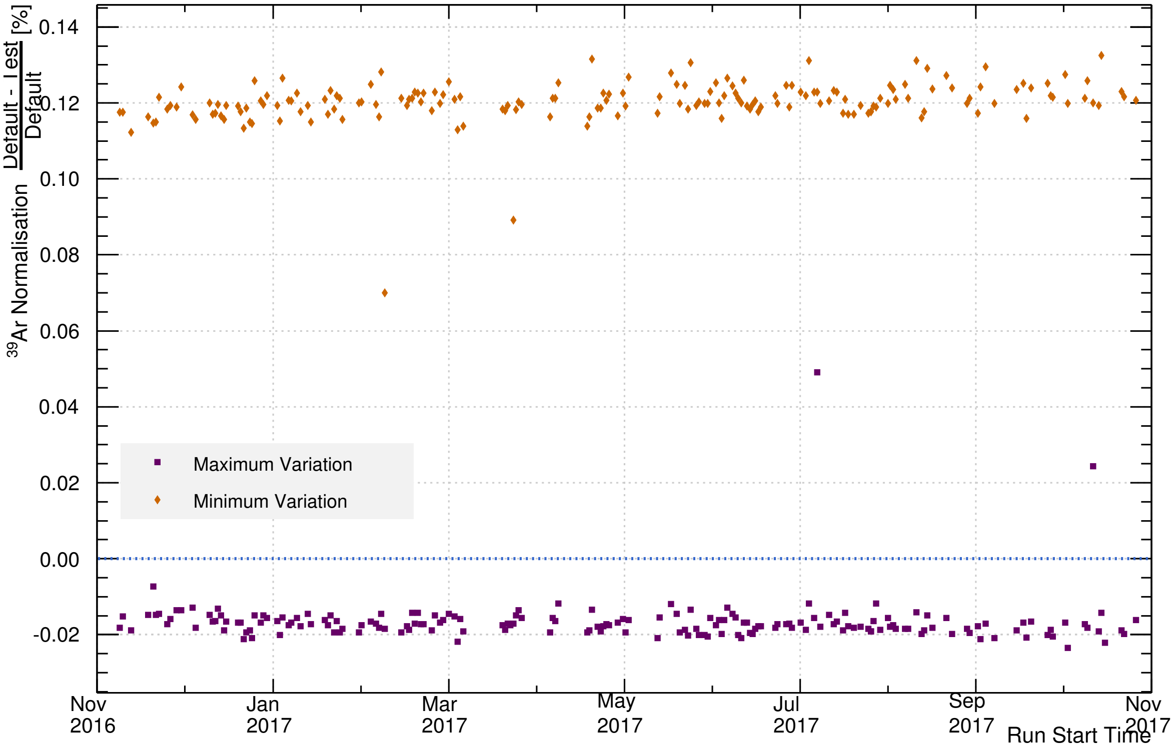

Figure 5.7: Effect on the ^{39}Ar normalisation for maximum and minimum variations of the linear energy scale parameter.

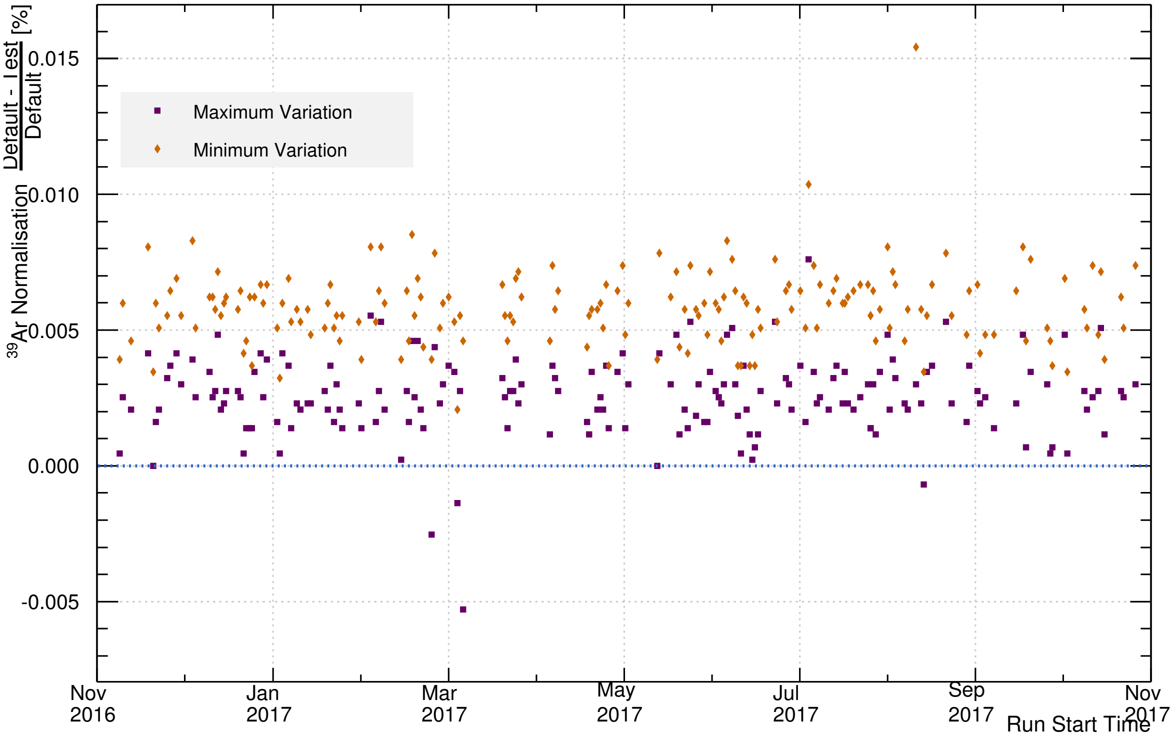

Figure 5.8: Effect on the ^{39}Ar normalisation for maximum and minimum variations of the quadratic energy scale parameter.

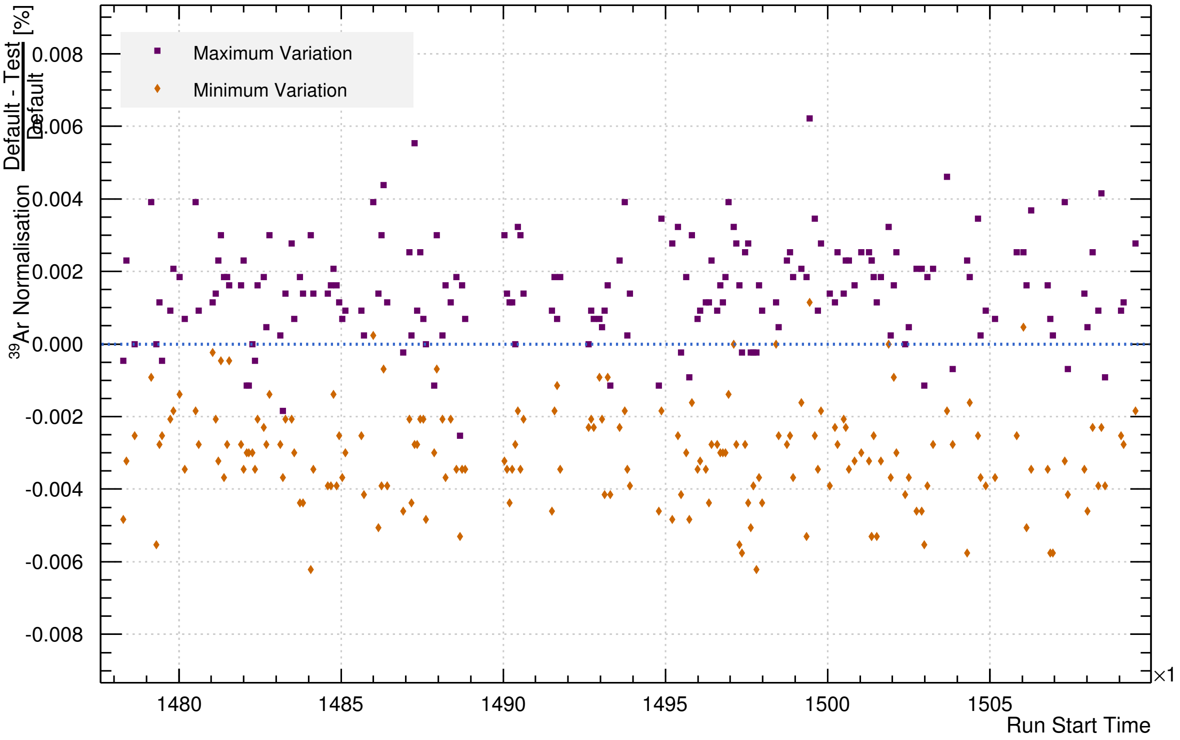

Figure 5.9: Effect on the ^{39}Ar normalisation for maximum and minimum variations of the linear energy resolution parameter.

For each parameter, one-half of the difference in the normalisations between the fits (2_{min}) & (2_{max}) is taken as the systematic uncertainty on the event count due to that parameter.

5.1.3 Calculating the ^{39}Ar Specific Activity

The calculation of the specific activity is done in several steps. First, The runtime is adjusted to livetime for the non-physics events removed by the calcut and dtmTrigSrc cuts. Next, the ^{39}Ar normalisations are extracted from the default fits to get the number of events. To this the prescaling and event selection efficiencies are applied, and then the pileup events are added back in. From this the rate of ^{39}Ar decays is calculated, and then the LAr mass is divided out to determine the specific activity. Contributions to the event count from ^{42}Ar and ^{85}Kr are assumed to be negligible in this calculation.

This procedure is shown in the following equations and the calculation is performed on a run-by-run basis. First, the runtime is adjusted for the non-physics events that have been removed to give the livetime:

$$\mathrm{T_{live}} = \mathrm{T_{run}} - (0.000013.5\ \mathrm{s}) \times \mathrm{N_{nonPhys}}, \tag{5.1}$$

where 13.5 μs is the width of the trigger window after the trigger at 2.5 μs, $\mathrm{T_{run}}$ is the runtime, and $\mathrm{N_{nonPhys}}$ is the number of events removed by the non-physics event removal cuts dtmTrigSrc and calcut. Next, the number of events from the fit, $\mathrm{N_{fit}}$, is calculated:

$$\mathrm{N_{fit}} = 10^{k_{\mathrm{Ar}}}, \tag{5.2}$$

where k_{Ar} is the measured ^{39}Ar normalisation parameter (recall the ^{39}Ar normalisation is the logarithm of the number of counts). This is then adjusted for product of the event selection efficiency from numEarlyPulses (99.99%) and the subeventN efficiency for correctly identifying single ^{39}Ar decays (99.87%), and the prescaling factor (100) is applied; this gives the total number of ^{39}Ar events from the fit:

$$\mathrm{N'_{fit}} = \left(\frac{\mathrm{N_{fit}}}{0.9999 \times 0.9987}\right) \times 100 \tag{5.3}$$

The pileup events are considered next, and there are two components: the number of surviving ^{39}Ar-^{39}Ar events and the number of ^{39}Ar removed by the subeventN cut. First, the number of surviving pileup events, $\mathrm{N_{SuPU}}$, is extracted from the fit which returns a normalisation, k_{SuPU}, that is the scaling fraction of the spectrum relative to an assumed default value of 1:

$$\mathrm{N_{SuPU}} = 2 \times (5.361\ \mathrm{Hz}) \times \mathrm{T_{run}} \times k_{\mathrm{SuPU}}, \tag{5.4}$$

where the factor of 2 accounts for the 2 simulated ^{39}Ar events whose combined energy build the surviving pileup spectrum and the 5.361 Hz is an estimate of the surviving pileup rate used in the fit. The runtime is used as an input to the fit to calculate starting values for the normalisations, and so the value is used here rather than the livetime. Second, the number of ^{39}Ar removed by the subeventN cut, $\mathrm{N_{SnPU}}$, is found by estimating the pileup rate and then the number of pileup events is calculated using the runtime; for each pileup event calculated in this manor, the number of ^{39}Ar events has previously been estimated to be 2.03 ± 0.11 in Section 4.4.2:

$$\mathrm{N_{SnPU}} = \mathrm{R_{PU}}(16\mu\mathrm{s}) \times 2.03, \tag{5.5}$$

where $\mathrm{R_{PU}}$ is the estimated pileup rate and the factor of 16 μs is for the full trigger window. The total number of pileup events, $\mathrm{N_{PU}}$ is the sum of Eqs. 5.4 and 5.5:

$$\mathrm{N_{PU}} = \mathrm{N_{SuPU}} + \mathrm{N_{SnPU}}. \tag{5.6}$$

Adding $\mathrm{N'_{fit}}$ and $\mathrm{N_{PU}}$ gives the total number of ^{39}Ar events in the run;

$$\mathrm{N_{^{39}Ar}} = \mathrm{N'_{fit}} + \mathrm{N_{PU}} \tag{5.7}$$

With both of these quantities the activity of ^{39}Ar decays can be calculated:

$$\mathrm{A_{^{39}Ar}} = \frac{\mathrm{N_{^{39}Ar}}}{\mathrm{T_{live}}}. \tag{5.8}$$

Finally, the specific activity is calculated:

$$\mathrm{SA} = \frac{\mathrm{A}_{^{39}\mathrm{Ar}}}{\mathrm{M}_{\mathrm{LAr}}} \tag{5.9}$$

Statistical and Systematic Uncertainties

The uncertainty on the event count from the fit, $\mathrm{N}_{\mathrm{fit}}$, is taken as the difference between the central value and 90% quantile of the parameter. The fit uncertainty for all runs is shown in Figure 5.10; the energy scale and resolution parameters are constrained in the fits and this uncertainty includes the parameter systematics.

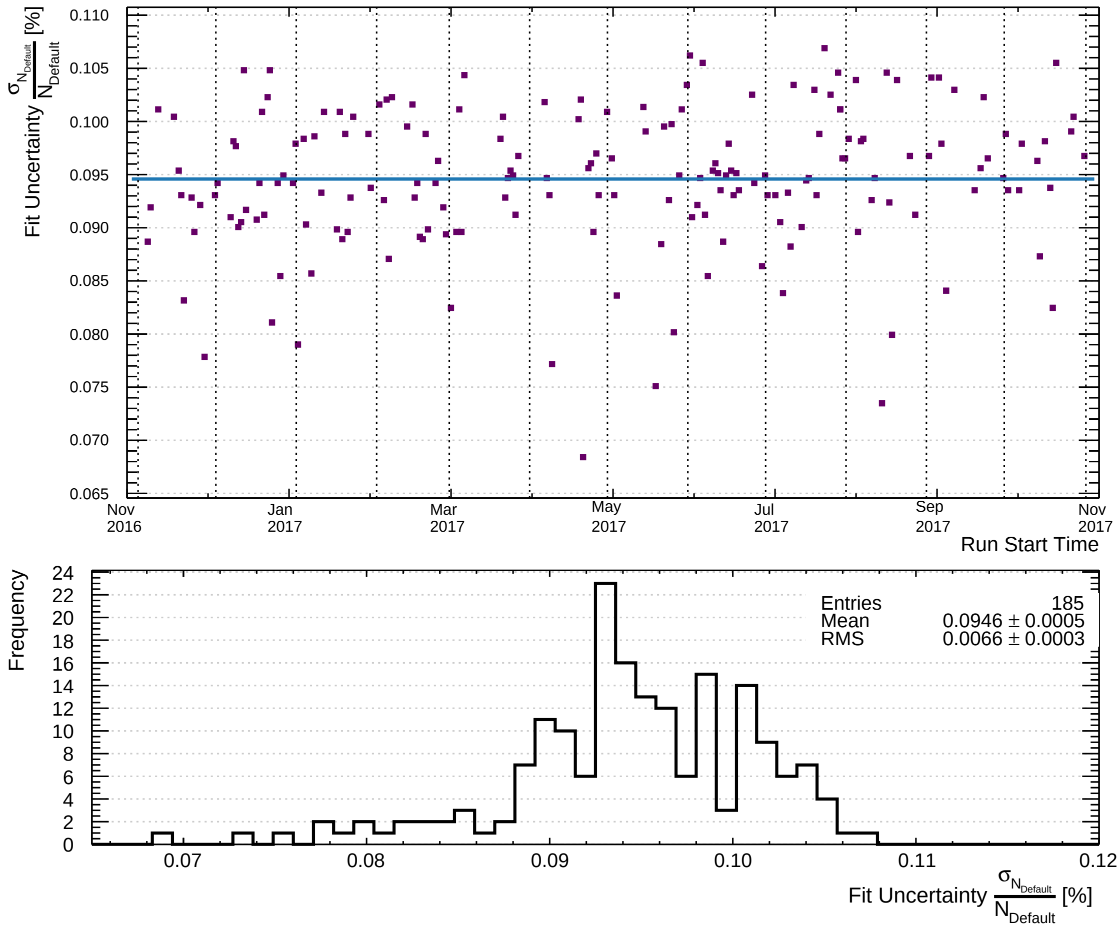

Figure 5.10: Fit uncertainties for all runs in the data set shown as a function of time (upper panel) and as a frequency histogram (lower panel). The uncertainty is taken as the difference between the central value and the upper 90% quantile of the fit. The linear fit to the distribution in time gives a mean value of 221,438 events.

The uncertainty on the event count is comprised of several different components which account for possible variations in the fits. The components are extracted from the maximum/minimum variation fit testing as a double check; see Figures 5.6, 5.7, 5.8, 5.9). The constant parameter is varied by ± 2.4σ for the known value of (1.2 ± 0.2)PE. Because this parameter is fixed in all fits to measure the specific activity, no maximum/minimum variations exist for the data set as they do for the other energy scale parameters; the value of 2.4 gives a maximum/minimum variation that is slightly larger than the variations in the other parameters to be conservative. The uncertainty for this parameter is shown in Figure 5.11.

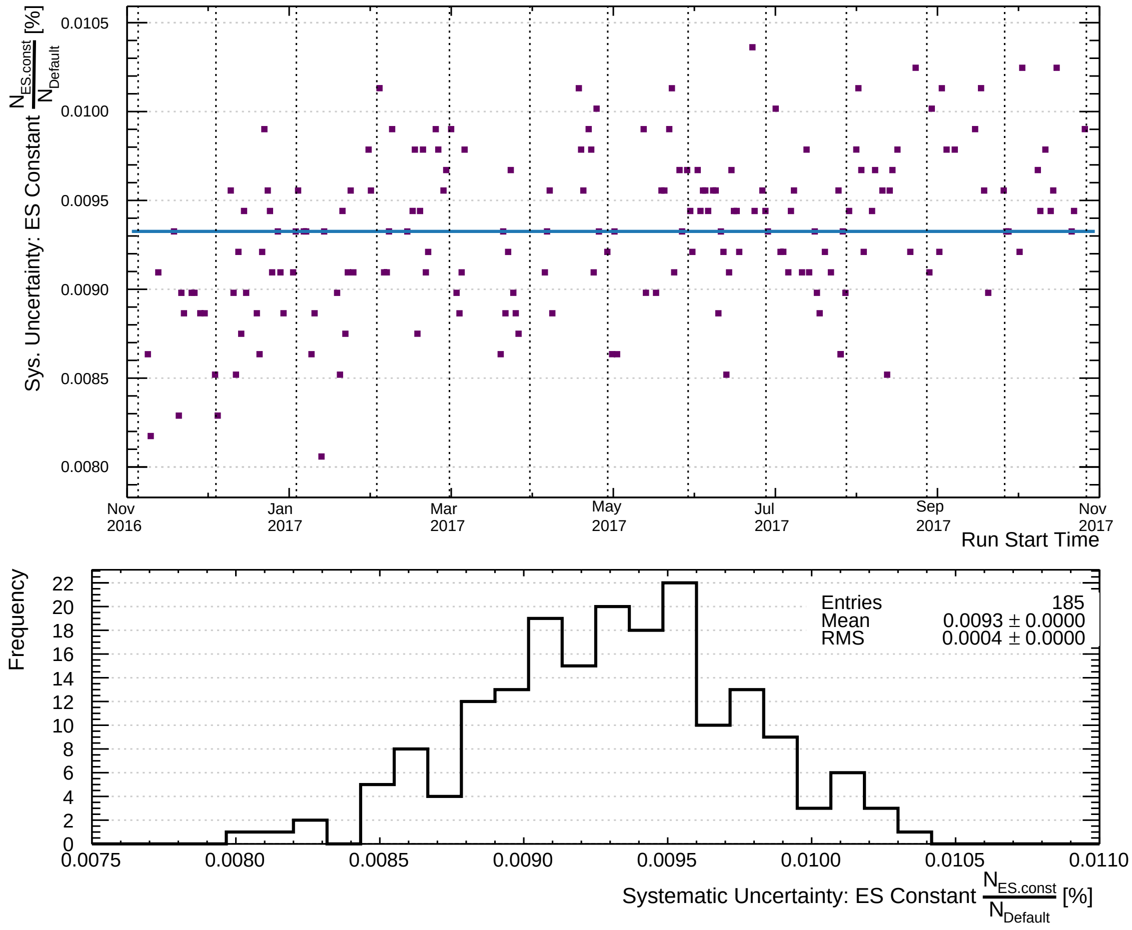

Figure 5.11: Systematic uncertainties from the constant energy scale parameters for all runs in the data set shown as a function of time (upper panel) and as a frequency histogram (lower panel). The uncertainty is taken as the difference between the normalisations for the maximum and minimum variation fits divided by the normalisation from the default fit. The linear fit to the distribution in time gives a mean value of 0.0093%.

The linear energy scale parameter is varied for each run from the central value measured by the default fit by half of the maximum difference across all runs. This difference was measured to be 0.096 PE/keV, with the maximum and minimum values measured to be 7.597 PE/keV and 7.406 PE/keV, respectively. The difference is 1.28%

of the mean value. The uncertainty on this parameter is shown in Figure 5.12.

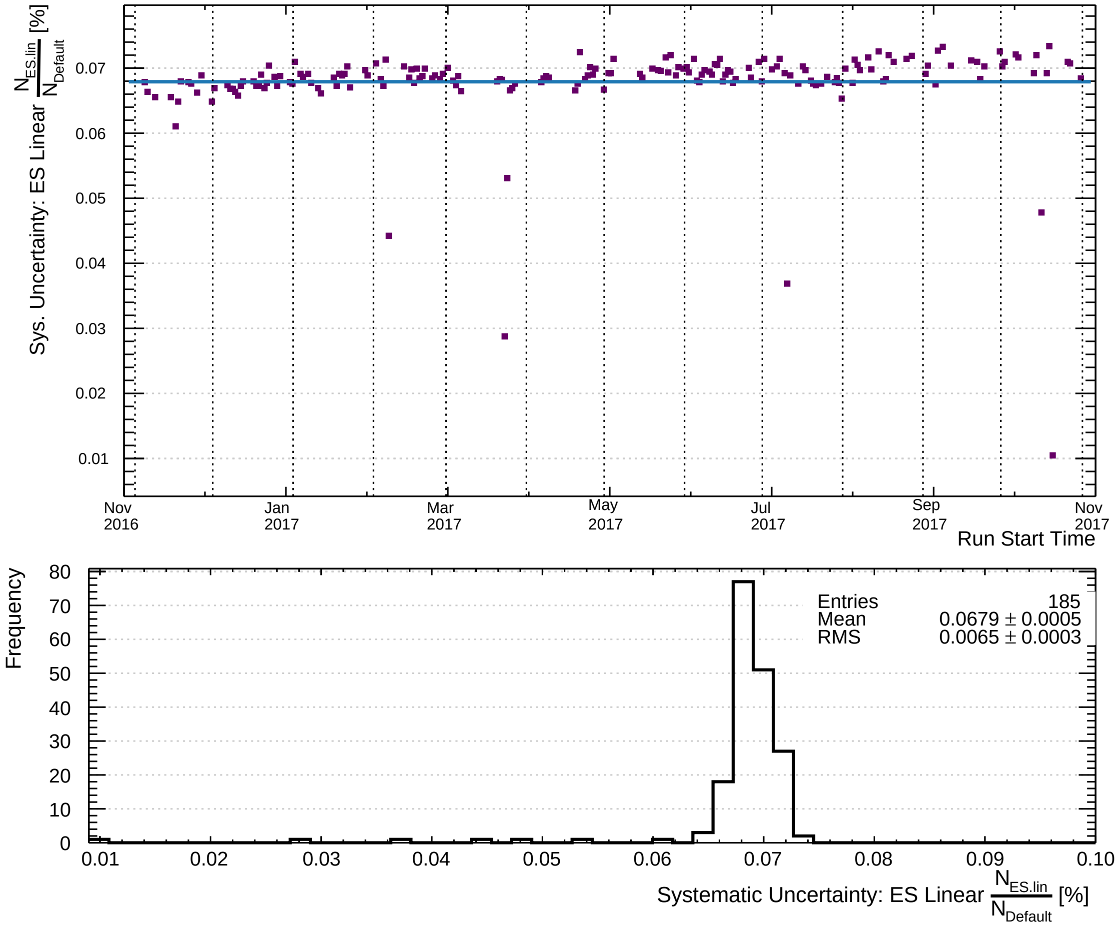

Figure 5.12: Systematic uncertainties from the linear energy scale parameters for all runs in the data set shown as a function of time (upper panel) and as a frequency histogram (lower panel). The uncertainty is taken as the difference between the normalisations for the maximum and minimum variation fits divided by the normalisation from the default fit. The linear fit to the distribution in time gives a mean value of 0.068%.

For the quadratic energy parameter is varied for each run from the central value measured by the default fit by half of the maximum difference across all runs. The difference was measured to be 0.000064 PE/keV^2, with the maximum and minimum values measured to be -0.000505 PE/keV^2 and -0.000632 PE/keV^2, respectively. The difference is 11.27% of the mean value. The uncertainty on this parameter is shown in Figure 5.13.

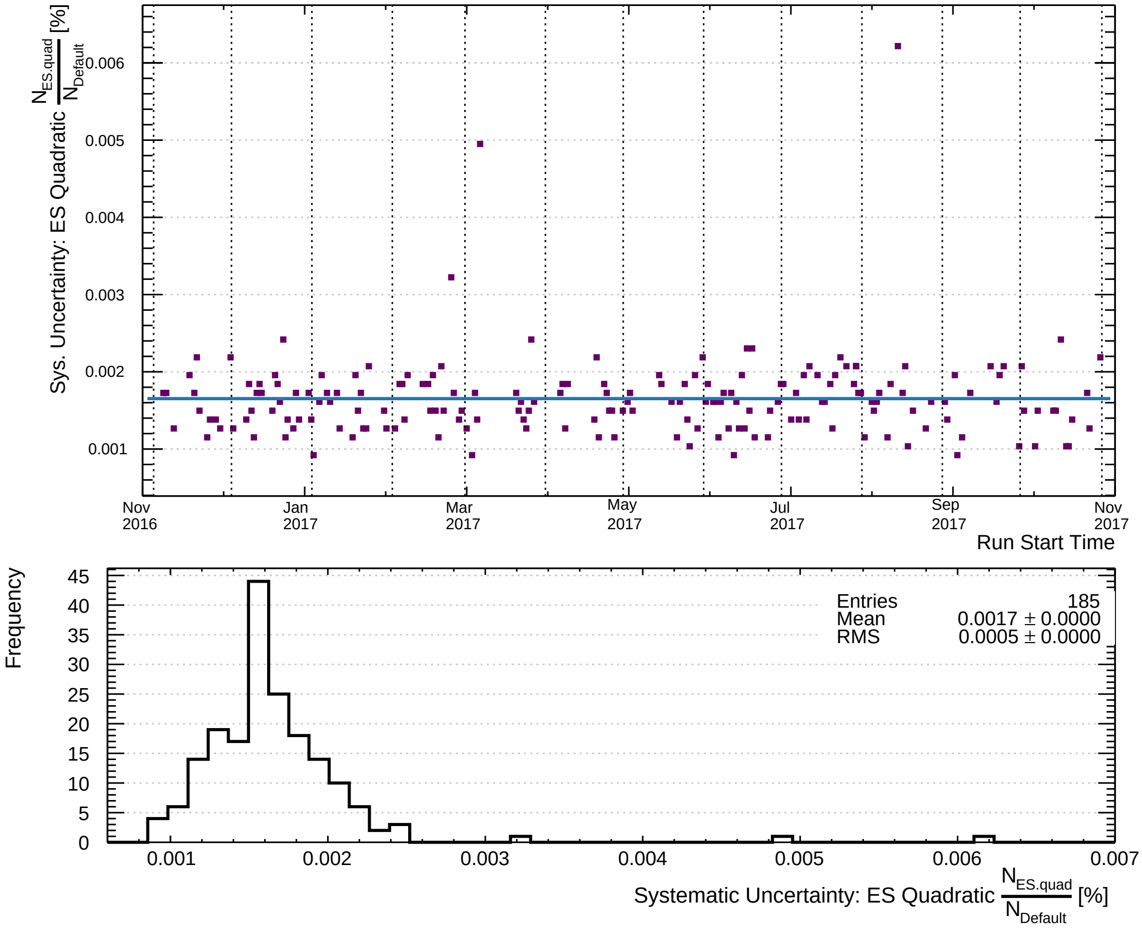

Figure 5.13: Systematic uncertainties from the quadratic energy scale parameters for all runs in the data set shown as a function of time (upper panel) and as a frequency histogram (lower panel). The uncertainty is taken as the difference between the normalisations for the maximum and minimum variation fits divided by the normalisation from the default fit. The linear fit to the distribution in time gives a mean value of 0.0017%

Finally, the linear energy resolution parameter is varied for each run from the central value measured by the default fit by half of the maximum difference across all runs. The difference was measured to be 0.48, with the maximum and minimum values measured to be 3.90 and 2.94, respectively. The difference is 14.06% of the mean value. The uncertainty on this parameter is shown in Figure 5.14.

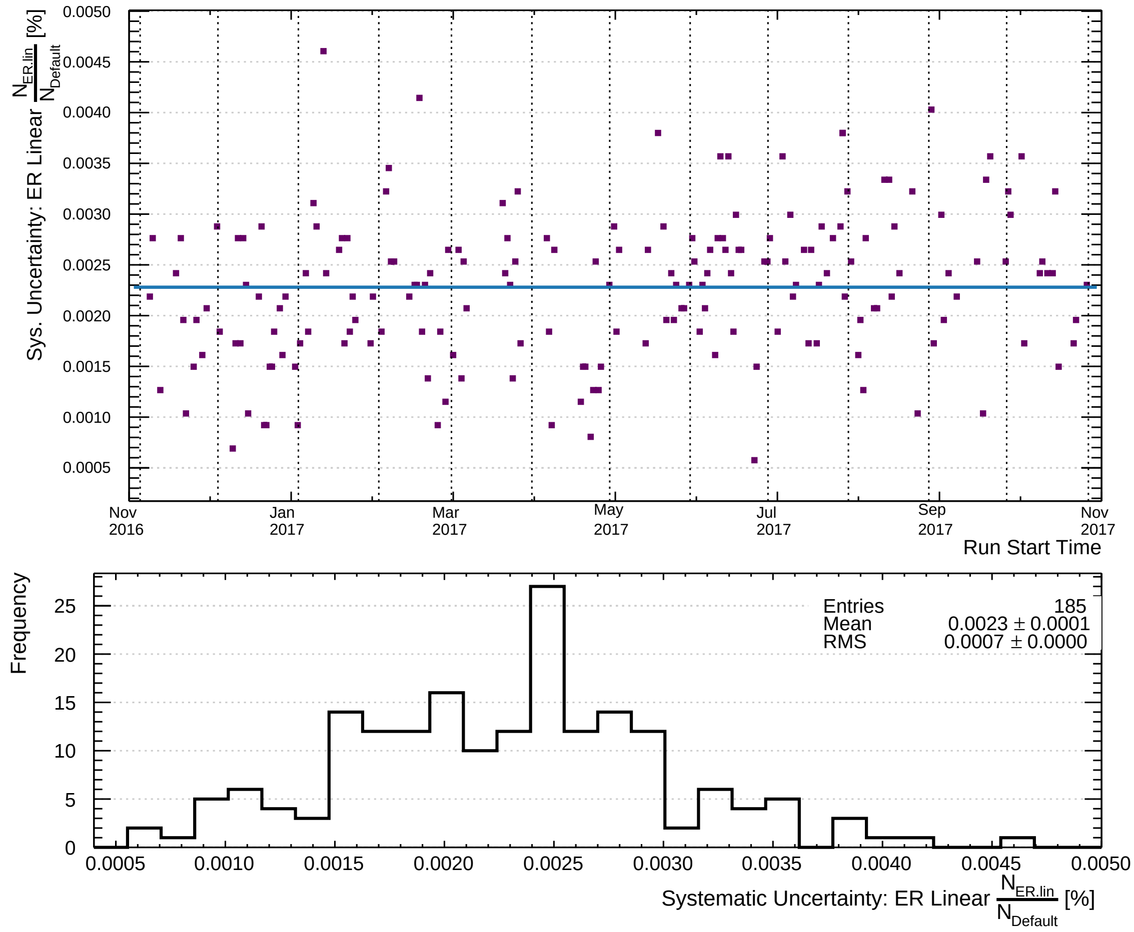

Figure 5.14: Systematic uncertainties from the linear energy resolution parameters for all runs in the data set shown as a function of time (upper panel) and as a frequency histogram (lower panel). The uncertainty is taken as the difference between the normalisations for the maximum and minimum variation fits divided by the normalisation from the default fit. The linear fit to the distribution in time gives a mean value of 0.0023%.

The previous four tests are used to confirm the validity of the fit. The average fit uncertainty across the data set is 0.095%; adding the values from the variation fits linearly for simplicity, the sum is 0.081% and is dominated by the linear energy scale uncertainty. The difference between this conservative estimate and the measured fit uncertainty represents a negligible change in the specific activity uncertainty.

The next component included in the specific activity uncertainty calculation is the difference between the fit models with the default Behrens & Janecke spectrum and the KSZ spectrum; Figure 5.15 shows the value for each run. Two populations are observed in this uncertainty where some fits have larger energy scale parameters relative to the default fit and return a normalisation much closer to the default; the reason for this effect is unknown. Rather than take an average of this uncertainty from both populations (0.03%), the average of the upper population of 0.04% is taken.

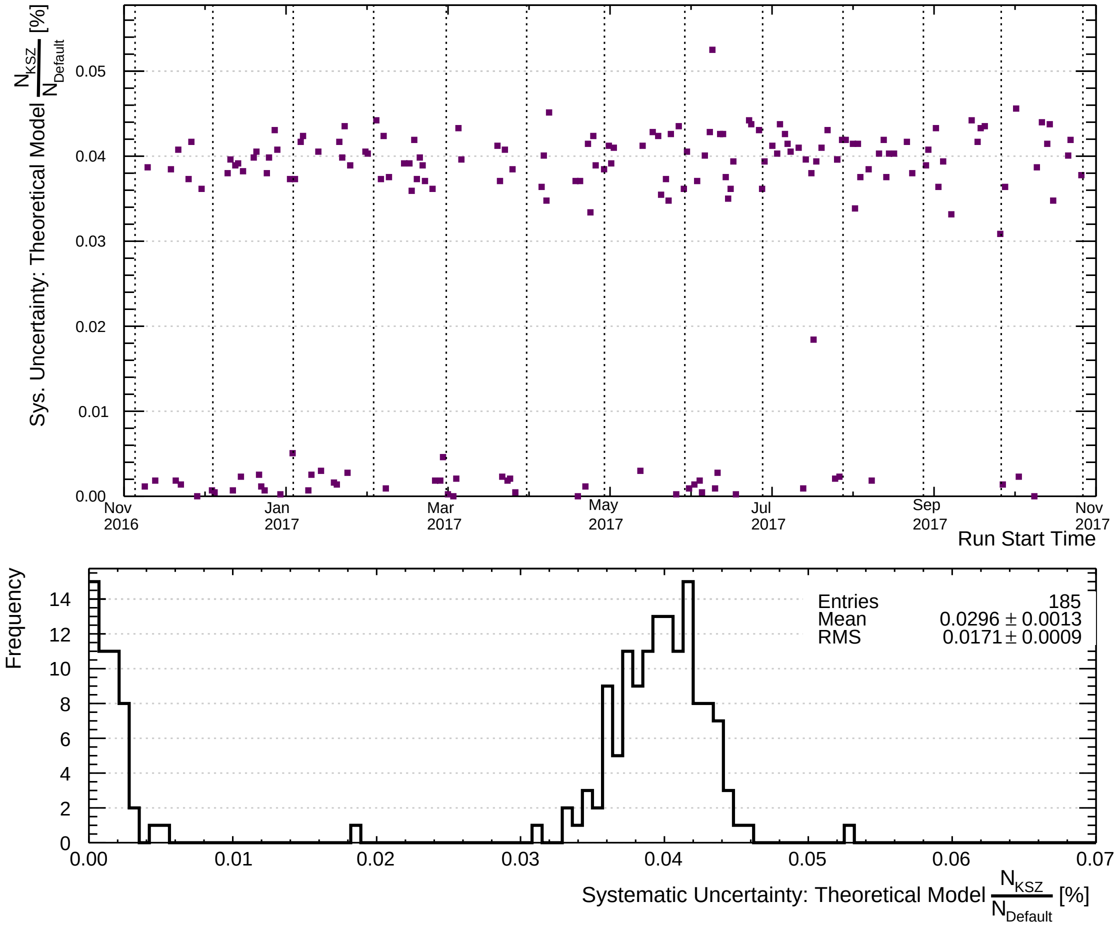

Figure 5.15: Systematic uncertainties from the theoretical fit model for all runs in the data set shown as a function of time (upper panel) and as a frequency histogram (lower panel). The uncertainty is taken as the ratio between the central value from the fit with the KSZ spectrum and the central value from the default fit.

For the ^{39}Ar pileup correction the uncertainty is taken as 5.4% of the number of pileup events. The value of 5.4% was derived from an assumed uncertainty in the ^{39}Ar activity and the LAr mass uncertainty added in quadrature. This plot is shown in Figure 5.16; the structure seen in the data is directly related to the observed structure in the trigger rate.

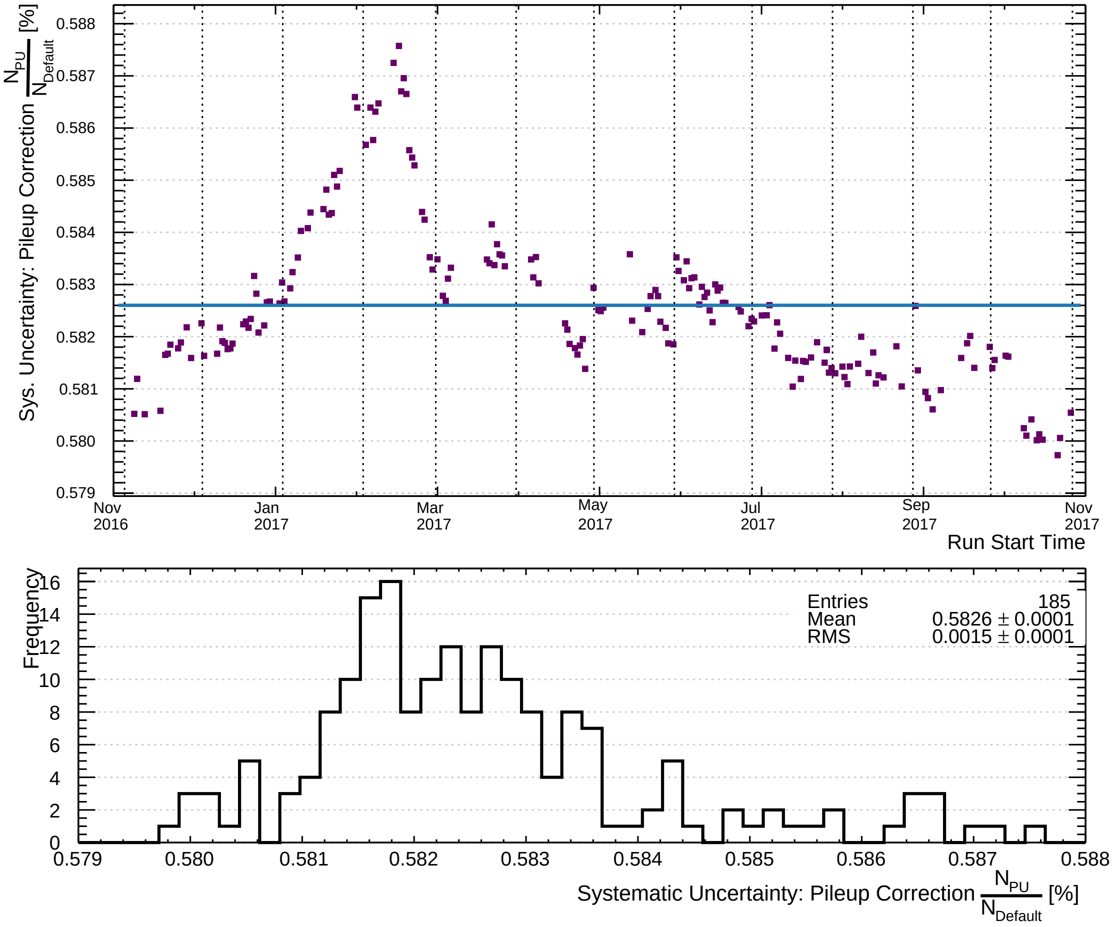

Figure 5.16: Systematic uncertainties from the pileup correction for all runs in the data set shown as a function of time (upper panel) and as a frequency histogram (lower panel). The uncertainty is taken as 5.4% of the number of pileup events added back to the event count due to subeventN pileup removal. The linear fit to the distribution in time gives a mean value of 0.58%.

The runtime adjustment is based on the number of non-physics events removed by dtmTrigSrc and calcut. Based on the nature of dtmTrigSrc it is taken that no ^{39}Ar are incorrectly identified with the wrong trigger value (apart from pileup events between an ^{39}Ar decay and the periodic trigger, but these have already been accounted for). It is unknown how many ^{39}Ar decays are lost to, for example, problems with the PMT baselines; the issues which cause calcut to flag and remove events are extremely difficult to simulate accurately. However, the number of events removed by calcut in any given run is very small and so the uncertainty is conservatively based on 100% of these events; this essentially assumes that all events removed by calcut could have been ^{39}Ar decays; this is shown in Figure 5.17. The uncertainty on the runtime of the run is taken as zero as this is simply the clock time between the first and last events and is accurate to much less than 1 second.

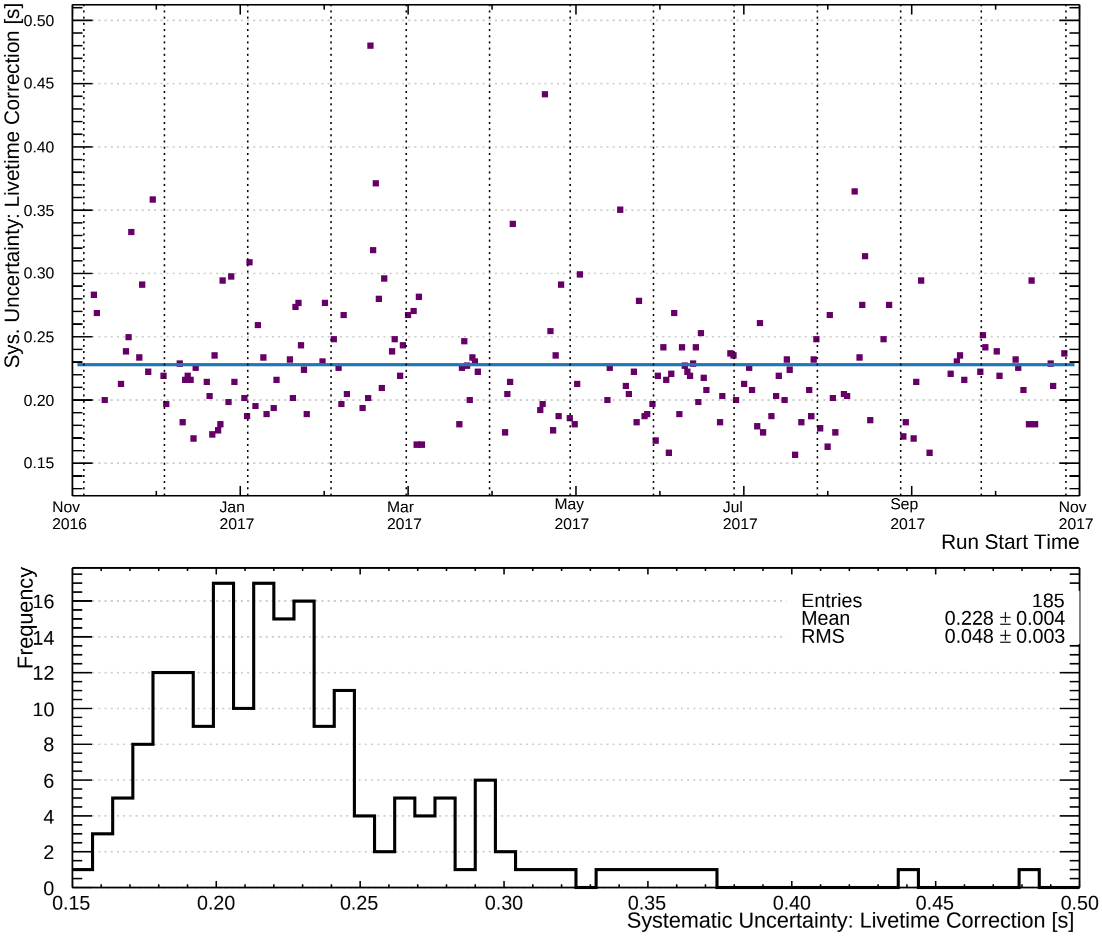

Figure 5.17: Systematic uncertainties from the runtime adjustment for all runs in the data set shown as a function of time (upper panel) and as a frequency histogram (lower panel). The uncertainty is taken as 16 μs for each event removed by calcut. The linear fit to the distribution in time gives a mean value of 0.23 seconds.

For the systematic uncertainty on the ^{39}Ar activity the two contributions are added in quadrature. The uncertainty is shown in Figure 5.18.

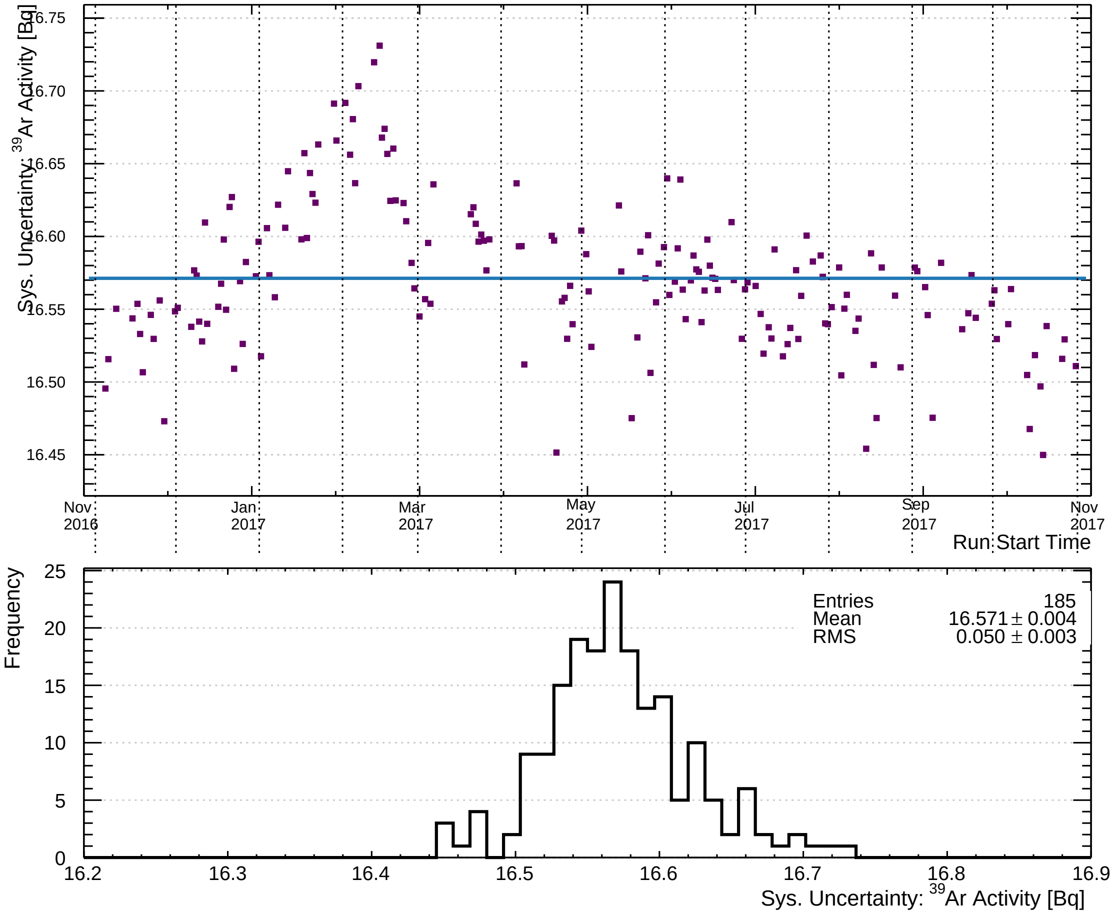

Figure 5.18: Systematic uncertainties from the ^{39}Ar activity for all runs in the data set shown as a function of time (upper panel) and as a frequency histogram (lower panel). The linear fit to the distribution in time gives a mean value of 16.67 Bq.

With this and the uncertainty on the LAr mass the uncertainty on the specific activity is calculated, with the two terms added in quadrature. Figure 5.19 shows the uncertainty.

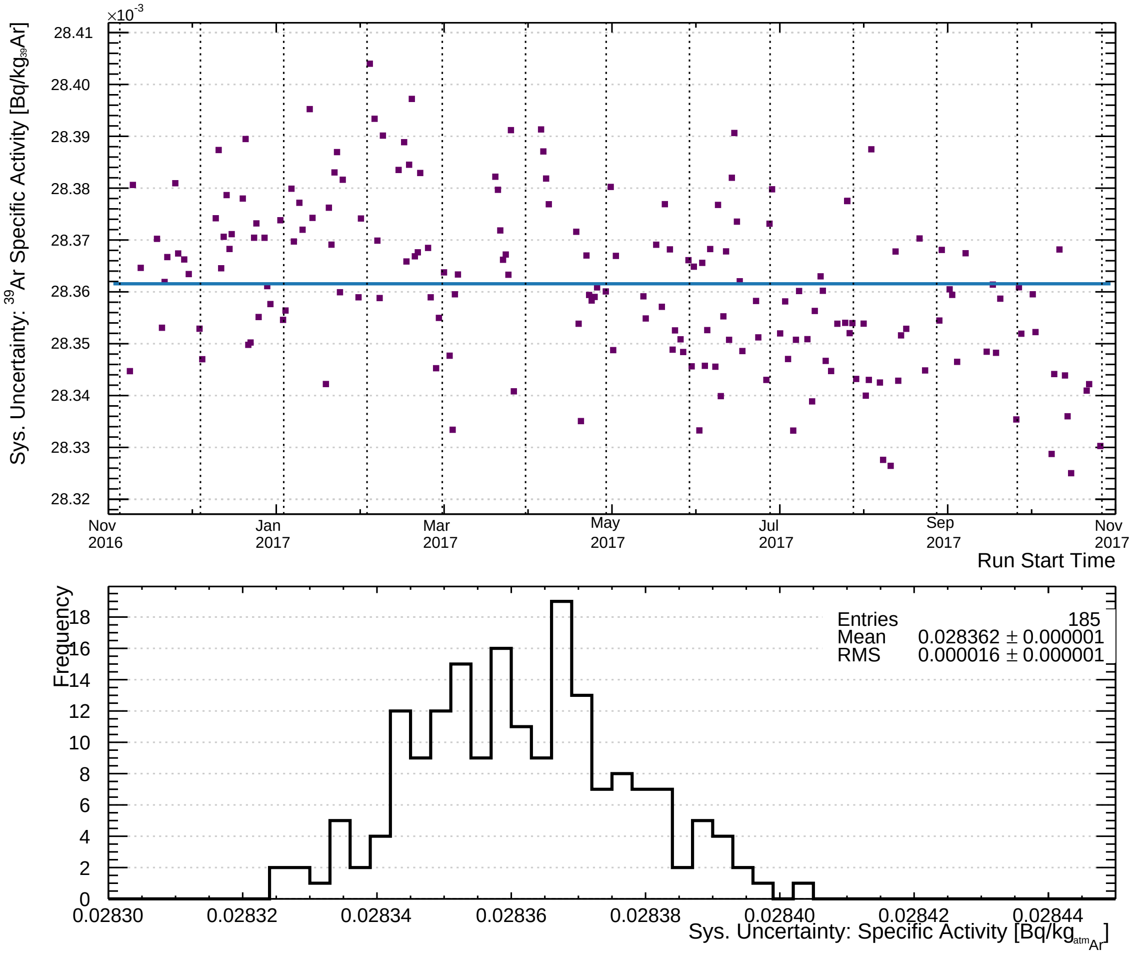

Figure 5.19: Systematic uncertainties from the ^{39}Ar specific activity for all runs in the data set shown as a function of time (upper panel) and as a frequency histogram (lower panel). The linear fit to the distribution in time gives a mean value of 0.028 Bq/kg$_{^{39}\mathrm{Ar}}$.

All of the mean uncertainties for the specific activity calculation are compiled together in Table 5.1. 185 individual measurements of the specific activity have been made. These measurements are presented together in Figure 5.20 as a frequency histogram and in Figure 5.21 as a graph over time. The frequency histogram is approximated by a Gaussian with a mean 0.953 Bq/kg$_{^{39}\mathrm{Ar}}$. Across the one-year data set a general, minor downward trend in the specific activity is seen. The change over one year is less than would be expected if it were due purely to the decay of ^{39}Ar (which would be about 0.25%); since the AV is a sealed system and no argon was added or removed during the data set, there must be an additional effect at work such as variations in the detector response over time. The systematic uncertainties are approximately a factor of 35 larger than the statistical fit uncertainties; the measurements agree well with one another within the systematic uncertainties .

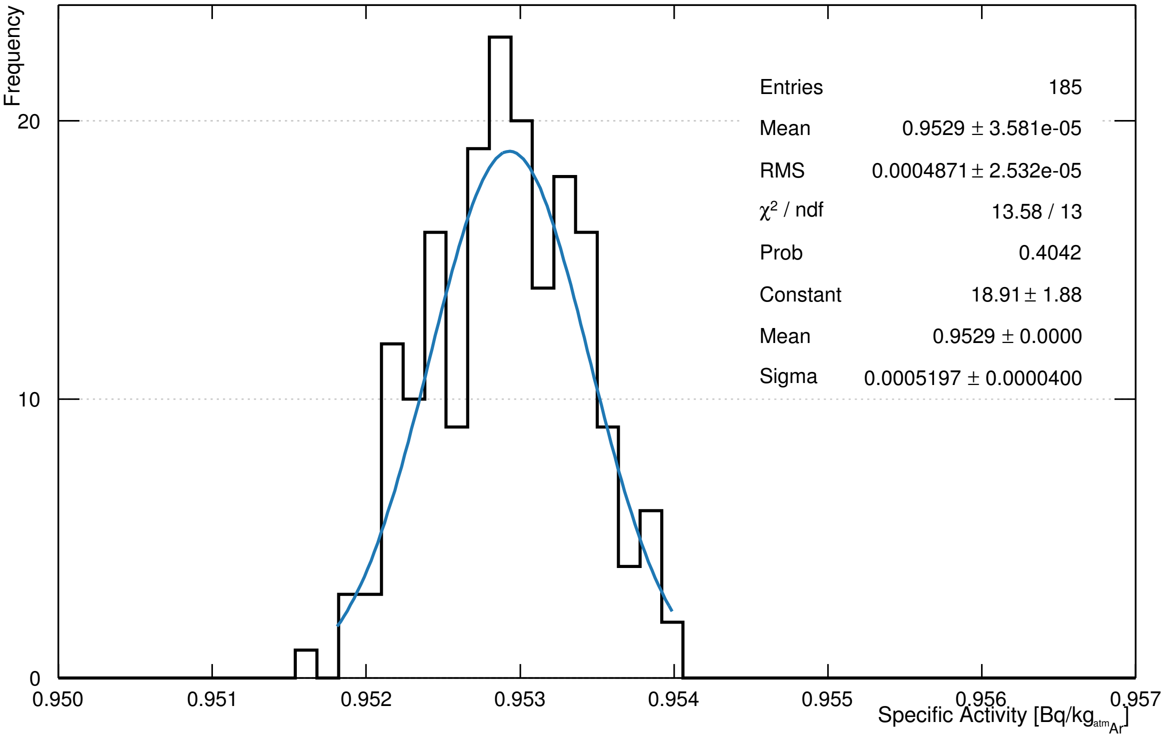

Figure 5.20: Frequency distribution of the specific activity measurements. The distribution is approximated by a Gaussian

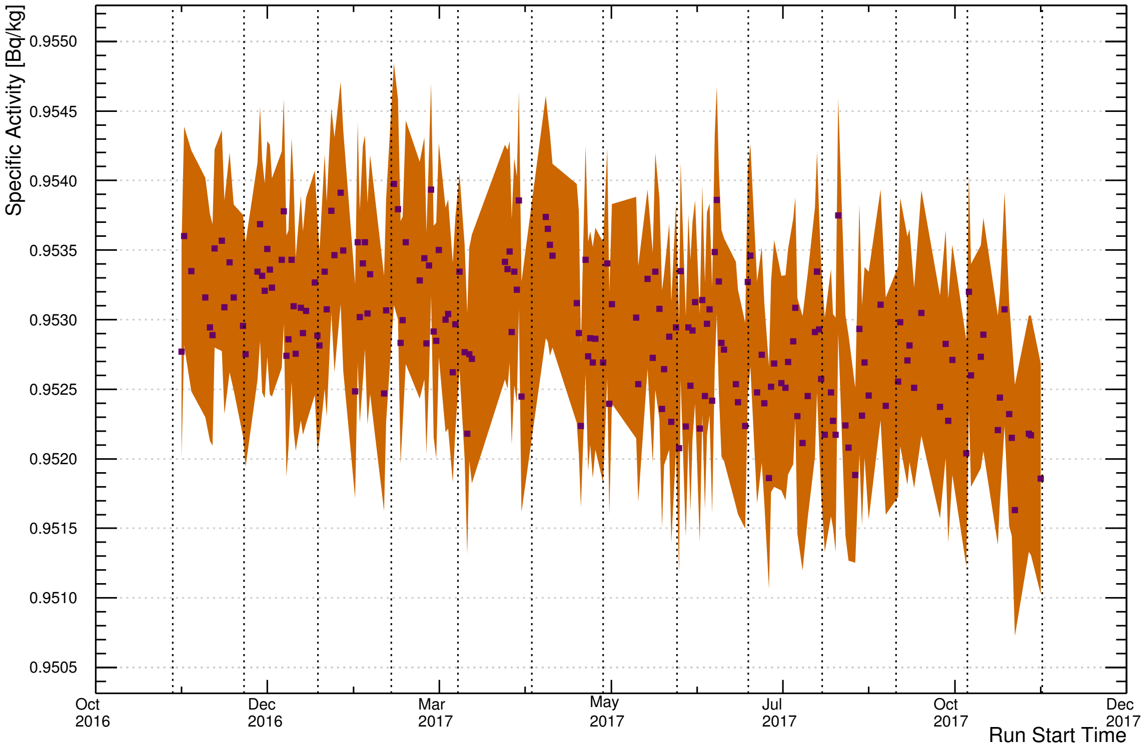

Figure 5.21: The specific activity measurements for each of the 185 runs in the data set are shown. The band shown is the 90% CI statistical fit uncertainty.

Fit Systematic Uncertainties
Specific Activity = $(0.953 \pm 0.028)\mathrm{Bq/kg}_{^{\mathrm{atm}}\mathrm{Ar}}$

Parameter	Fraction of Total Events [%]	% of Total Uncert.	Uncert. Contribution $[\mathrm{Bq/kg}_{^{\mathrm{atm}}\mathrm{Ar}}]$
Fit Uncertainty	0.0946	0.11	< 0.0001
Constant E-Scale (2_{min})	0.0093		
Constant E-Scale (2_{max})			
Linear E-Scale (2_{min})	0.068		
Linear E-Scale (2_{max})			
Quadratic E-Scale (2_{min})	0.0017		
Quadratic E-Scale (2_{max})			
Linear E-Res (2_{min})	0.0023		
Linear E-Res (2_{max})			

Other Systematic Uncertainties

Source	Uncertainty	% of Total Uncert.	Uncert. Contribution $[\mathrm{Bq/kg}_{^{\mathrm{atm}}\mathrm{Ar}}]$
LAr Mass	96 kg	96.76	0.0271
Pileup Event Correction	0.58%	3.09	0.0009
Theoretical Model	0.031%	0.04	< 0.0001
Livetime	0.23 s	$<< 0.1$	< 0.0001
Bin Width	Negligible		
Fit Range	Negligible		
Argon Age	Negligible		

Table 5.1: All systematic uncertainties for the ^{39}Ar specific activity fits. The pileup and theoretical model uncertainties are given as the ratio of the uncertainty to the fit normalisation. The maximum/minimum variation fits are not used in the uncertainty calculation, but rather are used as a simple check on the fit uncertainty.

5.1.4 ^{39}Ar Specific Activity and Atmospheric Concentration

For the one-year data set the specific activity is measured to be (0.953 ± 0.028) $\mathrm{Bq{\cdot}kg}^{-1}_{^{\mathrm{atm}}\mathrm{Ar}}$; this is the most precise measurement of the specific activity of ^{39}Ar in atmospheric argon ever made.

The isotopic concentration of ^{39}Ar in atmospheric argon can now be calculated with the measured specific activity and the known half-life. The specific activity of a pure sample of ^{39}Ar atoms is given by the following:

$$\mathrm{SA}_{(^{39}\mathrm{Ar})} = \frac{\mathrm{N_A} \cdot \ln(2)}{\mathrm{T}_{1/2} \cdot \mathrm{m}}, \tag{5.10}$$

where $\mathrm{N_A}$ is Avogadro's Number and m is the mass number of the isotope of interest. For ^{39}Ar, m = (38.964313 ± 0.000005) $\mathrm{g \cdot mol^{-1}}$ [74] and $\mathrm{T}_{1/2}$ = (269 ± 3) years [16]; based on these two values, the uncertainty on the specific activity of pure ^{39}Ar will be dominated by the half-life uncertainty. The specific activity of pure ^{39}Ar is then

$$\mathrm{SA}_{(^{39}\mathrm{Ar})} = 1.259 \times 10^{12}\ \mathrm{Bq} \cdot \mathrm{g}^{-1}_{^{39}\mathrm{Ar}}, \tag{5.11}$$

with uncertainty

$$\sigma_{\mathrm{SA}_{(^{39}\mathrm{Ar})}} = \left(\frac{3.388 \times 10^{14}\ \mathrm{g}^{-1}_{(^{39}\mathrm{Ar})} \cdot\ \mathrm{s}^{-1}}{\mathrm{T}^{2}_{1/2}\cdot} \right) \sigma_{\mathrm{T}_{1/2}} \tag{5.12}$$

$$= \pm 0.014 \times 10^{12}\ \mathrm{Bq} \cdot \mathrm{g}^{-1}_{^{39}\mathrm{Ar}}.$$

The isotopic concentration, C, is given by the following:

$$\mathrm{C} = \frac{\mathrm{SA}_{^{\mathrm{atm}}\mathrm{Ar}}}{\mathrm{SA}_{^{39}\mathrm{Ar}}}, \tag{5.13}$$

where $\mathrm{SA}_{^{\mathrm{atm}}\mathrm{Ar}}$ is the measured ^{39}Ar specific activity in atmospheric argon. The concentration of ^{39}Ar in atmospheric argon is (7.6 ± 0.2)x10^{-16} $\mathrm{g}_{^{39}\mathrm{Ar}}/\mathrm{g}_{^{\mathrm{atm}}\mathrm{Ar}}$.

5.2 Search for the Radiative Neutrinoless Double Electron Capture of ^{36}Ar

The results of the two methods used to search for this decay - the counting experiment and the fit to data - are presented in this section.

5.2.1 The Counting Experiment

A counting experiment to search for the neutrinoless double electron capture of ^{36}Ar has been performed, using the optimal ROI determined by the Monte Carlo tests (see Section 4.7.3). The ROI and sidebands are shown with data in Figure 5.22; the results of the counting experiment are compiled in Table 5.2.

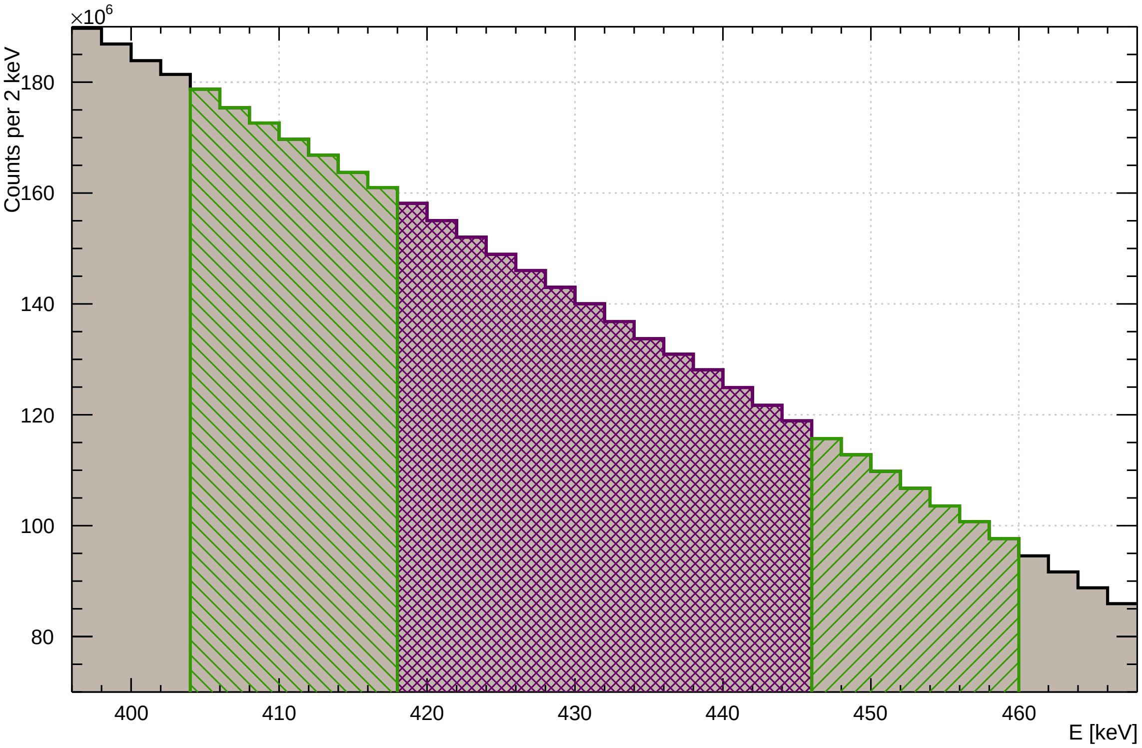

Figure 5.22: The optimal ROI is shown along with the sidebands used for the counting experiment. The ROI is 28 keV wide (in 14 bins) and centred as close as possible to the signal peak energy. The sidebands are each one-half the width of the ROI at 14 keV wide.

Figure 5.23 shows the ROI and sidebands overlayed with data for various ROI & sideband combinations.

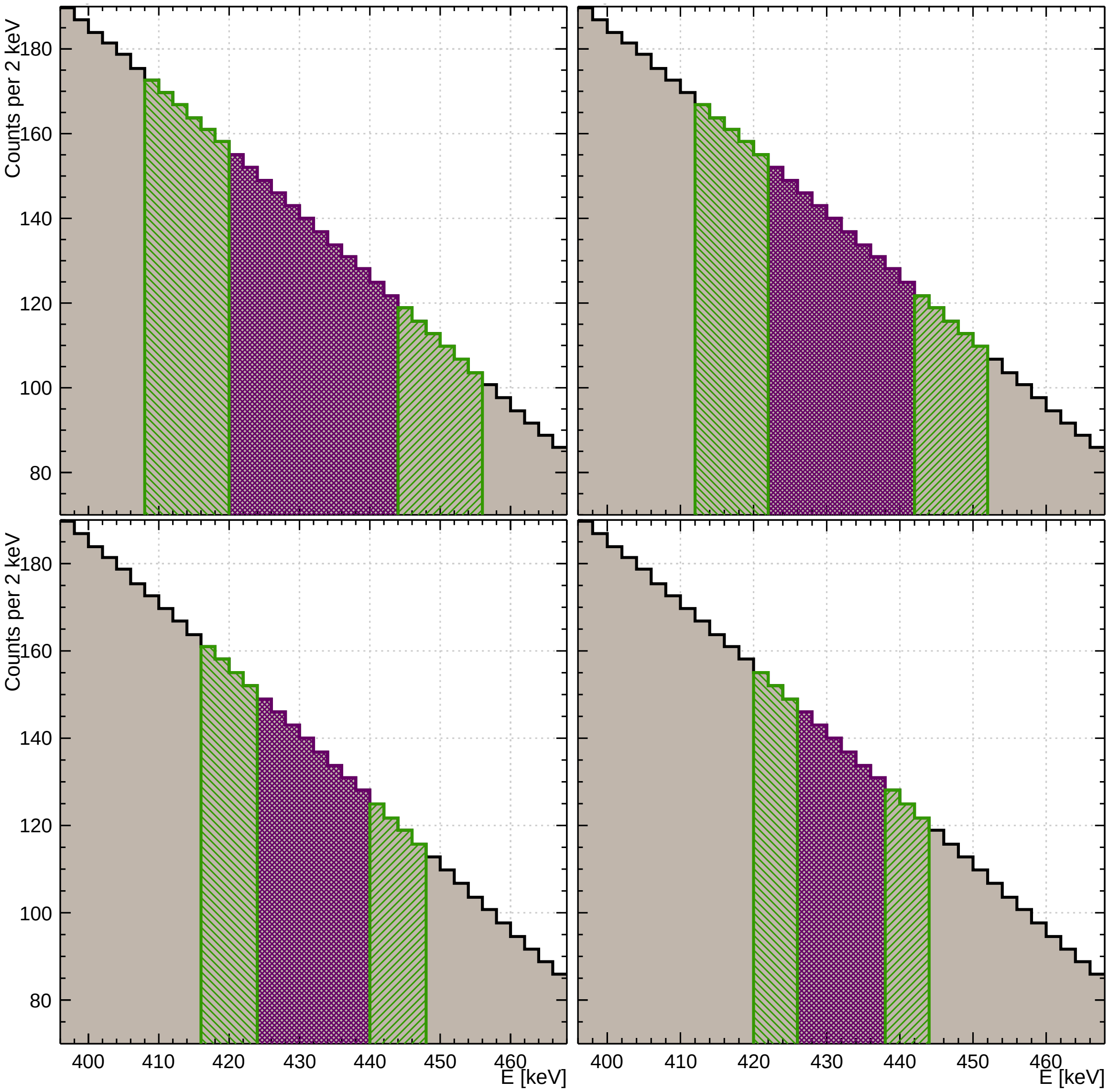

Figure 5.23: Top left, top right, bottom left, and bottom right: The ROI and sidebands are varied from the optimal values, with the ROI narrower by 4 keV and the sidebands narrower by 2 keV each for each iteration. They are numbered A1, A2, A3, and A4, respectively.

For each ROI/sideband combination in Figure 5.23 the counts from the sidebands and the ROI are given in Table 5.2.

Test	Left Band	Right Band	Estimated Background	ROI	Difference
Default	1,188,040,166	747,026,735	1,935,066,901 72,645	1,938,406,349	3,339,448 46
A1	992,059,223	667,534,623	1,659,593,846 67,253	1,661,344,448	1,750,602 26
A2	804,752,079	578,946,415	1,383,698,494 61,397	1,384,592,543	894,049 15
A3	626,225,882	481,257,731	1,107,483,612 54,913	1,107,628,002	144,390 3
A4	456,031,700	374,749,160	830,780,861 47,552	830,563,587	-217,274 -5

Table 5.2: Results of the ^{36}Ar counting experiment. The values listed are the counts in each region. The estimated background is the sum of the left and right sidebands; the second value in that column is the expected background fluctuation at 90% confidence ($1.65\sqrt{\#\text{ background}}$). The second number in the difference column is the ratio of the difference to the expected background variation.

An excess of events beyond the expected background fluctuation could normally indicate the presence of the signal one is searching for. However in this case it is more likely that the background is not perfectly linear and because the background is so large even small deviations from linear can correspond to many events. A simple check has been performed to verify the linearity of the background.

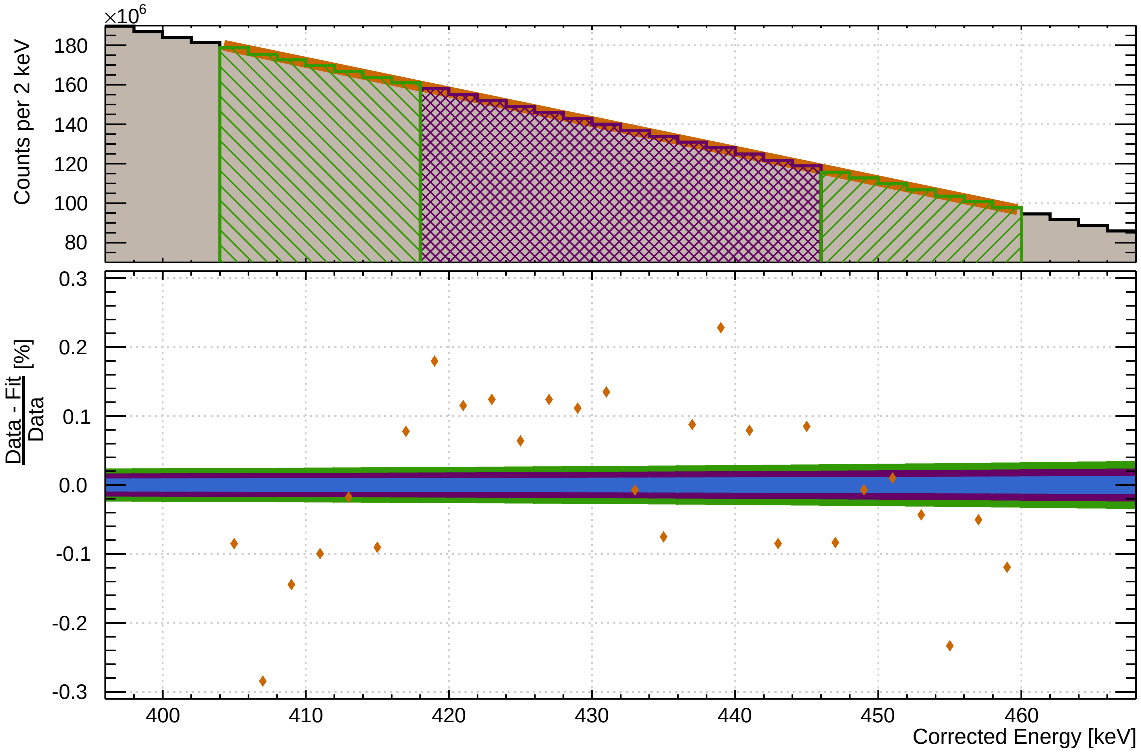

Figure 5.24: Top: A linear fit over the full search region including the sidebands, with the fit region highlighted in orange. Bottom: The per-bin residuals from the fit. In this plot the small discrepancies from linear are obvious. The coloured bands show the 1, 2, and 3σ intervals where σ is the square root of the counts in each bin.

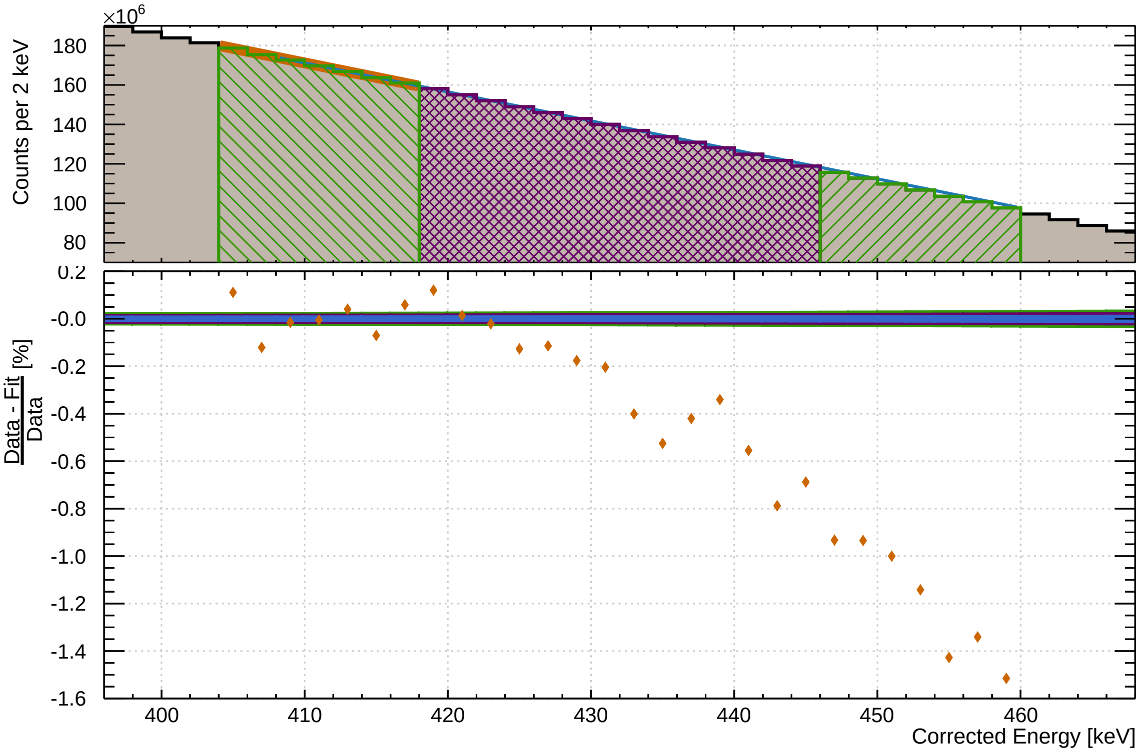

Figure 5.25: Top: A linear fit over the left sideband with the fit region highlighted in orange. Bottom: The per-bin residuals from the fit. In this plot the small discrepancies from linear are obvious. The coloured bands show the 1, 2, and 3σ intervals where σ is the square root of the counts in each bin.

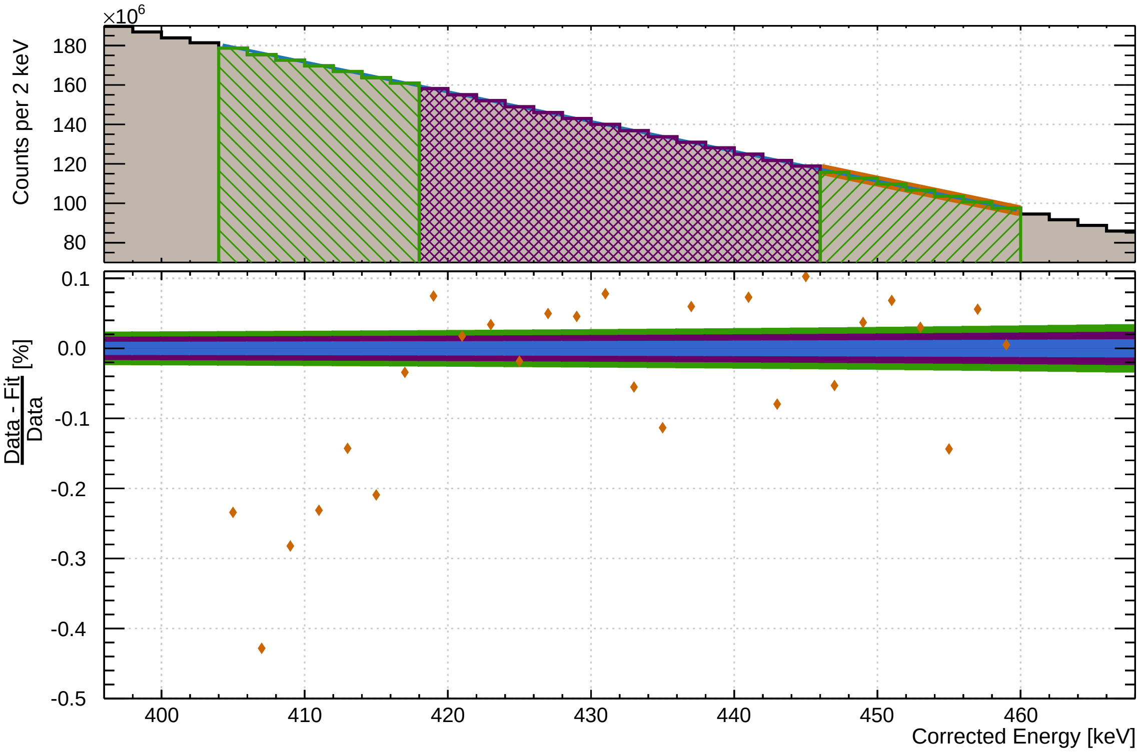

Figure 5.26: Top: A linear fit over the right sideband with the fit region highlighted in orange. Bottom: The per-bin residuals from the fit. In this plot the small discrepancies from linear are obvious. The coloured bands show the 1, 2, and 3σ intervals where σ is the square root of the counts in each bin.

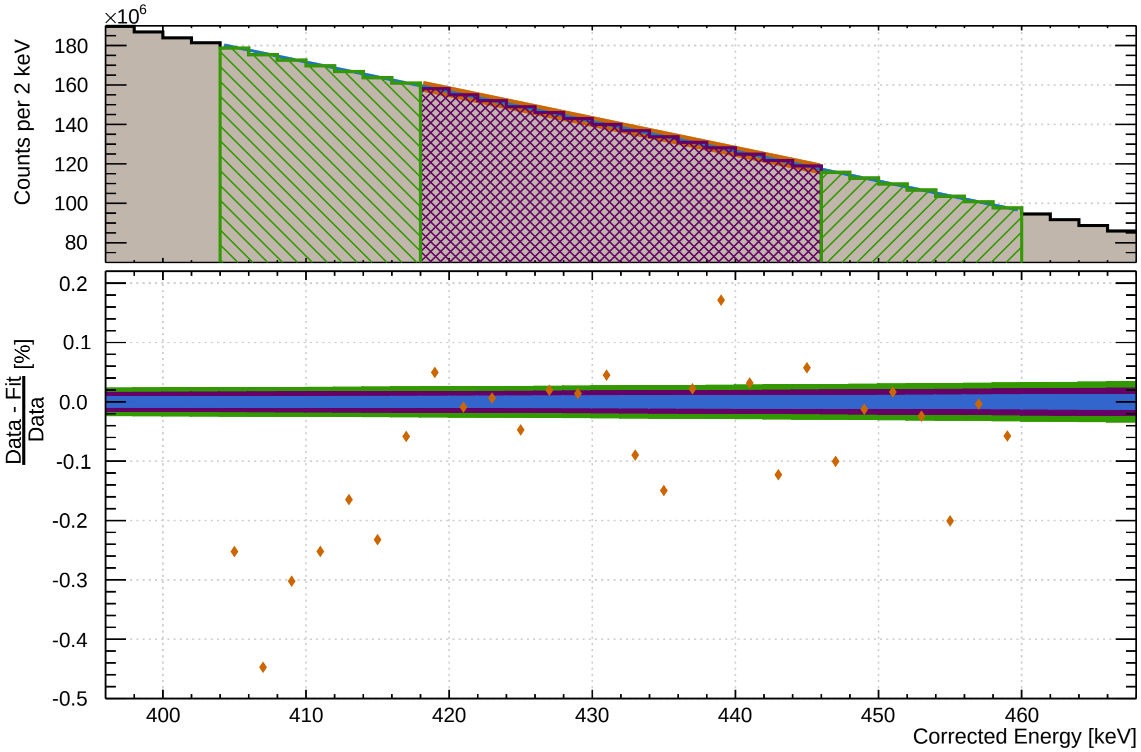

Figure 5.27: Top: A linear fit over the ROI with the fit region highlighted in orange. Bottom: The per-bin residuals from the fit. In this plot the small discrepancies from linear are obvious. The coloured bands show the 1, 2, and 3σ intervals where σ is the square root of the counts in each bin.

From these plots the deviations from a purely linear background become obvious; with residuals at about 1% or less one can see that the assumed linear model does not describe the data. Because of the very large background in the ^{36}Ar peak region it is concluded that with a counting experiment of this kind one is not able to make any claims about a half-life or half-life limit with any certainty.

5.2.2 Fit to Data

Several fits have been performed to search for this decay in the 247 day data set; the fits examine systematics by fixing either or both of the mean and width of the Gaussian peak model. The nominal fit lets both the peak mean and width float using Gaussian priors. The result of the nominal fit with all of the peak systematics included is shown in Figure 5.28. No signal is observed in any of the fits; for the nominal fit the lower limit on the half-life is measured to be $T_{1/2} > 4.8\text{x}10^{20}$ years at 90% CI.

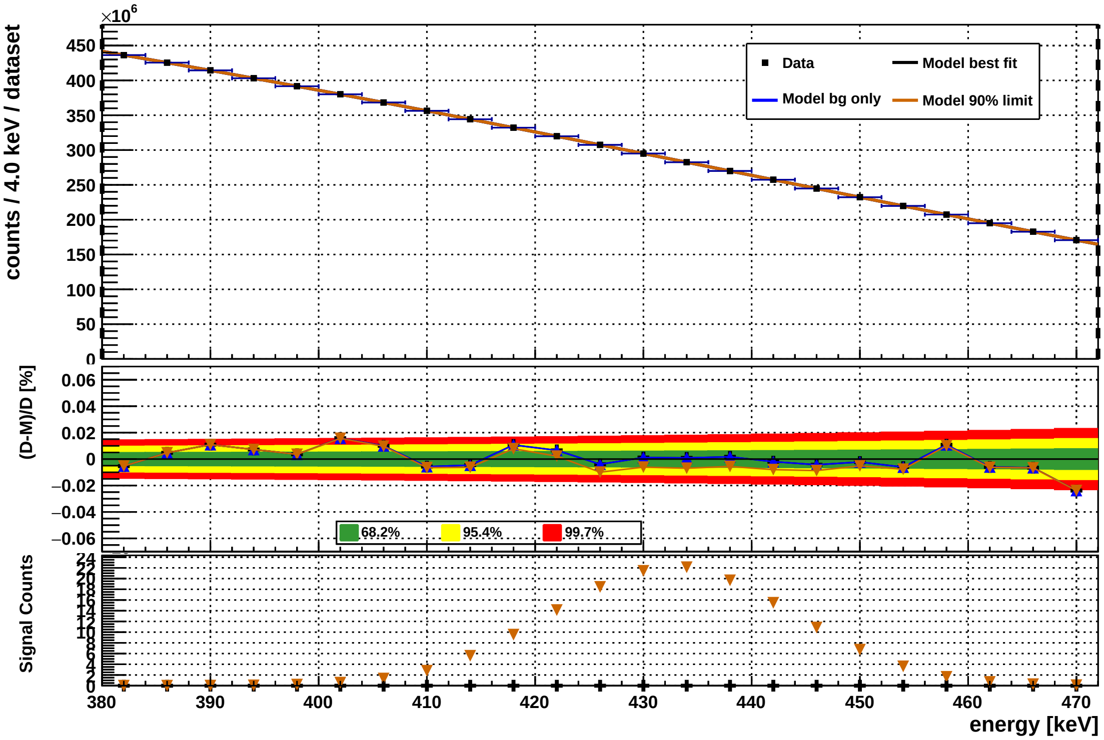

Figure 5.28: The nominal fit to data with all of the peak systematics included. The top panel shows the portion of the data spectrum on which the fit is performed. The middle panel shows the fit residuals along with 1, 2, and 3 σ bands. The bottom panel shows the estimated number of events in the region where the model best fit differs from the background only model.

Figure5.29 shows the knowledge update plots for the signal peak parameters in this fit. The inverse half-life fits a value of zero and so no signal is observed. Figure 5.30 shows the parameter correlations for all parameters in the fit.

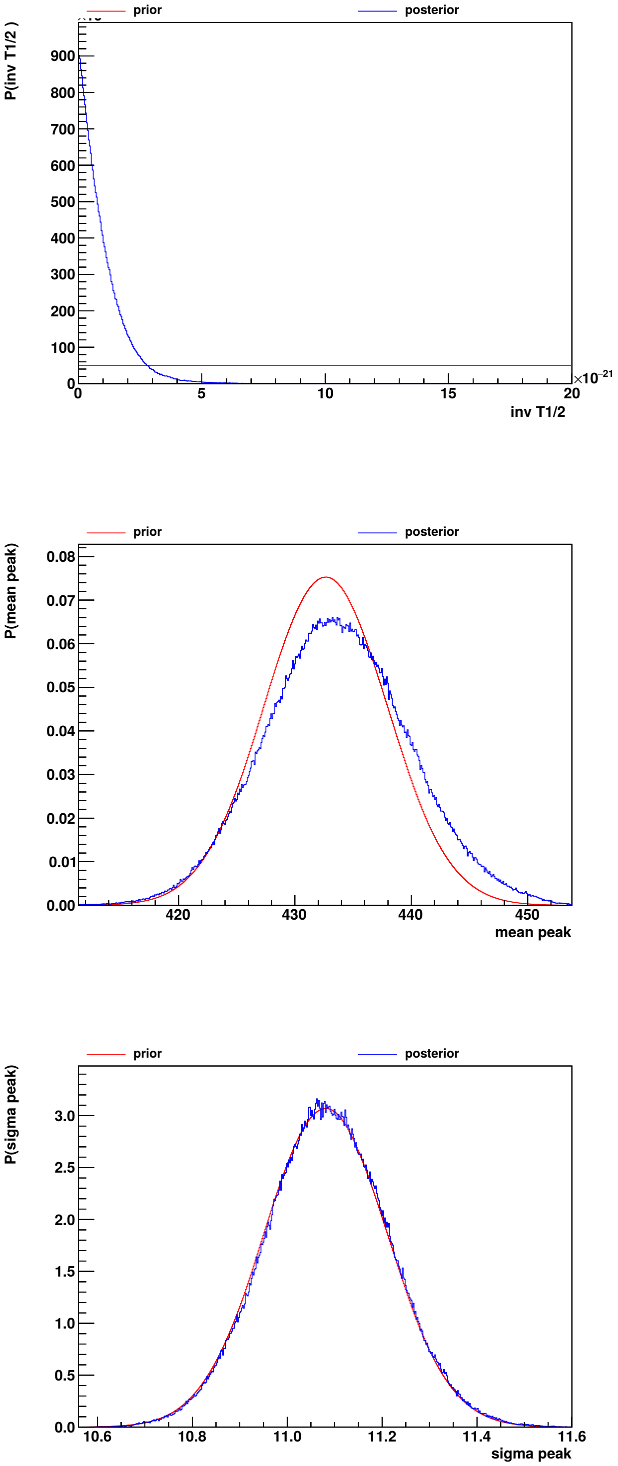

Figure 5.29: The knowledge update plots for the signal peak parameters in the ^{36}Ar fit. From the top down: The inverse half-life of the signal peak with a flat prior, the peak mean with a Gaussain fprior, and the peak width with a Gaussian prior.

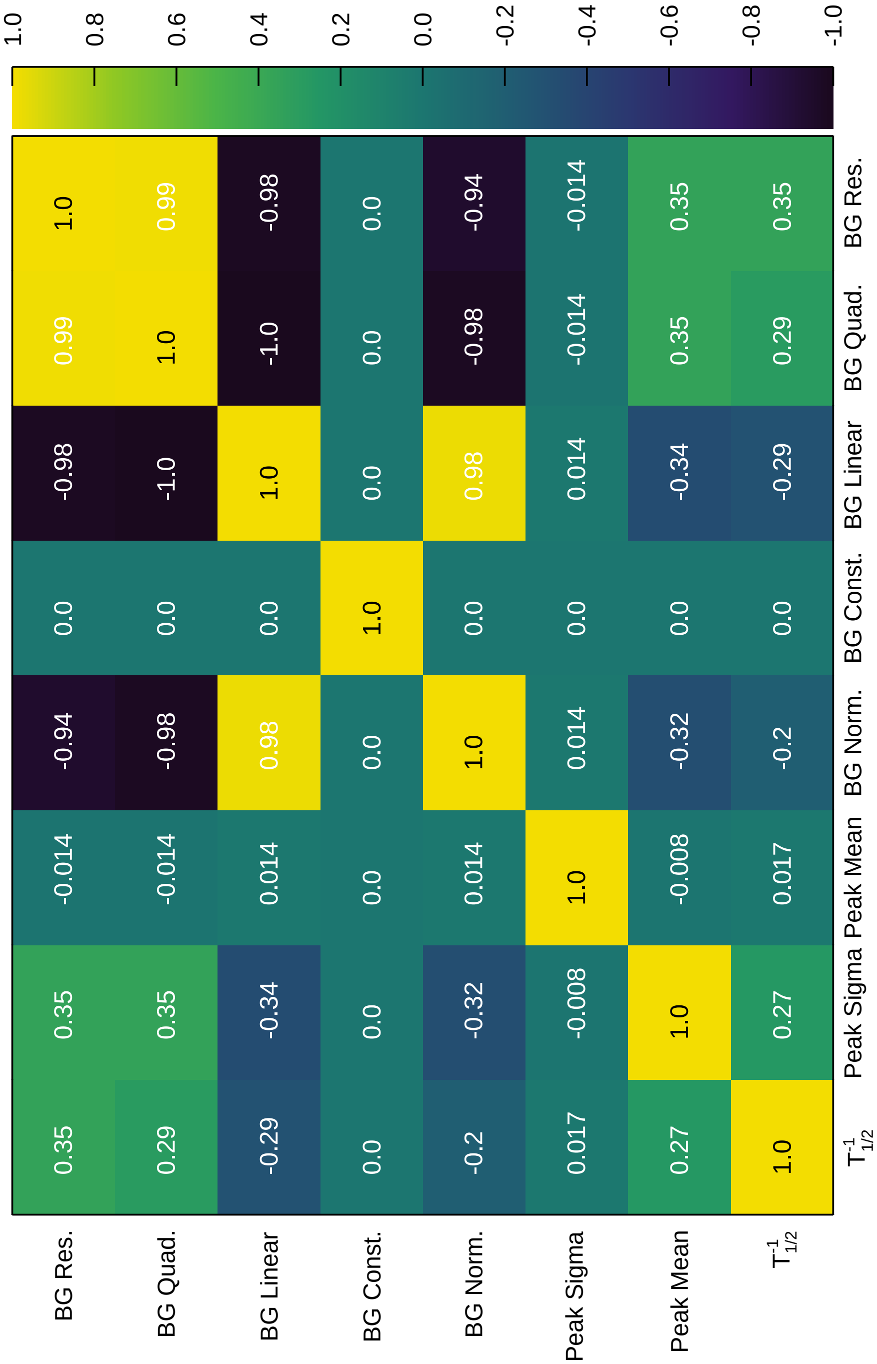

	BG Res.	BG Quad.	BG Linear	BG Const.	BG Norm.	Peak Mean	Peak Sigma	$T^{-1}_{1/2}$
BG Res.	1.0	0.99	-0.98	0.0	-0.94	-0.014	0.35	0.35
BG Quad.	0.99	1.0	-1.0	0.0	-0.98	-0.014	0.35	0.29
BG Linear	-0.98	-1.0	1.0	0.0	0.98	0.014	-0.34	-0.29
BG Const.	0.0	0.0	0.0	1.0	0.0	0.0	0.0	0.0
BG Norm.	-0.94	-0.98	0.98	0.0	1.0	0.014	-0.32	-0.2
Peak Sigma	-0.014	-0.014	0.014	0.0	0.014	1.0	-0.008	0.017
Peak Mean	0.35	0.35	-0.34	0.0	-0.32	-0.008	1.0	0.27
$T^{-1}_{1/2}$	0.35	0.29	-0.29	0.0	-0.2	0.017	0.27	1.0

Figure 5.30: Parameter correlations from the ^{36}Ar fits. From bottom left to bottom right the parameters are: BG Res. - background model resolution parameter, BG Quad. - background model quadratic energy parameter, BG Linear - background model linear energy parameter, BG Norm. - background model normalisation parameter, Peak Sigma - width of the Gaussian signal model, Peak Mean - mean of the Gaussian signal model, $T^{-1}_{1/2}$ - inverse half-life parameter.

When the peak mean or width (or both) are fixed the limit improves. The fit which removes the peak width systematic fixes the width to 11.1 keV. This fit is shown in Figure 5.31; no signal is observed and the lower limit on the half-life is measured to be $T_{1/2} > 4.71\text{x}10^{20}$ years, which is a weakening over the nominal value of about 1.5%. The fit which removes the peak mean systematic fixes the peak mean at 433 keV. This fit is shown in Figure 5.32; no signal is observed and the lower limit on the half-life is measured to be $T_{1/2} > 5.73\text{x}10^{20}$ years, which is an improvement over the nominal value of about 19.9% over the nominal fit. With both the peak mean and the width fixed to 433 keV and 11.1 keV, respectively, this limit improves though not as much as when only the peak systematic is removed. The fit is shown in Figure 5.33; again, no signal is observed and the lower limit on the half-life is measured to be $T_{1/2} > 5.68\text{x}10^{20}$ years. This is an improvement over the nominal value of about 18.8%. It is clear from these fits that the dominant systematic is the peak mean.

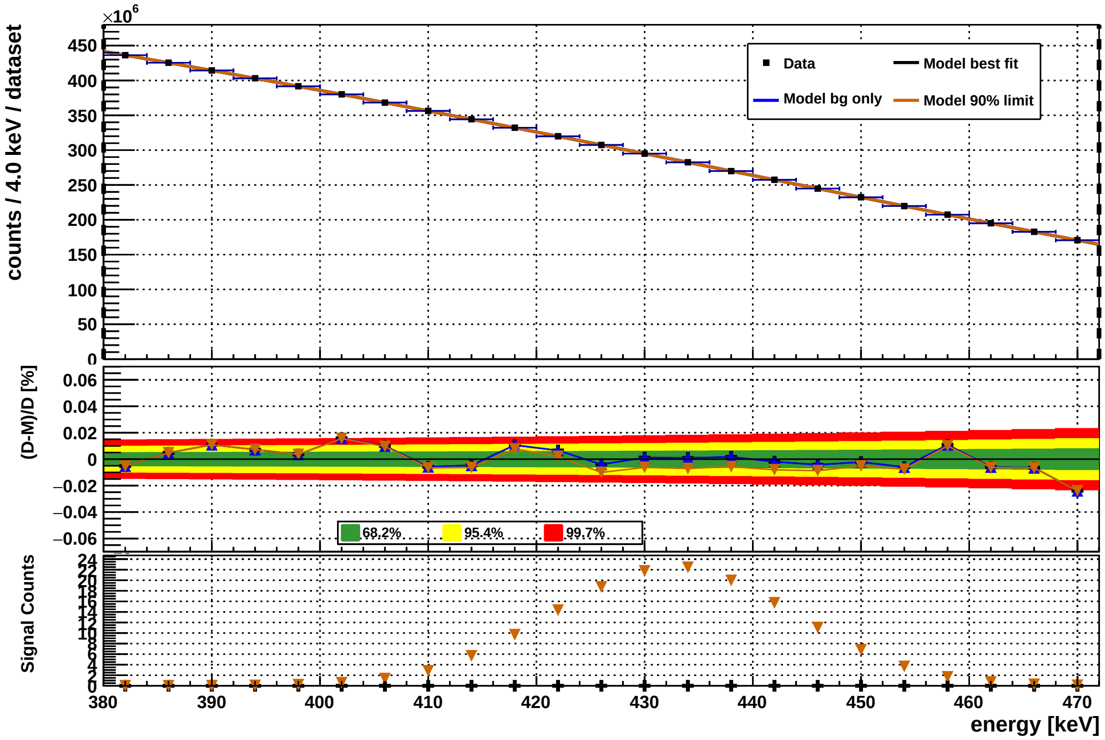

Figure 5.31: A test fit to data with just the peak mean systematic included; the peak width systematic is turned off by fixing the parameter. The top panel shows the portion of the data spectrum on which the fit is performed. The middle panel shows the fit residuals along with 1, 2, and 3 σ bands. The bottom panel shows the estimated number of events in the region where the model best fit differs from the background only model.

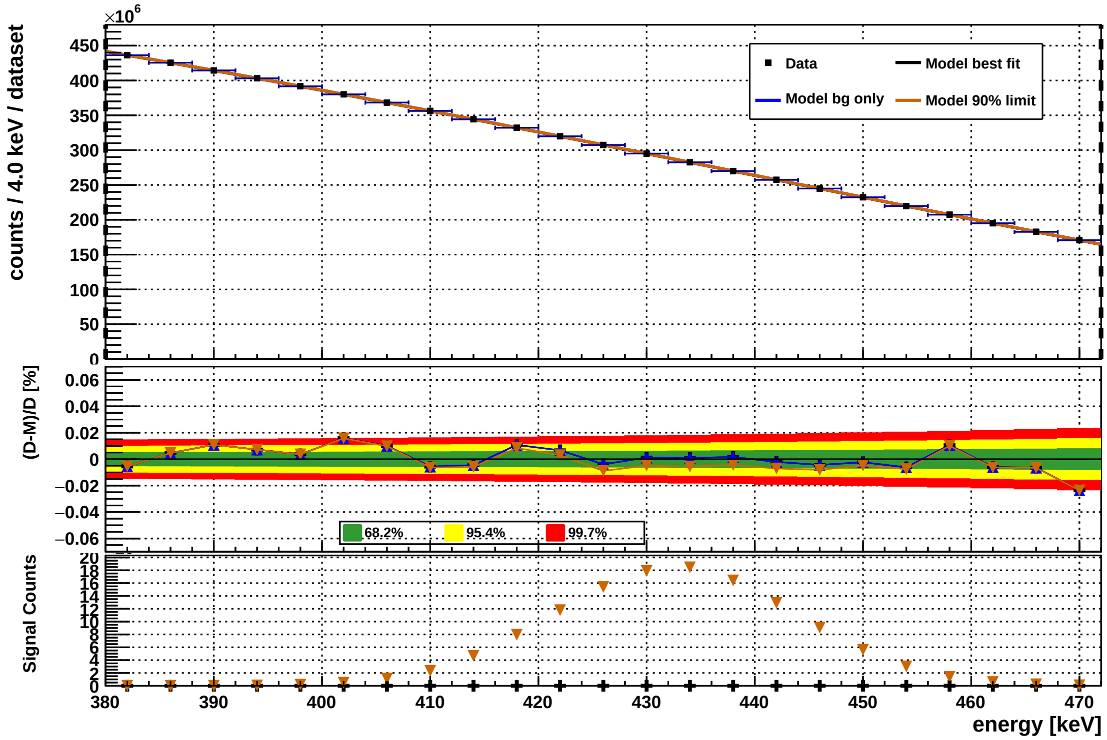

Figure 5.32: A test fit to data with just the peak width systematic included; the peak mean systematic is turned off by fixing the parameter. The top panel shows the portion of the data spectrum on which the fit is performed. The middle panel shows the fit residuals along with 1, 2, and 3 σ bands. The bottom panel shows the estimated number of events in the region where the model best fit differs from the background only model.

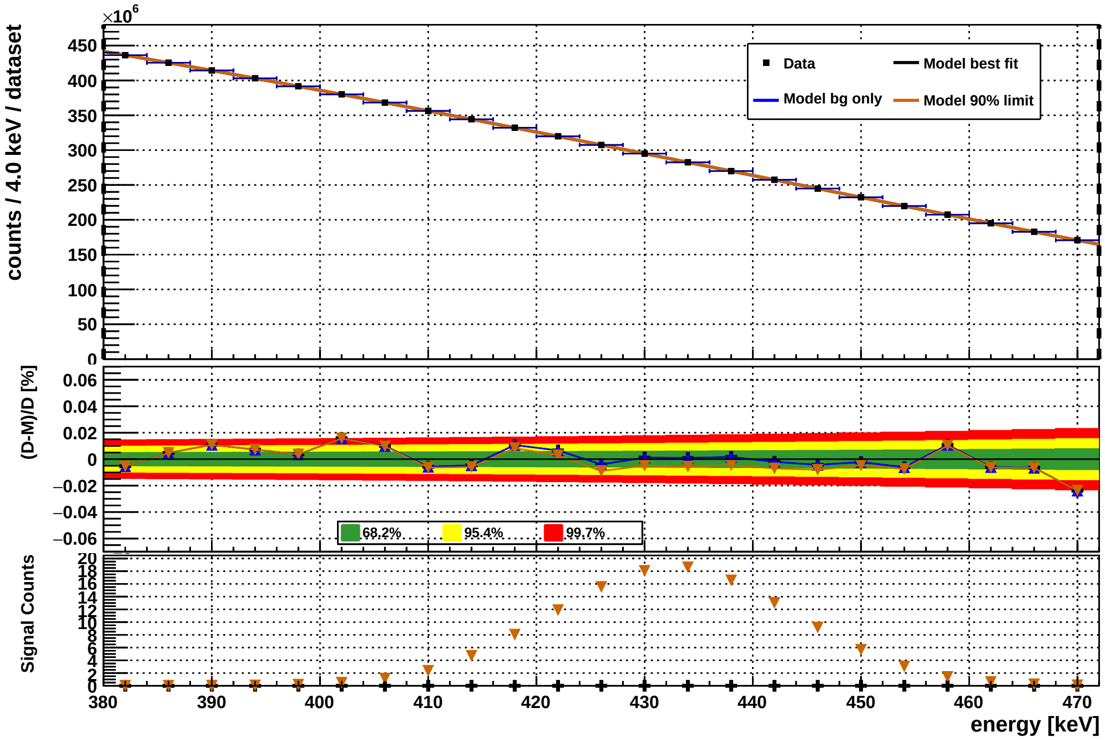

Figure 5.33: A test fit to data with both of the peak mean and width systematics turned off by fixing the parameters. The top panel shows the portion of the data spectrum on which the fit is performed. The middle panel shows the fit residuals along with 1, 2, and 3 σ bands. The bottom panel shows the estimated number of events in the region where the model best fit differs from the background only model.

Four additional test fits were performed to examine the stability of the half-life limit measurement. Two tests were performed in which the bin width was varied from the nominal width of 4 keV, and two tests where the the fit range is varied. For each of these fits the peak width and mean systematics are included. The first bin width test decreases the bin width to 2 keV. This fit is shown in Figure 5.34; no signal is observed and the lower limit on the half-life is measured to be $T_{1/2} > 5.06\text{x}10^{20}$ years, which is an improvement over the nominal value of 5.9%. The second bin width test double the bin width to 8 keV. This fit is shown in Figure 5.35; no signal is observed and the lower limit on the half-life is measured to be $T_{1/2} > 3.82\text{x}10^{20}$ years, which is a weakening of the half-life limit of 20.0% over the nominal value.

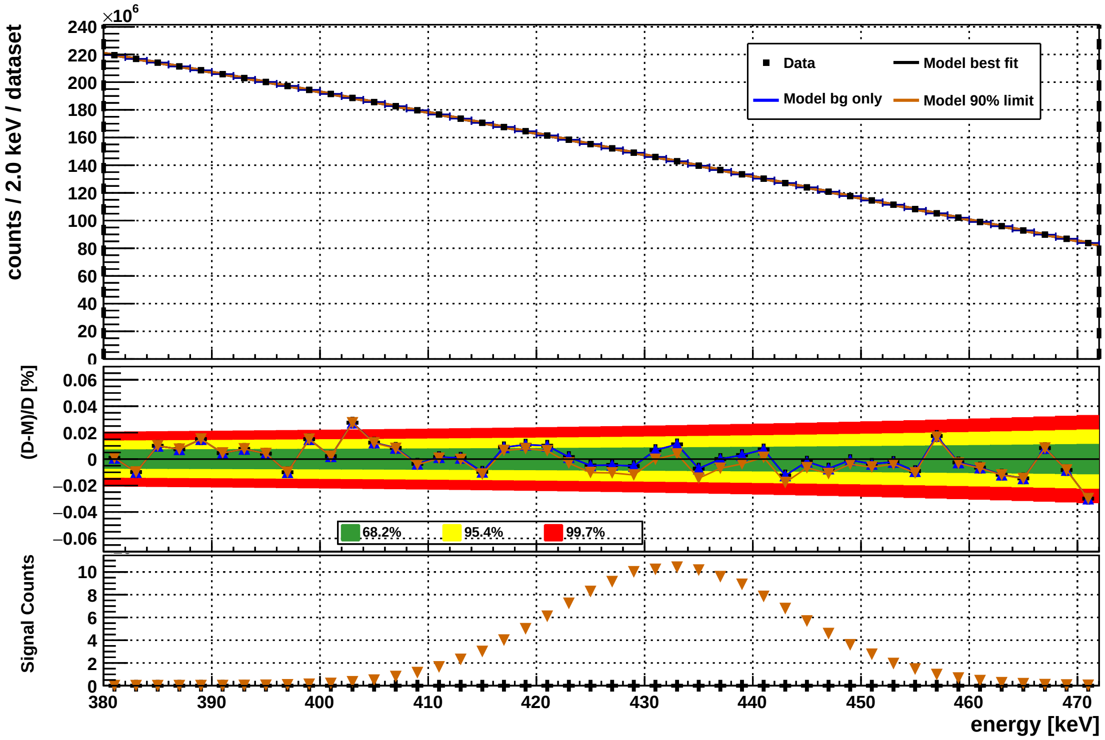

Figure 5.34: A test to examine systematics of the fit. In this plot the bin width is halved from the nominal value to 4 keV. The top panel shows the portion of the data spectrum on which the fit is performed. The middle panel shows the fit residuals along with 1, 2, and 3 σ bands. The bottom panel shows the estimated number of events in the region where the model best fit differs from the background only model.

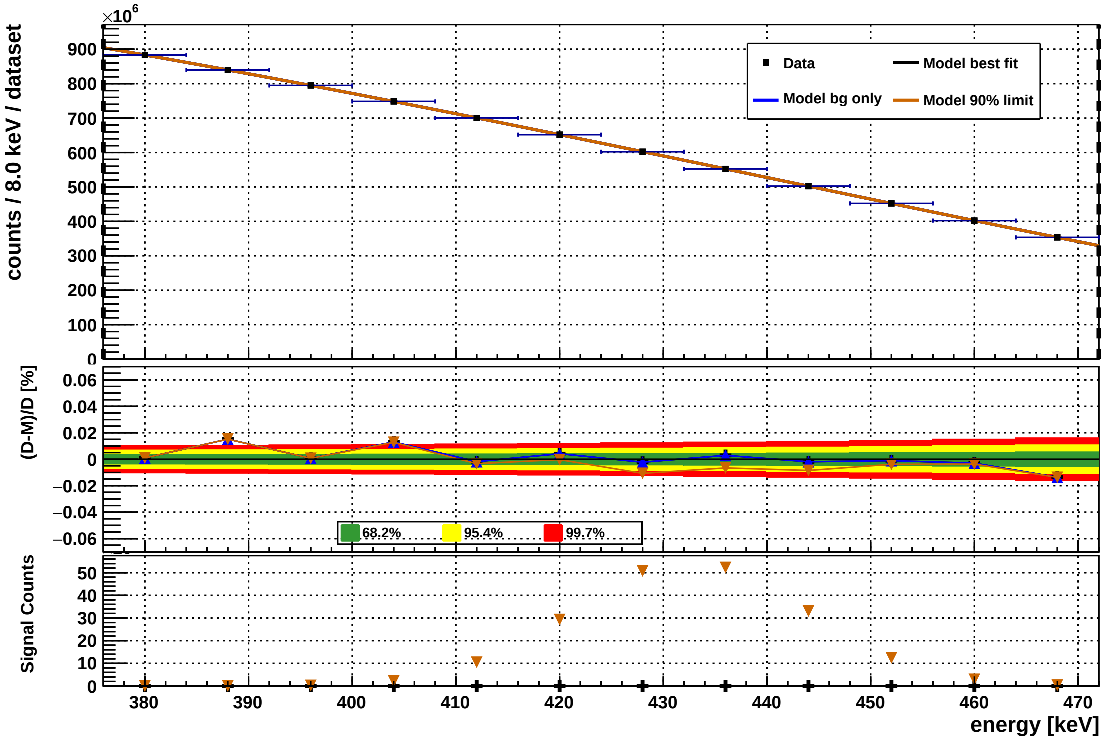

Figure 5.35: A test to examine systematics of the fit. In this plot the the bin width is doubled from the nominal value to 8 keV. The top panel shows the portion of the data spectrum on which the fit is performed. The middle panel shows the fit residuals along with 1, 2, and 3 σ bands. The bottom panel shows the estimated number of events in the region where the model best fit differs from the background only model.

For the first fit range test is increased from (380 - 470)keV to (370 - 480)keV. This fit is shown in Figure 5.36; no signal is observed and the half-life limit is measured to be $T_{1/2} > 9.79\text{x}10^{20}$ years, more than a factor of two improvement. The second test decreases the fit range to (390 - 460)keV. This fit is shown in Figure 5.37; no signal is observed and the half-life limits is measured to be $T_{1/2} > 2.48\text{x}10^{20}$ years. This limit is weaker than the nominal limit by more than half; the observed decrease here could be the result of removing outer portions of the peak region from the fit. The results of all of the fits are summarized in Table 5.3.

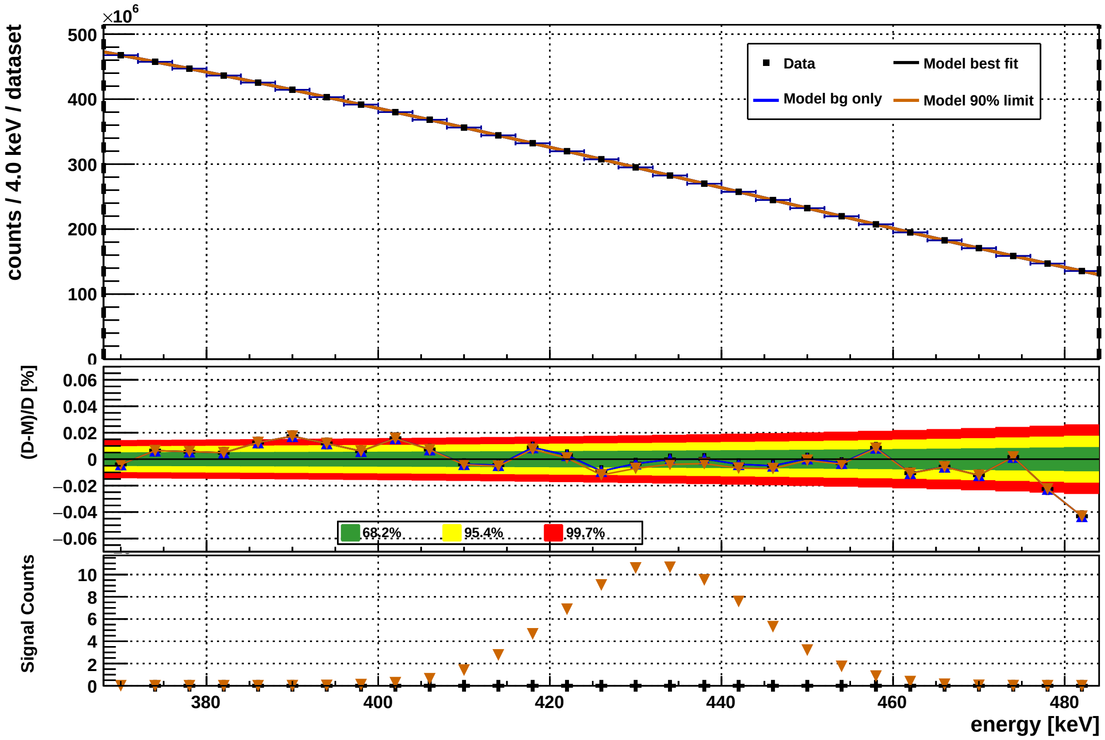

Figure 5.36: A test to examine systematics of the fit. In this plot the fit range is increased from the nominal range by 10 keV at both ends to (370 - 480)keV. The top panel shows the portion of the data spectrum on which the fit is performed. The middle panel shows the fit residuals along with 1, 2, and 3 σ bands. The bottom panel shows the estimated number of events in the region where the model best fit differs from the background only model.

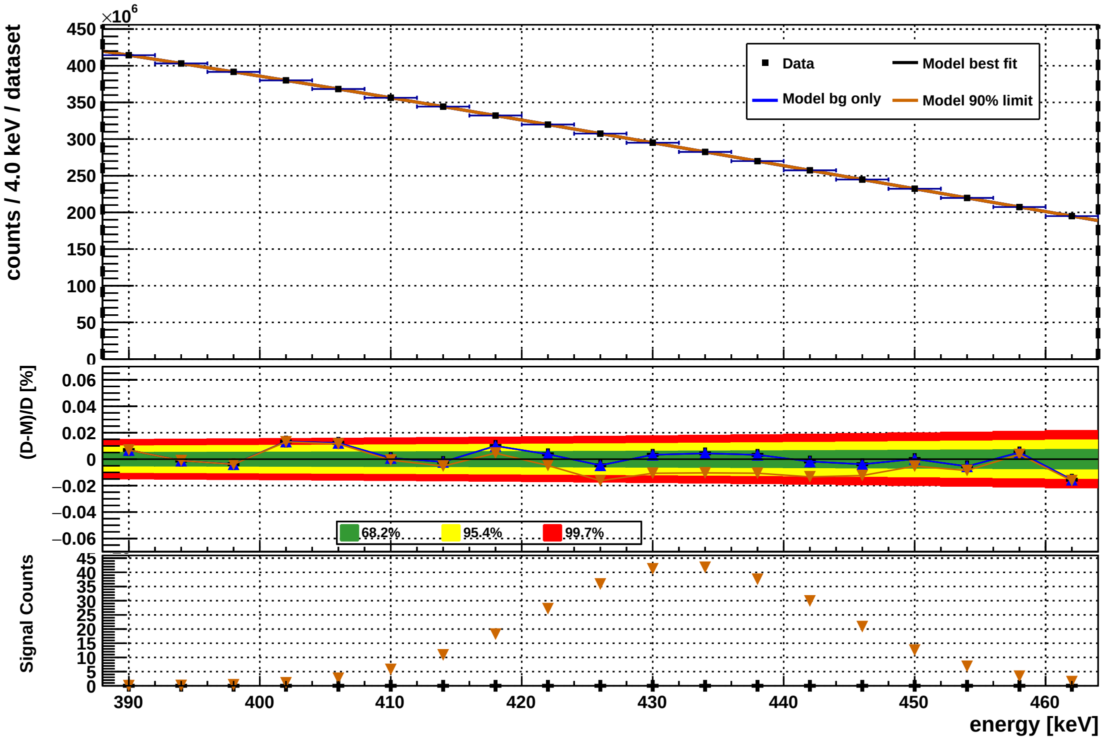

Figure 5.37: A test to examine systematics of the fit. In this plot the fit range is reduced from the nominal range by 10 keV at both ends to (390 - 460)keV. The top panel shows the portion of the data spectrum on which the fit is performed. The middle panel shows the fit residuals along with 1, 2, and 3 σ bands. The bottom panel shows the estimated number of events in the region where the model best fit differs from the background only model.

Fit Test	90% CI Half-life Limit [x10^{20} yr] IC Electron	Single Photon	Double Photon	From Fit	Fraction of Nominal Half-life
Nominal	4.8	3.90	3.76	4.8	1
No Mean Sys.	5.73	4.68	4.51	5.73	1.2
No Width Sys.	4.71	3.84	3.71	4.71	0.99
No Peak Sys.	5.67	4.63	4.47	5.68	1.2
2 keV Bins	5.05	4.13	3.98	5.06	1.1
8 keV Bins	3.82	3.12	3.01	3.82	0.80
Incr. Range	9.78	7.99	7.70	9.79	2.1
Decr. Range	2.48	2.02	1.95	2.48	0.52

Table 5.3: A summary of all fit results for the ^{36}Ar 0νECEC search. In the 'No Mean Sys.' and 'No Width Sys.' fits the systematic corresponding to the peak mean and width, respectively, are removed from the fit by fixing their value. In the 'No Peak Sys.' fit they are both removed from the fit. The bin width variation fits vary the width from the nominal value of 4 keV. The range variation fits vary the fit range by +10 keV and then by -10 keV at each bound from the nominal range of (380 - 470)keV. The IC Electron, Single Photon, and Double Photon columns correct the measured half-life for the signal detection efficiencies measured by MC of 99.9%, 81.6%, and 78.7%, respectively.

Chapter 6

Conclusions

The specific activity of ^{39}Ar has been measured to be (0.953 ± 0.028) Bq·kg$^{-1}_{\mathrm{^{atm}Ar}}$, corresponding to a concentration of (7.6 ± 0.2)x10^{-16}g$_{\mathrm{^{39}Ar}}$/g$_{\mathrm{^{atm}Ar}}$. This is the most precise measurement of the ^{39}Ar specific activity in atmospheric argon that exists and is in agreement with existing measurements by other groups. Existing measurements are compared to this work in Table 6.1.

Experiment	Specific Activity Bq·kg$^{-1}_{(\mathrm{^{atm}Ar})}$	^{39}Ar Concentration x10^{-16}g$_{\mathrm{^{39}Ar}}$/g$_{\mathrm{^{atm}Ar}}$
WArP (2007)	1.01 ± 0.10	8.0 ± 0.6
ArDM (2017)	0.95 ± 0.05	N/A
This work	0.953 ± 0.028	7.6 ± 0.2

Table 6.1: A comparison of existing ^{39}Ar specific activity measurements with this work. No concentration value is quoted by ArDM.

There are a few improvements that could be made for this measurement. First, as the uncertainty is dominated by the LAr mass uncertainty which is in turn dominated by the LAr fill level uncertainty, an improvement of the fill level measurement could be made. This could be achieved through a detailed MC study using different fill levels to characterize PMT rates when the PMTs are not submerged, partially submerged, and fully submerged. If the mass uncertainty could be reduced by a factor of 5 then it would be at roughly the level of the fit systematic uncertainties.

In DEAP-3600 the high rate of ^{39}Ar beta decays is dealt with in two ways; prescaling of the data in the ^{39}Ar spectrum region keeps the data rate reasonable and the space required for data storage minimized, while keeping enough of the spectrum that precise measurements can be made. For future, larger, argon-based low background experiments (such as WIMP searches) the ^{39}Ar may be significantly more challenging to deal with.

Sources of argon have been found underground that have substantially reduced concentrations of cosmogenically activated ^{39}Ar; the concentration is at least an order of magnitude lower than in atmospheric argon while still being comprised mainly of ^{40}Ar. The ^{39}Ar concentration in underground argon was initially measured to be $g_{^{39}\mathrm{Ar}}/g_{^{\mathrm{ug}}\mathrm{Ar}} <= 4\mathrm{x}10^{-17}$ [75], which is roughly 5% of the concentration in atmospheric argon. It has subsequently been measured to be even lower, having a concentration more than 100 times lower than that in atmospheric argon; the relative concentration is $g_{^{39}\mathrm{Ar}}/g_{^{\mathrm{ug}}\mathrm{Ar}} <= 0.0065(g_{^{39}\mathrm{Ar}}/g_{^{\mathrm{atm}}\mathrm{Ar}})$ [76]. While this could be a potential solution to the issue of ^{39}Ar, the cost of this argon is expected to be greater.

^{36}Ar is an isotope which can undergo the exotic decay process of double electron capture, and so could possibly undergo the more exotic decay process of neutrinoless double electron capture. A search for this decay has been performed by two methods. The first method to search for the decay was simple counting experiment; due to the extremely large ^{39}Ar-dominated background it has been determined that a counting experiment of this kind cannot be performed with the simple assumptions that have been used. The second method was a likelihood fit to the data using the Bayesian Analysis Toolkit based on Bayes' Theorem; no signal is observed in the fit and a lower limit on the half-life of ^{36}Ar is measured to be $T_{1/2} > 4.8\mathrm{x}10^{20}$ years at 90% CI.

One way to improve this measurement would be to improve the energy calibration.

Currently the calibration includes gamma peaks which are at much higher energies than the potential ^{36}Ar signal region and additionally includes points along the ^{39}Ar spectrum. The ^{39}Ar is not a good calibration source due to the broad spectrum, uncertainty in the endpoint energy, and pileup/ERB background contamination at the endpoint. A potential in-situ calibration source that has been proposed for DEAP-3600 is $^{83\mathrm{m}}$Kr, which could be injected into the LAr. The decay of this isotope would produce a monoenergetic peak at about 42 keV (roughly 320 PE). Including such a peak in the calibration would bracket the ^{36}Ar peak region and could improve the calibration and in turn improve DEAP-3600's sensitivity to this decay.

References

[1] P. A. R. Ade *et al.*, *Planck 2013 results. XVI. Cosmological parameters,* Astron. Astrophys. **571**, A16 (2014).

[2] C. L. Bennett *et al.*, *Nine-Year Wilkinson Microwave Anisotropy Probe (WMAP) Observations: Final Maps and Results,* Astrophys. J. Suppl. **208**, 20 (2013).

[3] K. Nakamura *et al.*, *Review of Particle Physics,* Journal of Physics G **37**, 179 (2010).

[4] E. Majorana, *Teoria simmetrica dellelettrone e del positrone,* Nuovo Cim. **14**, 171 (1937).

[5] F. Zwicky, *On the Masses of Nebulae and of Clusters of Nebulae,* Astrophys. J. **86**, 217 (1937).

[6] F. Zwicky, *On the Large Scale Distribution of Matter in the Universe,* Phys. Rev. **61**, 489 (1942).

[7] V. C. Rubin, W. K. Ford, Jr., and N. Thonnard, *Extended rotation curves of high-luminosity spiral galaxies. IV. Systematic dynamical properties, Sa through Sc,* Astrophys. J. **225**, L107 (1978).

[8] V. C. Rubin, N. Thonnard, and W. K. Ford, Jr., *Rotational properties of 21 SC galaxies with a large range of luminosities and radii, from NGC 4605 /R = 4kpc/ to UGC 2885 /R = 122 kpc/,* Astrophys. J. **238**, 471 (1980).

[9] V. C. Rubin, W. K. Ford, Jr., N. Thonnard, and D. Burstein, *Rotational properties of 23 SB galaxies,* Astrophys. J. **261**, 439 (1982).

[10] V. C. Rubin, D. Burstein, W. K. Ford, Jr., and N. Thonnard, *Rotation velocities of 16 SA galaxies and a comparison of Sa, Sb, and SC rotation properties,* Astrophys. J. **289**, 81 (1985).

[11] M. Markevitch *et al.*, *Direct constraints on the dark matter self-interaction cross-section from the merging galaxy cluster 1E0657-56,* Astrophys. J. **606**, 819 (2004).

[12] *Bullet cluster image, Chandra Observatory*, accessed online, 2006, http://chandra.harvard.edu/photo/2006/1e0657/1e0657_scale.jpg.

[13] D. Gastler *et al.*, *Measurement of scintillation efficiency for nuclear recoils in liquid argon,* Phys. Rev. **C85**, 065811 (2012).

[14] W. Creus *et al.*, *Scintillation efficiency of liquid argon in low energy neutron-argon scattering,* JINST **10**, P08002 (2015).

[15] P. Agnes *et al.*, *Measurement of the liquid argon energy response to nuclear and electronic recoils,* (ArXiv preprint 1801.06653, 2018).

[16] R. Stoenner, O. Schaeffer, and S. Katcoff, *Half-Lives of Argon-37, Argon-39, and Argon-42,* Science **148**, 1325 (1965).

[17] M. Wang *et al.*, *The Ame2012 atomic mass evaluation,* Chinese Physics C **36**, 1603 (2012).

[18] H. Behrens and J. Jänecke, *Special formulae for allowed, first forbidden, L-th non unique forbidden, and (L-1)-th-unique forbidden beta-decays*, 1969, springer-Verlag Berlin Heidelberg, Part of SpringerMaterials.

[19] J. Kostensalo, J. Suhonen, and K. Zuber, *Spectral shapes of forbidden argon β decays as background component for rare-event searches,* J. Phys. **G45**, 025202 (2018).

[20] J. Toivanen and J. Suhonen, *Microscopic quasiparticle-phonon description of odd-A Xe isotopes,* Journal of Physics G: Nuclear and Particle Physics **21**, 1491 (1995).

[21] P. Benetti *et al.*, *Measurement of the specific activity of ar-39 in natural argon,* Nucl. Instrum. Meth. **A574**, 83 (2007).

[22] J. Calvo *et al.*, *Backgrounds and pulse shape discrimination in the ArDM liquid argon TPC,* (ArXiv preprint 1712.01932, 2017).

[23] M. Doi and T. Kotani, *Neutrinoless modes of double beta decay,* Prog. Theor. Phys. **89**, 139 (1993).

[24] R. Mulliken, *Potential Curves of Diatomic Rare-Gas Molecules and Their Ions, with Particular Reference to* Xe_2*,* J. Chem. Phys. **52**, 5170 (1970).

[25] S. Kubota *et al.*, *Evidence of the existence of exciton states in liquid argon and exciton-enhanced ionization from xenon doping,* Phys. Rev. B **13**, 1649 (1976).

[26] T. Heindl *et al.*, *The scintillation of liquid argon,* Europhys. Lett. **91**, 62002 (2010).

[27] A. Hitachi *et al.*, *Effect of ionization density on the time dependence of luminescence from liquid argon and xenon,* Phys. Rev. B **27**, 5279 (1983).

[28] M. Roush, M. Wilson, and W. Hornyak, *Pulse shape discrimination,* Nuclear Instruments and Methods **31**, 112 (1964).

[29] P. A. Amaudruz *et al.*, *Measurement of the scintillation time spectra and pulse-shape discrimination of low-energy* β *and nuclear recoils in liquid argon with DEAP-1,* Astropart. Phys. **85**, 1 (2016).

[30] P. A. Amaudruz *et al.*, *Radon backgrounds in the DEAP-1 liquid argon based Dark Matter detector,* Astropart. Phys. **62**, 178 (2015).

[31] B. Aharmim *et al.*, *Measurement of the Cosmic Ray and Neutrino-Induced Muon Flux at the Sudbury Neutrino Observatory,* Phys. Rev. **D80**, 012001 (2009).

[32] *SNOLAB User's Handbook, rev. 2*, published online, 2006, http://snolab2008.snolab.ca/snolab_users_handbook_rev02.pdf.

[33] *Sudbury neutrino observatory proposal*, published online, 1987, http://www.iaea.org/inis/collection/NCLCollectionStore/_Public/21/016/21016751.pdf?r=1.

[34] G. T. Ewan, W. F. Davidson, and C. G. Hargrove, *The Sudbury Neutrino Observatory - an introduction,* Phys. Canada **48**, 112 (1992).

[35] R. L. Helmer, *Tau lepton physics. Proceedings, 6th International Workshop, TAU 2000, Victoria, Canada, September 18-21, 2000,* Nucl. Phys. Proc. Suppl. **98**, 157 (2001).

[36] Q. R. Ahmad *et al.*, *Measurement of the rate of* $\nu_e + d \rightarrow p + p + e^-$ *interactions produced by* ^8B *solar neutrinos at the Sudbury Neutrino Observatory,* Phys. Rev. Lett. **87**, 071301 (2001).

[37] Q. R. Ahmad *et al.*, *Direct evidence for neutrino flavor transformation from neutral current interactions in the Sudbury Neutrino Observatory,* Phys. Rev. Lett. **89**, 011301 (2002).

[38] S. N. Ahmed *et al.*, *Measurement of the total active B-8 solar neutrino flux at the Sudbury Neutrino Observatory with enhanced neutral current sensitivity,* Phys. Rev. Lett. **92**, 181301 (2004).

[39] B. Aharmim *et al.*, *Combined Analysis of all Three Phases of Solar Neutrino Data from the Sudbury Neutrino Observatory,* Phys. Rev. **C88**, 025501 (2013).

[40] *Metamorphosis in the particle world*, online press release, 2015, https://www.nobelprize.org/nobel_prizes/physics/laureates/2015/press.html.

[41] *Photomultiplier Tube 5912 Datasheet*, 1998, hamamatsu Photonics K.K.

[42] P. A. Amaudruz *et al.*, *Design and Construction of the DEAP-3600 Dark Matter Detector,* Submitted to: Astropart. Phys. (2017).

[43] M. Bodmer *et al.*, *Measurement of Optical Attenuation in Acrylic Light Guides for a Dark Matter Detector,* JINST **9**, P02002 (2014).

[44] B. Littlejohn *et al.*, *UV Degradation of the Optical Properties of Acrylic for Neutrino and Dark Matter Experiments,* JINST **4**, T09001 (2009).

[45] C. M. Nantais, Master's thesis, Queen's University, 2014.

[46] J. E. Bonatt, Master's thesis, Queen's University, 2017.

[47] *National Nuclear Data Centre, Brookhaven National Laboratory*, online, http://www.nndc.bnl.gov/nudat2/, accessed July 25, 2017.

[48] *Argon*, online, http://www.rsc.org/periodic-table/element/18/argon.

[49] V. M. Gehman *et al.*, *Fluorescence Efficiency and Visible Re-emission Spectrum of Tetraphenyl Butadiene Films at Extreme Ultraviolet Wavelengths,* Nucl. Instrum. Meth. **A654**, 116 (2011).

[50] P. Giampa, *Proceedings, 6th Topical Workshop on Low Radioactivity Techniques (LRT 2017): Seoul, Korea, May 24-26, 2017,* AIP Conf. Proc. **1921**, 070005 (2018).

[51] B. Broerman *et al.*, *Application of the TPB Wavelength Shifter to the DEAP-3600 Spherical Acrylic Vessel Inner Surface,* JINST **12**, P04017 (2017).

[52] R. Francini *et al.*, *VUV-Vis optical characterization of Tetraphenyl-butadiene films on glass and specular reflector substrates from room to liquid Argon temperature,* (ArXiv preprint 1304.6117, 2013).

[53] *Photomultiplier Tubes: Basics and Applications, Third Edition, 2007*, online, https://www.hamamatsu.com/resources/pdf/etd/PMT_handbook_v3aE.pdf, accessed July 30, 2017.

[54] M. D. Lay and M. J. Lyon, *An experimental and Monte Carlo investigation of the R1408 Hamamatsu 8-inch photomultiplier tube and associated concentrator to be used in the Sudbury Neutrino Observatory,* Nucl. Instrum. Meth. **A383**, 495 (1996).

[55] F. Halzen, *Topics in astroparticle and underground physics. Proceedings, 5th International Workshop, TAUP'97, Gran Sasso, Italy, September 7-11, 1997,* Nucl. Phys. Proc. Suppl. **70**, 409 (1998), [AIP Conf. Proc.433,no.1,265(1998)].

[56] I. M. Frank and I. E. Tamm, *Coherent visible radiation of fast electrons passing through matter,* Compt. Rend. Acad. Sci. URSS **14**, 109 (1937), [Usp. Fiz. Nauk93,no.2,388(1967)].

[57] D. Mei and A. Hime, *Muon-induced background study for underground laboratories,* Phys. Rev. **D73**, 053004 (2006).

[58] 2017, internal DEAP document.

[59] T. Lindner, *Proceedings, 21st International Conference on Computing in High Energy and Nuclear Physics (CHEP 2015): Okinawa, Japan, April 13-17, 2015,* J. Phys. Conf. Ser. **664**, 082026 (2015).

[60] *NIST eStar*, online, https://physics.nist.gov/PhysRefData/Star/Text/ESTAR.html.

[61] *Information Notice No. 83-16: Contamination of the Auburn Steel Company Property with Cobalt-60*, online, https://www.nrc.gov/reading-rm/doc-collections/gen-comm/info-notices/1983/in83016.html.

[62] *IAEA Bulletin: Lessons Learned the Hard Way*, online, https://web.archive.org/web/20100718065554/http://www.iaea.org/ Publications/Magazines/Bulletin/Bull472/htmls/lessons_learned.html.

[63] R. Acciarri *et al.*, *Effects of Nitrogen contamination in liquid Argon,* JINST **5**, P06003 (2010).

[64] R. Acciarri *et al.*, *Proceedings, 11th Topical Seminar on Innovative Particle and Radiation Detectors (IPRD08): Siena, Italy,* Nucl. Phys. Proc. Suppl. **197**, 70 (1-4 October 2008), [Nucl. Instrum. Meth.607,169(2009)].

[65] B. J. P. Jones *et al.*, *A Measurement of the Absorption of Liquid Argon Scintillation Light by Dissolved Nitrogen at the Part-Per-Million Level,* Journal of Instrumentation 8 **7**, (2013).

[66] P. A. Amaudruz *et al.*, *First results from the DEAP-3600 dark matter search with argon at SNOLAB,* (ArXiv preprint 1707.08042, 2017).

[67] *Thermophysical Properties of Argon*, online, http://webbook.nist.gov/cgi/fluid.cgi?ID=C7440371&Action=Page, accessed February 28, 2017.

[68] P. A. Amaudruz *et al.*, *In-situ characterization of the Hamamatsu R5912-HQE photomultiplier tubes used in the DEAP-3600 experiment,* (ArXiv preprint 1705.10183, 2017).

[69] B. Lehnert, *Private communication, DEAP collaboration,* (2017).

[70] A. Caldwell, D. Kollar, and K. Kroninger, *BAT: The Bayesian Analysis Toolkit,* Comput. Phys. Commun. **180**, 2197 (2009).

[71] R. Bayes, *An essay toward solving a problem in the doctrine of chances,* Phil. Trans. Roy. Soc. Lond. **53**, 370 (1764).

[72] M. Burghardt, *Private communication, DEAP collaboration,* (2017).

[73] B. Lehnert, *Private communication, DEAP collaboration,* (2017).

[74] S. I. Sukhoruchkin and Z. N. Soroko, *Atomic Mass and Nuclear Binding Energy for Ar-39 (Argon),* Landolt Börnstein 1214 (2009).

[75] D. Acosta-Kane *et al.*, *Topics in astroparticle and underground physics. Proceedings, 10th International Conference, TAUP 2007, Sendai, Japan, September 11-15, 2007,* Nucl. Instrum. Meth. **A587**, 46 (2008), [J. Phys. Conf. Ser.120,042015(2008)].

[76] J. Xu *et al.*, *A Study of the Residual* ^{39}*Ar Content in Argon from Underground Sources,* Astropart. Phys. **66**, 53 (2015).

Appendix A

Natural Decay Chains: Gamma Backgrounds in DEAP-3600

This section lists the gamma backgrounds from the natural decay chain nuclides present in both the PMT glass and in the AV acrylic. Gammas that could be backgrounds to the ^{36}Ar 0νECEC decay are listed seperately from other prominent gammas. For the ^{36}Ar 0νECEC backgrounds, gammas with an intensity greater than 0.01% are listed. For all other gammas a minimum intensity of 5% is chosen as a lower limit. Three decay chains are listed - ^{232}Th, ^{238}U, and ^{235}U - in Tables A.1, A.2, and A.3, respectively.

Isotope	Energy [keV]	Intensity [%]	Gammas per 10^8 ^{232}Th Decays
Possible ^{36}Ar 0νECEC Backgrounds			
^{228}Ac	409.46	1.92	$1.92\text{x}10^6$
	440.44	0.121	$1.21\text{x}10^5$
	463.00	4.40	$4.40\text{x}10^6$
^{212}Pb	415.2	0.013	1.31x104
^{212}Bi	433.7	0.017	$1.7\text{x}10^4$
	452.98	0.363	$3.63\text{x}10^6$
	473.0	0.050	$5.0\text{x}10^4$
^{208}Tl	485.95	0.049	$4.9\text{x}10^4$
Other Prominent Gammas			
^{228}Ac	338.32	11.27	$1.127\text{x}10^7$
	911.20	25.8	$2.58\text{x}10^7$
	968.97	15.8	$1.58\text{x}10^7$
^{212}Pb	238.63	43.6	$4.36\text{x}10^7$
^{212}Bi$_\beta$	727.33	6.67	$4.27\text{x}10^6$
^{208}Tl	277.37	6.6	$2.37\text{x}10^6$
	510.77	22.60	$8.12\text{x}10^6$
	583.19	85.0	$3.055\text{x}10^7$
	860.56	12.50	$4.49\text{x}10^6$
	2614.51	99.754	$3.585\text{x}10^7$

Table A.1: Gammas from the ^{232}Th decay chain. A schematic of the decay chain is shown in Figure 3.13

Isotope	Energy [keV]	Intensity [%]	Gammas per 10^8 ^{238}U Decays
Possible ^{36}Ar 0νECEC Backgrounds			
^{214}Pb	462.02	0.212	2.12x10^5
	480.43	0.337	3.37x10^5
	487.14	0.432	4.32x10^5
^{214}Bi$_\beta$	386.78	0.295	2.95x10^5
	388.89	0.402	4.02x10^5
	394.05	0.013	1.3x10^4
	396.02	0.026	2.60x10^4
	405.72	0.169	1.69x10^5
	452.92	0.030	3.0x10^4
	454.79	0.292	2.92x10^5
	461.08	0.051	5.1x10^4
	469.77	0.132	1.32x10^5
	474.44	0.099	9.9x10^4
	485.92	0.022	2.2x10^4
	487.95	0.028	2.8x10^4
^{210}Tl	480	2.0	400
^{210}Bi$_\beta$	368.9	0.66	6.6x10^5
^{206}Tl	453.3	93	123
	457.2	22	29
Other Prominent Gammas			
^{214}Pb	241.995	7.25	7.25x10^6
	295.223	18.42	1.842x10^7
	351.923	35.60	3.56x10^7
^{214}Bi$_\beta$	609.320	45.49	4.549x10^7
	1120.294	14.92	1.492x10^7
	1238.122	5.834	5.834x10^6
	1764.491	15.30	1.530x10^7
^{210}Tl	296	79	1.58x10^4
	799.6	98.96	1.979x10^4
	860	6.9	1.38x10^3

	1070	12	2.4x10^3
	1110	6.9	1.38x10^3
	1210	17	3.4x10^3
	1316	21	4.2x10^3
	2010	6.9	1.38x10^3
	2360	8	1.6x10^3
	2430	9	1.8x10^3
	216.4	74	98
	247.2	8.4	11
	265.7	86	113
	564.2	5.5	7
	686.5	91	120
^{206}Tl	1021.5	69	91
	1139.9	5.9	4

Table A.2: Gammas from the ^{238}U decay chain. A schematic of the decay chain is shown in Figure 3.14

Isotope	Energy [keV]	Intensity [%]	Gammas per 10^8 ^{235}U Decays
Possible ^{36}Ar 0νECEC Backgrounds			
^{235}U	387	0.040	4.0x10^4
^{231}Pa	379.35	0.050	5.0x10^4
	407.806	0.036	3.6x10^6
^{227}Th	362.63	0.051	5.03x10^4
	383.51	0.025	2.47x10^6
^{223}Fr	369.38	0.099	9.9x10^4
^{223}Ra	362.05	0.046	4.54x10^4
	362.9	0.015	1.48x10^4
	371.676	0.487	4.80x10^5
	372.9	0.05	4.93x10^4
	376.1	0.013	1.28x10^4
	382.8	0.014	1.38x10^4
	430.6	0.019	1.87x10^4
	432.12	0.035	3.45x10^4
^{219}Rn	401.81	6.6	6.6x10^6
^{215}Bi	419.1	20.0	15
^{211}Pb	362.07	0.043	4.3x10^4
	404.85	3.78	3.78x10^6
	427.09	1.76	1.76x10^6
Other Prominent Gammas			
^{235}U	143.76	10.96	1.096x10^7
	185.715	57.0	5.70x10^7
	205.316	5.02	5.02x10^6
^{231}Th	84.214	6.6	6.6x10^6
^{231}Pa	27.36	10.5	1.05x10^7
^{227}Th	50.13	8.4	8.28x10^6
	235.96	12.9	12.7x10^7
^{223}Fr$_\beta$	50.09	34	28
	79.651	8.7	7
^{223}Ra	81.069	15.0	1.50x10^6
	83.787	24.7	2.47x10^7
	94.868	5.69	5.69x10^6

	154.208	5.70	5.70x10^{6}
	269.463	13.9	1.39x10^{7}
^{219}Rn	271.23	10.8	1.08x10^{7}
^{215}Bi	200.39	6.4	5
^{211}Bi$_{\alpha}$	351.07	13.02	1.30x10^{7}

Table A.3: Gammas from the ^{238}U decay chain. A schematic of the decay chain is shown in Figure 3.14

Appendix B

Potential Gamma Backgrounds in DEAP-3600

This section examines gamma backgrounds that have not previously been considered. Table B.1 summarizes the results of a gamma peak search performed on a window of (430 ± 70)keV. Decays with a half-life of less than 20 days (0.055 years) or with intensities less than 0.01% are not considered.

Isotope	Energy [keV]	Half-life [years]	Decay Mode	BR [%]	Intensity [%]
Electrical Components May Contain:					
^{105}Ag	370.17	0.113	EC	100	0.73
^{105}Ag	392.64	0.113	EC	100	1.98
^{105}Ag	401.65	0.113	EC	100	0.174
^{105}Ag	408.00	0.113	EC	100	0.040
^{105}Ag	414.66	0.113	EC	100	0.29
^{105}Ag	420.94	0.113	EC	100	0.105
^{105}Ag	437.12	0.113	EC	100	0.25
^{105}Ag	442.25	0.113	EC	100	4.72
^{105}Ag	443.37	0.113	EC	100	10.5
^{105}Ag	446.74	0.113	EC	100	0.12

^{108m}Ag	433.937	438	EC	91.3	90.5
^{110m}Ag	365.448	0.6838	β	98.64	0.094
^{110m}Ag	387.075	0.6838	β	98.64	0.0525
^{110m}Ag	396.894	0.6838	β	98.64	0.037
^{110m}Ag	446.812	0.6838	β	98.64	3.70
^{110m}Ag	467.01	0.6838	β	98.64	0.0252
^{133}Ba	383.8485	10.551	EC	100	8.94
^{7}Be	477.6035	0.1457	EC	100	10.44
^{115m}Cd	484.47	0.122	β	100	0.29
^{115m}Cd	492.351	0.122	β	100	0.01
^{175}Hf	433.0	0.1917	EC	100	1.44
^{178m2}Hf	426.383	31	IT	N/A	******
^{178m2}Hf	454.05	31	IT	N/A	*******
^{179m2}Hf	362.52	0.0686	IT	N/A	39.6
^{179m2}Hf	409.72	0.0686	IT	N/A	21.5
^{179m2}Hf	453.59	0.0686	IT	N/A	68.0
^{181}Hf	475.99	0.1161	β	100	0.703
^{181}Hf	482.18	0.1161	β	100	80.15
^{103}Ru	443.810	0.1075	β	100	0.339
^{103}Ru	497.075	0.1075	β	100	91.0
^{113}Sn	391.698	0.3151	EC	100	64.97
^{125}Sb	380.452	2.7582	β	100	1.517
^{125}Sb	427.874	2.7582	β	100	29.6
^{125}Sb	443.54	2.7582	β	100	0.306
^{125}Sb	463.365	2.7582	β	100	10.49
^{75}Se	400.657	0.3279	EC	100	11.41
^{75}Se	419.1	0.3279	EC	100	0.012
^{184}Re	384.25	0.4627	EC	25.50	3.17
^{184}Re	482.98	0.104	EC	100	0.019
^{134}Cs	475.365	2.065	β	100	1.477
^{56}Co	411.38	0.2115	EC	100	0.024
^{56}Co	486.54	0.2115	EC	100	0.054
^{166m}Ho	365.75	1200	β	100	2.448
^{166m}Ho	410.797	1200	β	100	0.017
^{166m}Ho	410.949	1200	β	100	11.20
^{166m}Ho	451.542	1200	β	100	2.91

^{166m}Ho	464.832	1200	β	100	1.20
^{166m}Ho	476.378	1200	β	100	0.036
^{166m}Ho	496.923	1200	β	100	0.124
^{192}Ir	374.485	0.2021	EC	4.76	0.727
^{192}Ir	420.51	0.2021	EC	4.76	0.069
^{192}Ir	484.575	0.2021	EC	4.76	3.31
^{192}Ir	489.06	0.2021	EC	4.76	0.438
^{192}Ir	416.469	0.2021	β	95.24	0.670
^{192}Ir	468.069	0.2021	β	95.24	47.84
^{102}Rh	415.25	0.5676	EC	78.0	0.030
^{102}Rh	418.52	0.5676	EC	78.0	0.120
^{102}Rh	456.42	0.5676	EC	78.0	0.080
^{102}Rh	468.58	0.5676	EC	78.0	2.9
^{102}Rh	475.06	0.5676	EC	78.0	46.0
^{102}Rh	415.25	3.742	EC	99.77	2.1
^{102}Rh	418.52	3.742	EC	99.77	9.4
^{102}Rh	420.4	3.742	EC	99.77	3.2
^{102}Rh	475.06	3.742	EC	99.77	95

Table B.1: Gamma lines that exist in and around the ^{36}Ar 0νECEC peak region.

Rare Earth Metals and Exotic Elements

Some elements not listed here such as Europium (Eu), Terbium (Tb), Curium (Cm), Lutetium (Lu), Promethium (Pm), Californium (Cf), and Mendelevium (Md) have gamma emissions in the ^{39}Ar peak region; they are not commonly used in electronics applications and are extremely unlikely to be present in any significant quantities in DEAP-3600.

Electronic Components

These elements could potentially be present in some of the electrical components in DEAP-3600, though any concentrations are unknown:

Ruthenium (Ru) is sometimes used in electrical contacts.

Antimony (Sb) and tin (Sn) are potentially used in solders and may be present in some small quantities outside the AV.

Silver (Ag) is used in electronics; contacts, heat sinks, conductors, etc.

Hafnium (Hf) is used as a getter in vacuum tubes, in filaments and electrondes, and in microprocessors.

Barium (Ba) is used as a getter in vacuum tubes.

Beryllium (Be) is used in electronic components.

Cadmium (Cd) is used in electrical/heat conductive alloys, and possibly in solder.

Selenium (Se) may be used in glass for various reasons.

Cesium (Cs) is used as a getter in vacuum tubes.

Rhenium (Re) is used in electrical contacts.

Other

These elements may be present in other detector components:

Cobalt (Co) is used in stainless steel.

Tellurium (Te) is used in various alloys, including stainless steel.

Holmium (Ho) is used in some high-powered magnets.

Iridium (Ir) was once used in pen tips; it is very rare.

Rhodium (Rh) is used in platinum and palladium alloys.